

**Density Functional Theory  
and Dynamical Mean Field Theory:  
Applications to Correlated Electron Materials**

DISSERTATION

zur Erlangung des Doktorgrades  
der Naturwissenschaften

vorgelegt beim Fachbereich Physik  
der Johann Wolfgang Goethe-Universität  
in Frankfurt am Main

von

Johannes Ferber

aus München

Frankfurt am Main 2012

vom Fachbereich Physik der Johann Wolfgang Goethe-Universität  
als Dissertation angenommen.

Dekan: Prof. Dr. Joachim Stroth

Gutachter: Prof. Dr. Roser Valentí

Jun. Prof. Dr. Lorenz Bartosch

# Zusammenfassung

Die vorliegende Arbeit ist der theoretischen Beschreibung von Festkörpersystemen gewidmet, deren elektronische Eigenschaften wesentlich durch Korrelationen beeinflusst werden. In diesem Zusammenhang sind Korrelationen als der wechselseitige Einfluß der Elektronen mittels der Coulombabstoßung zu verstehen, der sich nicht durch ein auf alle Elektronen wirkendes, gemittelt Potential beschreiben läßt. Die Dynamik der Elektronen wird dabei durch den tatsächlichen, d.h. nicht nur mittleren, Abstand zu den anderen –insbesondere benachbarten– Elektronen bestimmt. Diese Korrelation beeinflusst die Physik der betroffenen Materialien in mannigfaltiger Weise: in vielen Fällen verhalten sich die Ladungsträger in Transportmessungen und spektroskopischen Experimenten wie bewegliche Elektronen im Metall, jedoch mit stark erhöhten effektiven Massen, die bis um das Tausendfache über den Massen freier Elektronen liegen. Für noch stärkere Korrelationen erfolgt eine weitere Einschränkung der Beweglichkeit bis hin zu einem Metall-Isolator Übergang. Weitere Eigenschaften sind reichhaltige Phasendiagramme als Funktion von Temperatur, Druck und Dotierung, sowie magnetische, elektronische und strukturelle Eigenschaften, die sich durch hohe Empfindlichkeit gegenüber äußeren Bedingungen wie dem angelegten magnetischen Feld auszeichnen. Der am intensivsten untersuchte Effekt ist jedoch die unkonventionelle Hochtemperatursupraleitung, die in verschiedenen Klassen korrelierter Materialien auftritt, wobei Wirkungsprinzipien und Zusammenhänge mit elektronischen Korrelationen weiterhin ungeklärt sind.

Andererseits entziehen sich Korrelationen der Beschreibung durch herkömmliche Bandstrukturmethoden wie der Dichtefunktionaltheorie (DFT) in der lokalen Dichtenäherung (LDA), die die Coulombwechselwirkungen zwischen den Elektronen nur auf der Ebene eines zeitlich gemittelten Potentials berücksichtigen. Diese Mittelung ist notwendig, da sich das durch die paarweisen Wechselwirkungen bedingte kombinatorische Problem aufgrund der enormen Anzahl an Elektronen in einem Festkörper nicht direkt behandeln läßt. Als Ansatz zur Lösung dieses Problems hat sich seit Beginn der 1990er Jahre die dynamische Molekularfeldtheorie (DMFT) etabliert, die in der Lage ist, einen Grenzfall von korrelierten Elektronensystemen exakt zu behandeln, nämlich den Grenzfall unendlicher Dimensionalität. Dort besitzt jedes Elektron eine unendliche Anzahl direkt benachbarter Elektronen, wodurch räumliche Fluktuationen einzelner Nachbarn unwichtig werden und die elektronische Umgebung durch ein räumlich strukturloses, jedoch zeitabhängiges –also dynamisches– Feld beschrieben ist. Es findet somit eine räumliche, jedoch keine zeitliche Mittelung des Potentials statt, und die zeitliche Dynamik jedes Elektrons bleibt erhalten. Obwohl dieser Grenzfall in realen System offensichtlich nicht realisiert werden kann, hat er sich als sehr nützlich erwiesen und liefert in vielen Fällen qualitativ und quantitativ zuverlässige Ergebnisse.

Zunächst blieb die Anwendung der DMFT auf die Behandlung minimaler Modelle wie des Hubbardmodells beschränkt. In vielen korrelierten Systemen, einschließlich der in dieser Arbeit untersuchten Materialien, wird das Verhalten jedoch maßgeblich durch das Zusammenspiel der Korrelationen mit den mikroskopischen Details –wie der exakten Kristallstruktur und der elektronischen Bandstruktur– bestimmt, die wiederum zuverlässig durch Bandstrukturrechnungen beschrieben werden. Seit der Jahrtausendwende sind daher verschiedene Ansätze zur Kopplung von Bandstrukturmethoden und DMFT entstanden, insbesondere für die Kombination von DFT und DMFT, genannt LDA+DMFT. Dieser

methodische Rahmen ermöglicht heute im Prinzip *ab-initio* Rechnungen, d.h. Rechnungen ohne freie Parameter, auch für korrelierte Systeme.

Im ersten Kapitel führen wir zunächst den mikroskopischen Hamiltonian im Festkörper ein, von dem wir Gittermodelle zur vereinfachten Beschreibung der elektronischen Struktur ableiten; wir gelangen so zum Hubbardmodell, dem paradigmatischen Modell für korrelierte Elektronen. Wir geben zudem eine knappe Einführung in die im Rahmen dieser Arbeit untersuchten Materialien, wobei es sich um Eisenpniktide sowie Ladungstransfersalze handelt. Bei beiden Klassen von Materialien handelt es sich um geschichtete Systeme, die bei tiefen Temperaturen (und zum Teil bei Dotierung oder unter Druck) unkonventionelle Supraleitung zeigen und in denen die niederenergetischen Elektronen in räumlich eng begrenzten atomaren Eisen-*d* Orbitalen (im Falle der Eisenpniktide) bzw. Orbitalen mit molekularem Charakter (im Falle der Ladungstransfersalze) sitzen und dadurch eine starke Wechselwirkung erfahren.

Im zweiten Kapitel schließt sich eine Beschreibung der DFT an, der Standardmethode zur Berechnung struktureller und elektronischer Eigenschaften von Festkörpern. Dabei gehen wir insbesondere auf die Näherungen ein, die bei der Umsetzung der –formal exakten– DFT in nutzbare Implementierungen erfolgen und diskutieren die resultierenden Schwächen im Hinblick auf die Beschreibung korrelierter Systeme. Eine Abmilderung dieser Schwächen kann im Rahmen der sogenannten LDA+U Methode erfolgen, einer Erweiterung der DFT, die wir im letzten Teil des Kapitels diskutieren.

In Vorbereitung auf die Untersuchung optischer Eigenschaften korrelierter Systeme in den weiteren Kapiteln führen wir dann die mikroskopischen Grundlagen der optischen Leitfähigkeit im dritten Kapitel ein. Wir zeigen die Verbindung zwischen der optischen Leitfähigkeit und experimentell zugänglichen Größen wie der Reflektivität auf und leiten den Formalismus für die Berechnung in DFT sowie LDA+DMFT her.

Im vierten Kapitel wenden wir uns den Eisenpniktiden zunächst im Rahmen einer DFT-Untersuchung zu, wobei der Schwerpunkt auf der Beschreibung der optischen und magnetischen Eigenschaften in der sogenannten SDW-Phase liegt, einer magnetisch geordneten Phase, in der viele undotierte Eisenpniktide bei tiefen Temperaturen vorliegen. Die SDW-Phase ist der supraleitenden Phase im Phasendiagramm benachbart (wobei die Supraleitung unter Verdrängung der magnetischen Ordnung unter Druck oder bei Dotierung eintritt), ist im Gegensatz zu dieser jedoch durch die DFT theoretisch zugänglich. Allerdings führen Quantenfluktuationen in den Eisenpniktiden zu einer starken Reduzierung der magnetischen Momente gegenüber den Vorhersagen aus DFT-Rechnungen. Wir schlagen daher einen Ansatz zur Reduzierung der magnetischen Momente bei gleichzeitiger Erhaltung der elektronischen Struktur im Rahmen der LDA+U Methode vor. Damit sind wir in der Lage, für verschiedene Eisenpniktide Trends in den magnetischen Momenten zu reproduzieren und die wesentlichen Merkmale der optischen Leitfähigkeit korrekt zu beschreiben, allerdings unter Verwendung freier Parameter, nämlich der Wechselwirkungsstärke  $U$  sowie einer Massen- bzw. Energienormierung. Wir stellen jedoch fest, daß diese Parameter für die untersuchten Systeme nur geringe Materialabhängigkeit aufweisen und damit eine einheitliche Beschreibung möglich machen.

Das fünfte Kapitel beginnt mit einer Beschreibung der Grundlagen der DMFT und der Herleitung des zugehörigen Formalismus. Ausgehend vom Grenzfall der unendlichen Dimensionalität läßt sich die Lösung des ursprünglichen Gitterproblems darin auf die Lösung eines (zu bestimmenden) Quantenstörstellenproblems abbilden, was zu einer erheblichen konzeptionellen und numerischen Vereinfachung führt. Im Anschluß gehen wir auf die

Kopplung von DFT und DMFT ein, wobei der Schwerpunkt auf der Konstruktion einer für DMFT benötigten räumlich lokalisierten und orthogonalen Basis aus den in DFT ermittelten Wellenfunktionen liegt. Zuletzt beschreiben wir den zur eigentlichen Lösung des Quantenstörstellenproblems benutzten Quanten-Monte-Carlo Algorithmus.

Der Quanten-Monte-Carlo Algorithmus ist in imaginärer Zeit bzw. imaginären Frequenzen formuliert und die Auswertung der gelieferten Korrelationsfunktionen erfordert daher eine analytische Fortsetzung von der imaginären auf die reelle Achse in der komplexen Ebene. Aufgrund der analytischen Struktur der Korrelationsfunktionen ist diese Fortsetzung in der Praxis sehr empfindlich gegenüber dem statistischen Rauschen aus dem Monte-Carlo Sampling und die Ergebnisse sind oft stark methodenabhängig. Im sechsten Kapitel stellen wir den am weitesten verbreiteten Ansatz für die analytische Fortsetzung vor, die Maximum Entropy Methode, und vergleichen Varianten und Erweiterungen derselben. Dabei behandeln wir auch den Fall bosonischer Korrelationsfunktionen, wie er z.B. für die optische Leitfähigkeit auftritt.

Der so entwickelte methodische Rahmen für LDA+DMFT wird im siebten Kapitel auf das Eisenpniktid LiFeAs angewandt. Dort wird der Einfluß der durch die DMFT berücksichtigten Korrelationen auf verschiedene Aspekte der elektronischen Struktur und insbesondere auf die Fermiflächen untersucht, was schließlich eine vereinheitlichte Interpretation verschiedener Experimente an diesem Material erlaubt.

Im achten Kapitel setzen wir die LDA+DMFT Studien an zwei weiteren Eisenpniktiden –LaFePO und LiFeP– fort und machen die Vorhersage, daß diese beiden Systeme –obwohl nach verschiedenen Kriterien als schwach korreliert zu bewerten– eine topologische Änderung ihrer Fermiflächen bei Berücksichtigung elektronischer Korrelationen zeigen. Wir setzen dieses Ergebnis in Beziehung mit den beobachteten Charakteristika der Supraleitung in diesen Systemen.

Im neunten Kapitel dieser Arbeit präsentieren wir die ersten LDA+DMFT Rechnungen an dem molekularen Kristall  $\kappa$ -(BEDT-TTF)<sub>2</sub>Cu[N(CN)<sub>2</sub>]Cl, welcher zur Klasse der organischen Ladungstransfersalze gehört. Dazu stellen wir als Erweiterung des Konzepts der lokalisierten Basis mit atomarem Charakter die Konstruktion einer Basis mit molekularem Charakter vor. Wie im vierten Kapitel wenden wir uns hier der Untersuchung optischer Eigenschaften zu. Im Unterschied zu den Eisenpniktiden finden wir Signaturen starker Korrelationen in Teilen des Spektrums und identifizieren die Herkunft experimentell beobachteter Anregungen in der optischen Leitfähigkeit.



# *Abstract*

The study of systems whose properties are governed by electronic correlations is a corner stone of modern solid-state physics. Often, such systems feature unique and distinct properties like Mott metal-insulator transitions, rich phase diagrams, and high sensitivity to subtle changes in the applied conditions. Whereas the standard approach to electronic structure calculations, density functional theory (DFT), is able to address the complexity of real-world materials but is known to have serious limitations in the description of correlations, the dynamical mean-field theory (DMFT) has become an established method for the treatment of correlated fermions, first on the level of minimal models and later in combination with DFT, termed LDA+DMFT.

This thesis presents theoretical calculations on different materials exhibiting correlated physics, where we aim at covering a range in terms of systems –from rather weakly correlated to strongly correlated– as well as in terms of methods, from DFT calculations to combined LDA+DMFT calculations. We begin with a study on a selection of iron pnictides, a recently discovered family of high-temperature superconductors with varying degree of correlation strength, and show that their magnetic and optical properties can be assessed to some degree within DFT, despite the correlated nature of these systems. Next, extending our analysis to the inclusion of correlations in the framework of LDA+DMFT, we discuss the electronic structure of the iron pnictide LiFeAs which we find to be well described by Fermi liquid theory with regard to many of its properties, yet we see distinct changes in its Fermi surface upon inclusion of correlations. We continue the study of low-energy properties and specifically Fermi surfaces on two more iron pnictides, LaFePO and LiFeP, and predict a topology change of their Fermi surfaces due to the effect of correlations, with possible implications for their superconducting properties. In our last study, we close the circle by presenting LDA+DMFT calculations on an organic molecular crystal on the verge of a Mott metal-insulator transition; there, we find the spectral and optical properties to display signatures of strong electronic correlations beyond Fermi liquid theory.





# Contents

<b>1</b>	<b>Introduction</b>	<b>1</b>
1.1	From the Ab-initio Hamiltonian to the Hubbard Model . . . . .	1
1.2	Iron Pnictides . . . . .	3
1.3	Charge Transfer Salts . . . . .	4
<b>2</b>	<b>Density Functional Theory and Extensions for Correlated Systems</b>	<b>5</b>
2.1	The Kohn-Sham Approach . . . . .	7
2.2	Basis Sets . . . . .	9
2.3	LDA+U . . . . .	11
<b>3</b>	<b>Optical Conductivity</b>	<b>17</b>
3.1	Optical Conductivity in Linear Response . . . . .	18
3.2	$f$ -sum Rule . . . . .	21
3.3	Optical Conductivity in the Limit of Infinite Dimensions . . . . .	23
3.4	Multiband Case . . . . .	24
3.5	Optical Conductivity in LAPW . . . . .	26
<b>4</b>	<b>Conductivity Spectra of Iron Pnictides in the Spin Density Wave Phase</b>	<b>29</b>
4.1	Introduction . . . . .	29
4.2	Computational Details . . . . .	30
4.3	Results . . . . .	31
4.3.1	Density of States . . . . .	31
4.3.2	Optical Conductivity . . . . .	33
4.4	Conclusions . . . . .	37

<b>5</b>	<b>LDA+DMFT – Dynamical Mean-Field Theory for Real Materials</b>	<b>39</b>
5.1	Dynamical Mean-Field Theory . . . . .	39
5.2	LDA+DMFT . . . . .	45
5.2.1	Construction of a Localized Basis . . . . .	46
5.2.2	Construction of a Molecular Wannier Basis . . . . .	49
5.2.3	Selfconsistency . . . . .	50
5.2.4	Full Charge Selfconsistency . . . . .	51
5.3	CT-HYB Impurity Solver . . . . .	52
<b>6</b>	<b>Analytic Continuation</b>	<b>59</b>
6.1	Maximum Entropy Method . . . . .	60
6.2	Stochastic Analytic Continuation . . . . .	61
6.3	Analytic Continuation of Self Energies . . . . .	63
6.4	Analytic Continuation of Bosonic Response Functions . . . . .	65
<b>7</b>	<b>Correlation Effects in LiFeAs</b>	<b>67</b>
7.1	Introduction . . . . .	67
7.2	Methods and Interaction Parameters . . . . .	68
7.3	Results . . . . .	69
7.3.1	Sensitivity Analysis . . . . .	74
7.3.2	Coherence-Incoherence Crossover . . . . .	76
7.4	Conclusions . . . . .	77
<b>8</b>	<b>Fermi Surface Topology of LaFePO and LiFeP</b>	<b>79</b>
8.1	Introduction . . . . .	79
8.2	Computational Details . . . . .	80
8.3	Results . . . . .	80
8.3.1	Sensitivity Analysis . . . . .	85
8.4	Conclusions . . . . .	85
<b>9</b>	<b>LDA+DMFT for molecular crystals: <math>\kappa</math>-(BEDT-TTF)<sub>2</sub>Cu[N(CN)<sub>2</sub>]Cl</b>	<b>87</b>
9.1	Introduction . . . . .	87
9.2	Computational Details . . . . .	88
9.3	Results . . . . .	89
9.4	Conclusions . . . . .	94

---

<b>10 Summary and Outlook</b>	<b>95</b>
<b>A Fourier Transforms and Expansion Coefficients</b>	<b>97</b>
A.1 Impurity Green's Function . . . . .	100
A.2 Impurity Self Energy . . . . .	100
A.3 Hybridization Function . . . . .	102
A.4 Lattice Green's Function . . . . .	102
A.5 Convolution of Lattice Green's Functions . . . . .	102
<b>B Interaction Matrix Elements for Multiorbital Systems</b>	<b>105</b>
<b>C Calculation of Observables in LDA+DMFT</b>	<b>109</b>
C.1 Spectral Functions . . . . .	109
C.2 Mass Enhancements . . . . .	110
C.3 Fermi Surfaces and de Haas-van Alphen Frequencies . . . . .	110
C.4 Optical Conductivities . . . . .	110
<b>D Spherical Harmonics</b>	<b>113</b>
<b>Bibliography</b>	<b>115</b>



# 1. Introduction

In this chapter, we will first discuss the microscopic Hamiltonian for the electron dynamics in solids and discuss common simplifications in form of models. We will then give a brief introduction to the actual materials under investigation in this thesis.

## 1.1 From the Ab-initio Hamiltonian to the Hubbard Model

The *ab-initio* Hamiltonian governing the electronic properties in solids is given by

$$H = \sum_i^{N_e} \left[ \underbrace{-\frac{\hbar^2}{2m_e} \nabla_i^2}_T - \underbrace{\frac{e^2}{4\pi\epsilon_0} \sum_I^{N_I} \frac{Z_I}{|\mathbf{r}_i - \mathbf{R}_I|}}_V \right] + \underbrace{\frac{1}{2} \frac{e^2}{4\pi\epsilon_0} \sum_{i \neq j}^{N_e} \frac{1}{|\mathbf{r}_i - \mathbf{r}_j|}}_U, \quad (1.1)$$

for a system of  $N_e$  electrons and  $N_I$  ions where  $\mathbf{r}_i$  ( $\mathbf{R}_I$ ) denotes the position of electron  $i$  (ion  $I$ ) with electric charge  $-e$  ( $eZ_I$ ) and mass  $m_e$ , respectively. The Hamiltonian thus consists of three terms, the kinetic energy of the electrons  $T$ , the electron-ion Coulomb interaction  $V$ , and the electron-electron Coulomb interaction  $U$ . We already employed the Born-Oppenheimer approximation here, namely that the ions can be treated as spatially fixed due to their large mass and the electrons as moving in the electrostatic potential of the static ionic lattice.

The difficulty in solving the Hamiltonian (1.1) lies in the combinatorics of the two-particle electron-electron interaction which prevents separating  $H$  into a sum of one-particle Hamiltonians: while the electron-ion interaction  $V$  can be cast into a potential (termed lattice potential or external potential) in which the electrons move independently, the same is not true for the electron-electron interaction.

There is a fundamental dichotomy between two approaches dealing with this problem. The first approach deals with the Hamiltonian (1.1) directly by employing dramatic approximations on the  $U$  term. This approach is followed by density functional theory <sup>1</sup> (DFT),

---

<sup>1</sup>More exactly, it is followed by practical implementations of DFT, in particular through approximations made for the exchange-correlation energy. As a theory, DFT is exact.

as described in Ch. 2. This approach is free of parameters and allows calculations based only on first principles (*ab-initio*).

The other approach makes simplifications already on the level of the Hamiltonian by investigating minimal models which (ideally) capture the relevant interaction physics. By definition, these models require parameterization, though, thereby losing the *ab-initio* character of the original problem and introducing a potential source of ambiguity.

A first simplification is achieved by the mapping of the continuum problem (1.1) onto a lattice model in a basis of localized Wannier states. In second quantization, the resulting Hamiltonian reads

$$H = - \sum_{\nu\mu} \sum_{ij} \sum_{\sigma} t_{ij}^{\nu\mu} c_{i,\nu,\sigma}^{\dagger} c_{j,\mu,\sigma} + \frac{1}{2} \sum_{\nu\nu'\mu\mu'} \sum_{ijkl} \sum_{\sigma\sigma'} V_{ijkl}^{\nu\mu\nu'\mu'} c_{i,\nu,\sigma}^{\dagger} c_{j,\mu,\sigma'}^{\dagger} c_{l,\mu',\sigma'} c_{k,\nu',\sigma}, \quad (1.2)$$

where the creation (annihilation) operator  $c_{i,\nu,\sigma}^{\dagger}$  ( $c_{i,\nu,\sigma}$ ) creates (annihilates) an electron with spin  $\sigma$  in the band  $\nu$  at the site  $\mathbf{R}_i$ . The Hamiltonian (1.2) consists of a hopping term parameterized by the  $t$ 's, reflecting the noninteracting dispersion due to the kinetic energy and the potential in Eq. (1.1), and an interaction term parameterized by the  $V$ 's. However, even this simplified model contains an infinite number of parameters  $\{t_{ij}^{\nu\mu}, V_{ijkl}^{\nu\mu\nu'\mu'}\}$ . In order to limit the number of parameters, often only the largest contributions to the Hamiltonian are kept. From the Wannier functions, it can be shown that for the interaction term the onsite contribution largely dominates,

$$V_{ijkl}^{\nu\mu\nu'\mu'} = U^{\nu\mu\nu'\mu'} \delta_{ij} \delta_{ik} \delta_{il}, \quad (1.3)$$

leading to the Hamiltonian

$$H = - \sum_{\nu\mu} \sum_{ij} \sum_{\sigma} t_{ij}^{\nu\mu} c_{i,\nu,\sigma}^{\dagger} c_{j,\mu,\sigma} + \frac{1}{2} \sum_{\nu\nu'\mu\mu'} \sum_i \sum_{\sigma\sigma'} U^{\nu\mu\nu'\mu'} c_{i,\nu,\sigma}^{\dagger} c_{i,\mu,\sigma'}^{\dagger} c_{i,\mu',\sigma'} c_{i,\nu',\sigma}. \quad (1.4)$$

This is the model that is effectively solved in Chs. 7, 8, and 9 in the framework of LDA+DMFT (within the approximations imposed by LDA, DMFT, and the employed solver, cf. the respective chapters). If the Hamiltonian is furthermore restricted to one band ( $\nu = \nu' = \mu = \mu' = 1$ ), one arrives at

$$H = - \sum_{ij} \sum_{\sigma} t_{ij} c_{i,\sigma}^{\dagger} c_{j,\sigma} + U \sum_i n_{i,\uparrow} n_{i,\downarrow}, \quad (1.5)$$

(with  $n_{i,\sigma} = c_{i,\sigma}^{\dagger} c_{i,\sigma}$ ) which will be used in Ch. 5 to motivate and derive the equations for DMFT and the employed impurity solver.

Finally, if only nearest neighbor (NN) terms are considered in the hopping,

$$t_{ij} = \begin{cases} t & \text{if } i \text{ NN of } j \\ 0 & \text{otherwise} \end{cases}, \quad (1.6)$$

one obtains the Hubbard model,

$$H = -t \sum_{\langle i,j \rangle} \sum_{\sigma} (c_{i,\sigma}^{\dagger} c_{j,\sigma} + \text{h.c.}) + U \sum_i n_{i,\uparrow} n_{i,\downarrow}, \quad (1.7)$$

the paradigmatic model for strongly correlated fermions on a lattice;  $\langle i, j \rangle$  restricts the sum to nearest neighbor pairs. Although appearing simple (in the grand canonical ensemble, the

model is fully specified by the parameters  $t$  and  $U$ , the underlying lattice, the temperature, and the filling), an exact solution for the Hubbard model is not available, except for the case of one dimension [Bethe31, Lieb68], and the study of this model has evolved into a whole field of research on its own. The charge and spin degrees of freedom of the Hubbard model give rise to a variety of different phases like Fermi liquid, Mott insulator, antiferromagnet, charge- and spin-density wave, superconductor, and others. The difficulty in solving the Hubbard model and –at the same time– its rich physics both originate from the fact that the interaction term (which is diagonal in real space) and the hopping term (which is diagonal in  $\mathbf{k}$  space) cannot be diagonalized simultaneously but compete with each other: considering *e.g.* the half filled case at low temperatures, the system is for weak interactions in a metallic, or Fermi liquid, phase which is described by noninteracting, yet mass-enhanced quasiparticles. At a critical interaction strength, the charge degrees of freedom freeze out as double occupations become energetically very unfavorable and hopping between the sites is strongly suppressed: the system has entered an insulating phase, called Mott insulator. Hence, in the limit of strong interactions ( $U/t \rightarrow \infty$ ) and for half filling, only the spin degrees of freedom persist and the Hubbard model simplifies to the quantum Heisenberg model. For large interactions but away from half filling, double occupancies are also forbidden, but the presence of empty sites still allows for motion of charge carriers: this limit is described by the  $t - J$  model [Chao77].

In Ch. 5, we will first introduce dynamical mean-field theory as a non-perturbative approach to the treatment of the Hubbard model in a special limit, the limit of infinite dimensions, and subsequently show how to combine the *ab-initio* approach and model calculations in the framework of LDA+DMFT.

## 1.2 Iron Pnictides

In 2008, the discovery of superconductivity at a transition temperature of 26 K in fluorine-doped LaFeAsO [Kamihara08] marked the beginning of a global research effort dedicated to the study of this new class of iron-based superconductors, with observed transition temperatures up to  $\sim 56$  K [Wu09b] to date. In the following, we give a very brief overview over some basic properties of these compounds; for further reading, a number of reviews is already available, see *e.g.* Refs. [Johnston10, Paglione10, Lumsden10, Stewart11, Hirschfeld11].

The basic building blocks of the iron-based superconductors are layers of FePn/Ch tetrahedra where the pnictogen “Pn” stands for As or P (iron pnictides) and the chalcogen “Ch” includes S, Se, and Te (iron chalcogenides). In the following, we refer to all these materials as iron pnictides. In terms of crystal structures, there are currently six families of iron pnictides known; the largest families in terms of the number of known compounds are the “122” family (with *e.g.* BaFe<sub>2</sub>As<sub>2</sub> and SrFe<sub>2</sub>As<sub>2</sub> as representatives) and the “1111” family (with LaFeAsO as most studied example). In all compounds, the states close to the Fermi energy are predominantly occupied by the Fe  $3d$  electrons where typically all five orbitals contribute to the low-energy physics and have to be retained in calculations. In the normal state, the iron pnictides are metals, with two or more hole bands crossing the Fermi level near the  $\Gamma$  point and two electron bands crossing near the  $M$  point (in most compounds). This is reflected by the formation of typically four or five Fermi surface sheets.

While the superconducting pairing mechanism in the iron pnictides is not known, it may be related to the coexistent, respectively neighboring, magnetism in the phase diagram. Most

parent (*i.e.* undoped) compounds exhibit a non-superconducting ground state with antiferromagnetic (AF) stripe-type order[Ishida09]. Upon (electron or hole) doping[Kamihara08] or application of external pressure[Torikachvili08], superconductivity emerges (up to some maximal doping level) and the AF order is either suppressed (*e.g.* in LaFeAsO) or persists over some finite doping range (in the 122 systems). Due to the good Fermi surface nesting in many parent compounds, the onset of the AF order is often attributed to a spin-density wave (SDW) instability[Singh09]; however, the mechanism of the magnetic ordering is not conclusively understood yet and might also include the formation of local moments.

As for the superconductivity in the iron pnictides, the gap symmetry is generally believed to be of s-type, probably involving a sign change of the order parameter between the electron and hole sheets of the Fermi surface in most materials[Hirschfeld11]; for the actual gap structure, there is evidence for strong diversity among the different compounds, including both nodal and nodeless gaps. In many cases, the angle of the bonds in the tetrahedra as well as the height of the Pn/Ch above the Fe plane seem to be indicators for the superconducting transition temperature[Kuroki09].

The correlation strength in the iron pnictides is subject to sizable variation between the different families, from rather weak correlations in the 1111 family (*e.g.* LaFePO) to strongly correlated compounds in the 11 family (*e.g.* FeSe). LDA+DMFT studies favoring an itinerant scenario with rather moderate correlation strength (*e.g.* for the description of the antiferromagnetically ordered state) are found *e.g.* in Refs. [Aichhorn09, Skornyakov09, Skornyakov10], whereas other authors point out the effects of strong correlations[Yang09, Si08, Haule08, Yildirim08, Han09, Ma09].

### 1.3 Charge Transfer Salts

The organic charge transfer salts are a family of unconventional superconductors encompassing a range of materials with rather different ground states and properties. In general, charge transfer salts are formed when a number of donor molecules jointly donate an electron to an anion molecule, leaving behind a hole which is shared among the donors. Typically, the donor molecules are stacked in layers which are separated by planes of the anion molecules. The anion layers, however, do not contribute to the low-energy physics of the materials and the electronic properties can for many purposes be regarded as two-dimensional. While being chemically complex, the electronic structure of the materials is simple and is often reduced to a single-band Hubbard model on various lattices at half or one-quarter filling[Powell06].

The charge transfer salts are uniquely well-suited as model systems as they are available in very pure samples and allow to be finely tuned through their phase diagram by chemical substitution, magnetic fields, or moderate pressures. They are strongly correlated and their observed phases include –besides the superconducting phase– metals, Fermi liquids, Mott insulators, antiferromagnets, and spin liquids[Kanoda11, Powell11].

The superconductivity in the charge transfer salts occurs in proximity to a Mott insulating phase and is supposed to be closely related to antiferromagnetism, like in the cuprates or the iron pnictides. The symmetry of the superconducting gap is not settled yet, but there is substantial evidence that the superconducting state is unconventional and experiments suggest a nodal gap and *d*-wave symmetry[Arai01, Shimizu10]. Among all organic compounds, the charge transfer salt  $\kappa$ -(BEDT-TTF)<sub>2</sub>Cu[N(CN)<sub>2</sub>]Cl studied in Ch. 9 has the highest transition temperature  $T_c = 12.5$  K [Williams90] (at a small hydrostatic pressure of 0.3 kbar).



## 2. Density Functional Theory and Extensions for Correlated Systems

In solid state physics, the most successful method for the calculation of material properties is density functional theory (DFT). It is routinely applied for calculating lattice properties (equilibrium volumes, lattice parameters, atomic positions, phonon spectra, elastic constants) as well as electronic properties (band structures, optical excitation spectra, band gaps). However, whereas lattice properties are usually reproduced with an accuracy of a few percent as they are linked to the total energy of the ground state, the calculation of electronic structures, while being sufficiently accurate in many cases, can suffer from systematic errors. In particular, the band gaps of insulators and semiconductors are often underestimated, and many insulators are even metals in DFT; this is most pronounced in materials with partially filled  $d$ - or  $f$ -shells, where –due to the short electron-electron distance in these narrow orbitals– electronic correlations are particularly strong.

There are different reasons for these limitations, both from a fundamental and a practical point of view, that will become manifest in the discussion of DFT below but are briefly mentioned here. First, while constituting a formally exact theory for ground state properties, the application of DFT to excited states (like the calculation of band structures, *i.e.* of excitation energies of electrons being added to or removed from the system) is not rigorously justified, since the underlying Hohenberg-Kohn theorem only holds for the ground state. Furthermore, the solution of the DFT equations typically involves mapping the interacting system to a fictitious non-interacting system –the Kohn-Sham system– whose electronic structure, in principle, cannot be considered an approximation to the real electronic structure; yet its energy eigenvalues are commonly interpreted as the single-particle energies of the real system. Moreover, in practice, approximations have to be made also for the ground state to describe exchange and correlation effects, with the local density approximation (LDA) as the most prominent example.

Despite these shortcomings, DFT is also tremendously successful in the calculation of electronic properties and in many cases yields good agreement with experimental data. Moreover, its versatility and solid theoretical foundation allow for continuous improvement of the involved approximations within the DFT framework. Importantly, DFT is also well-suited for the combination with many body methods like static and dynamical mean-field

theories that we will use in this thesis to address the issue of strongly correlated systems. Many reviews on density functional theory are available; the following overview is inspired in particular by the presentation in Ref. [Capelle06].

At its most basic level, DFT rephrases the many body problem (1.1) as the problem of minimizing a functional of the electron density  $\rho(\mathbf{r})$  which is given by

$$\rho(\mathbf{r}) = \langle \Psi | \sum_i^{N_e} \delta(\mathbf{r} - \mathbf{r}_i) | \Psi \rangle . \quad (2.1)$$

The promotion of  $\rho(\mathbf{r})$  to the status of the key variable in DFT is based on the fundamental theorem behind DFT, the Hohenberg-Kohn theorem[Hohenberg64]. It states that for ground states, Eq. (2.1) can be inverted, *i.e.* the ground state density uniquely determines the (many body) ground state wave function and consequently all ground state observables. At first glance this appears to result in a tremendous loss of information, given that the wave function is a function of  $N_e$  vectorial variables  $\mathbf{r}_1, \dots, \mathbf{r}_{N_e}$ , whereas the density is a function of only one vectorial variable  $\mathbf{r}$ . However, the ground state wave function must not only reproduce the ground state density but also minimize the energy.

From this, the second Hohenberg-Kohn theorem can be derived which is the most important from the point of view of practical applications: not only is the total energy a functional of the electron density,  $E = E[\rho(\mathbf{r})]$ , but it is minimized at the ground state density  $\rho_0(\mathbf{r})$ , *i.e.*  $E$  has the variational property

$$E_0 = E[\rho_0] \leq E[\tilde{\rho}] , \quad (2.2)$$

with  $E_0$  the ground state energy and  $\tilde{\rho}$  a trial density which integrates to the total number of electrons. The constraint on the total particle number obtained from  $\rho$  can be taken into account by means of a Lagrange multiplier  $\mu$  (the chemical potential), replacing the constrained minimization of  $E$  by an unconstrained one,

$$\delta \left\{ E[\rho] - \mu \left( \int d^3r \rho(\mathbf{r}) - N_e \right) \right\} = 0 , \quad (2.3)$$

from which an Euler-Lagrange equation follows,

$$\frac{\delta E[\rho]}{\delta \rho(\mathbf{r})} = \mu . \quad (2.4)$$

Formally, the total energy functional can be written in terms of the three contributions identified in the Hamiltonian (1.1),

$$E[\rho] = T[\rho] + U[\rho] + V[\rho] , \quad (2.5)$$

where  $T[\rho]$  and  $U[\rho]$  are universal functionals, *i.e.* their functional form does not depend on the system under investigation. However, this form is not known explicitly, and we will discuss approximation schemes below. In contrast,  $V[\rho]$  has a known analytical form,

$$V[\rho] = \int d^3r \rho(\mathbf{r}) v(\mathbf{r}) , \quad (2.6)$$

with the Coulomb potential of the ions

$$v(\mathbf{r}) = -\frac{e^2}{4\pi\epsilon_0} \sum_I^{N_{\text{Ion}}} \frac{Z_I}{|\mathbf{r} - \mathbf{R}_I|} , \quad (2.7)$$

but is material specific. In fact, all information about the material is contained in  $v(\mathbf{r})$ .<sup>1</sup>

The unknown functional form of  $T[\rho]$  and  $U[\rho]$  calls for approximations. An illustrative example is the Thomas-Fermi approximation where only the Hartree term in  $U[\rho]$  is retained,

$$U[\rho] \approx U_H[\rho] = \frac{1}{2} \frac{e^2}{4\pi\epsilon_0} \int d^3r \int d^3r' \frac{\rho(\mathbf{r})\rho(\mathbf{r}')}{|\mathbf{r} - \mathbf{r}'|}, \quad (2.8)$$

*i.e.* the full interaction energy is approximated by the classical electrostatic interaction energy of the distribution  $\rho(\mathbf{r})$ .

For the kinetic energy term, an analytical expression in terms of the density is known only for a uniform electron gas (with average density  $n$ ) of noninteracting electrons which we call  $T_{\text{non}}^{\text{hom}}(n)$ ; note that  $T_{\text{non}}^{\text{hom}}(n)$  is a function, not a functional. This is exploited to approximate  $T[\rho]$  as

$$T[\rho] \approx \int d^3r T_{\text{non}}^{\text{hom}}(\rho(\mathbf{r})), \quad (2.9)$$

*i.e.* not only is the interacting electron system taken as noninteracting, but a local density approximation (LDA) is employed which substitutes the inhomogeneous system by a sum (or integral) over small volume units, each with constant density.

While the local density approximation can often be applied successfully to the so-called exchange-correlation energy that we will encounter in the following, it turns out to be too crude of an approximation for the kinetic energy in most applications. However, the LDA ansatz for the kinetic energy can be dropped in the framework of the Kohn-Sham approach [Kohn65], the most widely used method for practical DFT.

## 2.1 The Kohn-Sham Approach

The Kohn-Sham (KS) approach does not work exclusively in terms of the density, but to some extent returns to the language of (single-particle) wave functions. As a result, the KS framework formally resembles a single-particle theory, although many body effects are still included via the so-called exchange-correlation functional.

In the KS approach, the kinetic energy is decomposed into a term  $T_{\text{non}}$ , representing noninteracting particles (of density  $\rho$ ), and the remainder  $T_c$ ,

$$T[\rho] = T_{\text{non}}[\rho] + T_c[\rho], \quad (2.10)$$

where  $T_{\text{non}}$  can be expressed in terms of the single-particle KS orbitals,

$$T_{\text{non}} = -\frac{\hbar^2}{2m_e} \sum_i^{N_e} \int d^3r \psi_i^*(\mathbf{r}) \nabla^2 \psi_i(\mathbf{r}) \quad (2.11)$$

---

<sup>1</sup>This offers a slightly different point of view regarding the equivalent information contained in  $\rho$  and  $\Psi$ : being the solution to the Schrödinger equation,  $\Psi$  is determined by the Hamiltonian  $H$ . However, the specific form of  $H$  only differs with the external potential which is also a function of only one variable. In fact, the Hohenberg-Kohn theorem also states that  $v(\mathbf{r})$  is uniquely determined by  $\rho_0$ , up to an additive constant. Interestingly, this also means that  $\rho_0$  not only fixes the ground state wave function but also that of all excited states.

with density ( $f_i$  being the occupation of orbital  $i$ )

$$\rho(\mathbf{r}) = \sum_i^{N_e} f_i |\psi_i(\mathbf{r})|^2, \quad (2.12)$$

without resorting to a local density approximation or the like.<sup>2</sup> The exact energy functional (2.5) is thus given as

$$E[\rho] = T_{\text{non}}[\{\psi_i[\rho]\}] + U_H[\rho] + V[\rho] + \underbrace{T[\rho] - T_{\text{non}}[\{\psi_i[\rho]\}] + U[\rho] - U_H[\rho]}_{E_{xc}[\rho]}, \quad (2.13)$$

where all otherwise neglected terms have been cast into the universal exchange-correlation energy  $E_{xc}[\rho]$ . Physically,  $E_{xc}$  contains the contributions from the exchange energy and from correlations ( $T_c$  is part of the correlations), hence the name. Again, the functional form of  $E_{xc}[\rho]$  is unknown, and for its (approximate) determination one faces the same problems that motivated expression (2.9) for the kinetic term, namely inhomogeneity and the many body nature of exchange and correlation. Assuming homogeneity, the difficulties due to the many body nature can be efficiently addressed, though: the exchange energy of the homogeneous electron gas is known exactly, and for the correlation energy highly accurate Quantum Monte Carlo results are available[Ceperley80]. Regarding the inhomogeneity, the local density approximation in the spirit of Eq. (2.9),

$$E_{xc}[\rho] \approx E_{xc}^{\text{LDA}}[\rho] = \int d^3r \epsilon_{xc}(\rho(\mathbf{r})), \quad (2.14)$$

works astonishingly well for a huge variety of systems, including many that are quite different from the reference system of the LDA, namely from a system with slowly varying electron density.

The Euler-Lagrange equation now reads

$$\frac{\delta T_{\text{non}}[\{\psi_i[\rho]\}]}{\delta \rho(\mathbf{r})} + v_H(\mathbf{r}) + v(\mathbf{r}) + v_{xc}(\mathbf{r}) = \mu, \quad (2.15)$$

with  $v(\mathbf{r})$  the external potential (2.7),  $v_{xc}(\mathbf{r}) = \frac{\delta E_{xc}[\rho]}{\delta \rho(\mathbf{r})}$ , and the Hartree potential  $v_H(\mathbf{r})$  following from the expression (2.8) for the Hartree energy,

$$v_H(\mathbf{r}) = \frac{\delta U_H[\rho]}{\delta \rho(\mathbf{r})} = \frac{e^2}{4\pi\epsilon_0} \int d^3r' \frac{\rho(\mathbf{r}')}{|\mathbf{r} - \mathbf{r}'|}. \quad (2.16)$$

Since  $T_{\text{non}}[\{\psi_i[\rho]\}]$  is now written as an orbital functional, a direct minimization with respect to  $\rho(\mathbf{r})$  is not possible, though. However, the wave functions  $\{\psi_i\}$  are the solutions of a set of  $N_e$  one-electron Schrödinger equations,

$$\left[ -\frac{\hbar^2}{2m_e} \nabla^2 + \frac{e^2}{4\pi\epsilon_0} \int d^3r' \frac{\rho(\mathbf{r}')}{|\mathbf{r} - \mathbf{r}'|} + v(\mathbf{r}) + v_{xc}(\mathbf{r}) \right] \psi_i(\mathbf{r}) = \epsilon_i \psi_i(\mathbf{r}). \quad (2.17)$$

These are the Kohn-Sham equations. It is important to note that, in principle, they only serve the purpose of replacing the minimization of  $E[\rho]$  by the solution of a noninteracting Schrödinger equation. The noninteracting KS system is therefore purely auxiliary, only

<sup>2</sup>According to the Hohenberg-Kohn theorem, all  $\psi_i(\mathbf{r})$  are functionals of  $\rho$  and so is  $T_{\text{non}}$  (although with an unknown form) which we make transparent by writing  $T_{\text{non}}[\{\psi_i[\rho]\}]$  henceforth.

the density  $\rho(\mathbf{r})$  obtained from the KS orbitals via Eq. (2.12) is physical. In particular, the KS eigenvalues  $\varepsilon_i$  are not physical single-particle energies (in fact, they are Lagrange multipliers). Nevertheless, they typically bear a semiquantitative resemblance with the true energy spectrum and are therefore commonly interpreted as approximations to the real single-particle energies. Since the KS system is noninteracting, this amounts to a mean-field approximation, albeit with a sophisticated mean-field  $v_H(\mathbf{r}) + v(\mathbf{r}) + v_{xc}(\mathbf{r})$ .

As both  $\rho(\mathbf{r})$  and  $v_{xc}(\mathbf{r})$  depend on the KS orbitals, *i.e.* on the solution of the KS equations, the KS equations are nonlinear and have to be solved self-consistently: starting from an initial guess for the density, the KS equations are solved numerically, a new density is obtained from Eq. (2.12), and a new cycle is started. This prescription is repeated until convergence (*e.g.* in the energy, the density, and/or some other observable) is attained.

## 2.2 Basis Sets

In practice, numerical solutions of the KS equations proceed by expanding the KS orbitals in a suitable set of basis functions  $\{\phi_{n\mathbf{k}}(\mathbf{r})\}$ ,

$$\psi_{i\mathbf{k}}(\mathbf{r}) = \sum_n^P c_i^n \phi_{n\mathbf{k}}(\mathbf{r}), \quad (2.18)$$

(with  $\mathbf{k}$  the lattice momentum,  $P$  the number of basis functions, and  $c_i^n$  the expansion coefficients) and solving the resulting secular equation for the coefficients  $c_i^n$  and the eigenvalues (we suppress the  $\mathbf{k}$  index here),

$$\begin{pmatrix} \langle \phi_1 | H_{\text{KS}} | \phi_1 \rangle & \langle \phi_1 | H_{\text{KS}} | \phi_2 \rangle & \cdots \\ \langle \phi_2 | H_{\text{KS}} | \phi_1 \rangle & \langle \phi_2 | H_{\text{KS}} | \phi_2 \rangle & \cdots \\ \vdots & \vdots & \ddots \end{pmatrix} \begin{pmatrix} c_i^1 \\ c_i^2 \\ \vdots \end{pmatrix} = \varepsilon_i \begin{pmatrix} \langle \phi_1 | \phi_1 \rangle & \langle \phi_1 | \phi_2 \rangle & \cdots \\ \langle \phi_2 | \phi_1 \rangle & \langle \phi_2 | \phi_2 \rangle & \cdots \\ \vdots & \vdots & \ddots \end{pmatrix} \begin{pmatrix} c_i^1 \\ c_i^2 \\ \vdots \end{pmatrix}, \quad (2.19)$$

where  $H_{\text{KS}}$  is the Kohn-Sham Hamiltonian. Note that the basis functions are not necessarily orthogonal; this is reflected by the overlap matrix with matrix elements  $\langle \phi_i | \phi_j \rangle$  on the right hand side.

A variety of different basis sets exists, each with individual strengths and weaknesses. Ideally, a basis set is both efficient, *i.e.* it attains high accuracy with a small number of basis functions, and unbiased, *i.e.* it does not favor a particular kind of result. These requirements are to some extent conflicting, and actual basis sets aim to balance them, often with stronger focus on one property or the other. In this thesis, we make use of a basis set combining augmented plane waves (APW) and linearized augmented plane waves (LAPW); these basis sets will therefore be discussed in the following.

The (L)APW basis[Andersen75, Wimmer81] exploits the fact that close to the atomic nuclei, the crystalline potential in a solid is similar to the one of a single atom, whereas far away from the nuclei, the potential is weakly varying and the electrons move rather freely. Consequently, the space is divided into nonoverlapping atomic spheres, termed muffin-tin (MT) spheres, which are located at the atomic positions, and the interstitial (I) region between the MT spheres. Inside the MT sphere, the KS orbital is then expressed

by atomiclike functions, whereas in the interstitial region the (L)APW simply takes the form of a plane wave,

$$\phi_{\mathbf{G},\mathbf{k}}^{\text{LAPW}}(\mathbf{r}) = \begin{cases} \frac{1}{\sqrt{V}} e^{i(\mathbf{k}+\mathbf{G})\mathbf{r}}, & \mathbf{r} \in \text{I} \\ \sum_{\ell,m} \left[ A_{\ell,m}^{\alpha,\mathbf{k}+\mathbf{G}} u_{\ell}^{\alpha}(r, E_{1,\ell}^{\alpha}) + B_{\ell,m}^{\alpha,\mathbf{k}+\mathbf{G}} \dot{u}_{\ell}^{\alpha}(r, E_{1,\ell}^{\alpha}) \right] Y_{\ell,m}(\vartheta, \varphi), & \mathbf{r} \in \text{MT} \end{cases}, \quad (2.20)$$

where  $\mathbf{G}$  is a reciprocal lattice vector,  $V$  the unit cell volume,  $Y$  a spherical harmonic (D.1),  $r$  and  $\{\vartheta, \varphi\}$  are the radial and angular parts of the position vector  $\mathbf{r}$ , respectively, and  $u_{\ell}^{\alpha}(r, E_{1,\ell}^{\alpha})$  and  $\dot{u}_{\ell}^{\alpha}(r, E_{1,\ell}^{\alpha})$  are the solutions to the radial part of the Schrödinger equation of an isolated atom  $\alpha$  and their energy derivatives, respectively, evaluated at energy  $E_{1,\ell}^{\alpha}$ . The coefficients  $A_{\ell,m}$  and  $B_{\ell,m}$  are determined from the requirement that the wave function inside the MT sphere matches the plane wave outside the sphere over the complete surface of the sphere in value (otherwise the kinetic energy would not be well-defined) and slope.<sup>3</sup> The form of the LAPW basis is derived from the APW basis which misses the  $B_{\ell,m}\dot{u}_{\ell}$  term within the MT sphere. It turns out, however, that for an accurate description of a state in terms of APWs, one has to set the energy  $E$  in the argument of  $u$  equal to the respective eigenenergy, which leads to a nonlinear secular problem (the eigenenergy is part of the solution). Therefore, the LAPW basis substitutes this energy by a linearization energy  $E_{1,\ell}^{\alpha}$  (the index '1' is used in order to differentiate from an energy that appears in the local orbitals below) and the first term in the corresponding Taylor expansion (hence the derivative term  $\dot{u}$  and the matching slope as criteria for the fixing of the  $B_{\ell,m}$  coefficients). The linearization energies are then input parameters which are chosen close to the (at this point unknown) energy of the respective orbital (*i.e.* the energy of the center of the respective band(s) with that dominating orbital character); typically, the linearization energies can be guessed from the solution of the respective atomic problem.

The wave function expansion in Eq. (2.20) is appropriate for valence states. In contrast, core states are tightly bound to the nucleus and do not participate in the chemical bonding with other atoms. Such core states are treated the same as in isolated atoms (and thus very efficiently), but subject to the potential due to the valence states. In addition, so-called semi-core states are not completely confined in the core, but a treatment in the basis (2.20) poses problems for the choice of the linearization energy, since the semicore band may have the same  $\ell$  quantum number as the valence band (but a different shell  $n$ ) and there is no choice for  $E_{1,\ell}$  that fits both bands (they might be very different in energy). The LAPW basis is therefore complemented by local orbitals (LO),

$$\phi_{\alpha,\ell,m}^{\text{LAPW,LO}}(\mathbf{r}) = \left[ A_{\ell,m}^{\alpha,\text{LO}} u_{\ell}^{\alpha}(r, E_{1,\ell}^{\alpha}) + B_{\ell,m}^{\alpha,\text{LO}} \dot{u}_{\ell}^{\alpha}(r, E_{1,\ell}^{\alpha}) + C_{\ell,m}^{\alpha,\text{LO}} u_{\ell}^{\alpha}(r, E_{2,\ell}^{\alpha}) \right] Y_{\ell,m}(\vartheta, \varphi), \quad (2.21)$$

which have no  $\mathbf{k}$ -dependence and are defined only inside the MT sphere of a particular atom  $\alpha$ . The semi-core state –described by the  $C_{\ell,m}$  term– is peaked at an energy  $E_{2,\ell}^{\alpha} \neq E_{1,\ell}^{\alpha}$  ( $E_{2,\ell}^{\alpha}$  is close to its atomic value and thus approximately known) and is described by a single radial function  $u_{\ell}^{\alpha}$  (there is no sum over  $\ell, m$  in Eq. (2.21)) due to its quasi-atomic nature. The coefficients  $A_{\ell,m}$ ,  $B_{\ell,m}$ , and  $C_{\ell,m}$  are obtained by normalizing the orbital and setting its value and slope at the MT boundary to zero; *i.e.* the local orbital is completely contained in the MT sphere.

---

<sup>3</sup>Strictly speaking, an exact matching cannot be attained with a limited number of  $A/B$  coefficients, but it can be made sufficiently accurate from a practical point of view with a reasonably small number of coefficients.

Alternatively, the energy dependence of the APW basis can be circumvented by another linearization scheme termed APW+lo where 'lo' stands for 'local orbitals' but (confusingly) of another type than the 'LO' orbitals above. The APW+lo basis set contains two kinds of functions. The first kind are the regular APWs, but evaluated at a fixed energy  $E_{1,\ell}^\alpha$  (*i.e.* not at self-consistently determined KS energies, which is to be avoided due to performance reasons),

$$\phi_{\mathbf{G},\mathbf{k}}^{\text{APW}}(\mathbf{r}) = \begin{cases} \frac{1}{\sqrt{V}} e^{i(\mathbf{k}+\mathbf{G})\mathbf{r}}, & \mathbf{r} \in \text{I} \\ \sum_{\ell,m} A_{\ell,m}^{\alpha,\mathbf{k}+\mathbf{G}} u_\ell^\alpha(r, E_{1,\ell}^\alpha) Y_{\ell,m}(\vartheta, \varphi), & \mathbf{r} \in \text{MT} \end{cases}, \quad (2.22)$$

where  $A_{\ell,m}$  is again determined from the requirement for  $\phi_{\mathbf{G},\mathbf{k}}^{\text{APW}}(\mathbf{r})$  to be continuous at the MT sphere boundary. Since the APW basis (2.22) is known to be insufficiently accurate (which led to the construction of the LAPW basis), it is augmented with a second type of function for the physically important orbitals which is defined only within the MT sphere,

$$\phi_{\alpha,\ell,m}^{\text{APW,lo}}(\mathbf{r}) = \left[ A_{\ell,m}^{\alpha,\text{lo}} u_\ell^\alpha(r, E_{1,\ell}^\alpha) + B_{\ell,m}^{\alpha,\text{lo}} \dot{u}_\ell^\alpha(r, E_{1,\ell}^\alpha) \right] Y_{\ell,m}(\vartheta, \varphi), \quad (2.23)$$

with  $A_{\ell,m}$  and  $B_{\ell,m}$  chosen such that the value and the slope of  $\phi^{\text{APW,lo}}$  vanish at the MT sphere boundary.

In analogy to the LOs introduced in Eq. (2.21) for LAPW, the APW+lo basis can be extended by LOs which, however, do not contain the  $B_{\ell,m} \dot{u}_\ell$  term of Eq. (2.21). Again, the two coefficients  $A_{\ell,m}$  and  $B_{\ell,m}$  of the LOs are determined by normalization and zero value at the MT boundary.

The LAPW and APW+lo basis functions can be employed simultaneously, as done in the LAPW/APW+lo code WIEN2K[Blaaha01] used in the present work.

## 2.3 LDA+U

Despite its many applications, DFT is known to yield qualitatively wrong electronic structures for some classes of systems among which we focus on those with strong electronic correlations. There, two approximations made along the way turn out to be particularly detrimental. The first is the identification of the auxiliary single-particle KS system with the many body Schrödinger equation; this is equivalent to a mean-field approach. In an interacting system, the electronic structure cannot be described in terms of single-particle states and energies anymore. Instead, integrating out all but one electronic degrees of freedom in the many body wave function yields a mixed state which can be interpreted as result of the scattering induced by the Coulomb interactions; this manifests itself *e.g.* as an energy broadening of the spectral function which cannot be reproduced by the KS energies.

Secondly, the LDA (and other commonly used approximations to  $E_{xc}$ ) is known to miss the derivative discontinuity in  $E_{xc}$  with respect to the total particle number which is a central aspect of Mott physics; this discontinuity is one among a couple of known properties of the *exact* exchange-correlation functional which can serve as constraints or guides in the construction of approximations for  $E_{xc}$ . As a consequence, LDA underestimates band gaps and the effect of electronic correlations. In order to (partially) overcome this limitation,

a couple of extensions to DFT have been proposed among which we will single out and discuss the LDA+U method in the following.

The LDA+U approach introduced by Anisimov *et al.* [Anisimov91] is a modification of LDA<sup>4</sup> that adds an intra-atomic Hubbard  $U$  repulsion term in the energy functional for the orbitals considered correlated. In the LDA selfconsistency cycle, this additional interaction term is then treated in a mean-field (Hartree-Fock) manner. Reviews covering many aspects of the LDA+U approach have been provided in Refs. [Anisimov93] and [Ylvisaker09].

In general, the LDA+U functional can be written as the LDA (or LSDA, GGA *etc.*) functional, augmented with a correction  $\Delta E$ ,

$$E_{\text{LDA+U}} = E_{\text{LDA}} + \Delta E \quad , \quad \Delta E = H_{\text{int}} - E_{\text{dc}} \quad , \quad (2.24)$$

where the interaction term takes the form of Eq. (B.19),

$$H_{\text{int}} = \sum_{m>m',\sigma} (V_{mm'mm'}^{ee} - V_{mm'm'm}^{ee}) n_{m,\sigma} n_{m',\sigma} + \frac{1}{2} \sum_{m,m',\sigma} V_{mm'mm'} n_{m,\sigma} n_{m',-\sigma} \quad , \quad (2.25)$$

and  $E_{\text{dc}}$  is a double counting correction that we will discuss below. In accordance with common nomenclature, we define  $U_{mm'} \equiv V_{mm'mm'}^{ee}$  and  $J_{mm'} \equiv V_{mm'm'm}^{ee}$ , using which Eq. (2.25) becomes

$$H_{\text{int}} = \frac{1}{2} \sum_{m,m',\sigma} U_{mm'} n_{m,\sigma} n_{m',-\sigma} + \sum_{m>m',\sigma} (U_{mm'} - J_{mm'}) n_{m,\sigma} n_{m',\sigma} \quad . \quad (2.26)$$

The addition of the Hubbard-like interaction (2.26) necessitates a so-called double-counting correction to account for the fact that interactions are already included in the LDA functional. Since an exact expression for the interactions included in LDA is not known,<sup>5</sup> the double counting correction is only approximate, and different double counting schemes have been proposed [Anisimov91, Anisimov93, Held07]. For all double counting corrections, some averaged total energy of the system of correlated electrons is subtracted, but the rationale for the construction of this average differs between the various schemes. We discuss two widely used schemes, the fully localized limit and the around mean-field scheme. Note that the same double counting corrections are also used in LDA+DMFT, cf. Eq. (5.25): since the form of the interaction term is general and identical in LDA+U and LDA+DMFT, so is the double counting, *i.e.* on the level of the double counting there is no difference whether the Hubbard term is included in a static or dynamic mean-field way.

The original approach [Anisimov91, Czyżyk94] to an appropriate LDA+U functional can be written in a fluctuation form around the average occupation of a correlated (spin-) orbital (we present the spin-polarized version here),

$$\Delta E = \frac{1}{2} \sum_{m,m',\sigma} U_{mm'} (n_{m,\sigma} - \bar{n}_\sigma) (n_{m',-\sigma} - \bar{n}_{-\sigma}) + \sum_{m>m',\sigma} (U_{mm'} - J_{mm'}) (n_{m,\sigma} - \bar{n}_\sigma) (n_{m',\sigma} - \bar{n}_\sigma) \quad , \quad (2.27)$$

<sup>4</sup>Following common notation, we use LDA as synonym for the original DFT approach without reference to the functional form of the exchange-correlation energy which can be LDA, GGA, *etc.*

<sup>5</sup>The one-particle Hamiltonian is not obtained from Hartree-Fock theory, *i.e.* from a self-consistent mean-field solution, but from density functional theory with an empirical one-particle potential which prevents from defining an exact double-counting term.



where  $\bar{n}_\sigma = \frac{1}{2\ell+1} \sum_m n_{m,\sigma}$ . In this form, the double counting correction is already implicitly included by taking the occupations relative to the respective average occupation. This can be transformed into the form of Eq. (2.24),

$$E_{\text{dc}}^{\text{AMF}} = \frac{1}{2}UN^2 - \frac{U + 2\ell J}{2\ell + 1} \frac{1}{2} \sum_\sigma N_\sigma^2, \quad (2.28)$$

with  $N_\sigma = \sum_m n_{m,\sigma}$ ; here, we used the summation rules  $\sum_m U_{mm'} = (2\ell + 1)U$  and  $\sum_m J_{mm'} = U + (2\ell)J$  for the (spherically averaged) parameters  $U$  and  $J$ , *i.e.* we are working with what is referred to as the Slater  $U$  and  $J$  in Appendix B. This expression for  $E_{\text{dc}}$  is called the around mean-field (AMF) scheme.

Another approach[Anisimov93, Czyżyk94] for the double counting correction takes the total Coulomb energy of an ensemble of  $N$  electrons as starting point. Through basic combinatorics, this energy is given by

$$\langle H_{\text{int}} \rangle^{\text{FLL}} = \frac{1}{2}UN(N-1) - \frac{1}{2}J \sum_\sigma N_\sigma(N_\sigma - 1) = E_{\text{dc}}^{\text{FLL}}, \quad (2.29)$$

which directly serves as double counting correction. This form of the double counting correction is termed the fully localized limit (FLL, also called atomic limit: AL) scheme.

Importantly, since the interaction term (2.26) is universal, the difference between different LDA+U functionals stems solely from the double counting term.<sup>6</sup>

In order to identify the character of the different contributions to  $\Delta E$ , we separate out the isotropic part of the interaction,

$$U_{mm'} = U + U_{mm'}^{\text{aniso}}, \quad J_{mm'} = J + J_{mm'}^{\text{aniso}}, \quad (2.30)$$

and write Eq. (2.26) as  $H_{\text{int}} = H_{\text{int}}^{\text{iso}} + H_{\text{int}}^{\text{aniso}}$ , with

$$H_{\text{int}}^{\text{iso}} = \frac{1}{2}U \sum_\sigma N_\sigma(N - N_\sigma) + \frac{1}{2}(U - J) \left( \sum_\sigma N_\sigma^2 - \sum_{m,\sigma} n_{m,\sigma}^2 \right), \quad (2.31)$$

$$H_{\text{int}}^{\text{aniso}} = \frac{1}{2} \sum_{m,m',\sigma} U_{mm'}^{\text{aniso}} n_{m,\sigma} n_{m',-\sigma} + \sum_{m>m',\sigma} (U_{mm'}^{\text{aniso}} - J_{mm'}^{\text{aniso}}) n_{m,\sigma} n_{m',\sigma}. \quad (2.32)$$

The total (interaction minus dc correction term) LDA+U energy correction with the FLL double counting correction then reads

$$\Delta E^{\text{FLL}} = -\frac{U - J}{2} \sum_{m,\sigma} n_{m,\sigma}^2 + \frac{U - J}{2} N + H_{\text{int}}^{\text{aniso}}, \quad (2.33)$$

*i.e.* the isotropic part (that we will discuss in the following) only depends on an effective parameter  $U_{\text{eff}} \equiv U - J$ ; we make use of this fact in Ch. 4, where we use  $U_{\text{eff}}$  as control parameter. Note, however, that  $H_{\text{int}}^{\text{aniso}}$  depends on  $U$  and  $J$  separately; using  $U_{\text{eff}} = U - J$  and  $J_{\text{eff}} = 0$  as parameters amounts to  $U_{mm'} = U_{\text{eff}} = U - J$  and  $J_{mm'} = 0$  for  $m \neq m'$ ,

<sup>6</sup>In addition, different LDA+U implementations also differ in the choice of the projection method: as LDA+U operates in a localized basis (like LDA+DMFT), the orbital occupations  $n_{m,\sigma}$  have to be determined by projection of the Kohn-Sham states onto the correlated orbitals. Depending on the employed DFT basis set and implementation details, this projection is performed in different ways. See Sec. 5.2.1 for details of the projector construction for LDA+DMFT in the LAPW basis used in this work.

cf. Appendix B, *i.e.* we are neglecting the anisotropy of the interaction and the effect of the Hund's rule coupling. Rewriting Eq. (2.33) as

$$\Delta E^{\text{FLL}} = \frac{U - J}{2} \sum_{m,\sigma} n_{m,\sigma} (1 - n_{m,\sigma}) + H_{\text{int}}^{\text{aniso}}, \quad (2.34)$$

one observes that the energy correction is positive semidefinite for  $U_{\text{eff}} > 0$  and only vanishes for (spin-projected) integer occupations. This models the Mott gap, but also favors polarized states. In Ch. 4, we make use of this property for reducing magnetic moments (high-spin states) by means of an FLL type LDA+U correction with negative  $U_{\text{eff}}$ .

For the total AMF energy correction one obtains

$$\begin{aligned} \Delta E^{\text{AMF}} &= -\frac{U - J}{2} \sum_{m,\sigma} n_{m,\sigma}^2 + \frac{U - J}{2(2\ell + 1)} \sum_{\sigma} N_{\sigma}^2 + H_{\text{int}}^{\text{aniso}} \\ &= -\frac{U - J}{2} \sum_{m,\sigma} n_{m,\sigma}^2 + \frac{U - J}{4(2\ell + 1)} (M^2 + N^2) + H_{\text{int}}^{\text{aniso}}, \end{aligned} \quad (2.35)$$

with  $M = N_{\uparrow} - N_{\downarrow}$ . Whereas the first term  $-\frac{U-J}{2} \sum_{m,\sigma} n_{m,\sigma}^2$  tends to enhance orbital polarization as for the FLL functional, it is –with respect to magnetism– in most cases overcompensated by the  $\frac{U-J}{4(2\ell+1)} M^2$  term which penalizes magnetism. This can be understood from the fluctuation form (2.27) which favors an even distribution of the electrons across the spin channels.

Some more insight can be gained from the orbital potentials. In order for the energy correction to be incorporated into the KS equations, the functional derivative  $\frac{\partial \Delta E}{\partial n_{m,\sigma}(\mathbf{r})}$  is used to obtain a correction to the LDA potential, representing the interaction in a mean-field (Hartree-Fock) manner,

$$V_{m,\sigma}(\mathbf{r}) = V_{\text{LDA}}(\mathbf{r}) + U_{mm} n_{m,-\sigma} + \sum_{m' \neq m} U_{mm'} (n_{m',-\sigma} + n_{m',\sigma}) - J_{mm'} n_{m',\sigma} - V_{m,\sigma}^{\text{dc}}, \quad (2.36)$$

with  $V_{m,\sigma}^{\text{dc}} = \frac{\partial E_{\text{dc}}}{\partial n_{m,\sigma}}$ . Note that spin-flip (B.7) and pair-hopping (B.6) terms cannot be cast into this (single-particle) potential; this is the rationale for including only density-density terms in the interaction Hamiltonian (2.25).

The orbital potentials of the double counting corrections (2.28) and (2.29) evaluate to

$$V_{m,\sigma}^{\text{dc,FLL}} = \frac{\partial E_{\text{dc}}^{\text{FLL}}}{\partial n_{m,\sigma}} = U(N - 1/2) - J(N_{\sigma} - 1/2), \quad (2.37)$$

$$V_{m,\sigma}^{\text{dc,AMF}} = \frac{\partial E_{\text{dc}}^{\text{AMF}}}{\partial n_{m,\sigma}} = U(N - \bar{n}_{\sigma}) - J(N_{\sigma} - \bar{n}_{\sigma}). \quad (2.38)$$

We will also use these expressions in LDA+DMFT to obtain the double-counting-corrected self energy from the impurity self energy.

The total orbital potential, *i.e.* the sum of (2.36) and (2.37), or (2.38), is then given by

$$V_{m,\sigma}^{\text{FLL}} = V_{\text{LDA}}(\mathbf{r}) - (U - J) [n_{m,\sigma} - 1/2] + V_{m,\sigma}^{\text{aniso}}, \quad (2.39)$$

$$V_{m,\sigma}^{\text{AMF}} = V_{\text{LDA}}(\mathbf{r}) - (U - J) [n_{m,\sigma} - \bar{n}_{\sigma}] + V_{m,\sigma}^{\text{aniso}}, \quad (2.40)$$

where we again separated the isotropic contribution from the anisotropic term

$$V_{m,\sigma}^{\text{aniso}} = U_{mm}^{\text{aniso}} n_{m,-\sigma} + \sum_{m' \neq m} U_{mm'}^{\text{aniso}} (n_{m',-\sigma} + n_{m',\sigma}) - J_{mm'}^{\text{aniso}} n_{m',\sigma}. \quad (2.41)$$

The orbital potential shifts the LDA orbital energies depending on the orbital occupation. In the case of half filling, the FLL and AMF orbital potentials are identical, and the energy shift is  $-\frac{U-J}{2}$  for occupied and  $\frac{U-J}{2}$  for unoccupied orbitals, giving rise to lower and upper Hubbard bands with the correct energy separation.<sup>7</sup> In the general case away from half filling, the splitting for the AMF functional is done with respect to the (spin projected) average occupation, whereas the FLL functional always splits occupied and unoccupied states symmetrically.

Since quantum fluctuations are largely suppressed in the Mott insulator, LDA+U –despite being a mean-field approach– often provides a correct picture of the Mott physics. In many cases, LDA+U therefore offers a greatly improved description of strongly correlated materials. However, LDA+U fails to describe the (possibly strongly) correlated metallic phase of many transition metal oxides and heavy fermion systems, which we will encounter also among the materials under investigation in this thesis. Whereas correlation effects play a significant role and may even lead to the formation of Hubbard bands in these materials, the low-energy dynamics are often still well described by long-lived, yet renormalized, quasiparticles. In order to capture the physics of this intermediate regime, we will employ the LDA+DMFT technique described in Ch. 5.

---

<sup>7</sup>This also restores the discontinuity of the exact exchange-correlation potential mentioned above, see Ref. [Anisimov93].



### 3. Optical Conductivity

The study of the optical properties of materials is one of the most widely used techniques for the investigation of the electronic structure and important for both fundamental research as well as technological applications. Representative for the broad range of applications of optical studies, we discuss in this thesis optical properties from different points of view: in Ch. 4 for the investigation of gap features of an ordered phase in the iron pnictides within DFT, and in Ch. 9 for the study of correlation effects (like the appearance of Hubbard features and the suppression of the Drude weight) in the charge transfer salts within LDA+DMFT.

In this chapter, we introduce the framework for the calculation of the optical conductivity  $\sigma(\omega)$  in DFT as well as LDA+DMFT and relate it to experimentally accessible quantities. Expressions will be given in the cgs unit system; the final results for the optical conductivity can easily be transformed into the SI unit system by multiplication by a factor  $1/(4\pi\epsilon_0)$  with  $\epsilon_0$  being the vacuum permittivity.

Macroscopically, the response of a medium to incident light is characterized by absorption  $A$ , reflection  $R$ , and transmission  $T$  of the energy of the light, with  $A + R + T = 1$ . The frequency-dependence of  $A$ ,  $R$ , and  $T$  is one of the basic experimental sources for the electron dynamics in solid state physics. While absorption is caused by an in-phase response to the perturbation, the transmission is associated with a phase shift of the light. Since transmission experiments require very thin slices for a direct measurement of the phase shift, which can not always be prepared experimentally, in many cases the optical properties are inferred from the reflectivity given by (for normally incident light)

$$R(\omega) = \left| \frac{1 - \tilde{n}(\omega)}{1 + \tilde{n}(\omega)} \right|^2 = \frac{(n - 1)^2 + \kappa^2}{(n + 1)^2 + \kappa^2}, \quad (3.1)$$

where  $\tilde{n}(\omega)$  is the complex refractive index,  $\tilde{n} \equiv n - i\kappa$ , with  $n$  the refractive index and  $\kappa$  the extinction coefficient. We will see in the following how  $\tilde{n}(\omega)$  is related to the relevant microscopic quantities, namely to the dielectric function  $\epsilon(\omega)$  and the optical conductivity  $\sigma(\omega)$ . Importantly,  $\tilde{n}(\omega)$  is an analytic function which allows to extract  $n(\omega)$  and  $\kappa(\omega)$  from the frequency-dependence of  $R(\omega)$  using Kramers-Kronig analysis.

Microscopically, if a system is subject to an external electric field, a redistribution of charges occurs and currents are induced. In linear response, the optical conductivity is the

response function connecting the induced current density  $\mathbf{j}(\mathbf{q}, \omega)$  and the applied electric field  $\mathbf{E}(\mathbf{q}, \omega)$ ,

$$j_\alpha(\mathbf{q}, \omega) = \sum_\beta \sigma_{\alpha\beta}(\mathbf{q}, \omega) E_\beta(\mathbf{q}, \omega), \quad (3.2)$$

where  $\alpha, \beta$  are spatial indices, *i.e.*  $\sigma(\mathbf{q}, \omega)$  is a tensor in general. For energies in the optical frequency range, the linear dispersion relation for photons,  $\epsilon(\mathbf{q}) = c|\mathbf{q}|$ , implies very small photon momenta compared to the electron momenta in the Brillouin zone. One therefore only considers the long-wavelength limit  $\mathbf{q} \rightarrow 0$ , and thus assumes the electronic transitions induced by the light to be direct, *i.e.* occurring without a momentum transfer.

Furthermore, the dielectric function is the response function relating the electrical flux density  $\mathbf{D}(\omega)$  and  $\mathbf{E}(\omega)$  (we already assume  $\mathbf{q} = 0$  here),

$$D_\alpha(\omega) = \sum_\beta \epsilon_{\alpha\beta}(\omega) E_\beta(\omega). \quad (3.3)$$

The dielectric function can directly be expressed in terms of the optical conductivity,<sup>1</sup>

$$\epsilon(\omega) = 1 + \frac{4\pi i \sigma(\omega)}{\omega}, \quad (3.4)$$

and is, on the other hand, related to the complex refractive index as

$$\epsilon(\omega) = \tilde{n}^2(\omega). \quad (3.5)$$

The knowledge of  $\tilde{n}(\omega)$ , *e.g.* from reflectivity measurements, hence allows to obtain the microscopic quantities  $\epsilon(\omega)$  and  $\sigma(\omega)$ .

In the following sections of this chapter, we will derive expressions for  $\sigma(\omega)$  from the microscopic point of view –following in part the presentation in Ref. [Blümer02]– and discuss the diagrammatic simplifications in the DMFT limit of infinite dimensions.

### 3.1 Optical Conductivity in Linear Response

The interaction of a charged particle (here: electron) at position  $\mathbf{r}$  with an external electric field can be fully described in terms of a shift of its momentum,

$$\mathbf{p} \rightarrow \tilde{\mathbf{p}} = \mathbf{p} - \frac{e}{c} \mathbf{A}(\mathbf{r}, t), \quad (3.6)$$

where  $\mathbf{A}(\mathbf{r}, t)$  is the vector potential,  $e$  the electron charge, and  $c$  the speed of light. The electronic Hamiltonian then reads

$$H = \frac{1}{2m} \sum_{i=1}^{N_e} \left( \mathbf{p}_i - \frac{e}{c} \mathbf{A}(\mathbf{r}_i, t) \right)^2 + H_{\text{int}}, \quad (3.7)$$

where  $H_{\text{int}}$  may contain arbitrary interactions. The total current is expressed as

$$\int d^3r \mathbf{j}(\mathbf{r}, t) = \sum_{i=1}^{N_e} e \mathbf{v}_i, \quad (3.8)$$

---

<sup>1</sup>We suppress the spatial indices here.

with the current density  $\mathbf{j}(\mathbf{r}, t)$  and the velocity operator  $\mathbf{v}_i = \nabla_{\mathbf{p}_i} H = \nabla_{\mathbf{k}_i} H / \hbar$ , and evaluates to

$$\int d^3r \mathbf{j}(\mathbf{r}, t) = \frac{e}{m} \sum_{i=1}^{N_e} \left( \mathbf{p}_i - \frac{e}{c} \mathbf{A}(\mathbf{r}_i, t) \right). \quad (3.9)$$

The current density can be divided into a diamagnetic contribution,

$$\mathbf{j}^{\text{dia}}(\mathbf{r}, t) = -\frac{e^2}{mc} \sum_{i=1}^{N_e} \mathbf{A}(\mathbf{r}_i, t) \delta(\mathbf{r} - \mathbf{r}_i), \quad (3.10)$$

and a paramagnetic contribution, which in symmetrized form reads

$$\mathbf{j}^{\text{para}}(\mathbf{r}, t) = \frac{e}{2m} \sum_{i=1}^{N_e} (\mathbf{p}_i \delta(\mathbf{r} - \mathbf{r}_i) + \delta(\mathbf{r} - \mathbf{r}_i) \mathbf{p}_i). \quad (3.11)$$

The thermal expectation value in the presence of the vector potential thus reads

$$\langle \mathbf{j}(\mathbf{r}, t) \rangle_{\mathbf{A}} = \langle \mathbf{j}^{\text{para}}(\mathbf{r}, t) \rangle_{\mathbf{A}} + \langle \mathbf{j}^{\text{dia}}(\mathbf{r}, t) \rangle_{\mathbf{A}} = \langle \mathbf{j}^{\text{para}}(\mathbf{r}, t) \rangle - \frac{e^2}{mc} \mathbf{A}(\mathbf{r}, t) \langle n(\mathbf{r}, t) \rangle_{\mathbf{A}}, \quad (3.12)$$

where  $n(\mathbf{r}, t)$  is the electron density.

We first calculate the diamagnetic contribution to the optical conductivity. In linear response, only terms which are at most linear in  $\mathbf{A}$  are included, therefore  $\langle n(\mathbf{r}, t) \rangle_{\mathbf{A}}$  is evaluated in zeroth order,  $\langle n(\mathbf{r}, t) \rangle_{\mathbf{A}} = n$  with  $n$  the average density (since we are in the long-wavelength limit). Assuming an applied electric field with harmonic time dependence,  $\mathbf{E}(\mathbf{r}, t) = \mathbf{E}(\mathbf{q}, \omega) e^{i(\mathbf{q}\mathbf{r} - [\omega + i\eta]t)}$  ( $\eta > 0$  being a convergence factor to ensure  $E(t \rightarrow -\infty) = 0$ ), the vector potential is given by

$$\mathbf{A}(\mathbf{r}, t) = -\frac{ic}{\omega + i\eta} \mathbf{E}(\mathbf{q}, \omega) e^{i(\mathbf{q}\mathbf{r} - [\omega + i\eta]t)}, \quad (3.13)$$

and the diamagnetic current density becomes

$$\langle \mathbf{j}^{\text{dia}}(\mathbf{q}, t) \rangle_{\mathbf{A}} = \frac{ine^2}{m(\omega + i\eta)} \mathbf{E}(\mathbf{q}, \omega) e^{i(\mathbf{q}\mathbf{r} - [\omega + i\eta]t)}. \quad (3.14)$$

After Fourier transform,

$$\langle \mathbf{j}^{\text{dia}}(\mathbf{q}, \omega) \rangle_{\mathbf{A}} = \int_0^\infty dt e^{i(\omega + i\eta)t} \langle \mathbf{j}^{\text{dia}}(\mathbf{q}, t) \rangle_{\mathbf{A}} = \frac{ine^2}{m(\omega + i\eta)} \mathbf{E}(\mathbf{q}, \omega) e^{i\mathbf{q}\mathbf{r}}, \quad (3.15)$$

this yields the diamagnetic contribution to the optical conductivity (after taking the limit  $\mathbf{q} \rightarrow 0$ ),

$$\sigma_{\alpha\beta}^{\text{dia}}(\omega, \mathbf{q} \rightarrow 0) = \frac{ine^2}{m(\omega + i\eta)} \delta_{\alpha\beta}, \quad (3.16)$$

with Kronecker delta  $\delta_{\alpha\beta}$  since the response is restricted to the same vector as the perturbing field as evident from Eq. (3.15).

For the evaluation of the paramagnetic contribution to the optical conductivity, the calculation of  $\langle \mathbf{j}^{\text{para}}(\mathbf{q}, \omega) \rangle_{\mathbf{A}}$  in linear order in  $\mathbf{A}$  is required. In linear response theory, the

expectation value  $\langle B \rangle_{\mathbf{A}}$  of an operator  $B$  subject to a perturbation  $\mathbf{A}$  is given by the correlation  $\langle\langle B, H' \rangle\rangle$ ,

$$\langle B \rangle_{\mathbf{A}}(\omega) = \langle B \rangle_0(\omega) + \langle\langle B, H' \rangle\rangle(\omega + i\eta) = \langle B \rangle_0(\omega) - \frac{i}{\hbar} \int_0^{\infty} dt \langle\langle [B(t), H'(0)] \rangle\rangle_0 e^{i(\omega+i\eta)t}, \quad (3.17)$$

where  $\langle \dots \rangle_0$  are unperturbed expectation values, the time evolution of  $B(t)$  is in the interaction picture, and  $H'$  denotes the (linear) perturbing part of the Hamiltonian,

$$H'(t) = -\frac{e}{mc} \sum_{i=1}^{N_e} \mathbf{p}_i \mathbf{A}(\mathbf{r}_i, t) = -\frac{1}{c} \int d^3r \mathbf{j}^{\text{para}}(\mathbf{r}, t) \mathbf{A}(\mathbf{r}, t) = -\frac{V}{c} \mathbf{j}^{\text{para}}(-\mathbf{q}, t) \mathbf{A}(\mathbf{q}, t), \quad (3.18)$$

where for the last equality we transformed to reciprocal space,  $\mathbf{O}(\mathbf{r}) = \int d^3q \mathbf{O}(\mathbf{q}) e^{i\mathbf{q}\mathbf{r}}$ ,  $\mathbf{O} = \{\mathbf{j}, \mathbf{A}\}$ .

Hence, we obtain for the (spatial)  $\alpha$ -component of the paramagnetic current density

$$\begin{aligned} \langle j_{\alpha}^{\text{para}}(\mathbf{q}, \omega) \rangle_{\mathbf{A}} &= \langle\langle j_{\alpha}^{\text{para}}(\mathbf{q}), H' \rangle\rangle(\omega + i\eta) \\ &= \frac{iV}{(\omega + i\eta)} \sum_{\beta} \langle\langle j_{\alpha}^{\text{para}}(\mathbf{q}), j_{\beta}^{\text{para}}(-\mathbf{q}) \rangle\rangle(\omega + i\eta) \cdot \mathbf{E}_{\beta}(\mathbf{q}, \omega), \end{aligned} \quad (3.19)$$

from which the paramagnetic contribution to the optical conductivity follows,

$$\sigma_{\alpha\beta}^{\text{para}}(\omega, \mathbf{q} \rightarrow 0) = \frac{V}{\hbar(\omega + i\eta)} \int_0^{\infty} dt \langle\langle [j_{\alpha}^{\text{para}}(t), j_{\beta}^{\text{para}}(0)] \rangle\rangle e^{i(\omega+i\eta)t}. \quad (3.20)$$

This is the formalism for the optical conductivity in the continuum case. On a lattice, we consider the respective quantities and label the electronic states by their crystal momentum  $\mathbf{k}$  and spin  $\sigma$ . In the following, we first derive expressions in the single-band case which also serves for the discussion of the DMFT limit of infinite dimensions later on. The generalization to the multiband case follows in Sec. 3.4.

Replacing the bare electron mass by the band mass,

$$\frac{1}{m} \rightarrow \frac{1}{\hbar^2} \frac{\partial^2}{\partial \mathbf{k}^2} \epsilon_{\mathbf{k}, \sigma}, \quad (3.21)$$

with  $\epsilon_{\mathbf{k}, \sigma}$  the noninteracting band dispersion, and switching to second quantization in the momentum representation, the  $\alpha$ -component of the diamagnetic current density (3.10) is expressed as

$$\mathbf{j}_{\alpha}^{\text{dia}}(\mathbf{q}, t) = -\frac{e^2}{V\hbar^2 c} A_{\alpha}(\mathbf{q}, t) \sum_{\mathbf{k}, \sigma} \frac{\partial^2 \epsilon_{\mathbf{k}+\mathbf{q}, \sigma}}{\partial k_{\alpha}^2} c_{\mathbf{k}, \sigma}^{\dagger} c_{\mathbf{k}+\mathbf{q}, \sigma} \quad (3.22)$$

with the total volume  $V$ .

The paramagnetic current density operator (3.11) is expressed in terms of the Fermi velocity which takes the role of the optical transition matrix element,<sup>2</sup>

$$\mathbf{v}_{\mathbf{k}+\mathbf{q}, \sigma} = \frac{1}{\hbar} \nabla_{\mathbf{k}} \epsilon_{\mathbf{k}+\mathbf{q}, \sigma}, \quad (3.23)$$

<sup>2</sup>Note that the optical transition matrix element can be written in the form (3.23), respectively (3.38) only in the limit  $\mathbf{q} \rightarrow 0$ . Otherwise, it takes a different form, cf. [Stauber10], Eq. (19). However, we eventually always evaluate the matrix element in the long-wavelength limit.



and takes the form

$$j_{\alpha}^{\text{para}}(\mathbf{q}) = \frac{e}{V} \sum_{\mathbf{k}, \sigma} v_{\mathbf{k}+\mathbf{q}, \sigma, \alpha} c_{\mathbf{k}, \sigma}^{\dagger} c_{\mathbf{k}+\mathbf{q}, \sigma}. \quad (3.24)$$

The contributions to the optical conductivity  $\sigma_{\alpha\beta} = \sigma_{\alpha\beta}^{\text{dia}} + \sigma_{\alpha\beta}^{\text{para}}$  are then given by

$$\sigma_{\alpha\beta}^{\text{dia}}(\omega, \mathbf{q} \rightarrow 0) = \frac{ie^2}{V\hbar^2(\omega + i\eta)} \delta_{\alpha\beta} \sum_{\mathbf{k}, \sigma} \langle n_{\mathbf{k}, \sigma} \rangle \frac{\partial^2}{\partial k_{\alpha}^2} \epsilon_{\mathbf{k}, \sigma}, \quad (3.25)$$

$$\begin{aligned} \sigma_{\alpha\beta}^{\text{para}}(\omega, \mathbf{q} \rightarrow 0) &= \frac{ie^2}{V(\omega + i\eta)} \sum_{\mathbf{k}, \mathbf{k}', \sigma, \sigma'} v_{\mathbf{k}, \sigma, \alpha} v_{\mathbf{k}', \sigma', \beta} \langle \langle n_{\mathbf{k}, \sigma}, n_{\mathbf{k}', \sigma'} \rangle \rangle (\omega + i\eta) \\ &= \frac{e^2}{V\hbar(\omega + i\eta)} \sum_{\mathbf{k}, \mathbf{k}', \sigma, \sigma'} v_{\mathbf{k}, \sigma, \alpha} v_{\mathbf{k}', \sigma', \beta} \int_0^{\infty} dt \langle [n_{\mathbf{k}, \sigma}(t), n_{\mathbf{k}', \sigma'}(0)] \rangle e^{i(\omega + i\eta)t}. \end{aligned} \quad (3.26)$$

Important conclusions can be drawn from this form. Firstly, the paramagnetic contribution vanishes in the noninteracting case, since

$$n_{\mathbf{k}, \sigma}(t) = e^{iH_{\text{int}}t/\hbar} n_{\mathbf{k}, \sigma}(0) e^{-iH_{\text{int}}t/\hbar} = n_{\mathbf{k}, \sigma}(0) \text{ for } H_{\text{int}} = 0 \Rightarrow [n_{\mathbf{k}, \sigma}(t), n_{\mathbf{k}', \sigma'}(0)] = 0. \quad (3.27)$$

This also holds in the case of static mean-field theories like Hartree-Fock, where  $H_{\text{int}} \propto \sum_{\mathbf{k}, \mathbf{k}', \sigma, \sigma'} \langle n_{\mathbf{k}', \sigma'} \rangle n_{\mathbf{k}, \sigma}$  and therefore  $[H_{\text{int}}, n_{\mathbf{k}, \sigma}] = 0$ . It is, however, not true in the Hubbard model (and hence in DMFT) with interactions local in real space: there,  $H_{\text{int}} \propto \sum_i n_{i, \uparrow} n_{i, \downarrow}$ , and  $[n_{i, \sigma'}, n_{\mathbf{k}, \sigma}] \neq 0$ . With vanishing paramagnetic contribution, only the diamagnetic term is left, of which the real part reads

$$\text{Re } \sigma_{\alpha\beta}(\omega) = \frac{\pi e^2}{V\hbar^2} \delta_{\alpha\beta} \delta(\omega) \sum_{\mathbf{k}, \sigma} \langle n_{\mathbf{k}, \sigma} \rangle \frac{\partial^2}{\partial k_{\alpha}^2} \epsilon_{\mathbf{k}, \sigma}, \quad (3.28)$$

*i.e.* there is no finite frequency response in the noninteracting (or static mean-field) case. However, note that this is only true in the single-band scenario that we consider here: while intraband contributions to the paramagnetic term also vanish in the multiband case, offdiagonal terms corresponding to interband transitions are in general still present,  $[c_{\nu}^{\dagger} c_{\nu'}, c_{\nu''}^{\dagger} c_{\nu'''}] \neq 0$  (cf. Sec. 3.4).

Besides these observations, there is in fact a more intimate relation between the diamagnetic and paramagnetic conductivity: namely, one can find a contribution to the paramagnetic term that exactly cancels the diamagnetic term. This is discussed in more detail in the following section on the  $f$ -sum rule.

## 3.2 $f$ -sum Rule

If the paramagnetic contribution to the optical conductivity vanishes under the conditions discussed in Sec. 3.1, the total weight of the real part of  $\sigma_{\alpha\beta}(\omega)$  is obtained by integrating the diamagnetic term (3.28),

$$\int_0^{\infty} d\omega \text{Re } \sigma_{\alpha\beta}(\omega) = \frac{\pi e^2}{2V\hbar^2} \delta_{\alpha\beta} \sum_{\mathbf{k}, \sigma} \langle n_{\mathbf{k}, \sigma} \rangle \frac{\partial^2}{\partial k_{\alpha}^2} \epsilon_{\mathbf{k}, \sigma}, \quad (3.29)$$

which *e.g.* for the case of a homogeneous gas of free electrons reduces to

$$\int_0^\infty d\omega \operatorname{Re} \sigma_{\alpha\beta}(\omega) = \frac{\pi n e^2}{2m} \delta_{\alpha\beta}, \quad (3.30)$$

recovering the well-known Thomas-Reiche-Kuhn  $f$ -sum rule [Thomas25].

In the case of a general dispersion, the sum rule (3.29) can formally still be written in the form of Eq. (3.30),

$$\int_0^\infty d\omega \operatorname{Re} \sigma_{\alpha\beta}(\omega) = \frac{\pi \langle n \rangle e^2}{2m_{\text{opt}}} \delta_{\alpha\beta}, \quad (3.31)$$

hence defining an optical band mass  $m_{\text{opt}}$ . We further note that the sum rule is linked to the plasma frequency  $\omega_p = 4\pi \langle n \rangle e^2 / m_{\text{opt}}$ ,

$$\int_0^\infty d\omega \operatorname{Re} \sigma_{\alpha\beta}(\omega) = \frac{\omega_p^2}{8} \delta_{\alpha\beta}. \quad (3.32)$$

In the following, we will show, however, that the sum rule (3.29) strictly holds also in the case of electronic interactions, *i.e.* for non-vanishing paramagnetic current correlation. To that end, we express the integral in Eq. (3.20) by its spectral representation,

$$\int_0^\infty dt \langle [j_\alpha^{\text{para}}(t), j_\beta^{\text{para}}(0)] \rangle e^{i(\omega+i\eta)t} = \frac{i\hbar}{Z} \sum_{nn'} \frac{\langle n | j_\alpha^{\text{para}} | n' \rangle \langle n' | j_\beta^{\text{para}} | n \rangle}{\hbar\omega - (E_{n'} - E_n) + i\eta} \left( e^{-\beta E_n} + e^{-\beta E_{n'}} \right), \quad (3.33)$$

where  $|n\rangle, |n'\rangle$  are eigenstates of the unperturbed Hamiltonian and  $Z$  the partition function of the unperturbed Hamiltonian. Note that the spectral representation corresponds to the semiclassical picture of a sum of Lorentz oscillators with resonance frequencies determined by the electronic energy levels and oscillator strengths governed by the respective wave functions. The delta functions in Eq. (3.33) can then be seen as the limiting case of the Lorentz function for small damping.

Then,

$$\begin{aligned} \operatorname{Re} \sigma_{\alpha\beta}^{\text{para}}(\omega) &\propto -\operatorname{Im} \left[ \lim_{\eta \rightarrow 0} \frac{1}{\omega + i\eta} \cdot \lim_{\eta \rightarrow 0} \sum_{nn'} \frac{\langle n | j_\alpha^{\text{para}} | n' \rangle \langle n' | j_\beta^{\text{para}} | n \rangle}{\hbar\omega - (E_{n'} - E_n) + i\eta} \left( e^{-\beta E_n} + e^{-\beta E_{n'}} \right) \right] \\ &= \mathcal{P} \frac{1}{\omega} \cdot \sum_{nn'} \langle n | j_\alpha^{\text{para}} | n' \rangle \langle n' | j_\beta^{\text{para}} | n \rangle \left( e^{-\beta E_n} + e^{-\beta E_{n'}} \right) \frac{\pi}{\hbar} \delta \left( \omega - \frac{E_{n'} - E_n}{\hbar} \right) \\ &\quad + \pi \delta(\omega) \cdot \sum_{nn'} \mathcal{P} \frac{\langle n | j_\alpha^{\text{para}} | n' \rangle \langle n' | j_\beta^{\text{para}} | n \rangle}{\hbar\omega - (E_{n'} - E_n)} \left( e^{-\beta E_n} + e^{-\beta E_{n'}} \right), \end{aligned} \quad (3.34)$$

where  $\mathcal{P}$  denotes the principal part. Integration yields

$$\begin{aligned} \int_0^\infty \operatorname{Re} \sigma_{\alpha\beta}^{\text{para}}(\omega) &\propto \frac{1}{2} \sum_{nn'} \frac{\hbar}{E_{n'} - E_n} \langle n | j_\alpha^{\text{para}} | n' \rangle \langle n' | j_\beta^{\text{para}} | n \rangle \left( e^{-\beta E_n} + e^{-\beta E_{n'}} \right) \frac{\pi}{\hbar} \\ &\quad + \frac{\pi}{2} \sum_{nn'} \frac{\langle n | j_\alpha^{\text{para}} | n' \rangle \langle n' | j_\beta^{\text{para}} | n \rangle}{-(E_{n'} - E_n)} \left( e^{-\beta E_n} + e^{-\beta E_{n'}} \right) = 0, \end{aligned} \quad (3.35)$$

*i.e.* the paramagnetic current does not contribute to the  $f$ -sum rule. The factor  $\frac{1}{2}$  stems from the fact that the summation is limited to terms with  $E_{n'} > E_n$  and terms with  $E_{n'} = E_n$  contribute only with half of their weight, due to the integration from zero

to infinity. For the same reason, the Dirac delta peak in the second term of Eq. (3.34) contributes only with half of its weight.

As can be seen from the spectral representation (3.34), the paramagnetic contribution is composed of a delta function with negative weight at  $\omega = 0$  and a set of simple poles at the resonance frequencies  $\omega_{nn'} = (E_{n'} - E_n)/\hbar$ , which are responsible for the finite frequency response. As the diamagnetic term exhibits only a zero-frequency response, a finite frequency response thus signals the presence of interactions, reflecting the finite lifetime of the quasiparticles.

Moreover, the relative contributions of the paramagnetic and the diamagnetic term to the total conductivity are not independent. It can be shown that the zero-frequency delta peak of the paramagnetic optical conductivity (3.34) exactly cancels the real part of the diamagnetic optical conductivity (3.28), cf. *e.g.* Ref. [Blümer02]. For  $T = 0$ , the zero-frequency Drude peak is thus replaced by a Drude peak with (reduced) weight due to the (renormalized) quasiparticles that still possess infinite lifetime at the Fermi surface within Fermi liquid theory. For  $T > 0$ , all lifetimes are finite and the Drude peak broadens. Importantly, the cancelation of the diamagnetic term allows for only considering the paramagnetic current for the optical properties (for finite frequencies): as shown in Eq. (3.35), the weight of the finite frequency response equals the weight of the negative delta function at  $\omega = 0$  and thus –due to the relation to the diamagnetic current– the total weight according to the  $f$ -sum rule. We will therefore only consider the paramagnetic contribution in the following.

### 3.3 Optical Conductivity in the Limit of Infinite Dimensions

The correlation function in Eq. (3.26) can be expressed in a diagrammatic expansion in terms of interacting Green's function lines and particle-hole irreducible vertex functions  $\Gamma$  as shown in Fig. 3.1,

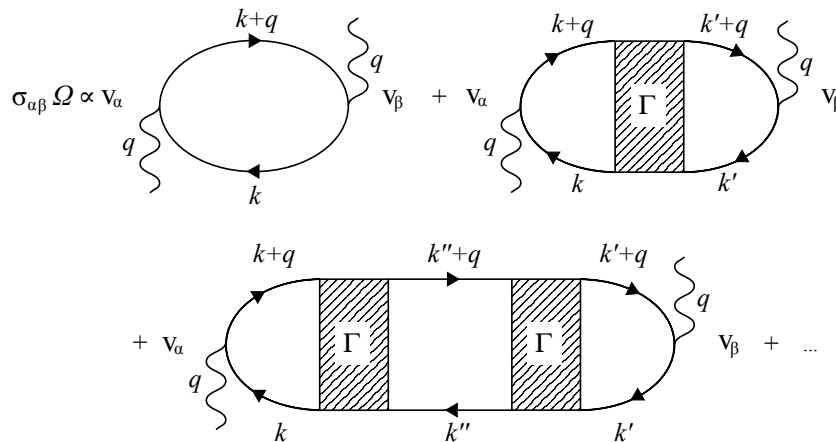


Figure 3.1: Ladder expansion of the optical conductivity in terms of irreducible vertex functions.

where we already went over to imaginary frequencies  $\omega + i\eta \rightarrow i\Omega$  with bosonic Matsubara frequency  $\Omega$  (the current operators have bosonic correlations relations),<sup>3</sup>

<sup>3</sup>Fermionic Matsubara frequencies are labeled by  $\omega_n$  in the following.

$$\begin{aligned}
& \sum_{\mathbf{k}, \mathbf{k}', \sigma, \sigma'} v_{\mathbf{k}, \sigma, \alpha} v_{\mathbf{k}', \sigma', \beta} \langle\langle n_{\mathbf{k}, \sigma}, n_{\mathbf{k}', \sigma'} \rangle\rangle(\Omega) = \\
& = \lim_{\mathbf{q} \rightarrow 0} \sum_{\mathbf{k}, \sigma} \frac{1}{\beta} \sum_{\omega_n} v_{\mathbf{k}+\mathbf{q}, \sigma, \alpha} G_{\mathbf{k}+\mathbf{q}, \sigma}(i\omega_n + i\Omega) G_{\mathbf{k}, \sigma}(i\omega_n) v_{\mathbf{k}, \sigma, \beta} \\
& + \lim_{\mathbf{q} \rightarrow 0} \sum_{\mathbf{k}, \mathbf{k}', \sigma, \sigma'} \frac{1}{\beta^2} \sum_{\omega_n, \omega_{n'}} v_{\mathbf{k}+\mathbf{q}, \sigma, \alpha} G_{\mathbf{k}+\mathbf{q}, \sigma}(i\omega_n + i\Omega) G_{\mathbf{k}, \sigma}(i\omega_n) \\
& \quad \times \Gamma_{\sigma\sigma'}(\mathbf{k}, i\omega_n; \mathbf{k}', i\omega_{n'}; \mathbf{q}, i\Omega) G_{\mathbf{k}', \sigma'}(i\omega_{n'}) G_{\mathbf{k}'+\mathbf{q}, \sigma'}(i\omega_{n'} + i\Omega) v_{\mathbf{k}'+\mathbf{q}, \sigma', \beta} + \dots
\end{aligned} \tag{3.36}$$

However, in the limit  $d \rightarrow \infty$  it can be shown [Georges96] that the irreducible vertex  $\Gamma$  becomes a purely local quantity (like  $\Sigma$ , cf. Sec. 5.1), *i.e.* exhibits no momentum dependence, thereby decoupling the two momentum summations over  $\mathbf{k}, \mathbf{k}'$  in Eq. (3.36). Assuming inversion symmetry, *i.e.*  $\epsilon_{-\mathbf{k}, \sigma} = \epsilon_{\mathbf{k}, \sigma}$ , the current vertices possess odd parity with respect to  $\mathbf{k}$ ,  $\mathbf{v}_{-\mathbf{k}, \sigma} = -\mathbf{v}_{\mathbf{k}, \sigma}$ , while the Green's functions have even parity, and summations involving only one (decoupled) current vertex  $\mathbf{v}_{\mathbf{k}, \sigma}$  vanish for  $\mathbf{q} \rightarrow 0$ . This leaves only the bubble contribution, *i.e.* the first term in the expansion (3.36),

$$\sigma_{\alpha\beta}^{\text{para}}(\Omega, \mathbf{q} \rightarrow 0) = \frac{e^2}{V\Omega\beta} \sum_{\mathbf{k}, \sigma, \omega_n} v_{\mathbf{k}, \sigma, \alpha} v_{\mathbf{k}, \sigma, \beta} G_{\mathbf{k}, \sigma}(i\omega_n + i\Omega) G_{\mathbf{k}, \sigma}(i\omega_n). \tag{3.37}$$

We note that interactions only enter via the evaluation of the (interacting) Green's functions. The Fermi velocity (3.23), on the other hand, is independent of the interaction.

### 3.4 Multiband Case

In the general case of multiple bands labeled by band index  $\nu$ , the generalized Fermi velocity is given by the dipole matrix element,

$$v_{\mathbf{k}, \sigma, \alpha}^{\nu\nu'}(\mathbf{q}) = \frac{1}{m} \langle \mathbf{k}, \nu, \sigma | p_\alpha | \mathbf{k} + \mathbf{q}, \nu', \sigma \rangle, \tag{3.38}$$

with  $p_\alpha$  the momentum operator along the electric field polarization of the incoming light. The form in Eq. (3.38) reduces to the one in Eq. (3.23) for  $\nu = \nu'$ . In fact, the odd parity with respect to momentum which is necessary for the disappearance of the vertex corrections for  $d \rightarrow \infty$  only holds for the diagonal elements  $\nu = \nu'$ ; for the offdiagonal elements, the parity depends on the crystal symmetry, so that in general the full four-point correlation function has to be evaluated, which in imaginary time reads

$$\begin{aligned}
(\Pi_{\alpha\beta})_{\nu\nu'}^{\nu\nu'}(\mathbf{q}, \tau) & = -V \left\langle T_\tau (j_\alpha^{\text{para}})_{\nu'}^\nu(\mathbf{q}, \tau) (j_\alpha^{\text{para}})_{\nu''}^{\nu''}(-\mathbf{q}, 0) \right\rangle \\
& = -\frac{e^2}{V} \sum_{\mathbf{k}, \mathbf{k}', \sigma, \sigma'} \left\langle T_\tau c_{\nu, \mathbf{k}, \sigma}^\dagger(\tau) v_{\mathbf{k}, \sigma, \alpha}^{\nu\nu'}(\mathbf{q}) c_{\nu', \mathbf{k}+\mathbf{q}, \sigma}(\tau) c_{\nu'', \mathbf{k}', \sigma'}^\dagger(0) v_{\mathbf{k}', \sigma', \beta}^{\nu''\nu''}(-\mathbf{q}) c_{\nu''', \mathbf{k}'-\mathbf{q}, \sigma'}(0) \right\rangle.
\end{aligned} \tag{3.39}$$

By choosing to neglect vertex corrections, this can be cast into the form of Eq. (3.37): in Wicks' theorem, the correlation function (3.39) is given by a product of single-particle

Green's functions with all possible pairings and with the sign given by the number of times two fermion operators are interchanged,

$$\begin{aligned}
(\Pi_{\alpha\beta})_{\nu\nu''\nu'''}^{\nu\nu'}(\mathbf{q}, \tau) &= \frac{e^2}{V} \sum_{\mathbf{k}, \mathbf{k}', \sigma, \sigma'} v_{\mathbf{k}, \sigma, \alpha}^{\nu\nu'}(\mathbf{q}) v_{\mathbf{k}', \sigma', \beta}^{\nu''\nu'''}(-\mathbf{q}) \\
&\quad \times \left\langle T_{\tau} c_{\nu', \mathbf{k}+\mathbf{q}, \sigma}(\tau) c_{\nu'', \mathbf{k}', \sigma'}^{\dagger}(0) \right\rangle \left\langle T_{\tau} c_{\nu''', \mathbf{k}'-\mathbf{q}, \sigma'}(0) c_{\nu, \mathbf{k}, \sigma}^{\dagger}(\tau) \right\rangle \\
&= \frac{e^2}{V} \sum_{\mathbf{k}, \sigma} v_{\mathbf{k}, \sigma, \alpha}^{\nu\nu'}(\mathbf{q}) v_{\mathbf{k}+\mathbf{q}, \sigma, \beta}^{\nu''\nu'''}(-\mathbf{q}) G_{\mathbf{k}+\mathbf{q}, \sigma}^{\nu'\nu''}(\tau) G_{\mathbf{k}, \sigma}^{\nu'''\nu}(-\tau), \quad (3.40)
\end{aligned}$$

where we used that  $G_{\mathbf{k}, \mathbf{k}', \sigma, \sigma'} \propto \delta_{\mathbf{k}, \mathbf{k}'} \delta_{\sigma, \sigma'}$ . With

$$\sigma_{\alpha, \beta}^{\text{para}}(\Omega, \mathbf{q} \rightarrow 0) = \frac{1}{\Omega} \sum_{\nu\nu''\nu'''}^{\nu\nu'} (\Pi_{\alpha\beta})_{\nu\nu''\nu'''}^{\nu\nu'}(\mathbf{q} \rightarrow 0, \Omega), \quad (3.41)$$

we obtain (after Fourier transform of  $\Pi(\tau)$ ) the generalization of Eq. (3.37),

$$\sigma_{\alpha, \beta}^{\text{para}}(\Omega, \mathbf{q} \rightarrow 0) = \frac{e^2}{V\Omega\beta} \sum_{\nu\nu''\nu'''}^{\nu\nu'} \sum_{\mathbf{k}, \sigma} v_{\mathbf{k}, \sigma, \alpha}^{\nu\nu'} v_{\mathbf{k}, \sigma, \beta}^{\nu''\nu'''} \sum_{\omega_n} G_{\mathbf{k}, \sigma}^{\nu'\nu''}(i\omega_n + i\Omega) G_{\mathbf{k}, \sigma}^{\nu'''\nu}(i\omega_n), \quad (3.42)$$

where we omitted the argument  $\mathbf{q} = 0$  in the Fermi velocities. This is the final expression for the optical conductivity as used in our LDA+DMFT optical studies presented in Ch. 9; see Sec. C.4 for details on the actual numerical calculation of  $\sigma$  and the subsequent analytic continuation to real frequencies.

We will furthermore derive a common expression for the optical conductivity in real frequency space in terms of spectral functions. Since  $G_{\mathbf{k}, \sigma}^{\nu\nu'}(i\omega_n)$  is analytic in the upper half plane, we can use Eq. (6.2) and write

$$G_{\mathbf{k}, \sigma}^{\nu\nu'}(i\omega_n) = \int_{-\infty}^{\infty} d\omega \frac{A_{\mathbf{k}, \sigma}^{\nu\nu'}(\omega)}{i\omega_n - \omega}, \quad (3.43)$$

with the respective spectral function  $A(\omega)$ . Having established the analytical dependence on  $i\omega_n$ , the Matsubara sum in Eq. (3.42) can be executed,

$$\frac{1}{\beta} \sum_{\omega_n} \frac{1}{i\omega_n + i\Omega - \omega} \frac{1}{i\omega_n - \omega'} = \frac{f(\omega) - f(\omega')}{i\Omega - \omega' + \omega}, \quad (3.44)$$

with  $f(\omega)$  the Fermi function,  $f(\omega) = 1/(1 + e^{\beta(\hbar\omega - \mu)})$ , arriving at

$$\sigma_{\alpha, \beta}^{\text{para}}(\Omega, \mathbf{q} \rightarrow 0) = \frac{e^2}{V\Omega} \sum_{\nu\nu''\nu'''}^{\nu\nu'} \sum_{\mathbf{k}, \sigma} v_{\mathbf{k}, \sigma, \alpha}^{\nu\nu'} v_{\mathbf{k}, \sigma, \beta}^{\nu''\nu'''} \int_{-\infty}^{\infty} d\omega' \int_{-\infty}^{\infty} d\omega'' A_{\mathbf{k}, \sigma}^{\nu'\nu''}(\omega') A_{\mathbf{k}, \sigma}^{\nu'''\nu}(\omega'') \frac{f(\omega') - f(\omega'')}{i\Omega - \omega'' + \omega'}. \quad (3.45)$$

In order to return to a real frequency representation, we apply Wick rotation  $i\Omega \rightarrow \omega + i\eta$ ,

$$\begin{aligned}
\text{Re } \sigma_{\alpha, \beta}^{\text{para}}(\omega, \mathbf{q} \rightarrow 0) &= \frac{e^2}{V} \mathcal{P} \frac{1}{\omega} \sum_{\nu\nu''\nu'''}^{\nu\nu'} \sum_{\mathbf{k}, \sigma} v_{\mathbf{k}, \sigma, \alpha}^{\nu\nu'} v_{\mathbf{k}, \sigma, \beta}^{\nu''\nu'''} \int_{-\infty}^{\infty} d\omega' \int_{-\infty}^{\infty} d\omega'' A_{\mathbf{k}, \sigma}^{\nu'\nu''}(\omega') A_{\mathbf{k}, \sigma}^{\nu'''\nu}(\omega'') \\
&\quad \times (f(\omega') - f(\omega'')) \pi \delta(\omega - \omega'' + \omega') \\
&= \frac{\pi e^2}{V} \sum_{\nu\nu''\nu'''}^{\nu\nu'} \sum_{\mathbf{k}, \sigma} v_{\mathbf{k}, \sigma, \alpha}^{\nu\nu'} v_{\mathbf{k}, \sigma, \beta}^{\nu''\nu'''} \int_{-\infty}^{\infty} d\omega' A_{\mathbf{k}, \sigma}^{\nu'\nu''}(\omega') A_{\mathbf{k}, \sigma}^{\nu'''\nu}(\omega' + \omega) \frac{f(\omega') - f(\omega' + \omega)}{\omega}. \quad (3.46)
\end{aligned}$$

Without rigorous derivation, we note that optical transitions in the dipole approximation are tied to selection rules ( $n$  denoting the main quantum number,  $\ell$  the orbital quantum number,  $m$  the magnetic quantum number, and  $\sigma$  the spin),

$$\Delta\ell = \ell' - \ell = \pm 1 \quad , \quad \Delta m = m' - m = 0, \pm 1 \quad , \quad \Delta\sigma = \sigma' - \sigma = 0 \quad , \quad (3.47)$$

stating that transitions can only occur if the initial state  $|n, \ell, m, \sigma\rangle$  and the final state  $|n', \ell', m', \sigma'\rangle$  differ by  $\Delta\ell$ ,  $\Delta m$ , and  $\Delta\sigma$ . The reason for the  $\ell$  selection rule is the odd parity of the dipole operator (3.38) which only couples states of different parity, whereas the  $m$  selection rule depends on the polarization of the incident light beam ( $\Delta m = 0$  for linearly polarized light,  $\Delta m = -1$  for right-hand circularly polarized light,<sup>4</sup> and  $\Delta m = 1$  for left-hand circularly polarized light). On the other hand, the electric dipole operator does not depend on the spin, therefore the component of the electron spin is not changed by absorption or emission of dipole radiation, hence  $\Delta\sigma = 0$ . Other transitions are called forbidden and can only be induced by higher-order terms in the multipole expansion of the vector potential, *i.e.* quadrupole terms, octupole terms *etc.*. In the following we will demonstrate how these selection rules enter when calculating the optical conductivity in the LAPW basis.

### 3.5 Optical Conductivity in LAPW

Here, we provide some notes on the calculation of the optical conductivity in the framework of DFT and specifically for the LAPW basis set.

Instead of writing the optical conductivity in terms of spectral functions (*i.e.* densities of states in DFT) on an energy continuum, we want to express  $\sigma(\omega)$  by the discrete Kohn-Sham energies  $\epsilon_{\mathbf{k},\sigma}^\nu$ . In DFT, the Green's functions in Eq. (3.42) are (formally) noninteracting and diagonal in Bloch space,

$$G_{\mathbf{k},\sigma}^{\nu\nu'}(i\omega_n) = \frac{\delta_{\nu\nu'}}{i\omega_n - \epsilon_{\mathbf{k},\sigma}^\nu} \quad , \quad (3.48)$$

and we obtain in analogy to Eq. (3.45),

$$\sigma_{\alpha\beta}^{\text{para}}(\Omega, \mathbf{q} \rightarrow 0) = \frac{e^2}{V\Omega} \sum_{\nu\nu', \mathbf{k}, \sigma} v_{\mathbf{k},\sigma,\alpha}^{\nu\nu'} (v_{\mathbf{k},\sigma,\beta}^{\nu\nu'})^* \frac{f(\epsilon_{\mathbf{k},\sigma}^{\nu'}) - f(\epsilon_{\mathbf{k},\sigma}^\nu)}{i\Omega - \epsilon_{\mathbf{k},\sigma}^\nu + \epsilon_{\mathbf{k},\sigma}^{\nu'}} \quad , \quad (3.49)$$

and, after continuation to real frequencies,

$$\sigma_{\alpha\beta}^{\text{para}}(\omega, \mathbf{q} \rightarrow 0) = \frac{\pi e^2}{V\omega} \sum_{\nu\nu', \mathbf{k}, \sigma} v_{\mathbf{k},\sigma,\alpha}^{\nu\nu'} (v_{\mathbf{k},\sigma,\beta}^{\nu\nu'})^* (f(\epsilon_{\mathbf{k},\sigma}^{\nu'}) - f(\epsilon_{\mathbf{k},\sigma}^\nu)) \left( -\delta(\omega) + \delta(\omega - (\epsilon_{\mathbf{k},\sigma}^\nu - \epsilon_{\mathbf{k},\sigma}^{\nu'})) \right) \quad , \quad (3.50)$$

with the two contributions to the paramagnetic current that we already identified in Eq. (3.34) and of which we only consider the finite frequency response.

As a remark to the optical selection rules mentioned above, we briefly sketch how the angular and magnetic momentum selection rules in Eq. (3.47) are realized in LAPW [Ambrosch-Draxl06].

<sup>4</sup>Here, light is considered right-hand (left-hand) circularly polarized if the electric field vector circulates clockwise (anti-clockwise) when looking towards the light beam.

Due to the split representation of the LAPW basis functions (2.20), the momentum matrix element (3.38) is a sum of contributions from the atomic MT spheres as well as from the interstitial region,

$$\langle \mathbf{k}, \nu | \mathbf{p} | \mathbf{k}, \nu' \rangle = \sum_{\alpha} \langle \mathbf{k}, \nu | \mathbf{p} | \mathbf{k}, \nu' \rangle_{\text{MT}_{\alpha}} + \langle \mathbf{k}, \nu | \mathbf{p} | \mathbf{k}, \nu' \rangle_{\text{I}}. \quad (3.51)$$

Here, we only analyze the matrix elements between initial and final states with pure angular momentum character, *i.e.* the matrix elements between the LAPW basis states within the MT spheres, and define

$$\Phi_{\ell, m}^{\ell', m'} \equiv \langle w_{\ell', m'} Y_{\ell', m'} | \mathbf{p} | w_{\ell, m} Y_{\ell, m} \rangle, \quad (3.52)$$

where  $w_{\ell, m}$  is the radial part, *i.e.* includes the  $A$  and  $B$  terms of Eq. (2.20). We express  $\mathbf{p} = -i\hbar\nabla$  in spherical coordinates,

$$\partial x \pm i\partial y = \sin\vartheta e^{\pm i\varphi} \frac{\partial}{\partial r} + \frac{1}{r} e^{\pm i\varphi} \left( \cos\vartheta \frac{\partial}{\partial\vartheta} \pm \frac{i}{\sin\vartheta} \frac{\partial}{\partial\varphi} \right), \quad (3.53)$$

$$\partial z = \cos\vartheta \frac{\partial}{\partial r} - \frac{1}{r} \sin\vartheta \frac{\partial}{\partial\vartheta}. \quad (3.54)$$

By evaluating  $\partial x \pm i\partial y$  instead of  $\partial x$  and  $\partial y$  separately, the derivatives of the spherical harmonics take a simpler form; the  $x$ - and  $y$ - component will then be calculated as linear combinations. We demonstrate the evaluation of Eq. (3.52) for the first component  $\partial x + i\partial y$  in the following. By using the relations for the spherical harmonics given in Appendix D, the application of  $\partial x + i\partial y$  yields

$$\begin{aligned} (\partial x + i\partial y) w_{\ell, m}(r) Y_{\ell, m}(\vartheta, \varphi) &= \frac{\partial w_{\ell, m}}{\partial r} \sin\vartheta e^{i\varphi} Y_{\ell, m} + \frac{1}{r} w_{\ell, m} e^{i\varphi} \left( \cos\vartheta \frac{\partial}{\partial\vartheta} + \frac{i}{\sin\vartheta} \frac{\partial}{\partial\varphi} \right) Y_{\ell, m} \\ &= \left( w'_{\ell, m} - \frac{l}{r} w_{\ell, m} \right) F_{\ell, m}^{(1)} Y_{\ell+1, m+1} \\ &\quad + \left( w'_{\ell, m} + \frac{l+1}{r} w_{\ell, m} \right) F_{\ell, m}^{(2)} Y_{\ell-1, m+1}, \end{aligned} \quad (3.55)$$

where the definitions for  $F^{(1)}$  and  $F^{(2)}$  are given in Appendix D. Here and in the following, we dropped the argument of the radial part  $w$ ; for our purpose,  $w(r)$  is a numerically given function and  $w'$  denotes its derivative. The matrix element then reads

$$\begin{aligned} \Phi_{\ell, m}^{\ell', m'} \{x + iy\} &= \int_{\text{MT}_{\alpha}} w_{\ell', m'}^* Y_{\ell', m'}^* (\partial x + i\partial y) w_{\ell, m} Y_{\ell, m} \\ &= \int_0^{R_{\alpha}} r^2 dr w_{\ell', m'}^* \left( w'_{\ell, m} - \frac{l}{r} w_{\ell, m} \right) F_{\ell, m}^{(1)} \oint d\Omega Y_{\ell', m'}^* Y_{\ell+1, m+1} \\ &\quad + \int_0^{R_{\alpha}} r^2 dr w_{\ell', m'}^* \left( w'_{\ell, m} + \frac{l+1}{r} w_{\ell, m} \right) F_{\ell, m}^{(2)} \oint d\Omega Y_{\ell', m'}^* Y_{\ell-1, m+1} \\ &= R_{\ell, m}^{\ell', m'} \delta_{\ell', \ell+1} \delta_{m', m+1} + T_{\ell, m}^{\ell', m'} \delta_{\ell', \ell-1} \delta_{m', m+1}, \end{aligned} \quad (3.56)$$

where we used the orthogonality of the spherical harmonics, and  $R$  and  $T$  are defined as

$$R_{\ell, m}^{\ell', m'} = F_{\ell, m}^{(1)} S_{\ell, \ell'} \quad , \quad T_{\ell, m}^{\ell', m'} = F_{\ell, m}^{(2)} \tilde{S}_{\ell, \ell'}, \quad (3.57)$$

with

$$S_{\ell, m}^{\ell', m'} = \int_0^{R_{\alpha}} r^2 dr w_{\ell', m'}^* \left( w'_{\ell, m} - \frac{l}{r} w_{\ell, m} \right), \quad (3.58)$$

$$\tilde{S}_{\ell, m}^{\ell', m'} = \int_0^{R_{\alpha}} r^2 dr w_{\ell', m'}^* \left( w'_{\ell, m} + \frac{l+1}{r} w_{\ell, m} \right). \quad (3.59)$$

The selection rules are reflected by the Kronecker deltas in Eq. (3.56): transitions are only allowed between initial and final states that differ by  $\pm 1$  in angular momentum,  $\Delta\ell = \pm 1$ . Also, we obtain  $\Delta m = 1$ , the reason being that the component  $\partial x + i\partial y$  of the dipole matrix element describes the response to left-hand circularly polarised light.



# 4. Conductivity Spectra of Iron Pnictides in the Spin Density Wave Phase

J. Ferber, Y.-Z. Zhang, H. O. Jeschke, and R. Valentí,  
Phys. Rev. B. **82**, 165102 (2010)

In this chapter, we study the optical conductivity of LaFeAsO, BaFe<sub>2</sub>As<sub>2</sub>, and SrFe<sub>2</sub>As<sub>2</sub> in the spin-density wave (SDW) state within DFT in the framework of the spin-polarized generalized gradient approximation (GGA) and GGA+U. We find two quantities to be essential for the optical features, the Fe magnetic moments and the renormalization of the kinetic energy. In order to recover the small Fe magnetic moments observed experimentally, GGA+ $U_{\text{eff}}$  with a suitable choice of negative on-site interaction  $U_{\text{eff}} = U - J$  was considered. Reminiscent of the fact that GGA+ $U_{\text{eff}}$  with a positive  $U_{\text{eff}}$  is a simple approximation for reproducing a gap with correct amplitude in correlated insulators, a negative  $U_{\text{eff}}$  can be understood as a way to suppress magnetism as we will show below. Moreover, we apply a renormalization of the kinetic energy to the resulting spectra, which mimics the mass enhancement of the charge carriers due to electronic correlations. With these considerations, the resulting optical spectra reproduce the SDW gap and a number of experimentally observed features related to the antiferromagnetic (AF) order as well as the optical conductivity in the normal state. Also, an orbital-resolved analysis of the optical conductivity reveals significant contributions from all Fe  $3d$  orbitals.

## 4.1 Introduction

As laid out in Sec. 1.2, in several families of the iron pnictides high temperature superconductivity emerges in close proximity to an AF ground state with stripe-type order. The AF transition is induced by an SDW instability below a critical temperature  $T_{\text{SDW}}$  which is either preceded or coincidental with a structural transition from a tetragonal to an orthorhombic phase. Upon doping or application of pressure, the AF order is suppressed and superconductivity emerges.

Many features of the electronic structure of the iron pnictides are directly reflected in their optical properties: the low-frequency region of the conductivity spectrum is governed by

the itinerant carrier contribution and directly shows the effect of correlations in the area under the Drude region which is proportional to the kinetic energy of the electrons; the infrared regime above the Drude peak is dominated by gap features induced by either the SDW gap (cf. Fig. 4.1) or the superconducting gap; finally, the visible part of the spectrum reflects the band structure in the normal state. Consequently, a number of experimental studies have been performed on the optical properties of the iron pnictides in the normal state, the SDW state, as well as in the superconducting state [Hu08, Drechsler08, Nakajima10, Chen10, Wu10, Wu09a, Gorshunov10, Lucarelli10, Dusza11]. The SDW state is characterized by (i) the appearance of a peak in the optical conductivity at the SDW gap frequency, (ii) an anisotropic dc response, and (iii) an almost isotropic response in the infrared and optical region of the spectrum. On the other hand, while several theoretical works based on LDA [Qazilbash09] and LDA+DMFT [Haule08, Laad09] have been done on the paramagnetic phase, there is still a lack of DFT calculations for the optical conductivity in the SDW state (with the exception of Ref. [Sanna11] which appeared after our publication).

Here we report optical studies in the framework of density functional theory on three iron pnictides in the SDW state, namely the 1111 compound LaFeAsO, and the 122 compounds  $A\text{EFe}_2\text{As}_2$  ( $A\text{E}=\text{Ba},\text{Sr}$ ). This provides an insight into the microscopic origin of the optical features in the SDW state and allows for an assessment of DFT regarding its applicability to the iron pnictides.

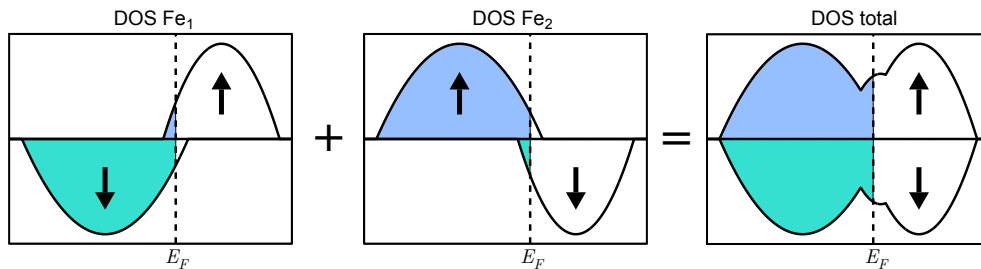


Figure 4.1: Schematic illustration of the formation of a gap in the density of states (DOS) due to the antiferromagnetic order.  $\text{Fe}_1$  denotes the iron site with majority spin down whereas  $\text{Fe}_2$  is the site with majority spin up.

## 4.2 Computational Details

We performed electronic structure calculations with the full potential linearized augmented plane wave method as implemented in WIEN2K [Blaha01]. The selfconsistency cycle employed 2048  $\mathbf{k}$  points in the full Brillouin zone (FBZ) using GGA in the Perdew-Burke-Ernzerhof variant for the exchange-correlation potential [Perdew96]; the optical properties were evaluated with 16384  $\mathbf{k}$  points in the FBZ. Experimental lattice parameters and atomic positions were used for  $\text{BaFe}_2\text{As}_2$  [Huang08] and  $\text{SrFe}_2\text{As}_2$  [Tegel08]. For LaFeAsO, the optimized structure from Ref. [Zhang10] was used. For the optical properties, the `optics` [Ambrosch-Draxl06] code package in WIEN2K was modified to allow for an orbital character resolved analysis.

We are working in the framework of ‘GGA+U’ where ‘ $U$ ’ ( $\equiv U_{\text{eff}} = U - J$ ) describes the competition between the (spherically averaged) on-site Coulomb interaction  $U$  and the

(spherically averaged) on-site exchange coupling  $J$  (within the Fe 3d subshell). In this context, the FLL double counting correction (2.29) was applied. According to Eq. (2.34), the expression for the correction to the GGA functional then reads

$$\Delta E^{\text{FLL}} = \frac{U - J}{2} \sum_{m,\sigma} n_{m,\sigma} (1 - n_{m,\sigma}) + H_{\text{int}}^{\text{aniso}}, \quad (4.1)$$

where  $n_{m,\sigma}$  is the spin-projected occupation in orbital  $m$ . In particular, the isotropic part of this expression (which we consider for our discussion since it is significantly larger than the anisotropic part) only depends on the difference  $U - J$ .

In order to allow for the stripe-type AF order, we consider a doubled ( $\sqrt{2} \times \sqrt{2} \times 1$ ) unit cell with AF order along the  $a$  axis of the supercell and ferromagnetic (FM) arrangement along the  $b$  axis (*i.e.* the supercell is rotated  $45^\circ$  with respect to the original unit cell), as observed experimentally. In the following, the orbital characters are labeled with respect to the coordinate system of this supercell. Spin-polarized calculations with AF order are labeled with ‘GGA(AF)’ (‘GGA+U(AF)’), respectively).

Spin-orbit coupling is not taken into account in our calculations, and therefore all off-diagonal elements  $\alpha \neq \beta$  in the optical conductivity (3.50) vanish due to the orthorhombic symmetry of our materials.

As for the Drude peak, the zero-temperature delta peak is for practical calculations augmented with a lifetime broadening (scattering rate)  $\Gamma$ ,

$$\delta(\omega) \rightarrow \frac{\Gamma}{\pi(\omega^2 + \Gamma^2)}. \quad (4.2)$$

According to Eq. (3.32), the weight of the Drude peak is given by  $\omega_p^2/4$ , and the Drude contribution to the optical conductivity is hence

$$\sigma_D = \frac{\Gamma \omega_p^2}{4\pi(\omega^2 + \Gamma^2)}. \quad (4.3)$$

The total squared plasma frequency is given by  $\omega_p^2 = \sum_{n,\sigma} \omega_p(n,\sigma)^2$  with  $\omega_p(n,\sigma)^2$  the squared plasma frequency for band  $n$  and spin  $\sigma$ . Note that we consider only one overall Drude peak, despite the possibility of two or more Drude peaks due to multiple bands crossing the Fermi surface. However, the Lorentz distribution is stable, *i.e.* a sum of Lorentz distributions (4.3) is again of the form (4.3) with the total squared plasma frequency as above and  $\Gamma_{\text{tot}} = \sum_{n,\sigma} \Gamma(n,\sigma)$ . Consequently, only the carrier scattering rate is left as a free parameter which cannot be determined within a DFT approach. For our purposes,  $\Gamma$  is chosen close to experimental values in the SDW state[Hu08]. Given these considerations, all relevant information about the Drude peak is contained in the plasma frequency  $\omega_p$ .

## 4.3 Results

### 4.3.1 Density of States

Preliminary to the analysis of the optical properties of the iron pnictides, we first start with the discussion of the density of states (DOS), since the optical conductivity is essentially

the joint density of states weighted with the transition matrix element and divided by the frequency, see Eq. (3.46). In particular, we find that the antiferromagnetic order and the magnitude of the magnetic moments crucially affect the optical properties which is reflected by the (partial) opening of a gap in the DOS.

For the iron pnictides, DFT calculations are known to strongly overestimate the magnetic moments on the Fe atoms in the SDW state ( $m \approx 2.0 \mu_B$  with GGA(AF) compared to  $0.4 \mu_B$  [Cruz08]– $0.6 \mu_B$  [Qureshi10] for LaFeAsO). This results in a too large SDW gap which in turn shifts the SDW features in the spectra to erroneously high energies. In order to reproduce the SDW gap correctly, we employ GGA+U with negative  $U_{\text{eff}}$  [Nakamura09a, Yi09] to reduce the overestimated magnetic moment from GGA(AF). Similar to the application of a positive  $U$  in GGA+U calculations to reproduce the correlated gap in Mott insulators, the negative  $U_{\text{eff}}$  can be understood as a simple way to suppress the tendency to magnetism within the mean-field approximation. This can be read off from the correction to the GGA functional in Eq. (4.1) which at negative  $U_{\text{eff}}$  energetically favors  $n_{m,\sigma} = 1/2$ , *i.e.* the paramagnetic case, and conversely penalizes (spin-projected) integer occupations, *i.e.* the fully polarized states.

The resulting Fe magnetic moments are listed in Tab. 4.1. With the same value  $U_{\text{eff}} = -1.2$  eV, the magnetic moments for all materials are reproduced correctly within the range of experimental results (LaFeAsO:  $m = 0.36 \mu_B$  [Cruz08]– $0.63 \mu_B$  [Qureshi10]; BaFe<sub>2</sub>As<sub>2</sub>:  $m = 0.87 \mu_B$  [Huang08]– $0.99 \mu_B$  [Su09]; SrFe<sub>2</sub>As<sub>2</sub>:  $m = 1 \mu_B$  [Jesche08]– $1.01 \mu_B$  [Kaneko08]). This is a suprising improvement over the GGA(AF) calculation where not only the magnetic moments are overestimated but also identical for all materials, without any indication of the correct trends.

Table 4.1: Optical parameters of the investigated compounds as obtained from the different calculation methods.  $\omega_p^{a(b)}$  is the plasma frequency in  $a(b)$ -direction.

Compound	Calc.	$\omega_p^a$ (eV)	$\omega_p^b$ (eV)	$m$ ( $\mu_B$ )
LaFeAsO	GGA	2.25	2.25	0
	GGA(AF)	0.87	0.82	1.98
	GGA+U(AF), $U_{\text{eff}} = -1.2$ eV	1.39	1.05	0.43
BaFe <sub>2</sub> As <sub>2</sub>	GGA	2.62	2.62	0
	GGA(AF)	0.62	0.65	1.98
	GGA+U(AF), $U_{\text{eff}} = -1.2$ eV	1.17	1.06	0.85
SrFe <sub>2</sub> As <sub>2</sub>	GGA	2.79	2.79	0
	GGA(AF)	0.64	0.64	1.98
	GGA+U(AF), $U_{\text{eff}} = -1.2$ eV	1.07	0.88	0.96

Note that the exact form of the GGA+U functional and thus the preference of low-spin or high-spin states depends on the double counting correction. A reduction of the magnetic moment can also be achieved by using positive  $U$  and around mean-field double counting [Ylvisaker09]. This approach was taken in Ref. [Cricchio10] and yields good agreement with the observed magnetic moments; however, sufficiently large  $U$ 's deplete the density of states around the Fermi energy and suppress the low-energy features of the optical conductivity that we are focusing on.

From this, it becomes clear that a comparison of the role of  $U$  and  $J$  with their model counterparts is not generally valid but needs to take into account the double counting correction under consideration.

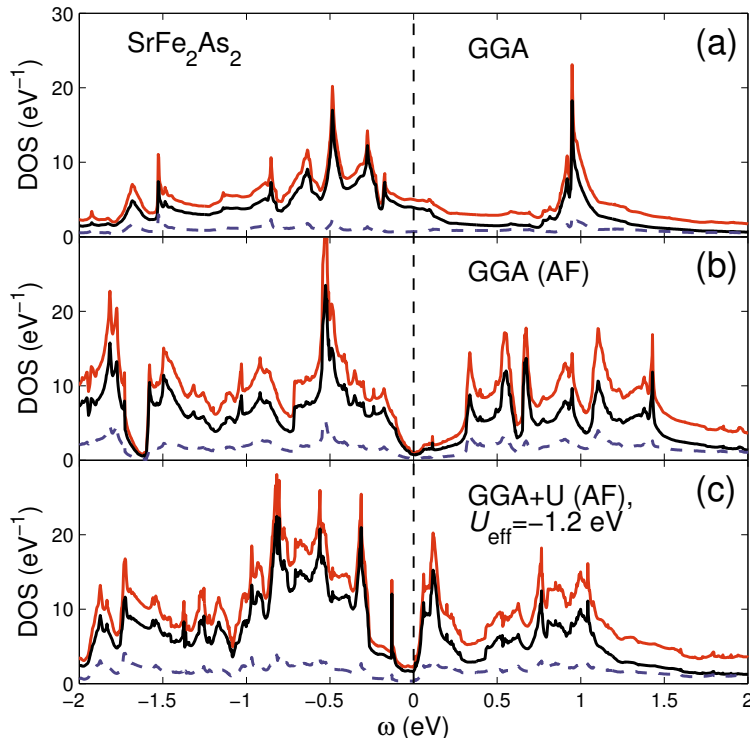


Figure 4.2: DOS of  $\text{SrFe}_2\text{As}_2$  for different values of  $U_{\text{eff}}$ .  $\omega = 0$  corresponds to the Fermi energy. As is well known, the Fe  $3d$  subshell dominates the DOS around the Fermi energy. The contributions from Sr, As, and the other Fe orbitals are small.

Fig. 4.2 shows the evolution of the DOS for different values of  $U_{\text{eff}}$  in  $\text{SrFe}_2\text{As}_2$ . Compared to the non-spin-polarized GGA DOS, a suppression around  $E_F$  is clearly visible in the AF calculations. For the parameter regimes shown in Fig. 4.2, only a partial opening of the gap is observed as some DOS persists around  $E_F$ ; full opening of the gap occurs at positive values of  $U_{\text{eff}}$ , *i.e.* for sufficiently strong Hubbard  $U$ . In contrast, for pronounced negative  $U_{\text{eff}}$  the magnetic moment is reduced and the SDW gap narrows accordingly. Almost over the whole energy range shown in the figure, the DOS is strongly distorted and shifted by the inclusion of the AF order compared to the non-spin-polarized GGA DOS. However, the suppression of the magnetic moments for  $U_{\text{eff}} = -1.2$  eV again renders the DOS qualitatively similar to the GGA DOS, except in the region around the Fermi energy. Thus, the optical properties can be expected to be close to those of the GGA case in the higher energy regions of the spectrum.

### 4.3.2 Optical Conductivity

As for the in-plane optical conductivity of the iron pnictides in the SDW state, experimental investigations on single crystals [Wu10, Hu08, Chen10, Lucarelli10, Dusza11] consistently report a number of common features, although the exact location of the features depends on the material under investigation. These features are: metallic behavior, *i.e.* the presence of a Drude-like conductivity at low frequencies ( $\lesssim 100$   $\text{cm}^{-1}$ ), a peak at

the SDW gap frequency ( $\approx 1000 \text{ cm}^{-1}$ - $1500 \text{ cm}^{-1}$ ), and a broad, less pronounced peak in the mid-infrared region ( $\approx 5000 \text{ cm}^{-1}$ - $6000 \text{ cm}^{-1}$ ) which almost does not depend on the temperature and is also present above  $T_{\text{SDW}}$ . The peaks are associated with a suppression of the spectral weight at lower energies (below  $\approx 1000 \text{ cm}^{-1}$  for the SDW peak, below  $\approx 5000 \text{ cm}^{-1}$  for the high-energy peak), which leads to a spectral weight transfer from lower to higher energies. Note that in the normal state the tetragonal symmetry leaves only two independent components in the dielectric tensor and thus the conductivity is defined as  $\sigma_{aa} = \sigma_{bb}$  for the Fe in-plane directions  $a$  and  $b$ , and  $\sigma_{cc}$  for the out-of-plane direction  $c$  perpendicular to  $a$  and  $b$ . In the SDW state, the stripe-like AF order introduces an anisotropy which lifts the degeneracy of the two in-plane components. However, whereas an anisotropic dc response is observed in detwinned samples [Chu10], no substantial anisotropy is experimentally found in the finite frequency spectra.

First, we analyze the low-energy Drude region of the spectrum as characterized by the plasma frequency. Since the SDW gap opening is only partial, the Drude peak is still present –expressed by a finite plasma frequency– both experimentally and in our calculations. The ratio of the kinetic energies which equals the ratio of the squares of the plasma frequencies,  $K_{\text{exp}}/K_{\text{band}} = (\omega_p^{\text{exp}})^2/(\omega_p^{\text{band}})^2$ , is commonly taken as a measure for the renormalization effect of the electronic correlations compared to band structure calculations. As specified in Tab. 4.1, the non-spin-polarized GGA value for *e.g.*  $\text{SrFe}_2\text{As}_2$  is  $\omega_p \approx 2.79 \text{ eV}$ , whereas the experimental value in the normal state is  $\omega_p \approx 1.7 \text{ eV}$  at 300 K [Hu08], yielding  $K_{\text{exp}}/K_{\text{band}} \approx 0.37$ . In the SDW state, the experimental plasma frequency is strongly reduced due to the removal of itinerant carriers from the Fermi surface by the opening of the SDW gap. Likewise, in our calculations, the inclusion of the SDW order reduces the number of bands crossing the Fermi surface, which also significantly reduces the plasma frequencies. The renormalization due to the correlations still persists, though: since directional plasma frequencies from detwinned samples are not available, a quantitative assessment is delicate, but a comparison with the results from Ref. [Hu08] for  $\text{BaFe}_2\text{As}_2$  and  $\text{SrFe}_2\text{As}_2$  indicates renormalizations of 0.3-0.5 for the 122 compounds, equivalent to mass enhancements of 2-3.

In the following, we therefore adopt a (heuristic) energy renormalization factor  $1/R$  for our optical conductivity spectra, where we choose  $R = 2.4$  for  $\text{BaFe}_2\text{As}_2$  and  $\text{SrFe}_2\text{As}_2$ . For  $\text{LaFeAsO}$ , we choose  $R = 2$  in the absence of experimental plasma frequencies in the SDW state, which reflects the supposedly less pronounced effect of correlations in the 1111 compounds.

In Fig. 4.3 we present an overview of the thus obtained in-plane optical conductivity in the low-frequency region. Figs. 4.3 (a)–(c) show a comparison of the experimental results with the calculation methods introduced in the previous section; the GGA+U(AF) results exhibit the SDW peak as the most prominent feature, located at the SDW gap frequency. For all compounds, the SDW peak emerges at the experimentally determined frequency only for the negative value of  $U_{\text{eff}}$  discussed above, and otherwise moves to higher frequencies. Fig. 4.4 displays the optical conductivity for  $\text{LaFeAsO}$  and  $\text{BaFe}_2\text{As}_2$  over a larger energy range.<sup>1</sup> As can be seen there, the GGA results without SDW order do not show any significant peak in the optical conductivity up to a (renormalized) energy of  $\approx 0.5 \text{ eV}$ . This can readily be read off from the density of states, where the GGA

<sup>1</sup>To facilitate the comparison to the experimental data, we multiplied the spectrum of  $\text{BaFe}_2\text{As}_2$  by a factor of two in Figs. 4.3 and 4.4. The absolute value of the optical conductivity depends on the reflectivity of the actual sample and details of the Kramers-Kronig procedure, and can significantly differ between experimental studies on the same material, cf. *e.g.* spectra for  $\text{BaFe}_2\text{As}_2$  in Refs. [Hu08] and [Dusza11].

DOS is essentially depleted up to 1 eV above  $E_F$ . For high frequencies, the GGA and GGA+U(AF) spectra are basically identical, as is to be expected. The observed mid-infrared peak around 0.5 eV in  $\text{BaFe}_2\text{As}_2$ , visible in Fig. 4.4 (b), is well reproduced in all calculations. For  $\text{LaFeAsO}$ , the experimental data is almost flat above approx. 0.3 eV which may be caused by a large scattering rate. This could be described if quantum fluctuations are treated properly and consequently a frequency-dependent self-energy is involved. However, as the focus of this work is the analysis of the features induced by the AF ordering, we concentrate on the low-energy features.

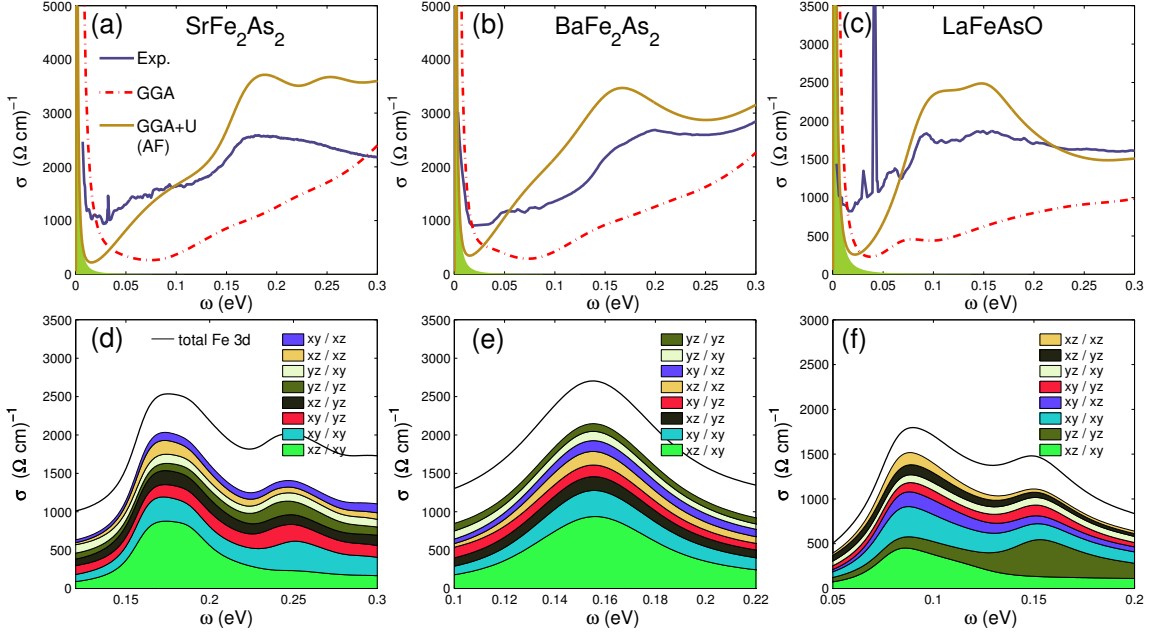


Figure 4.3: Real part of the optical conductivity of different iron pnictides in the SDW state, for  $U_{\text{eff}} = -1.2$  eV and energy renormalization factor  $1/R$ : (a),(d)  $\text{SrFe}_2\text{As}_2$ ,  $R = 2.4$  (experimental data taken from Ref. [Hu08]), (b),(e)  $\text{BaFe}_2\text{As}_2$ ,  $R = 2.4$  (Ref. [Dusza11]), and (c),(f)  $\text{LaFeAsO}$ ,  $R = 2$  (Ref. [Chen10]). The orbital characters are sorted by their contribution to the total conductivity, integrated over the energy range shown in the respective plot, with the largest contribution at the bottom (only the first eight contributions are displayed; smaller contributions have been omitted).

In Figs. 4.3 (d)–(f), the decomposition of the SDW peak into Fe 3d orbital characters of the initial and final states is shown. Following Eq. (3.50), the orbital-resolved optical conductivity reads

$$\sigma_{\alpha\alpha}^{m_i, m_f}(\omega) = \frac{\pi e^2}{V\omega} \sum_{v, c, \mathbf{k}, \sigma} W_{\mathbf{k}, c}^{m_f} |v_{\mathbf{k}, \alpha}^{cv}|^2 W_{\mathbf{k}, v}^{m_i} \delta(\omega - (\epsilon_{\mathbf{k}, \sigma}^c - \epsilon_{\mathbf{k}, \sigma}^v)), \quad (4.4)$$

where the band indices  $v$  ( $c$ ) denote occupied (empty) states, and  $W_{\mathbf{k}, \nu}^m$  formally denotes the relative weight of the Fe orbitals with magnetic quantum number  $m$  in the KS orbital  $|\mathbf{k}, \nu\rangle$ . Note that dipolar transitions among Fe 3d states are forbidden in the atomic limit due to the  $\ell$  selection rule (3.47). For the iron pnictides, the states around the Fermi energy are Fe 3d dominated with some As 4p contribution. This hybridization allows for transitions between initial and final states which are both Fe 3d dominated but owe their finite transition strength to Fe 3d  $\leftrightarrow$  As 4p transitions. This is taken into account

in Eq. (4.4) where the full wavefunction  $|\mathbf{k}, \nu\rangle$  is used for the calculation of the matrix element but the resulting optical conductivity is projected onto the Fe  $3d$  subspace. In particular, this projection omits the contribution from the interstitial region which has a significant DOS in the considered energy range but cannot be assigned an orbital character. However, as can be seen from the comparison of the SDW peaks in Figs. 4.3 (a)-(c) –which show the total optical conductivity– to the close-up in (d)-(f) –which only show the Fe  $3d$  contribution–, the Fe  $3d$  part resembles very well the structure of the total conductivity. Therefore, the contributions from the interstitial region as well as from the other atoms can be neglected for the orbital character analysis.

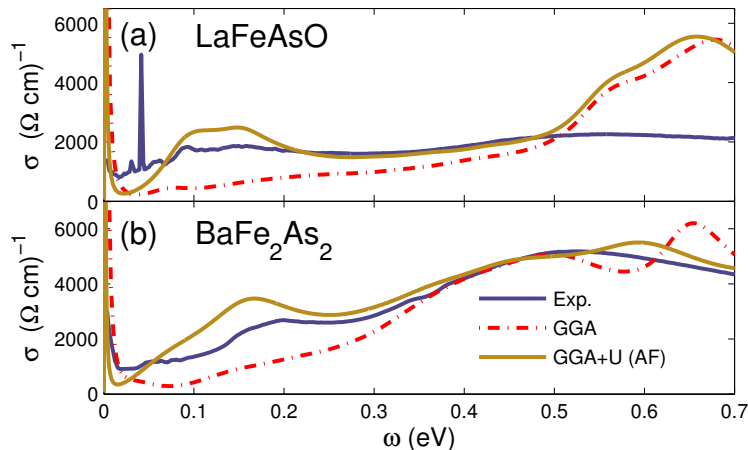


Figure 4.4: Optical conductivity in the higher energy region for (a) LaFeAsO and (b) BaFe<sub>2</sub>As<sub>2</sub>. Same experimental references and calculation parameters as in Fig. 4.3.

In the iron pnictides, the Fermi surface is crossed by multiple bands. Consequently, the optical properties also have multiband nature and one can expect contributions from several orbital characters. This is confirmed by our calculations where we observe no overly dominating character component in any part of the spectrum. The SDW peak structure differs from the rest of the spectrum in that it mainly contains  $t_{2g}$  character components; all  $t_{2g}$  components are larger than any  $e_g$  component.

As for the anisotropy due to the stripe-type SDW symmetry breaking, we find that it is strongly present in the GGA(AF) calculation (*i.e.* for  $U_{\text{eff}} = 0$ ) and for moderately negative values of  $U_{\text{eff}}$ , where  $\sigma_{bb}$  –the conductivity along the FM axis– shows a peak at significantly higher frequencies than  $\sigma_{aa}$ . As  $U_{\text{eff}}$  is decreased, the anisotropy is gradually suppressed and for the regime shown in Fig. 4.3, no pronounced anisotropy is present anymore, in accordance with the experimental observations. This can be understood considering the fact that while  $d_{xz}$  and  $d_{yz}$  are degenerate in the high temperature tetragonal phase, below the SDW transition temperature different band splittings and band shifts are produced by different magnetization and occupation number on these two orbitals. Therefore, the excitations along the  $x$  and  $y$  direction become inequivalent. As  $U_{\text{eff}}$  is decreased, the magnetization and consequently the symmetry breaking between the  $d_{xz}$  and  $d_{yz}$  orbitals is suppressed, leading to smaller differences between  $d_{xz}$  and  $d_{yz}$  orbitals and accordingly in the excitations along the  $x$  and  $y$  direction. Anisotropy can still be seen in the weak



double peak structure of LaFeAsO and SrFe<sub>2</sub>As<sub>2</sub> in Figs. 4.3 (a) and (c), respectively (d) and (f) (the conductivity shown in these plots is given by  $\sigma = (\sigma_{aa} + \sigma_{bb})/2$ ).<sup>2</sup>

It becomes clear from the dominating  $d_{xz}$  orbital contribution that the first sub-peak for SrFe<sub>2</sub>As<sub>2</sub> and LaFeAsO is dominated by the response along the AF direction  $\sigma_{aa}$ . For LaFeAsO, the second sub-peak is dominated by the  $d_{yz}$  contribution, indicating the relation to the response along the FM direction. We wish to point out that also this sub-peak is directly related to the AF order, though, as no peak is present in a purely ferromagnetic calculation (with the same absolute value of the magnetic moments).

Furthermore, for all compounds, the plasma frequencies and thus the dc conductivities exhibit a notable anisotropy between the  $a$  and  $b$  axes. Interestingly, the anisotropy develops differently in the 1111 compound than in the 122 compounds where the 1111 compound always features a higher conductivity along the  $a$  direction. In contrast,  $\sigma^b > \sigma^a$  in the 122 compounds for  $U_{\text{eff}} = 0$ , which is expected because of the larger lattice constant along the  $a$  axis and the orientation of the SDW vector along  $a$ . Unexpectedly, this no longer holds for negative  $U_{\text{eff}}$  where we find  $\sigma^a > \sigma^b$  also for the 122 compounds. This is in agreement with recent experiments on underdoped BaFe<sub>2</sub>As<sub>2</sub> where the magnetic domains were (partially) detwinned in a magnetic field in order to reveal the in-plane anisotropy in the resistivity[Chu10].

## 4.4 Conclusions

In summary, we have demonstrated that DFT is capable of reproducing a number of features associated with the SDW state in iron pnictides. However, this comes at the cost of a negative  $U_{\text{eff}}$  in the context of GGA+U calculations and a renormalization of the kinetic energy. This can be viewed as a route to mimic the effects of quantum fluctuations at the mean-field level and therefore as a driving force for suppressing the overestimated Fe magnetic moments obtained from GGA(AF). However, the agreement of the obtained magnetic moments with experimental results for all materials with the same value of  $U_{\text{eff}}$  and the correct shape of the conductivity spectra indicate the reliability of the approach. Therefore, we conclude that the employed GGA+U framework with negative  $U_{\text{eff}}$  mainly reduces the magnetic moment but does not distort the overall band structure too seriously. We find that all features of the experimental conductivity spectra can be identified in our results; this, in particular, excludes the formation of Hubbard bands or large spectral weight transfer due to correlations in these materials which would not be obtainable with our approach. This suggests that our effective description is surprisingly well suited for the SDW state in the iron pnictides.

---

<sup>2</sup>For BaFe<sub>2</sub>As<sub>2</sub>, the situation is slightly different as the experimental results in Ref. [Dusza11] are given separately along the AF and FM axis where only the AF direction (in the experimental as well as in the calculated spectra) is presented in Figs. 4.4 and 4.3; we therefore do not discuss the anisotropy in BaFe<sub>2</sub>As<sub>2</sub> here.



# 5. LDA+DMFT – Dynamical Mean-Field Theory for Real Materials

In Ch. 2, we pointed out the strengths and limitations of the standard approach to electronic structure calculations, density functional theory in the local density approximation. The known failure of DFT for materials with strong electronic correlations motivated the introduction of the LDA+U approach, described in Sec. 2.3. However, LDA+U stays on the level of a static mean-field approach: in the Green’s function language, it yields a self energy which is orbital-, spin-, and site-dependent but has no frequency-dependence (and no imaginary part). This allows to mimic the energy splitting leading to the formation of Hubbard bands, but is insufficient to describe the physics of quasiparticle bands. On the other side, dynamical mean-field theory (DMFT) is a method that extends the concept of static mean-field theories to strongly correlated electrons by retaining the frequency-dependence of the self energy, hence the name ‘dynamical’. In this chapter, we will review how to combine DFT with DMFT in order to account for (local) correlations beyond Hartree-Fock. The combination of these two methods[Anisimov97, Lichtenstein98, Kotliar06, Held07] goes under the name LDA+DMFT and has become an established method over the last decade, with numerous successful applications, see *e.g.* Refs. [Savrasov01, Lichtenstein01, Held01, Sekiyama04], to mention only a few. In the following, we start with an introduction to DMFT.

## 5.1 Dynamical Mean-Field Theory

As discussed in Ch. 1, a general solution for the Hubbard model is not available. Conventional analytical methods are therefore based on perturbation theory where the small expansion parameter can be  $U/t$  (weak-coupling expansion)[Penn66, Dongen94a],  $t/U$  (strong-coupling expansion)[Harris67, Dongen94b], or others, like  $1/T$  (high temperature expansion) or the density  $n$  (low density expansion). These limits are, however, not applicable for the investigation of *e.g.* the metal-insulator transition at half filling and low temperatures, the ‘drosophila’ of correlated electron physics.

DMFT provides another limit for correlated electron systems, the limit of infinite dimensions  $d \rightarrow \infty$ [Metzner89, Müller-Hartmann89]. More exactly, the small parameter is the

inverse coordination number  $1/Z$  (*i.e.* the inverse of the number of neighboring lattice sites) which *e.g.* in three dimensions takes values of  $1/6$ ,  $1/8$ , and  $1/12$  for the simple cubic, body centered cubic, and face centered cubic lattice, respectively. This limit is non-perturbative in  $U$  or  $t$ , *i.e.* the competition between the kinetic energy and the Coulomb interaction is preserved. As a tribute to the limit of infinite dimensions, only the local dynamics of the correlation problem is retained while off-site correlations are neglected. This results in a local, *i.e.* momentum-independent, self energy  $\Sigma(\mathbf{k}, \omega) \rightarrow \Sigma(\omega)$ .

For the derivation of the DMFT equations, let us first draw some analogy to the simple case of the Ising model,

$$H = -\frac{J}{2} \sum_{\langle ij \rangle} S_i S_j, \quad (5.1)$$

with exchange interaction  $J$  and  $S_i$  the spin at site  $R_i$ . In the Weiss mean-field approximation,  $H$  is replaced by

$$H^{\text{MF}} = -h^{\text{MF}} \sum_i S_i, \quad (5.2)$$

(plus a constant energy shift that we are neglecting here) with the mean-field

$$h^{\text{MF}} = J \sum_{j \text{ NN } i} \langle S_j \rangle = JZ \langle S \rangle, \quad (5.3)$$

which is proportional to the thermally averaged spin of the surrounding sites. However, in order for the energy per lattice site to remain finite in the limit  $Z \rightarrow \infty$ ,  $h^{\text{MF}}$  has to remain finite and the exchange interaction has to be scaled as  $J = J^*/Z$  with a constant (*i.e.*  $Z$ -independent)  $J^*$ . It is known that then the replacement of  $H$  with  $H^{\text{MF}}$  becomes exact in this limit: fluctuations in the bath of surrounding sites become unimportant for  $Z \rightarrow \infty$  and the environment is completely described by the single number  $h^{\text{MF}}$ . The resulting Hamiltonian  $H^{\text{MF}}$  is purely local and the problem reduces to an effective single-site problem.

In order to define a non-trivial  $Z \rightarrow \infty$  limit of the Hubbard Hamiltonian (1.7), one has to make sure that the competition between the kinetic and the interaction energy is preserved. Obviously, the purely local interaction as parameterized by  $U$  in Eq. (1.7) is independent of  $Z$  (and the lattice structure). For the kinetic term, let us first consider the case of the hypercubic lattice which for dimension  $d$  has coordination number  $Z = 2d$  and dispersion

$$\epsilon(\mathbf{k}) = -2t \sum_{i=1}^d \cos(k_i). \quad (5.4)$$

In the limit  $Z \rightarrow \infty$  this is an infinite sum over independent random numbers  $-2t \cos(k_i)$ , and the probability density of this sum is given by a Gaussian according to the central limit theorem. This probability distribution, however, equals the noninteracting density of states,  $D(\omega) = \sum_{\mathbf{k}} \delta(\omega - \epsilon_{\mathbf{k}})$ , which is hence given by

$$D(\omega) = \frac{1}{\sqrt{2\pi} t\sqrt{Z}} \exp \left[ -\frac{1}{2} \left( \frac{\omega}{t\sqrt{Z}} \right)^2 \right]. \quad (5.5)$$

For the density of states to have finite moments, one therefore requires the hopping  $t$  to scale as [Metzner89]

$$t = \frac{t^*}{\sqrt{Z}}, \quad t^* = \text{const.} \quad (5.6)$$

In analogy to Eq. (5.6), the scaling for general lattices and arbitrary neighbor order,<sup>1</sup> cf. Eq. (1.5), can be expressed in terms of  $Z_{\|i-j\|}$  where  $\|i-j\|$  denotes the distance from site  $i$  to site  $j$  in a suitable metric,<sup>2</sup> *i.e.*  $Z_1$  is the number of nearest neighbors,  $Z_2$  of next-nearest neighbors, and so on. The scaling then reads

$$t_{ij} = \frac{t_{ij}^*}{\sqrt{Z_{\|i-j\|}}} . \quad (5.7)$$

In the following, we discuss the resulting diagrammatic simplifications by power counting of the respective diagrams (Green's function lines). For that purpose, the scaling of the noninteracting and interacting Green's functions is required. While the scaling (5.7) was obtained using the  $\mathbf{k}$  space formulation, the following considerations are made in the real space formulation.

In the noninteracting limit  $U = 0$ , the kinetic energy of the Hamiltonian (1.5) is given by

$$E_{\text{kin}} = - \sum_{ij,\sigma} t_{ij} \langle c_{i,\sigma}^\dagger c_{j,\sigma} \rangle , \quad (5.8)$$

where  $\langle c_{i,\sigma}^\dagger c_{j,\sigma} \rangle$  can be interpreted as the amplitude for transitions between site  $i$  and  $j$ , whose square  $|\langle c_{i,\sigma}^\dagger c_{j,\sigma} \rangle|^2$  is proportional to the probability for an electron to hop from site  $i$  to  $j$ . Seen from site  $i$ , the sum of  $|\langle c_{i,\sigma}^\dagger c_{j,\sigma} \rangle|^2$  over all neighbors in distance  $\|i-j\|$  must yield a constant and since there are  $Z_{\|i-j\|}$  such neighbors,  $\langle c_{i,\sigma}^\dagger c_{j,\sigma} \rangle$  must scale as

$$\langle c_{i,\sigma}^\dagger c_{j,\sigma} \rangle \sim \mathcal{O} \left( \frac{1}{\sqrt{Z_{\|i-j\|}}} \right) , \quad \langle c_{i,\sigma}^\dagger c_{i,\sigma} \rangle \sim \mathcal{O}(1) . \quad (5.9)$$

Note that the scalings (5.7) and (5.9) exactly cancel the scaling  $\mathcal{O}(Z_{\|i-j\|})$  that comes from the summation over the  $Z_{\|i-j\|}$  neighbors  $j$  of site  $i$  in the sum of Eq. (5.8), hence the kinetic energy per site stays finite for  $Z_{\|i-j\|} \rightarrow \infty$ , as required.

The scaling (5.9) also holds for the (one-particle) Green's function  $G_{ij}(\tau)$  which is directly connected to  $\langle c_{i,\sigma}^\dagger c_{j,\sigma} \rangle$  via

$$G_{ij}(\tau = 0^+) = -\delta_{ij} + \langle c_{j,\sigma}^\dagger c_{i,\sigma} \rangle . \quad (5.10)$$

Since the scaling does not depend on the time evolution,  $G_{ij}(\tau) \sim \mathcal{O}(1/\sqrt{Z_{\|i-j\|}})$  holds at all times. This scaling of the Green's function (which we assume to hold also in the interacting case, *i.e.* for the interacting Green's function; we will verify this assumption in the end) is the origin of the diagrammatic simplifications arising in the limit  $Z_{\|i-j\|} \rightarrow \infty$ .

Let us consider the perturbation expansion of the self energy. It consists of so-called proper self energy diagrams, *i.e.* diagrams which are one-particle irreducible (they cannot be cut into two pieces by cutting a single Green's function line). We are therefore left with diagrams where any two vertices (that we identify with sites in the following) are connected by two, three, or more independent Green's function lines. However, diagrams with two Green's function lines connecting  $i$  and  $j$  can diagrammatically easily be shown to contain

<sup>1</sup>Here and in the following, we lift the restriction to nearest neighbors only, *i.e.*  $i$  and  $j$  are two arbitrary lattice sites.

<sup>2</sup>*E.g.* in the (hyper)cubic lattice,  $\|i-j\| = \sum_{n=1}^d |R_n^{(i)} - R_n^{(j)}|$ , the so-called Manhattan metric which gives the smallest number of lattice steps between sites  $i$  and  $j$ .

self-energy insertions; after the insertion according to the Dyson equation, one arrives at a skeleton diagram, *i.e.* a diagram in terms of interacting Green's function lines with three such interacting lines connecting  $i$  and  $j$ . Thus, we only need to consider diagrams where  $i$  and  $j$  are connected by three (or more) Green's function lines. The scaling of these diagrams goes at most like  $1/\sqrt{Z_{\parallel i-j\parallel}}^3$  (or even less if there is another intermediate site  $k$  on the path). Taking into account the summation over the  $Z_{\parallel i-j\parallel}$  neighbors  $j$  of site  $i$  –there are  $Z_{\parallel i-j\parallel}$  such diagrams for every class (distance) of neighbors– the total contribution of these diagrams scales as  $1/\sqrt{Z_{\parallel i-j\parallel}}$  and is therefore suppressed in the limit  $Z_{\parallel i-j\parallel} \rightarrow \infty$ , but only for  $i \neq j$ : local diagrams  $i = j$  are of order  $\mathcal{O}(1)$  and there is no summation, hence their contribution is finite.

In summary, all diagrams contributing to the self energy are purely local and so is the self energy itself,

$$\Sigma_{ij}(\omega) \rightarrow \delta_{ij}\Sigma(\omega). \quad (5.11)$$

Accordingly, its Fourier transform becomes momentum-independent,

$$\Sigma(\mathbf{k}, \omega) \rightarrow \Sigma(\omega). \quad (5.12)$$

The derivation of the scaling of the Green's function above was limited to the noninteracting case, but for the power counting of the skeleton diagrams we assumed the same scaling for the (offdiagonal  $i \neq j$  elements of the) interacting Green's function. In fact, it follows from the momentum-independence of the self energy (5.12) together with the Dyson equation that  $G_{ij}(\tau) \sim \mathcal{O}(1/\sqrt{Z_{\parallel i-j\parallel}})$  also holds for the interacting Green's function[Held07].

The lattice problem is hence reduced to a local problem: an electron may still leave the site  $i$ , interact on other sites –thereby being dressed by some self energy  $\Sigma$ – and return to site  $i$  at a later time, but this is fully described by the local interacting Green's function containing the self energy. The other sites can thus be viewed as a bath which is described by a propagator and a self energy without the need to distinguish the other sites anymore. Only on the local site  $i$ , the full interacting many body problem has to be solved (which then in turn determines the self energy: again, the problem is nonlinear and has to be solved self-consistently).

The momentum-independence of the self energy has immediate consequences for the lattice Green's function which then can be written as

$$G(\mathbf{k}, i\omega_n) = \frac{1}{i\omega_n + \mu - \epsilon(\mathbf{k}) - \Sigma(i\omega_n)}, \quad (5.13)$$

with chemical potential  $\mu$ ; the local Green's function, *i.e.* the local projection of the lattice Green's function, takes the form

$$G(i\omega_n) = \sum_{\mathbf{k}} G(\mathbf{k}, i\omega_n) = \int_{-\infty}^{\infty} d\epsilon \frac{D(\epsilon)}{i\omega_n + \mu - \epsilon - \Sigma(i\omega_n)}, \quad (5.14)$$

with  $D(\epsilon)$  being the noninteracting density of states. Note that the lattice enters into the local Green's function only via  $D(\epsilon)$ .

Next, we turn to the actual calculation of  $\Sigma(i\omega_n)$ . The considerations above already indicate a relation of the  $Z_{\parallel i-j\parallel} \rightarrow \infty$  limit with a (quantum) impurity problem. In fact, the breakthrough for the actual numerical treatment of this limit was the insight of Georges and Kotliar[Georges92a] that the solution of this local problem can be obtained from the solution of an (auxiliary) Anderson impurity model subject to a selfconsistency condition.

To this end, the lattice model (1.5) is mapped to a local field theory (in 0 space + 1 time dimension) whose action can be written in Grassmann variable representation (cf. Ref. [Negele78]) as

$$S_{\text{loc}} = - \sum_{\sigma} \int_0^{\beta} d\tau_1 \int_0^{\beta} d\tau_2 c_{\sigma}^{\dagger}(\tau_1) \mathcal{G}_0^{-1}(\tau_1 - \tau_2) c_{\sigma}(\tau_2) + U \int_0^{\beta} d\tau n_{\uparrow}(\tau) n_{\downarrow}(\tau), \quad (5.15)$$

with a time dependent Green's function  $\mathcal{G}_0(\tau)$  ( $\tau$  being imaginary time) and Grassmann variables  $c_{\sigma}^{\dagger}$  ( $c_{\sigma}$ ) corresponding to the creation (annihilation) of an electron with the given spin on the impurity site;  $n_{\sigma} = c_{\sigma}^{\dagger} c_{\sigma}$  is the corresponding occupation number. This action is the formal analogy to the idea which underlies DMFT:  $\mathcal{G}_0$  (or, more exactly,  $\mathcal{G}_0^{-1}$ ) plays the role of a dynamical Weiss mean-field<sup>3</sup> which represents the retardation effect of the bath described above (and thereby the dynamical information of all other sites of the lattice). Note that  $\mathcal{G}_0$  is the bare (noninteracting) Green's function of the (effective) local problem; only the local interactions in the second term are considered explicitly.<sup>4</sup> However,  $\mathcal{G}_0$  in turn depends on the solution of the local problem and needs to be computed self-consistently.

For conceptual (and practical, depending on the impurity solver) reasons, it is desirable to relate this action back to a Hamiltonian formulation. For that purpose, we consider the Anderson impurity model (AIM) which describes interacting, localized electrons on a zero-dimensional ‘‘impurity’’ in a ‘‘bath’’ (collection) of uncorrelated states. Electrons can propagate in the bath or stay on the impurity where they are subject to a Coulomb repulsion. A coupling (hybridization) between the bath and the impurity allows electrons to hop from the impurity to the bath and back. The Hamiltonian of the AIM is given by

$$H_{\text{AIM}} = \underbrace{\sum_{\mathbf{k},\sigma} \epsilon(\mathbf{k}) a_{\mathbf{k},\sigma}^{\dagger} a_{\mathbf{k},\sigma}}_{H_{\text{bath}}} + \underbrace{\sum_{\mathbf{k},\sigma} [V(\mathbf{k}) a_{\mathbf{k},\sigma}^{\dagger} c_{\sigma} + \text{h.c.}]}_{H_{\text{hyb}}} + \underbrace{U c_{\uparrow}^{\dagger} c_{\uparrow} c_{\downarrow}^{\dagger} c_{\downarrow}}_{H_U} - \underbrace{\mu (c_{\uparrow}^{\dagger} c_{\uparrow} + c_{\downarrow}^{\dagger} c_{\downarrow})}_{H_0}, \quad (5.16)$$

where  $a_{\mathbf{k},\sigma}^{\dagger}$  ( $a_{\mathbf{k},\sigma}$ ) are creation (annihilation) operators for a bath state with momentum  $\mathbf{k}$  which hybridizes with the localized electrons  $c_{\sigma}^{\dagger}$  ( $c_{\sigma}$ ) via  $V(\mathbf{k})$ . Calculating the local action of  $H_{\text{AIM}}$  in the language of functional integrals,<sup>5</sup> one finds[Georges96] that the AIM in fact generates the action (5.15) if  $\mathcal{G}_0$  is chosen such that

$$\mathcal{G}_0^{-1}(i\omega_n) = i\omega_n + \tilde{\mu} - \sum_{\mathbf{k}} \frac{|V(\mathbf{k})|^2}{i\omega_n - \epsilon(\mathbf{k})}, \quad (5.17)$$

where  $\tilde{\mu} = \mu - \sum_{\mathbf{k}} \epsilon(\mathbf{k}) = \mu - \langle \epsilon \rangle$ , and  $F(i\omega_n) = \sum_{\mathbf{k}} |V(\mathbf{k})|^2 / (i\omega_n - \epsilon(\mathbf{k}))$  is called hybridization function.<sup>6</sup>

<sup>3</sup> $\mathcal{G}_0$  is also called ‘‘bath Green's function’’ or ‘‘effective environment’’.

<sup>4</sup>In multiorbital problems, the interaction term must obviously have the same form as in the original lattice Hamiltonian.

<sup>5</sup>This can be done exactly since the bath states in Eq. (5.16) enter only quadratically and hence can be integrated out analytically.

<sup>6</sup>In the particle-hole symmetric case, *e.g.* on the Bethe lattice, one obtains  $\tilde{\mu} = \mu$ . However, for spectra which are not particle-hole symmetric –as routinely encountered in LDA+DMFT– the chemical potential must be shifted by  $\langle \epsilon \rangle$  to ensure the correct high-frequency behavior of the hybridization function,  $\lim_{\omega_n \rightarrow \infty} F(i\omega_n) \propto 1/i\omega_n$ . See Appendix A for details on the high-frequency behavior.

We now have two interacting Green’s functions with local character, the local Green’s function (5.13), and the impurity Green’s function, *i.e.* the interacting Green’s function of the AIM,<sup>7</sup> which formally can be written as

$$G(\tau_1 - \tau_2) = -\langle T_\tau c(\tau_1) c^\dagger(\tau_2) \rangle_{S_{\text{loc}}} . \quad (5.18)$$

Without interactions, the impurity Green’s function equals the Weiss field,  $G = \mathcal{G}_0$ ; in the interacting case, an impurity solver needs to be employed. An impurity solver is a numerical or analytical approach for solving the AIM, in particular for obtaining the impurity Green’s function (5.18) given the Weiss field and the interaction parameters: according to Eq. (5.15), these quantities completely define the impurity problem. A solver can proceed by *e.g.* a direct sampling of the impurity Green’s function (5.18) like in Quantum Monte Carlo (QMC), or by some diagonalization of the AIM (5.16) like in Exact Diagonalization algorithms.

The impurity and the local Green’s function are not independent from each other, though. Formally, the mapping of the lattice model to the impurity problem is based on the topological identity of their respective irreducible diagrams. However, the obtained self energies are only identical if the lines of the diagrams –the Green’s functions– coincide. For a self-consistent solution, one therefore requires that the impurity Green’s function equals the local Green’s function. Only in this case the correct impurity problem is solved, *i.e.* the one which corresponds to the lattice model in infinite dimensions with density of states  $D(\epsilon)$ .

In order to find the corresponding impurity problem (the  $\mathcal{G}_0$ ) to a given local Green’s function  $G$ , we can make use of the (local) Dyson equation that connects these (local) quantities,

$$\mathcal{G}_0^{-1}(i\omega_n) = G^{-1}(i\omega_n) + \Sigma(i\omega_n) . \quad (5.19)$$

Note that in Eq. (5.19),  $G$  denotes the impurity Green’s function. Upon selfconsistency, the local and the impurity Green’s function are equal, and Eq. (5.19) also holds with  $G$  being the local Green’s function.

Based on these relations, the selfconsistency cycle can be formulated as follows:

1. Choose an initial self energy, *e.g.*  $\Sigma = 0$  for the noninteracting limit, or the Hartree expression  $\Sigma_m = \sum_{i \neq m} U_{mi} \langle n_i \rangle$  for the self energy of orbital  $m$ .
2. Calculate the local Green’s function (5.14).
3. Find a parameterization for the respective impurity problem: calculate the Weiss field  $\mathcal{G}_0$  using Eq. (5.19) (with  $G$  being the local Green’s function).
4. Solve the impurity problem, *i.e.* evaluate the impurity Green’s function. This step typically presents the major computational challenge in DMFT.
5. Obtain a new self energy from the Dyson equation (5.19) (with  $G$  being the impurity Green’s function).
6. Continue with step 2.

---

<sup>7</sup>The impurity Green’s function is also called “dressed Green’s function”.



This prescription is iterated until convergence in any or all of the involved Green's functions (self energy, impurity Green's function, Weiss field) is attained. Depending on the employed impurity solver, Fourier transforms might be necessary: *e.g.* the solver described in Sec. 5.3 is parameterized in imaginary time and obtains the impurity Green's function also in imaginary time, therefore Fourier transforms are to be performed between steps 3/4 and between steps 4/5, cf. Appendix A.

For QMC solvers operating in imaginary time/frequency, the calculation of dynamical quantities like spectra or susceptibilities in addition requires an analytic continuation to the real-frequency axis (outside the selfconsistency loop), see. Ch. 6.

In contrast to the Hubbard model, efficient solvers for the AIM have been developed over decades and a number of different solvers is available. One can distinguish between approximate solvers like the non-crossing approximation[Pruschke89] or iterated perturbation theory[Zhang93, Kajueter96], and numerically exact solvers like exact diagonalization[Caffarel94, Si94], the numerical renormalization group[Sakai94, Bulla98], and QMC algorithms. The QMC algorithm first applied to the DMFT impurity problem[Georges92b, Jarrell92, Rozenberg92] was the discrete-time Hirsch-Fye algorithm[Hirsch86]. Today, the state of the art is represented by so-called continuous-time QMC (CTQMC) algorithms. They can be formulated as weak-coupling[Rubtsov05, Gull08b] or strong-coupling expansion[Werner06a, Werner06b], where the Monte Carlo sampling of the configuration space is most efficiently performed in the respective limit of weak or strong interactions. In Sec. 5.3, we discuss the strong-coupling (hybridization expansion) CTQMC solver[Werner06a] employed in this thesis.

It is obvious from the local nature of the DMFT approximation that it cannot describe spatial fluctuations in the system. This is equivalent to saying that short- or long-range correlations are not considered, as necessary for *e.g.* quantum critical behavior or ordered states like *d*-wave superconductivity. In order to reintroduce non-local correlations beyond DMFT, two different approaches have been explored: the extension of single-site DMFT to clusters, and diagrammatic expansions around the local DMFT solution.

Cluster DMFT extensions are the more widely used approach and can be formulated in real space or in  $\mathbf{k}$  space. Within the real space approach –termed cellular DMFT[Kotliar01, Potthoff03] (CDMFT)– non-local correlations within the cluster are taken into account, *i.e.* the self energy acquires offdiagonal elements  $\Sigma_{ij}(\omega)$  for two sites  $i \neq j$  within the cluster, whereas correlations between different clusters are neglected. In contrast, the dynamical cluster approximation[Hettler98] (DCA) operates in  $\mathbf{k}$  space and lifts the momentum-independence of the self energy by dividing the first Brillouin zone (BZ) into patches, where  $\Sigma(\omega)$  is  $\mathbf{k}$ -independent within each patch but varies between the patches.

Cluster approaches thereby interpolate between single-site DMFT and the full lattice problem as the size of the cluster increases. For finite (and –due to numerical limitations– typically small) cluster sizes, they are restricted to relatively short-range correlations, however. Diagrammatic extensions of DMFT like the dual fermion approach[Rubtsov08] or the dynamical vertex approximation[Toschi07, Rohringer11] (DFA) are able to include also the effect of long-range spatial correlations.

## 5.2 LDA+DMFT

As in LDA+U, in LDA+DMFT the electron density obtained from DFT is assigned to orbitals which are separated into two subsystems: some orbitals are considered correlated

and treated by a many body interaction term (subject to a double counting correction), while others are left as uncorrelated and handled within DFT. LDA+DMFT can thus be assessed from two different points of view: either as an augmentation of the LDA Hamiltonian with an interaction term like in LDA+U, which is however solved in a dynamical rather than static mean-field manner; or –with respect to the correlated orbitals– as a DMFT approach, however considering the real lattice and band structure instead of a simplified lattice model like the Bethe lattice.

### 5.2.1 Construction of a Localized Basis

While the notion of orbitals and the separation into correlated and uncorrelated states are essential for the application of the method, the definition of these orbitals is not unique. Note that for the transition from the continuum model (1.1) to the lattice model (1.2), a basis of Wannier states centered at the atomic positions was assumed. These Wannier states carry the information on the lattice and are localized. However, the actual construction of a Wannier basis from the DFT Kohn-Sham states depends on the employed DFT basis set as well as on conceptual considerations.

The definition of this localized basis is straightforward in DFT implementations which already work in a localized basis, like linear muffin-tin orbitals [Andersen75, Anisimov97, Lichtenstein98] (LMTO) or  $N$ th-order muffin-tin orbitals [Andersen00, Pavarini04], where the DFT basis functions can directly be identified with the local orbitals, possibly after an orthogonalization procedure. Otherwise, a projection from the KS orbitals to the Wannier basis has to be performed, with which the local Green’s function (5.14) for atom  $\alpha$  (the atom with the correlated orbitals to be investigated in DMFT) reads<sup>8</sup>

$$G_{mm'}^\alpha(i\omega_n) = \sum_{\mathbf{k}, \nu, \nu'} P_{\nu m}^\alpha(\mathbf{k}) G_{\nu\nu'}(\mathbf{k}, i\omega_n) P_{\nu' m'}^{\alpha*}(\mathbf{k}), \quad (5.20)$$

where  $G_{\nu\nu'}$  is the lattice Green’s function with band indices  $\{\nu, \nu'\}$ ,  $\{m, m'\}$  label the (correlated) orbitals, and  $P_{\nu m}^\alpha(\mathbf{k})$  is the matrix element

$$P_{\nu m}^\alpha(\mathbf{k}) = \langle w_{\mathbf{k}, m}^\alpha | \psi_{\mathbf{k}, \nu} \rangle \quad (5.21)$$

of the projection operator

$$P^\alpha(\mathbf{k}) = \sum_{m \in \mathcal{C}} |w_{\mathbf{k}, m}^\alpha\rangle \langle w_{\mathbf{k}, m}^\alpha|, \quad (5.22)$$

with Bloch states (KS orbitals)  $\psi_{\mathbf{k}, \nu}$ , and Wannier states  $w_{\mathbf{k}, m}^\alpha$  that span the correlated subset  $\mathcal{C}$ .

In the same sense that the lattice Green’s function is ‘downfolded’ (projected) in Eq. (5.20) to obtain the local Green’s function, the (double-counting-corrected, see below) local self energy  $\Sigma_{mm'}^\alpha$  can be ‘unfolded’ to the Bloch basis,

$$\Sigma_{\nu\nu'}(\mathbf{k}, i\omega_n) = \sum_{\alpha, mm'} P_{\nu m}^{\alpha*}(\mathbf{k}) \Sigma_{mm'}^\alpha(i\omega_n) P_{\nu' m'}^\alpha(\mathbf{k}), \quad (5.23)$$

with which the lattice Green’s function is given by

$$[G^{-1}(\mathbf{k}, i\omega_n)]_{\nu\nu'} = (i\omega_n + \mu)\delta_{\nu\nu'} - H_{\nu\nu'}^0(\mathbf{k}) - \Sigma_{\nu\nu'}(\mathbf{k}, i\omega_n), \quad (5.24)$$

---

<sup>8</sup>We omit the spin index here and in the following.

where the LDA Hamiltonian  $H^0$  is diagonal in the Bloch basis,  $H_{\nu\nu'}^0(\mathbf{k}) = \delta_{\nu\nu'} \epsilon_\nu(\mathbf{k})$ .

Like in LDA+U, the inclusion of interactions in LDA+DMFT requires a double counting correction that accounts for the interactions already taken into account in the LDA formalism. The double counting correction is naturally expressed in terms of the occupations of the correlated orbitals, *i.e.* in the localized basis, and the local quantity reflecting the effect of interactions is the impurity self energy. We therefore apply the double counting correction directly to the impurity self energy  $\Sigma_{mm'}^{\alpha,\text{imp}}$ ,

$$\Sigma_{mm'}^\alpha(i\omega_n) = \Sigma_{mm'}^{\alpha,\text{imp}}(i\omega_n) - \Sigma_{mm'}^{\text{dc}}, \quad (5.25)$$

where  $\Sigma_{mm'}^{\text{dc}} = \delta_{mm'} V_m^{\text{dc}}$  with  $V_m^{\text{dc}}$  the orbital potential of the employed double counting correction, *e.g.*  $V_m^{\text{dc,FL}}L$  from Eq. (2.37) or  $V_m^{\text{dc,AMF}}$  from Eq. (2.38). Note, however, that the local Dyson equation (5.19) is written with the full impurity self energy,

$$[\mathcal{G}_0^\alpha(i\omega_n)^{-1}]_{mm'} = [G^\alpha(i\omega_n)^{-1}]_{mm'} + \Sigma_{mm'}^{\alpha,\text{imp}}(i\omega_n). \quad (5.26)$$

Regarding the actual form of the projection, different choices for the Wannier orbitals (and hence the projection operators) are possible. In any case, however, the resulting Wannier functions should be localized, orthogonal, and capture all (or most) of the spectral weight of the correlated states. Here we follow Ref. [Aichhorn09] which presents an approach based on the projection onto a set of atomiclike orbitals with subsequent orthonormalization[Ku02, Anisimov05] within the LAPW/APW+lo basis.

Let  $\{|\chi_m^\alpha\rangle\}$  denote a set of atomiclike orbitals (to be identified later within the LAPW/APW+lo basis) which can be expanded in the complete Bloch basis,

$$|\chi_{\mathbf{k},m}^\alpha\rangle = \sum_\nu \langle \psi_{\mathbf{k},\nu} | \chi_m^\alpha \rangle |\psi_{\mathbf{k},\nu}\rangle. \quad (5.27)$$

By choosing an energy window  $\mathcal{W}$  and restricting the sum to Bloch states with KS energies within  $\mathcal{W}$ , the truncated expansion yields modified, non-orthogonal orbitals,

$$|\tilde{\chi}_{\mathbf{k},m}^\alpha\rangle = \sum_{\nu \in \mathcal{W}} \langle \psi_{\mathbf{k},\nu} | \chi_m^\alpha \rangle |\psi_{\mathbf{k},\nu}\rangle. \quad (5.28)$$

The matrix elements of the (auxiliary) projection operator for this truncated subset,

$$\tilde{P}_{\nu m}^\alpha(\mathbf{k}) = \langle \tilde{\chi}_{\mathbf{k},m}^\alpha | \psi_{\mathbf{k},\nu} \rangle, \quad \nu \in \mathcal{W}, \quad (5.29)$$

form a non-unitary and, in general, non-square (as the number of included bands does not necessarily equal the number of correlated orbitals to be constructed) matrix at each  $\mathbf{k}$  point. The overlap is given by

$$O_{mm'}^{\alpha,\alpha'}(\mathbf{k}) = \sum_{\nu \in \mathcal{W}} \tilde{P}_{\nu m}^\alpha(\mathbf{k}) \tilde{P}_{\nu m'}^{\alpha'*}(\mathbf{k}), \quad (5.30)$$

which is used to orthonormalize the orbitals  $|\tilde{\chi}_{\mathbf{k},m}^\alpha\rangle$ , giving a set of Wannier-type functions  $\{|w_{\mathbf{k},m}^\alpha\rangle\}$ ,

$$|w_{\mathbf{k},m}^\alpha\rangle = \sum_{\alpha',m'} \left[ O^{-1/2}(\mathbf{k}) \right]_{mm'}^{\alpha\alpha'} |\tilde{\chi}_{\mathbf{k},m'}^{\alpha'}\rangle. \quad (5.31)$$

The corresponding orthonormalized projectors read

$$P_{\nu m}^\alpha(\mathbf{k}) = \sum_{\alpha',m'} \left[ O^{-1/2}(\mathbf{k}) \right]_{mm'}^{\alpha\alpha'} \tilde{P}_{\nu,m'}^{\alpha'}(\mathbf{k}). \quad (5.32)$$

The atomiclike orbital  $|\chi_m^\alpha\rangle$  that serves as a starting point for this approach can be chosen in different ways. In the LAPW/APW+lo basis, a common choice –which we also employ here– is the solution of the Schrödinger equation within the MT sphere,

$$|\chi_m^\alpha\rangle = |u_\ell^\alpha(E_{1,\ell}^\alpha) Y_{\ell,m}\rangle, \quad (5.33)$$

at the corresponding linearization energy  $E_{1,\ell}$ . From the definition of the basis (2.20)-(2.23) and using the orthonormality of the radial solutions and their energy derivatives,

$$\langle u_\ell^\alpha(E_{1,\ell}^\alpha) Y_{\ell,m} | u_{\ell'}^\alpha(E_{1,\ell'}^\alpha) Y_{\ell',m'} \rangle = \delta_{\ell\ell'} \delta_{mm'}, \quad (5.34)$$

$$\langle u_\ell^\alpha(E_{1,\ell}^\alpha) Y_{\ell,m} | \dot{u}_{\ell'}^\alpha(E_{1,\ell'}^\alpha) Y_{\ell',m'} \rangle = 0, \quad (5.35)$$

the matrix elements (5.29) of the auxiliary projection operator follow as

$$\tilde{P}_{\nu m}^\alpha(\mathbf{k}) = \sum_{\mathbf{G}} c_{\mathbf{G},\nu} A_{\ell,m}^{\alpha,\mathbf{k}+\mathbf{G}} + \sum_{n_{\text{lo}}=1}^{N_{\text{lo}}} c_\nu^{\text{lo}} A_{\ell,m}^{\alpha,\text{lo}} + \sum_{n_{\text{LO}}=1}^{N_{\text{LO}}} c_\nu^{\text{LO}} \left( A_{\ell,m}^{\alpha,\text{LO}} + C_{\ell,m}^{\alpha,\text{LO}} \tilde{O}_{\ell,m}^\alpha \right). \quad (5.36)$$

Here, the last contribution is due to the overlap of the radial solutions for different energies,

$$\tilde{O}_{\ell,m}^\alpha = \langle u_\ell^\alpha(E_{1,\ell}^\alpha) Y_{\ell,m} | u_\ell^\alpha(E_{2,\ell}^\alpha) Y_{\ell,m} \rangle \neq 1. \quad (5.37)$$

Note that the definition of  $|\chi_m^\alpha\rangle$  in Eq. (5.33) neglects the contributions from the energy derivate terms of the radial wave functions in the LAPW/APW+lo basis and hence misses spectral weight[Haule10]. The charge deficiency is typically very small, though.

Above we introduced the energy window  $\mathcal{W}$ , thereby truncating the expansion of the atomiclike local orbitals in the Bloch basis. The choice of this energy window is a basic parameter affecting the shape and degree of localization of the resulting Wannier functions. For instance, in the case of a small energy window –*i.e.* a window containing only bands with dominant desired (correlated) orbital character– and in the presence of hybridization of the correlated orbitals with other atomic characters, the atomic character of interest is not fully contained in the selected window. As a consequence, the atomic character of neighboring ligand sites mixes in and the Wannier orbitals have significant weight on the neighboring sites (leakage): with the limited number of Bloch basis functions it is not possible to include all of the correlated orbital character and cancel out the rest. A small energy window hence tends to yield spatially extended Wannier functions with a shape very different from atomic orbitals. Since the interaction parameters are the matrix elements of a screened interaction between the Wannier states, the large spatial extension must be reflected by rather small values for the interaction parameters.

The opposite case of a large energy window in turn allows to closely resemble atomic orbitals with well-defined orbital character but renders the Wannier functions highly localized; this requires unphysically large interaction parameters since the electrons are not as localized as suggested by the narrow Wannier functions. The size of the energy window can thus be viewed as a compromise between localization in real space and in the energy domain and a sensibly chosen window would typically include the bands with the correlated orbital character and the neighboring hybridized bands.

We now briefly mention two further technical aspects, namely the treatment of several equivalent correlated atoms in the unit cell and the exploitation of symmetries for the  $\mathbf{k}$ -summation in Eq. (5.20).

Firstly, in the discussion above (Eqs. (5.20)-(5.37)), we referred to atom  $\alpha$  as the single correlated atom in the unit cell. However, while multiple *inequivalent* correlated atoms

cannot be included in the single-site DMFT framework, the index  $\alpha$  can label multiple *equivalent* correlated atoms. In this case, the impurity problem has to be solved only once –for one of the equivalent atoms, say  $\alpha_1$ – and the impurity self energies  $\Sigma_{mm'}^{\alpha'}$ ,  $\alpha' \neq \alpha_1$  for the other equivalent sites are obtained via the application of space group symmetries to  $\Sigma_{mm'}^{\alpha_1}$ . That way, all self energies in the sum over  $\alpha$  in Eq. (5.23) are given with respect to the same coordinate system (the local coordinate system of atom  $\alpha_1$ ) and the sum can be executed.

Secondly, in the presence of unit cell symmetries, the summation over the full BZ in Eq. (5.20) can be restricted to a sum over the irreducible BZ supplemented by a symmetrization procedure. For a  $\mathbf{k}$ -dependent matrix  $\mathbf{F}^\alpha(\mathbf{k})$  in orbital space, which commutes with the space group symmetry operations, this is expressed as

$$\mathbf{F}^\alpha(i\omega_n) = \sum_{\mathbf{k}}^{\text{BZ}} \mathbf{F}^\alpha(\mathbf{k}, i\omega_n) = \sum_{s=1}^{N_s} \sum_{\mathbf{k}}^{\text{IBZ}} \mathcal{O}_s \mathbf{F}^{\alpha_s}(\mathbf{k}, i\omega_n) \mathcal{O}_s^\dagger, \quad (5.38)$$

where  $\mathcal{O}_s$  are the space group symmetry operations in orbital space and  $N_s$  the number of symmetry operations. Note that the symmetry operations in the sum require  $\mathbf{F}^{\alpha_s}$  to be calculated for different equivalent atoms  $\alpha_s$  although the projection is performed on a particular atom  $\alpha$ .

### 5.2.2 Construction of a Molecular Wannier Basis

The construction method based on projecting Bloch states onto atomiclike orbitals with subsequent orthonormalization as presented in Sec. 5.2.1 is fast and stable. In its standard form the projection method is, by definition, not designed for molecular orbitals, however. Here, we describe an extension in order to construct molecular Wannier functions using atomic orbitals as a starting point. This extended scheme was developed by K. Foyevtsova and used in the study on organic charge transfer salts in Ch. 9.

Its key element is the diagonalization of the occupation matrix written in the basis of atomic orbitals within the subspace of correlated bands. It assumes that a basic molecular unit is known and provides a linear combination of the orbitals of those atoms forming the given molecular unit.

Starting from the atomic auxiliary projectors  $\tilde{P}_{\nu m}^\alpha(\mathbf{k})$  in Eq. (5.29), we consider the occupation matrix for the narrow energy window  $\mathcal{W}'$  comprising correlated Bloch bands at  $\mathbf{k} = 0$ ,

$$Q_{m,m'}^{\alpha,\alpha'} = \sum_{\nu \in \mathcal{W}'} \tilde{P}_{\nu m}^\alpha(0) \tilde{P}_{\nu m'}^{\alpha'*}(0). \quad (5.39)$$

Note that only the atoms that form a specific molecule are involved, *e.g.* for the case of  $\kappa$ -(ET)<sub>2</sub>Cu[N(CN)<sub>2</sub>]Cl, we employed the 60 C 2*p* and 48 S 3*p* atomic orbitals on a (BEDT-TTF) dimer and diagonalized the respective occupation matrix within the four-band manifold at the Fermi level, cf. Ch. 9. The eigenvectors of  $Q_{m,m'}^{\alpha,\alpha'}$ , that correspond to the largest eigenvalues define the weights with which the atomic orbitals  $\{\alpha, m\}$  contribute to the molecular orbitals of interest. Often, only one molecular orbital is thus obtained, as in the case of  $\kappa$ -(ET)<sub>2</sub>Cu[N(CN)<sub>2</sub>]Cl. This molecular orbital (orbitals) will have the dominant weight in the states within the  $\mathcal{W}'$  interval. For this to hold at all  $\mathbf{k}$  vectors, in some cases care is needed to introduce due exponential Bloch factors for atoms located outside the reference unit cell.

If  $U_{mM}^\alpha$  is the eigenvector of the atomic orbital weights, then

$$\tilde{\mathcal{P}}_{\nu M}(\mathbf{k}) = \sum_{\alpha, m} U_{mM}^\alpha \tilde{P}_{\nu m}^\alpha(\mathbf{k}) \quad (5.40)$$

are molecular auxiliary projectors, with  $M$  being the molecular orbital index.  $U_{mM}^\alpha$  can be so applied to all symmetry related molecules in the unit cell.

Finally, the projectors  $\tilde{\mathcal{P}}_{\nu M}(\mathbf{k})$  are orthonormalized within the DMFT energy window  $\mathcal{W}$  which can be much larger than  $\mathcal{W}'$ , using

$$P_{\nu M}(\mathbf{k}) = \sum_{M'} \left[ O^{-1/2}(\mathbf{k}) \right]_{M, M'} \tilde{\mathcal{P}}_{\nu M}(\mathbf{k}), \quad (5.41)$$

with

$$O_{M, M'}(\mathbf{k}) = \sum_{\nu \in \mathcal{W}} \tilde{\mathcal{P}}_{\nu M}(\mathbf{k}) \tilde{\mathcal{P}}_{\nu M'}^*(\mathbf{k}). \quad (5.42)$$

### 5.2.3 Selfconsistency

In most implementations of LDA+DMFT, the LDA band structure calculation and the inclusion of correlations in DMFT are performed sequentially, *i.e.* the DMFT selfconsistency cycle is put on top of a converged LDA solution, but the DMFT solution is not fed back to LDA. We call this approach ‘one-shot’ scheme as opposed to full charge self-consistent LDA+DMFT calculations described below in Sec. 5.2.4. However, also in the one-shot scheme, the DMFT selfconsistency in LDA+DMFT differs from the pure model DMFT selfconsistency, mainly for two reasons: the selfconsistency now also includes the double counting correction, and the chemical potential has to be adapted in every iteration step in order to preserve the total electron count of the crystal, compensating for a possible charge transfer between correlated and uncorrelated states induced by the correlations.

The modified DMFT selfconsistency cycle for LDA+DMFT then consists of the following steps (assuming a converged LDA solution from which a localized basis according to Sec. 5.2.1 has been constructed):

1. Set the lattice self energy to zero,  $\Sigma_{\nu\nu'}(\mathbf{k}, i\omega_n) = 0$ , and calculate the total (noninteracting) charge within the energy window from the lattice Green’s function (5.24),  $N_{\text{tot}}^{\text{LDA}} = 1/\beta \sum_{\nu} \sum_{\mathbf{k}} \sum_{n=-\infty}^{\infty} e^{i\omega_n 0^+} G_{\nu\nu}(\mathbf{k}, i\omega_n)$ .
2. Calculate the noninteracting charges of the correlated orbitals from the local Green’s function (5.20) in order to obtain an initial guess for the double counting correction  $\Sigma^{\text{dc}}$ .
3. Choose an initial (double-counting-corrected) self energy  $\Sigma(i\omega_n)$  in Eq. (5.25), *e.g.*  $\Sigma(i\omega_n) = 0$  (corresponding to setting  $\Sigma^{\text{imp}}(i\omega_n)$  to  $\Sigma^{\text{dc}}$  calculated in step 2).
4. Calculate the local Green’s function (5.20).
5. Calculate the Weiss field using Eq. (5.26) from the local Green’s function and the impurity self energy  $\Sigma^{\text{imp}}$ , where  $\Sigma^{\text{imp}}(i\omega_n) = \Sigma^{\text{dc}}$  in the initial cycle (cf. step 3).
6. Solve the impurity problem.

7. Calculate a new double counting correction from the correlated charges returned by the solver.
8. Obtain a new impurity self energy from the Dyson equation (5.26).
9. Calculate the total (interacting) charge  $N_{\text{tot}}$  in the energy window and adapt the chemical potential, so that  $N_{\text{tot}} = N_{\text{tot}}^{\text{LDA}}$  (by employing an appropriate root finding algorithm, *e.g.* the false position method).
10. Continue with step 4.

This cycle is iterated until simultaneous convergence in the Green's functions, the double counting, and the chemical potential is attained.

### 5.2.4 Full Charge Selfconsistency

The one-shot scheme from Sec. 5.2.3 can be made fully self-consistent in the charge density by feeding the modified DMFT charge density back into the LDA calculation and closing the selfconsistency loop over both methods. This supposedly yields more accurate results for *e.g.* the total energy as required by structure relaxations, or low-energy features susceptible to small band shifts (like Fermi surfaces). While for many applications the difference between self-consistent and non-self-consistent LDA+DMFT calculations has been observed to be small, it depends on the change of the number of electrons in the different bands induced by the correlations: large charge transfers upon inclusion of correlations might indicate a need for self-consistent calculations. Also, if the charge transfer happens predominantly within the correlated band manifold, *e.g.* if the correlated states are separated from the uncorrelated states by a considerable band gap, one can expect a qualitatively correct description by the one-shot scheme, whereas significant charge transfers between correlated and uncorrelated bands might require a charge self-consistent treatment.

The LDA+DMFT charge density distribution in real space is given by

$$\rho(\mathbf{r}) = \sum_{\nu \notin \mathcal{W}} \rho_{\nu}^{\text{LDA}}(\mathbf{r}) + \sum_{\mathbf{k}} \sum_{\nu, \nu' \in \mathcal{W}} \langle \mathbf{r} | \psi_{\mathbf{k}, \nu} \rangle N_{\nu \nu'}(\mathbf{k}) \langle \psi_{\mathbf{k}, \nu'} | \mathbf{r} \rangle, \quad (5.43)$$

where

$$N_{\nu \nu'}(\mathbf{k}) = \frac{1}{\beta} \sum_{n=-\infty}^{\infty} e^{i\omega_n 0^+} G_{\nu \nu'}(\mathbf{k}, i\omega_n) \quad (5.44)$$

is the density matrix as obtained from the lattice Green's function. Note that  $G_{\nu \nu'}(\mathbf{k}, i\omega_n)$  and thus  $N_{\nu \nu'}(\mathbf{k})$  are typically non-diagonal with complex-valued offdiagonal elements since the lattice self energy (5.23) is in general non-diagonal (the self energy is diagonal in the orbital basis but not in the Bloch basis). In order to close the selfconsistency loop from DMFT to LDA, the charge density (5.43) has to be expanded in the given LDA basis set and passed to the DFT code; see Ref. [Aichhorn11] for details how to express  $\rho(\mathbf{r})$  in the LAPW/APW+lo basis set.

As the solution of the DMFT impurity problem is often computationally more expensive than an LDA iteration, a self-consistent LDA+DMFT cycle may start from a converged LDA solution. The number of internal LDA and DMFT iteration steps within one cycle of the outer LDA+DMFT loop is typically chosen from practical considerations like speed and stability of the convergence. Possible choices include *e.g.* one DMFT iteration after every LDA iteration or a fully converged DMFT calculation on top of every LDA iteration; the different iteration schemes should converge to the same final result.

### 5.3 CT-HYB Impurity Solver

In the following, we briefly review the principles underlying the current method of choice for the solution of quantum impurity models, the continuous-time Quantum Monte Carlo (CTQMC) approach. While the basic idea is common to the different existing variants of the method and will be presented in a generic way, for the further discussion we focus on the strong-coupling (hybridization expansion) formulation (CT-HYB) which is the most efficient in the case of multiple orbitals and intermediate interactions as encountered in the systems discussed in this thesis. A review of CTQMC algorithms for quantum impurity models is given in Ref. [Gull11] and pedagogical introductions can be found *e.g.* in Ref. [Gull08a] and by P. Werner in Ref. [Vollhardt11]; we mainly follow the notation in the latter reference.

In a quantum system with Hamiltonian  $H$ , the calculation of the expectation value of an observable  $A$  requires the evaluation of an operator expression,

$$\langle A \rangle = \frac{1}{Z} \text{Tr} \left[ A e^{-\beta H} \right], \quad (5.45)$$

where  $Z$  is the partition function,

$$Z = \text{Tr} \left[ e^{-\beta H} \right]. \quad (5.46)$$

The exponential can be expanded in a Taylor series and by inserting  $n$  sums over complete sets of basis states  $\{|i\rangle\}$  for each order  $n$ , the partition function can be written as [Sandvik91]

$$\begin{aligned} Z &= \sum_{n=0}^{\infty} \frac{(-\beta)^n}{n!} \text{Tr} [H^n] = \sum_{n=0}^{\infty} \sum_{i_1, \dots, i_n} \frac{(-\beta)^n}{n!} \langle i_1 | H | i_2 \rangle \langle i_2 | H | i_3 \rangle \cdots \langle i_n | H | i_1 \rangle \\ &\equiv \sum_{n=0}^{\infty} \sum_{i_1, \dots, i_n} p(i_1, \dots, i_n) \equiv \sum_{c \in \mathcal{C}} p(c), \end{aligned} \quad (5.47)$$

where the configuration space  $\mathcal{C}$  consists of sequences of  $n$  basis states  $c = (i_1, \dots, i_n)$  with weight  $p(c)$ . Even after a possible truncation of the expansion,  $\mathcal{C}$  is of a very high dimension so that Monte Carlo techniques are the only practical way of evaluation. In a Monte Carlo procedure, the average over the whole configuration space is approximated by the average over a sample of  $M$  configurations, selected with probabilities  $p(c_i)/Z$  (importance sampling),

$$\langle A \rangle = \frac{1}{Z} \sum_{c \in \mathcal{C}} A(c) p(c) \approx \langle A \rangle_{\text{MC}} = \frac{1}{M} \sum_{i=1}^M A(c_i). \quad (5.48)$$

For large  $M$ , the Monte Carlo estimate  $\langle A \rangle_{\text{MC}}$  is normally distributed around the exact value  $\langle A \rangle$  with a statistical error  $\Delta A = \sqrt{\text{Var}A/M}$ , where  $\text{Var}A$  is the variance of  $A$ . In general, the probability density  $p(c)/Z$  is very complicated and the configurations are best sampled by an ergodic and balanced Markov process for which the most prominent algorithm is the Metropolis algorithm [Metropolis53].

The Metropolis algorithm splits the probability  $w_{c_1 \rightarrow c_2}$  for the transition between the current configuration  $c_1$  and a new configuration  $c_2$  into a proposal and an acceptance part,  $w_{c_1 \rightarrow c_2} = w_{c_1 \rightarrow c_2}^{\text{prop}} w_{c_1 \rightarrow c_2}^{\text{acc}}$ : first, a new configuration  $c_2$  is proposed with probability



$w_{c_1 \rightarrow c_2}^{\text{prop}}$  (e.g.  $w_{c_1 \rightarrow c_2}^{\text{prop}} = 1/N$  for flipping the spin at a specific site  $i$  in an Ising model with  $N$  spins), and subsequently  $c_2$  is accepted with probability

$$w_{c_1 \rightarrow c_2}^{\text{acc}} = \min \left( 1, \frac{p(c_2) w_{c_2 \rightarrow c_1}^{\text{prop}}}{p(c_1) w_{c_1 \rightarrow c_2}^{\text{prop}}} \right), \quad (5.49)$$

and used as new configuration, or it is rejected and the current configuration  $c_1$  is used again. Note that the acceptance probability (5.49) depends on the ratio  $p(c_2)/p(c_1)$  which is typically a known quantity, whereas the absolute value of the probability density is often unknown (here due to the unknown partition function  $Z$ ); this is the reason for the popularity of the Metropolis algorithm.

The CTQMC algorithms are variants of so-called path integral or diagrammatic Monte Carlo algorithms. These methods are based on the stochastic sampling of a diagrammatic perturbation theory for the partition function with the general form

$$Z = \sum_{k=0}^{\infty} \sum_{\gamma \in \Gamma_k} \int_0^{\beta} d\tau_1 \cdots \int_{\tau_{k-1}}^{\beta} d\tau_k w(k, \gamma, \tau_1, \dots, \tau_k), \quad (5.50)$$

where the configurations are labeled by  $(k, \gamma, \tau_1, \dots, \tau_k)$  with  $k$  the expansion or diagram order and  $\tau_1, \dots, \tau_k \in [0, \beta)$  imaginary times of the vertices (this will become clearer below);  $\gamma$  includes all other (discrete) variables like spin or orbital indices. The weight of a configuration is given by  $p(k, \gamma, \tau_1, \dots, \tau_k) = w(k, \gamma, \tau_1, \dots, \tau_k) d\tau_1 \cdots d\tau_k$ .

While, in principle, each order in the expansion (5.50) can be sampled separately by Monte Carlo (after truncation of the series to some maximal expansion order), the idea of diagrammatic Monte Carlo is to sample all expansion orders in the same MC process by employing the Metropolis algorithm to traverse between one order and the next [Prokof'ev96]. Normally, only two types of updates are necessary and sufficient to satisfy ergodicity – *i.e.* to guarantee that any configuration can be reached from any other configuration in finite time –, updates inserting an additional vertex at time  $\tau$  (thereby increasing the expansion order by one), and updates removing an existing vertex (thereby reducing the expansion order by one). The proposal rate for the insertion of a vertex is given by the probability of picking an imaginary time location,  $w_{\text{insert}}^{\text{prop}} = \frac{d\tau}{\beta}$ , while for the removal of a randomly chosen vertex the probability is one over the number of available vertices at order  $k+1$ ,  $w_{\text{remove}}^{\text{prop}} = \frac{1}{k+1}$ . Thus, the acceptance ratio for the insertion reads

$$\begin{aligned} R_{\text{insert}} &= \frac{w(k+1, \gamma, \tau_1, \dots, \tau, \dots, \tau_k) d\tau_1 \cdots d\tau \cdots d\tau_k \frac{1}{k+1}}{w(k, \gamma, \tau_1, \dots, \tau_k) d\tau_1 \cdots d\tau_k \frac{\beta}{d\tau}} \\ &= \frac{w(k+1, \gamma, \tau_1, \dots, \tau, \dots, \tau_k)}{w(k, \gamma, \tau_1, \dots, \tau_k)} \frac{\beta}{k+1}, \end{aligned} \quad (5.51)$$

from which the acceptance rates follow,

$$w_{\text{insert}}^{\text{acc}} = \min(1, R_{\text{insert}}) \quad , \quad w_{\text{remove}}^{\text{acc}} = \min \left( 1, \frac{1}{R_{\text{insert}}} \right). \quad (5.52)$$

In the CTQMC methods, the impurity Hamiltonian (5.16) is split into two parts,  $H_{\text{AIM}} = H_a + H_b$ . The partition function (5.46) is then expanded in powers of  $H_b$  and written in an interaction representation with respect to  $H_a$ ,

$$\begin{aligned} Z &= \text{Tr} \left[ e^{-\beta H_a} T_{\tau} e^{-\int_0^{\beta} d\tau H_b(\tau)} \right] = \\ &= \sum_{k=0}^{\infty} (-1)^k \int_0^{\beta} d\tau_1 \cdots \int_{\tau_{k-1}}^{\beta} d\tau_k \text{Tr} \left[ e^{-\beta H_a} T_{\tau} H_b(\tau_k) H_b(\tau_{k-1}) \cdots H_b(\tau_1) \right], \end{aligned} \quad (5.53)$$

where  $T_\tau$  is the time ordering operator. In the weak-coupling formulations [Rubtsov05, Gull08b]  $H_a = H_0 + H_{\text{bath}} + H_{\text{hyb}}$ ,  $H_b = H_U$  (interaction expansion), whereas in the strong-coupling approach [Werner06a, Werner06b]  $H_a = H_0 + H_U + H_{\text{bath}}$ ,  $H_b = H_{\text{hyb}}$  (hybridization expansion); we concentrate on the latter in the following.

Since  $H_{\text{hyb}} = \sum_{\mathbf{p}\sigma} V_{\mathbf{p}} a_{\mathbf{p},\sigma}^\dagger c_\sigma + \sum_{\mathbf{p}'\sigma} V_{\mathbf{p}'}^* c_\sigma^\dagger a_{\mathbf{p}',\sigma} = \tilde{H}_{\text{hyb}} + \tilde{H}_{\text{hyb}}^\dagger$  (we replaced the index  $\mathbf{k}$  for the lattice momentum by  $\mathbf{p}$  to avoid confusion with the expansion order  $k$ ) consists of two terms corresponding to the annihilation and creation of electrons on the impurity, respectively, only terms with an equal number of  $\tilde{H}_{\text{hyb}}$  and  $\tilde{H}_{\text{hyb}}^\dagger$  in the expansion of  $H_{\text{hyb}}$  yield a nonzero trace. This allows to write the partition function in terms of configurations  $c = (\tau_1, \dots, \tau_k; \tau'_1, \dots, \tau'_k)$ ,

$$Z = \sum_{k=0}^{\infty} \int_0^\beta d\tau_1 \cdots \int_{\tau_{k-1}}^\beta d\tau_k \int_0^\beta d\tau'_1 \cdots \int_{\tau'_{k-1}}^\beta d\tau'_k \text{Tr} \left[ e^{-\beta H_a} T_\tau \tilde{H}_{\text{hyb}}(\tau_k) \tilde{H}_{\text{hyb}}^\dagger(\tau'_k) \cdots \tilde{H}_{\text{hyb}}(\tau_1) \tilde{H}_{\text{hyb}}^\dagger(\tau'_1) \right]. \quad (5.54)$$

Since the time evolution as given by  $H_a$  does not rotate the spin (in the one-orbital impurity model that we are considering here for the derivation; we comment on the general multiorbital case below), the contributions from each spin can be separated, and by inserting the explicit form of  $\tilde{H}_{\text{hyb}}$  and  $\tilde{H}_{\text{hyb}}^\dagger$  one finds

$$Z = \sum_{k_\uparrow=0}^{\infty} \sum_{k_\downarrow=0}^{\infty} \prod_{\sigma} \int_0^\beta d\tau_1 \cdots \int_{\tau_{k-1}}^\beta d\tau_k \int_0^\beta d\tau'_1 \cdots \int_{\tau'_{k-1}}^\beta d\tau'_k \times \prod_{\sigma} \sum_{\mathbf{p}_1, \dots, \mathbf{p}_k} \sum_{\mathbf{p}'_1, \dots, \mathbf{p}'_k} V_{\mathbf{p}_1} V_{\mathbf{p}'_1}^* \cdots V_{\mathbf{p}_k} V_{\mathbf{p}'_k}^* \times \text{Tr} \left[ e^{-\beta H_a} T_\tau \prod_{\sigma} c_\sigma(\tau_k) a_{\mathbf{p}_k, \sigma}^\dagger(\tau_k) a_{\mathbf{p}'_k, \sigma}(\tau'_k) c_\sigma^\dagger(\tau'_k) \cdots c_\sigma(\tau_1) a_{\mathbf{p}_1, \sigma}^\dagger(\tau_1) a_{\mathbf{p}'_1, \sigma}(\tau'_1) c_\sigma^\dagger(\tau'_1) \right], \quad (5.55)$$

where we omitted the spin index on the expansion order and the vertices for ease of notation, *e.g.*  $\tau_k$  should read  $\tau_{k\sigma}$  in full, and the products over spins extend until the next  $\times$ -operator. The bath and impurity operators in Eq. (5.55) can be separated because  $H_a$  does not mix the impurity and the bath,

$$Z = Z_{\text{bath}} \sum_{k_\uparrow=0}^{\infty} \sum_{k_\downarrow=0}^{\infty} \prod_{\sigma} \int_0^\beta d\tau_1 \cdots \int_{\tau_{k-1}}^\beta d\tau_k \int_0^\beta d\tau'_1 \cdots \int_{\tau'_{k-1}}^\beta d\tau'_k \times \text{Tr}_c \left[ e^{-\beta(H_0+H_U)} T_\tau \prod_{\sigma} c_\sigma(\tau_k) c_\sigma^\dagger(\tau'_k) \cdots c_\sigma(\tau_1) c_\sigma^\dagger(\tau'_1) \right] \times \frac{1}{Z_{\text{bath}}} \text{Tr}_a \left[ e^{-\beta H_{\text{bath}}} T_\tau \prod_{\sigma} \sum_{\mathbf{p}_1, \dots, \mathbf{p}_k} \sum_{\mathbf{p}'_1, \dots, \mathbf{p}'_k} V_{\mathbf{p}_1} V_{\mathbf{p}'_1}^* \cdots V_{\mathbf{p}_k} V_{\mathbf{p}'_k}^* a_{\mathbf{p}_k, \sigma}^\dagger(\tau_k) a_{\mathbf{p}'_k, \sigma}(\tau'_k) \cdots a_{\mathbf{p}_1, \sigma}^\dagger(\tau_1) a_{\mathbf{p}'_1, \sigma}(\tau'_1) \right], \quad (5.56)$$

where  $Z_{\text{bath}}$  is the bath partition function,

$$Z_{\text{bath}} = \text{Tr} \left[ e^{-\beta H_{\text{bath}}} \right] = \prod_{\sigma} \prod_{\mathbf{p}} \left( 1 + e^{-\beta \epsilon_{\mathbf{p}}} \right). \quad (5.57)$$

Importantly, as the bath is noninteracting, the trace over the bath states,  $\text{Tr}_a$ , can be expressed as a determinant (of a  $k \times k$  matrix) by employing the Wick theorem. The lowest expansion order, *i.e.*  $k_\sigma = 1$ ,  $k_{-\sigma} = 0$ , yields

$$\begin{aligned} & \frac{1}{Z_{\text{bath}}} \sum_{\mathbf{p}_1} \sum_{\mathbf{p}'_1} V_{\mathbf{p}_1} V_{\mathbf{p}'_1}^* \text{Tr}_a \left[ e^{-\beta H_{\text{bath}}} T_\tau a_{\mathbf{p}_1, \sigma}^\dagger(\tau_1) a_{\mathbf{p}'_1, \sigma}(\tau'_1) \right] \\ &= \sum_{\mathbf{p}} \frac{|V_{\mathbf{p}}|^2}{1 + e^{-\beta \epsilon_{\mathbf{p}}}} \begin{cases} e^{-\epsilon_{\mathbf{p}}(\beta - (\tau_1 - \tau'_1))} & , \tau_1 > \tau'_1 \\ -e^{-\epsilon_{\mathbf{p}}(\tau'_1 - \tau_1)} & , \tau_1 < \tau'_1 \end{cases} = F(\tau_1 - \tau'_1), \end{aligned} \quad (5.58)$$

with  $F(\tau)$  the Fourier transform of  $F(-i\omega_n)$ , the hybridization function introduced in Eq. (5.17). The hybridization function is therefore the natural input to the CT-HYB solver and contains all necessary information from the band structure calculation. For higher orders, one then obtains the determinant,

$$\begin{aligned} & \frac{1}{Z_{\text{bath}}} \text{Tr}_a \left[ e^{-\beta H_{\text{bath}}} T_\tau \prod_{\sigma} \sum_{\mathbf{p}_1, \dots, \mathbf{p}_k} \sum_{\mathbf{p}'_1, \dots, \mathbf{p}'_k} V_{\mathbf{p}_1} V_{\mathbf{p}'_1}^* \cdots V_{\mathbf{p}_k} V_{\mathbf{p}'_k}^* \right. \\ & \quad \left. a_{\mathbf{p}_k, \sigma}^\dagger(\tau_k) a_{\mathbf{p}'_k, \sigma}(\tau'_k) \cdots a_{\mathbf{p}_1, \sigma}^\dagger(\tau_1) a_{\mathbf{p}'_1, \sigma}(\tau'_1) \right] = \prod_{\sigma} \det \mathbf{F}_{\sigma}, \end{aligned} \quad (5.59)$$

where the elements of the  $k \times k$  matrix  $\mathbf{F}_{\sigma}$  are  $F_{\sigma}(i, j) = F_{\sigma}(\tau_i - \tau_j)$ . The weight of a configuration (now writing out all spin indices)  $c = (\tau_1^\uparrow, \dots, \tau_{k_\uparrow}^\uparrow; \tau_1^\downarrow, \dots, \tau_{k_\downarrow}^\downarrow; \tau_1^{\uparrow\downarrow}, \dots, \tau_{k_{\uparrow\downarrow}}^{\uparrow\downarrow})$  is then given by

$$\begin{aligned} p_c &= Z_{\text{bath}} \text{Tr}_c \left[ e^{-\beta(H_0 + H_U)} T_\tau \prod_{\sigma} c_{\sigma}(\tau_{k_{\sigma}}^{\sigma}) c_{\sigma}^{\dagger}(\tau'_{k_{\sigma}}{}^{\sigma}) \cdots c_{\sigma}(\tau_1^{\sigma}) c_{\sigma}^{\dagger}(\tau_1^{\prime\sigma}) \right] \\ & \times \prod_{\sigma} \det \mathbf{F}_{\sigma}(\tau_1^{\sigma}, \dots, \tau_{k_{\sigma}}^{\sigma}; \tau_1^{\prime\sigma}, \dots, \tau'_{k_{\sigma}}{}^{\sigma}) (d\tau)^{2k_{\sigma}}. \end{aligned} \quad (5.60)$$

The remaining trace here represents the contribution of the impurity whereas the determinants collect all bath evolutions that are compatible with the sequence of hoppings from and to the impurity in the given configuration. For a one-orbital model or in the case of multiple orbitals restricted to density-density interactions, the time evolution governed by  $H_0 + H_U$  commutes with the occupation number operator for each flavor (a flavor being a combined spin-orbital index). This suggests representing the time evolution on the impurity by a collection of time intervals (segments) for each flavor during which an electron of the respective flavor resides on the impurity. By using the fact that this occupation number representation is an eigenbasis of  $H_0 + H_U$ ,

$$H_0 + H_U = \begin{pmatrix} 0 & 0 & 0 & 0 \\ 0 & -\mu & 0 & 0 \\ 0 & 0 & -\mu & 0 \\ 0 & 0 & 0 & U - 2\mu \end{pmatrix} \text{ in basis } |0\rangle, |\uparrow\rangle, |\downarrow\rangle, |\uparrow\downarrow\rangle, \quad (5.61)$$

the trace in Eq. (5.60) can be evaluated analytically,

$$\text{Tr}_c \left[ e^{-\beta(H_0 + H_U)} T_\tau \prod_{\sigma} c_{\sigma}(\tau_{k_{\sigma}}^{\sigma}) c_{\sigma}^{\dagger}(\tau'_{k_{\sigma}}{}^{\sigma}) \cdots c_{\sigma}(\tau_1^{\sigma}) c_{\sigma}^{\dagger}(\tau_1^{\prime\sigma}) \right] = e^{\mu(l_{\uparrow} + l_{\downarrow}) - U l_{\text{overlap}}}, \quad (5.62)$$

with  $l_{\sigma}$  the total length of the segments (*i.e.* the occupation) for flavor (here: only spin)  $\sigma$  and  $l_{\text{overlap}}$  the total length of the overlap (*i.e.* the double occupation) between the flavors.

From this, we can finally define the transition rates for the Metropolis algorithm, where the insertion and removal of a segment serve as an ergodic set of updates.<sup>9</sup> A segment consists of a pair of a creation and an annihilation operator for a given flavor; for an insertion, first a random time  $\tau$  for the creation operator is selected with proposal probability  $d\tau/\beta$  (if the location is not already part of a segment, otherwise the move is rejected), and subsequently the annihilation operator is placed at a time  $\tau' > \tau$  in the interval of length  $l_{\max}$  between the creation operator and the beginning of the following segment with proposal probability  $d\tau'/l_{\max}$ . The proposal probability for an insertion hence reads

$$w_{\text{insert}}^{\text{prop}} = \frac{d\tau^2}{\beta l_{\max}}, \quad (5.63)$$

whereas the proposal rate for the removal of a given segment is just the probability of selecting that given segment from the  $k + 1$  segments at expansion order  $k + 1$ ,

$$w_{\text{remove}}^{\text{prop}} = \frac{1}{k + 1}. \quad (5.64)$$

This yields the acceptance ratio for the insertion in analogy to Eq. (5.51),

$$R_{\text{insert}} = e^{\mu\delta l - U\delta l_{\text{overlap}}} \frac{\det \mathbf{F}_{\sigma}(k_{\sigma} + 1)}{\det \mathbf{F}_{\sigma}(k_{\sigma})} \frac{\beta l_{\max}}{k_{\sigma} + 1}, \quad (5.65)$$

where  $\delta l$  is the length of the inserted segment and  $\delta l_{\text{overlap}}$  the resulting change in the overlap.

These rates are everything that is needed for the stochastic sampling of the partition function. With respect to the computational effort, the algorithm for the generation of segment configurations mainly consists of the computation of the hybridization matrix determinant and the calculation of the segment lengths and overlaps.

For the actual measurement of the impurity Green's function (5.18) (which constitutes the solution of the impurity problem) the idea is to identify in a given configuration a pair of a creation and an annihilation operator with distance  $\tau$  and remove the hybridization between them, *i.e.* to decouple them from the bath. A configuration for the partition function with order  $k$  and weight  $p_c^Z$  is thus turned into a configuration for the Green's function with order  $k - 1$  and weight  $p_c^G$ . Calculating the Monte Carlo average of  $G(\tau)$ ,

$$G(\tau) = \frac{1}{Z} \sum_c p_c^G = \frac{1}{Z} \sum_c p_c^Z \frac{p_c^G}{p_c^Z}, \quad (5.66)$$

amounts to accumulating  $p_c^G/p_c^Z$  (the  $1/Z \sum_c p_c^Z$  part is taken care of by the Monte Carlo importance sampling of the partition function, cf. Eq. (5.48)). Note that the removal of the hybridization leaves the local trace (5.62) invariant but the hybridization matrix now contains one row (corresponding to the removed annihilation operator) and one column (corresponding to the removed creation operator) less. The ratio of the weights then only contains the respective determinants,

$$\frac{p_c^G}{p_c^Z} = \frac{\det \mathbf{F}(k - 1)}{\det \mathbf{F}(k)}. \quad (5.67)$$

<sup>9</sup>Additional kinds of updates are possible and might increase the sampling efficiency drastically, *e.g.* in the case of symmetry broken phases.

This procedure is repeated for all pairs of creation and annihilation operators in each configuration (after appropriate thermalization, etc.). Recent improvements to the CT-HYB algorithm make it also possible to sample the impurity self energy directly[Hafermann12] or to accumulate the Green's function in other representations, *e.g.* in terms of expansion coefficients with respect to a basis of Legendre polynomials[Boehnke11].

If  $H_0 + H_U$  is not diagonal in the occupation number basis –as is the case for general interaction terms including pair-hopping (B.6) and spin-flip (B.7) terms– the segment picture is not applicable anymore and the computation of the trace (5.62) becomes much more computationally expensive. In this thesis, we therefore restrict ourselves to density-density interactions.

Many more details on the CT-HYB algorithm and its efficient implementation are given in Ref. [Gull08a].

In our discussion, we did not cover the fermionic sign problem which arises if diagrams contribute with negative weight to the sampling. While in general impurity models exhibit a less severe sign problem than lattice models, in the CT-HYB code the sign problem is further reduced by the combination of multiple diagrams into determinants and is in some cases even absent. For the systems considered in this thesis, the sign problem is not a major issue and will not be discussed here.



## 6. Analytic Continuation

Quantum Monte Carlo algorithms like the continuous-time QMC solver presented in Sec. 5.3, while being able to provide accurate estimates for correlation functions like Green's functions or self energies at finite temperatures, presently provide data only on the imaginary time or imaginary frequency axis. While static expectation values like occupancies and energies are directly accessible, real-frequency quantities such as spectra or response functions need to be extracted via an analytic continuation procedure. Mathematically, the analytic continuation is well defined: the (*e.g.* retarded) correlation function  $G^R(\omega)$  on the real axis and  $G(\omega_n)$  on the imaginary axis are analytic continuations of the same analytic function  $\mathcal{G}(z)$  (which is analytic everywhere except for the real line) with  $G^R(\omega) = \mathcal{G}(\omega + i\eta)$  and  $G(\omega_n) = \mathcal{G}(i\omega_n)$ , and if  $G(\omega_n)$  is known at a countable infinite number of imaginary frequencies,  $\mathcal{G}(z)$  and thus  $G^R(\omega)$  are uniquely determined.

In the following, we first treat the fermionic case, *i.e.* correlation functions defined on a grid of fermionic Matsubara frequencies  $\omega_n = (2n + 1)\pi/\beta$  with the inverse temperature  $\beta$ . The corresponding relations for bosons are stated in Sec. 6.4.

For fermions, we define the main quantity of interest, the spectral function, as

$$A(\omega) = -\frac{1}{\pi} \text{Im} G^R(\omega). \quad (6.1)$$

The spectral function is real-valued, positive definite, and satisfies a sum rule  $\int d\omega A(\omega) = \mathcal{N}$ .

Provided that  $|G(\omega_n)|$  falls off at least as fast as  $1/|\omega_n|$  for  $n \rightarrow \infty$ ,  $G(\omega_n)$  and  $A(\omega)$  are related by

$$G(\omega_n) = -\frac{1}{\pi} \int_{-\infty}^{\infty} d\omega \frac{\text{Im} G^R(\omega)}{i\omega_n - \omega} = \int_{-\infty}^{\infty} d\omega \frac{A(\omega)}{i\omega_n - \omega}. \quad (6.2)$$

Performing the discrete Fourier transform (A.1) and executing the Matsubara sum gives the corresponding relation in imaginary time,

$$G(\tau) = \int_{-\infty}^{\infty} d\omega \frac{e^{-\omega\tau}}{e^{-\beta\omega} + 1} A(\omega). \quad (6.3)$$

Analytic continuation is the inversion of Eq. (6.2), respectively Eq. (6.3), to obtain  $A(\omega)$  given the (noisy and incomplete) input data  $G(\omega_n)$  ( $G(\tau)$ , respectively). However, the

form of the kernel  $K(\tau, \omega) = \frac{e^{-\omega\tau}}{e^{-\beta\omega} + 1}$  makes direct inversion impossible:  $K$  becomes exponentially small at large positive ( $e^{-\omega\tau} \ll 1$ ) and negative ( $e^{-\omega\tau} \ll e^{-\beta\omega}$ ) frequencies, so that already at moderate temperatures only data values close to 0 and  $\beta$  of  $G(\tau)$  are meaningfully sampled; due to the incompleteness, *i.e.* limited  $\tau$  resolution, of the Monte Carlo data this impedes the calculation of  $A(\omega)$  away from the Fermi level. For all data points except 0 and  $\beta$ , the inversion of the kernel yields extremely large eigenvalues; this would not only require a very high numerical precision, but also leads to an enormous amplification of any statistical or numerical error in the input data. The same problems occur for the imaginary frequency kernel  $\frac{1}{i\omega_n - \omega}$ .

Another approach would be a least-square fit minimizing the  $\chi^2$  estimate

$$\chi^2[A] = \sum_{i,j} \left( \bar{G}_i - \int d\omega K(\tau_i, \omega) A(\omega) \right) [C^{-1}]_{ij} \left( \bar{G}_j - \int d\omega K(\tau_j, \omega) A(\omega) \right), \quad (6.4)$$

where  $\bar{G}_i$  is the QMC estimate for  $G(\tau = \tau_i)$  and  $C_{ij} = \overline{G_i G_j} - \bar{G}_i \bar{G}_j$  the covariance matrix. However, due to the incompleteness of the QMC data, the uniqueness of the fit is not guaranteed and in practise a multitude of different spectra with the same  $\chi^2$  is obtained. Also, this approach tends to overfit the data, resulting in statistically insignificant structure in  $A(\omega)$ .

## 6.1 Maximum Entropy Method

The most widely used approach to this problem is the maximum entropy method (MEM) [Jarrell96]. It selects the best solution (spectrum) consistent with the data, where the selection is made on the basis of relative prior probabilities of the possible solutions. The guiding principle of maximum entropy is that the prior probability of a given spectrum depends on its entropy, with the most likely spectrum being the one with the highest entropy. The entropy associated with a spectrum is given by

$$S[A] = - \int d\omega A(\omega) \ln \frac{A(\omega)}{D(\omega)} \quad (6.5)$$

relative to a default model  $D(\omega)$  (entropy is a relative function). The default model can incorporate any known features (*e.g.* moments) of the true spectrum but otherwise should be unbiased and featureless; in the simplest case, the default model is just a constant. Importantly, the default model needs to have the same normalization  $\mathcal{N}$  as  $A(\omega)$  which means the normalization needs to be known in advance (see Secs. 6.3 and 6.4 for details how to find the normalization of  $A(\omega)$  for correlation functions other than the one-particle Green's function). The entropy in Eq. (6.5) assumes its maximal value of zero if  $A(\omega) = D(\omega)$ . The prior probability  $P[A]$ , *i.e.* the probability of a given  $A(\omega)$  in the absence of input data  $\bar{G}$ , reads [Jarrell96]

$$P[A] \sim e^{\alpha S[A]}, \quad (6.6)$$

with a scaling parameter  $\alpha$  that will be discussed in detail below.

The posterior probability  $P[A|\bar{G}]$ , *i.e.* the conditional probability of  $A$  given  $\bar{G}$ , is related to  $P[A]$  by Bayes' theorem,

$$P[A|\bar{G}] = \frac{P[\bar{G}|A] P[A]}{P[\bar{G}]}, \quad (6.7)$$



where the probability  $P[\bar{G}]$  serves as a normalization constant; we will not give further attention to it for the rest of the discussion.  $P[\bar{G}|A]$  is called likelihood function and expresses the quality of the fit,

$$P[\bar{G}|A] \sim e^{-\chi^2/2}. \quad (6.8)$$

Thus,  $P[A|\bar{G}] \sim e^Q$ , where

$$Q = \alpha S - \frac{1}{2}\chi^2. \quad (6.9)$$

The MEM solution is given by the spectrum that maximizes  $Q$ . This can be viewed as maximization of the entropy constrained by the least squares with Lagrange multiplier  $\alpha^{-1}$ , or equivalently by a minimization of the least squares constrained by the entropy with Lagrange multiplier  $\alpha$ . The parameter  $\alpha$  balances the competition of the goodness-of-fit measure  $\chi^2$  and the entropic prior  $S[A]$ : in the limit  $\alpha \rightarrow 0$ , the least square fit is recovered, for  $\alpha \rightarrow \infty$  the spectral function maximizing  $Q$  is the default model. Approximating the exponentials in the probability distributions by Gaussians centered around the maximum of their respective arguments, an efficient numerical treatment of the optimization problem is possible, see Ref. [Jarrell96] for details.

The maximum entropy scheme introduced above is still ambiguous as long as no selection for  $\alpha$  has been made. Again using Bayesian arguments,  $\alpha$  can be eliminated by calculating a posterior probability for  $\alpha$ . Eq. (6.7) can be rewritten including  $\alpha$ ,

$$P[A, \alpha|\bar{G}] = \frac{P[\bar{G}|A, \alpha] P[A, \alpha]}{P[\bar{G}]}, \quad (6.10)$$

where  $P[A, \alpha] = P[A|\alpha] P[\alpha]$ . By integrating out  $A$ , one finds the marginal distribution, *i.e.* the conditional probability of  $\alpha$  given  $\bar{G}$ ,

$$P[\alpha|\bar{G}] \sim P[\alpha] \int \mathcal{D}A \frac{P[\bar{G}|A, \alpha] P[A|\alpha]}{P[\bar{G}]}. \quad (6.11)$$

Using  $P[\bar{G}|A, \alpha] \sim \exp(-\chi^2/2)$  and  $P[A, \alpha] \sim \exp(\alpha S)$  as above, all terms appearing in this equation are known except for  $P[\alpha]$  which is taken as constant or Jeffreys prior  $1/\alpha$ . Intuitively, the most likely  $\alpha^*$ , *i.e.* the  $\alpha$  that maximizes  $P[\alpha|\bar{G}]$ , is the one that generates the most likely spectra (for constant  $P[\alpha]$ ). The so-called classic MEM [Jarrell96] presents the spectrum at this optimal value  $\alpha^*$  as solution to the analytic continuation problem. In contrast, Bryan's [Bryan90] approach averages over all spectra, taking  $P[\alpha|\bar{G}]$  as weight factor. In our calculations, the two methods would always yield very similar results since  $P[\alpha|\bar{G}]$  is sharply peaked, see Fig. 6.1 (a),(c). There also exist other heuristic selection rules for  $\alpha$  like choosing it such that  $\chi^2 \approx N$  ( $N$  being the number of imaginary time bins) in the so-called historical MEM [Jarrell96].

In principle, Bayesian inference could also be used to eliminate other nuisance parameters, specifically the default model; this is intractable, however, given the large number of degrees of freedom. Also, empirically there is no sharp maximum in the probability density for the identification of the best default model. Conversely, this means that the dependence on the default model is in general weak.

## 6.2 Stochastic Analytic Continuation

While being based on a sound statistical rationale, the MEM often receives criticism due to its bias towards high entropy spectra: since a Gaussian has the highest entropy, the MEM

typically yields Gaussian-like features whereas sharp peaks are washed out. Stochastic analytic continuation [Sandvik98, Beach04] (also termed average spectrum method, stochastic averaging, stochastic maximum entropy method, or stochastic analytic inference) is an alternative to the MEM which mitigates this issue to some extent. We follow Ref. [Beach04] for the discussion of this method.

The basic assumption of stochastic analytic continuation is that all spectra with the same  $\chi^2$ , *i.e.* all spectra that fit the data equally well, are equally likely. A thermal average over all spectra, Boltzmann weighted according to  $\chi^2/\alpha$ ,

$$\langle A(\omega) \rangle_\alpha = \frac{1}{Z} \int \tilde{\mathcal{D}}A A(\omega) e^{-\chi^2/\alpha} \quad , \quad Z = \int \tilde{\mathcal{D}}A e^{-\chi^2/\alpha} \quad , \quad (6.12)$$

with an integration measure that restricts the integration to spectra that are positive and satisfy the norm rule,

$$\tilde{\mathcal{D}}A = \mathcal{D}A \theta[A] \delta\left(\int_0^1 d\omega A(\omega) - \mathcal{N}\right) \quad , \quad \theta[A] = \begin{cases} 1 & \text{if } A(\omega) \geq 0 \forall \omega \\ 0 & \text{otherwise} \end{cases} \quad , \quad (6.13)$$

should therefore yield a smooth spectrum where only the statistically significant features are preserved.<sup>1</sup> Compared to the posterior probability  $P[A|\tilde{G}]$  used in the MEM there is no explicit reference to the entropy.

It can directly be seen that the limiting cases of this method are the same as for the MEM: For  $\alpha \rightarrow 0$ , only the ground state configuration contributes and the corresponding spectral function is the least square fit. For  $\alpha \rightarrow \infty$ , the average in Eq. (6.12) includes every possible spectrum with the same weight. Thus, the averaged spectrum is independent of the input data and the default model is recovered.

Furthermore, Beach showed that there is an even closer relationship between the two methods. If  $\chi^2$  is taken as the Hamiltonian of a fictitious physical system, Eq. (6.12) describes the thermal average of the corresponding canonical ensemble at temperature  $\alpha$ . According to statistical mechanics, the average spectral function then minimizes the free energy

$$F = \chi^2 - \alpha S \quad , \quad (6.14)$$

with an entropy  $S$ , *i.e.* the averaging implicitly generates an entropy. In general, the functional form of  $S[A]$  is unknown, but in a mean-field treatment of the Hamiltonian  $\chi^2$  it equals the MEM entropy. Hence, stochastic analytic continuation is equivalent to the MEM at the mean-field level. In reality, the averaging also samples over spectra away from the mean-field solution, thereby including fluctuations about this saddle point; thus the stochastic analytic continuation can be viewed as a dynamic generalization of the MEM. Technically, it can be implemented as Monte Carlo process using *e.g.* the Metropolis algorithm.

In our experience, this method typically resolves more –respectively sharper– features than the MEM at the same value of  $\alpha$ , cf. Fig. 6.1 (c). Due to the Monte Carlo averaging, the computational effort is 2-3 orders of magnitude larger, however, and is potentially even increased by refining the method by *e.g.* parallel tempering [Beach04].

<sup>1</sup>For simplicity, we directly identify  $A(\omega)$  with the dimensionless field  $n(x)$  introduced by Beach. The general formalism allows for the introduction of the default model  $D(\omega)$  where  $n(x)$  describes the spectrum in terms of the default model. Hence, the direct identification of  $A$  and  $n$  amounts to  $D(\omega) \equiv 1$ .

Again,  $\alpha$  can be eliminated based on Bayesian inference[Fuchs10] by calculating its posterior probability and taking the spectral function at the maximum  $\alpha^*$ ,  $\langle A \rangle_{\alpha^*}$ , or by averaging over all spectra,  $\int d\alpha P[\alpha|\bar{G}] \langle A \rangle_{\alpha}$ . This, however, comes at the expense of an even higher numerical effort required for the root finding or the calculation of an  $\alpha$  grid, respectively. Sandvik proposed to examine the entropy as a function of  $\alpha$  and to identify the optimal  $\alpha$  at a maximum of the entropy right before a sharp drop (which is taken as indication for the appearance of spurious peaks).

### 6.3 Analytic Continuation of Self Energies

Above we described the analytic continuation of the one-particle Green's function which directly yields the spectral function. However, for quantities other than the spectral function, rather the (real-frequency) self energy than the full Green's function is required. If the self energy is obtained from the Dyson equation (5.19), two alternatives are offered, either the analytic continuation of both  $\mathcal{G}_0$  and  $G$  followed by the application of the Dyson equation in real frequencies, or the adoption of the Dyson equation in Matsubara frequencies, followed by the analytic continuation of  $\Sigma(i\omega_n)$ [Wang09]. It is not a priori clear which route is preferable: the high-frequency fluctuations in  $\Sigma$  will always be large as  $G, \mathcal{G}_0 \sim 1/\omega$  ( $1/(i\omega_n)$ , respectively) for  $\omega \rightarrow \infty$  ( $\omega_n \rightarrow \infty$ ) both in the real and imaginary frequency domain, which makes the inverted Green's functions large and the result of the subtraction noisy. If  $\Sigma(i\omega_n)$  is taken as input to the MEM, these fluctuations are possibly amplified in the maximum entropy procedure. On the other hand, first continuing  $\mathcal{G}_0$  and  $G$  might even lead to an unphysical sign as  $\text{Im} \Sigma(\omega + i\eta) < 0$  must hold for any causal self energy; nothing guarantees  $\mathcal{G}_0^{-1} - G^{-1}$  to be negative definite if the QMC data comprising  $G$  is noisy, however.

In our experience, the analytic continuation of the self energy often yields more reliable results and we prefer it over the direct continuation of the Green's functions also for the determination of the one-particle spectral function according to Eq. (C.1) or (C.2). While the spectral function for multiband systems typically shows a lot of (possibly sharp) features reminiscent of the noninteracting spectrum –which are hard to resolve in the MEM– the self energy possesses much less structure. Since the noninteracting spectrum is known on the real axis, it is desirable not to include it in the analytic continuation procedure but to continue only the self energy instead. Also, recent developments in CTQMC make it possible to sample the self energy directly[Hafermann12], which makes the problem of noisy Matsubara self energies due to the inversion in the Dyson equation obsolete.

In order to apply the analytic continuation formalism laid out above, the self energy needs to have the same analytic properties as the Green's function, namely it must be analytic in the upper/lower half plane, even under reflection on the real axis, vanishing for large frequencies, and its norm must be a known constant. The former two conditions are fulfilled as  $\Sigma$  is the difference of two analytic functions which are even under reflection on the real axis. For the latter properties, we note that the self energy has the asymptotic behavior as given in Eqs. (A.24) and (A.25). After subtraction of the Hartree term  $\sum_{i \neq m} U_{mi} \langle n_i \rangle$ , the remainder takes the form of a Green's function with normalization  $\sum_{i,l \neq m} U_{mi} U_{ml} (\langle n_i n_l \rangle - \langle n_i \rangle \langle n_l \rangle)$ . By defining a rescaled self energy,

$$\tilde{\Sigma}_m(i\omega_n) = \frac{\Sigma_m(i\omega_n) - \sum_{i \neq m} U_{mi} \langle n_i \rangle}{\sum_{i,l \neq m} U_{mi} U_{ml} (\langle n_i n_l \rangle - \langle n_i \rangle \langle n_l \rangle)}, \quad (6.15)$$

with normalization 1, we can thus directly use the kernel  $K(\omega_n, \omega) = \frac{1}{\pi} \frac{1}{i\omega_n - \omega}$  for the analytic continuation  $\tilde{\Sigma}(i\omega_n) \rightarrow \text{Im} \tilde{\Sigma}(\omega)$ . After the analytic continuation (and application of the Kramers-Kronig relations to obtain  $\text{Re} \tilde{\Sigma}(\omega)$  from  $\text{Im} \tilde{\Sigma}(\omega)$ ), the rescaling from Eq. (6.15) is reverted,  $\tilde{\Sigma}(\omega) \rightarrow \Sigma(\omega)$ .

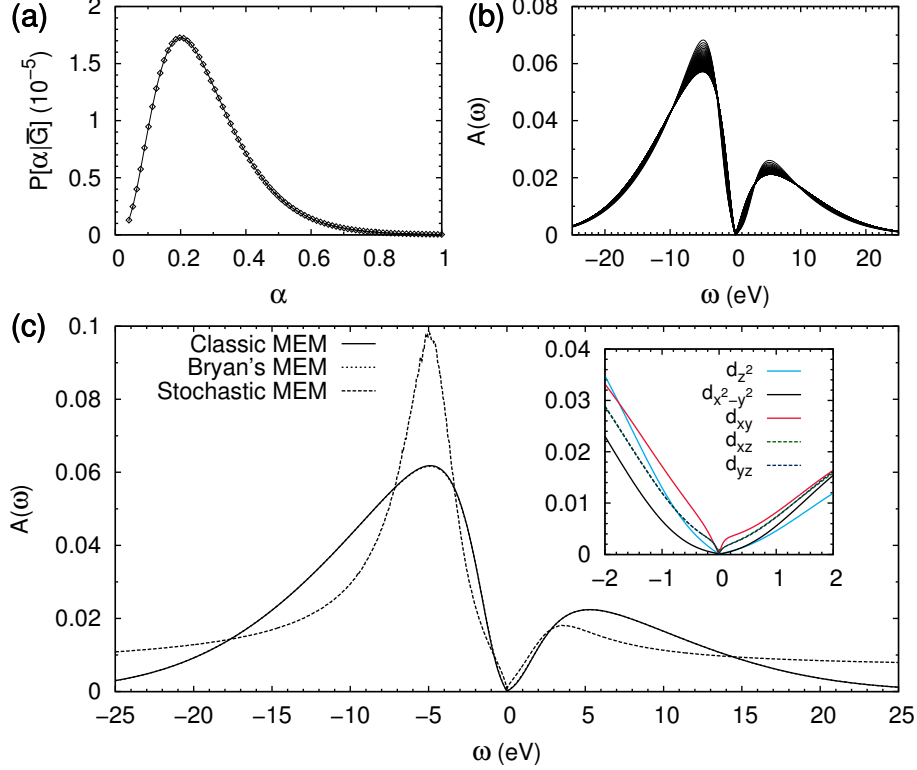


Figure 6.1: Results for the analytically continued Fe  $d_{22}$  self energy from the calculations discussed in Ch. 7 on LiFeAs,  $\beta = 160 \text{ eV}^{-1}$ ,  $U = 4 \text{ eV}$ ,  $J = 0.8 \text{ eV}$ . Panel (a): Probability distribution  $P[\alpha|\bar{G}]$  as a function of  $\alpha$ . The probability is sharply peaked around the classic MEM solution  $\alpha^* \approx 0.22$ . Panel (b): The MEM spectral function for all values of  $\alpha$  shown in Panel (a). Panel (c): Comparison of classic MEM, Bryan's method, and stochastic analytic continuation. For Bryan's method, the spectra in panel (b) were averaged with the probabilities in panel (a) as weight factors. The resulting averaged spectrum lies on top of the classic MEM solution. The spectrum from stochastic analytic continuation was calculated at the optimum  $\alpha^*$  as obtained in classic MEM; it shows more pronounced features and a shift in frequency of the peak at positive energies. In order to suppress the high-frequency tails of the self energy, a Gaussian default model with  $\sigma = 10 \text{ eV}$  has been employed for the spectra obtained from classic MEM and Bryan's method; the effect can be clearly recognized from the comparison with the stochastic analytic continuation result where a constant default model was used. The inset of panel (c) presents a close-up of the classic MEM results in the region around  $E_F$  for all orbital self energies. The analytic continuation results for the  $d_{xz}$  and  $d_{yz}$  orbitals are identical, reflecting the degeneracy due to the tetragonal structure. This allows to exclude the existence of spurious features which would be random and different between the orbitals and thus validates the used parameters.

For the one-particle spectral functions presented in this thesis, we performed analytic continuation of the self energy using classic MEM. In many cases, particularly in the iron

pnictides, the continued self energies extend over a large range in energy, possibly even diverging at the boundaries of the chosen output energy interval,<sup>2</sup> cf. Fig. 6.1 (c). This is problematic as in the MEM the normalization of the spectral function (here:  $\text{Im } \tilde{\Sigma}(\omega)$ ) is enforced in the given energy interval. Therefore, one needs to make sure that the whole spectral weight is in fact contained in the chosen energy interval, otherwise the spectral function will be distorted in order to attain the given normalization. For very slowly decaying or even diverging tails this can be achieved with an appropriate default model. We employed a Gaussian default model in our calculations, albeit with a width large enough not to introduce a substantial bias into the resulting spectrum (*e.g.*  $\sigma = 10$  eV).

## 6.4 Analytic Continuation of Bosonic Response Functions

For bosonic response functions, we note that not  $\text{Im } G^R(\omega)$  but  $-\text{sgn}(\omega) \text{Im } G^R(\omega)$  is positive definite and we may therefore define the spectral function as

$$A(\omega) = -\frac{1}{\pi} \frac{\text{Im } G^R(\omega)}{\omega}. \quad (6.16)$$

Inserting this into Eq. (6.2) yields the corresponding bosonic relation,

$$G(\Omega_n) = \int_{-\infty}^{\infty} d\omega \frac{\omega}{i\Omega_n - \omega} A(\omega), \quad (6.17)$$

with bosonic Matsubara frequencies  $\Omega_n = 2n\pi/\beta$ . This can be cast into a purely real form by making use of the symmetry of  $A(\omega)$  on the real axis,  $A(\omega) = A(-\omega)$  [Gunnarsson10],

$$\begin{aligned} G(\Omega_n) &= \int_{-\infty}^{\infty} d\omega \frac{\omega}{i\Omega_n - \omega} \frac{i\Omega_n + \omega}{i\Omega_n + \omega} A(\omega) = - \int_{-\infty}^{\infty} d\omega \left( \frac{i\Omega_n \omega}{\Omega_n^2 + \omega^2} + \frac{\omega^2}{\Omega_n^2 + \omega^2} \right) A(\omega) \\ &= - \int_{-\infty}^{\infty} d\omega \frac{\omega^2}{\Omega_n^2 + \omega^2} A(\omega). \end{aligned} \quad (6.18)$$

Note that the bosonic kernel  $K(\Omega_n, \omega) = -\frac{\omega^2}{\Omega_n^2 + \omega^2}$  is singular at  $\omega = 0$  since  $\Omega_n = 0$  for  $n = 0$ . Importantly, from Eq. (6.18) one can read off  $G(0) = -\int_{-\infty}^{\infty} d\omega A(\omega)$ , *i.e.* the normalization of  $A(\omega)$  is given by  $-G(0)$ .

If the desired response function is the optical conductivity  $\sigma(\omega)$ , one can directly relate  $\sigma(\omega) \propto A(\omega)$ , with the generic Green's function  $G(\Omega_n)$  in Eq. (6.18) taken as  $\tilde{\Pi}(\Omega_n)$  from Eq. (A.32). For the optical conductivities presented in this thesis, we performed the analytic continuation in Eq. (6.18) using the stochastic maximum entropy method with a constant default model.

---

<sup>2</sup>Note that this energy interval is only a parameter in the analytic continuation and not related to the energy window chosen for the construction of the localized correlated basis, cf. Sec. 5.2.1. Even though the analytically continued self energy often shows significant spectral weight outside the energy window of the correlated states, this spectral weight is projected out when calculating the respective lattice self energy (5.23).



# 7. Correlation Effects in LiFeAs

**J. Ferber**, K. Foyevtsova, R. Valentí, and H. O. Jeschke,  
*Phys. Rev. B.* **85**, 094505 (2012)

In Ch. 4, we discussed an effective description of the band structure and the optical properties of iron pnictides in the framework of density functional theory augmented with a frequency-independent renormalization of the kinetic energy. In this chapter and the next, we go beyond this approximation and apply the LDA+DMFT methodology laid out in Ch. 5 to some selected iron pnictides, namely LiFeAs, LiFeP, and LaFePO, and study the effects of correlations on the Fermi surface of these materials. In contrast to a mere renormalization of the kinetic energy which, by definition, does not change the Fermi surface, we find that electronic correlations in these systems induce distinctive changes in the Fermi surface; in the case of LiFeP and LaFePO we even predict a change in the Fermi surface topology.

In this chapter, we first discuss the role of electronic correlations in LiFeAs by studying the effects on band structure, mass enhancements, and Fermi surface. We conclude that LiFeAs shows characteristics of a moderately correlated metal, and that the strength of correlations is mainly controlled by the value of the Hund's rule coupling  $J$ . The hole pockets of the Fermi surface show a distinctive change in form and size with implications for the nesting properties. Our calculations are in good agreement with a number of recent experiments, including photoemission spectroscopy, de Haas-van Alphen (dHvA) measurements, and quasiparticle scattering interference.

## 7.1 Introduction

Among the various known iron pnictide classes, the 111 family comprising LiFeAs and LiFeP shows especially interesting features compared with the other families. Whereas superconductivity in many iron pnictide compounds develops in the vicinity of an SDW state upon doping or application of external pressure, LiFeAs and LiFeP (and LaFePO from the 1111 family) are non-magnetic and superconductivity evolves without additional doping or applied pressure. Of special relevance is LiFeAs where  $T_c \approx 18$  K [Tapp08, Pitcher08]

compared to  $T_c \approx 6$  K [Deng09] in LiFeP and  $T_c \approx 4$  K [Kamihara06] in LaFePO. In the 1111 and 122 family compounds (with LaFeAsO and BaFe<sub>2</sub>As<sub>2</sub> as typical examples), the SDW order is generally attributed to sizable nesting of the electron and hole Fermi pockets, see Ch. 1. For LiFeAs, the situation is not quite as clear: band structure calculations using DFT predict an AF ground state with stripe-like order as in the other pnictides, albeit in a shallow energy minimum compared to the non-magnetic state [Singh08, Zhang10]. In contrast, angle-resolved photoemission spectroscopy (ARPES) measurements report only poor nesting [Borisenko10]. In fact, recent neutron scattering measurements find strong SDW fluctuations [Taylor11, Qureshi12], with an incommensurate vector [Qureshi12] slightly shifted from the commensurate order observed in the other iron pnictide superconductors. Also functional renormalization group calculations [Platt11] predict SDW fluctuations to be the dominant instability. On the other side, recent dHvA experiments claim to be in good agreement with DFT regarding the topology of the Fermi surface [Putzke12].

It is of particular interest to identify the role of electronic correlations in this context. The band structure of LiFeAs features two shallow hole pockets around the Gamma point which generate a large density of states, and it has been suggested that this is essential for the way superconductivity emerges in this compound [Borisenko10, Brydon11]. These features of the electronic structure can also be expected to be rather susceptible to changes induced by correlations. Thus, this thesis aims to single out the effects of correlations on the Fermi surface and the low-energy properties of LiFeAs.

## 7.2 Methods and Interaction Parameters

We performed paramagnetic calculations using the ‘one-shot’ LDA+DMFT scheme described in Sec. 5.2.3 based on electronic structure calculations in WIEN2K. The LDA selfconsistency cycle employed 1080  $\mathbf{k}$  points in the irreducible Brillouin zone, using LDA for the exchange-correlation potential in the parameterization of Ref. [Perdew92]. We base our calculations on the experimental crystal structure as obtained from X-ray diffraction data [Morozov10] with space group  $P4/nmm$ . For comparison, we also performed calculations on the structure given in Ref. [Tapp08] for which we list mass enhancements in Tab. 7.1.

For the construction of the localized Wannier-like orbitals for DMFT, an energy window ranging from  $-5.5$  eV to  $2.85$  eV was chosen, comprising the Fe  $3d$  and As  $4p$  bands. For the solution of the DMFT impurity problem in the CT-HYB QMC solver (cf. Sec. 5.3), we used  $1 \times 10^7$  Monte Carlo sweeps throughout our calculations. Unless stated otherwise, the Monte Carlo sampling was done at a temperature  $T = 72.5$  K ( $\beta = 160$  eV<sup>-1</sup>).

For the interaction parameters, we use the definitions of  $U = F^0$  and  $J = (F^2 + F^4)/14$  in terms of Slater integrals (B.13) and the FLL double counting correction (2.37).

There is considerable disagreement in the literature about the size of the interaction parameters in the iron pnictides; in particular, the Coulomb interaction  $U$  strongly depends on the estimation method, whereas  $J$  is only moderately reduced from its atomic value. Self-consistent GW determination yields rather large numbers (*e.g.*  $U = 4.9$  eV,  $J = 0.76$  eV for BaFe<sub>2</sub>As<sub>2</sub> [Kutepov10]), with lower values being reported by constrained LDA (*e.g.*  $U = 3.1$  eV,  $J = 0.81$  eV for LaFeAsO [Anisimov09]) and constrained random-phase approximation (cRPA) (*e.g.*  $U = 2.9$  eV,  $J = 0.79$  eV for LaFeAsO [Aichhorn09]). For LiFeAs, interaction parameters obtained from cRPA have been reported in Ref. [Miyake10] for two low-energy



models, one constructed for the Fe  $3d$  bands only, the other one for a manifold containing Fe  $3d$  and As  $4p$  states. The choice of the model affects the value of the interaction parameters in two ways: a model with more bands renders the associated Wannier functions more localized and thereby increases the value of the matrix elements of the interaction. Also, since the interaction strength is derived as a partially screened Coulomb interaction where screening channels within the low-energy space are subtracted, the exclusion of more screening channels in a model with more bands increases the interactions. This is reflected by very different interaction parameters for the two models,  $U = 2.45$  eV and  $J = 0.61$  eV for the  $d$  model compared with  $U = 4.95$  eV and  $J = 0.87$  eV for the  $dp$  model.

However, as pointed out in Ref. [Miyake08], the appropriate model for our LDA+DMFT approach is a hybrid model where the Wannier functions are constructed from a  $dp$  model, but only  $d$ - $d$  transitions are excluded from the screening since we only treat the  $d$  states as correlated in our DMFT procedure. This means that the  $d$  model systematically underestimates the interactions for our setup whereas the  $dp$  model systematically overestimates them. In light of these uncertainties we report in the following results for  $U = 4$  eV,  $J = 0.8$  eV, and include a discussion about the sensitivity of our results to the choice of interaction parameters in Sec. 7.3.1.

In the following, orbital characters are labeled in a coordinate system which is  $45^\circ$  rotated with respect to the crystallographic axes, *i.e.*  $x$  and  $y$  point to nearest Fe neighbors in the Fe-As plane.

### 7.3 Results

In Figs. 7.1 and 7.2, we compare the momentum-integrated and momentum-resolved spectral function for LiFeAs obtained within LDA+DMFT with their LDA counterparts, namely the density of states (Fig. 7.1) and the LDA band energies (Fig. 7.2). Note that the LDA bands in Fig. 7.2 were renormalized by a factor of 2.17 corresponding to the orbitally averaged value of the mass renormalization.

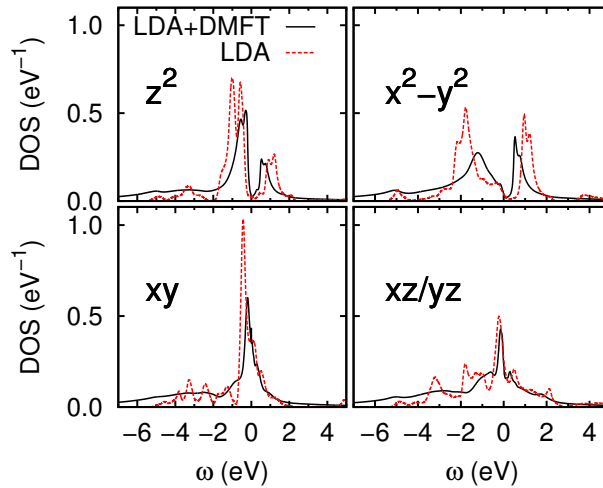


Figure 7.1: Orbital-resolved comparison between LDA density of states (red dotted lines) and the LDA+DMFT spectral function  $A(\omega)$  (black full lines). The interaction parameters used were  $U = 4$  eV,  $J = 0.8$  eV.

The momentum-integrated spectral function  $A(\omega)$  shows a band width reduction but no substantial spectral weight transfer, *i.e.* no formation of Hubbard bands. The momentum-resolved spectral function  $A(\mathbf{k}, \omega)$  in Fig. 7.2 displays well-defined excitations around the Fermi level and stronger correlation-induced broadening of the states at higher binding energies. The broadening affects the states below the Fermi level more strongly where coherent quasiparticles can be identified down to approx. 0.3 eV below  $E_F$ . For the states above  $E_F$ , the crossover to rather diffuse structures occurs at approx. 0.7 eV. On a quantitative level, at temperature  $T = 72.5$  K, the scattering rates (or, equivalently, inverse lifetimes)  $-\text{Im} \Sigma(i0^+)$  are small, see Tab. 7.1, supporting the picture of well-defined, long-lived quasiparticles. The renormalized LDA bands give a good approximation only close to the Fermi level (the mass enhancement in Eq. (C.3) holds strictly only at  $\omega = 0$ ); states away from  $E_F$  are less renormalized.

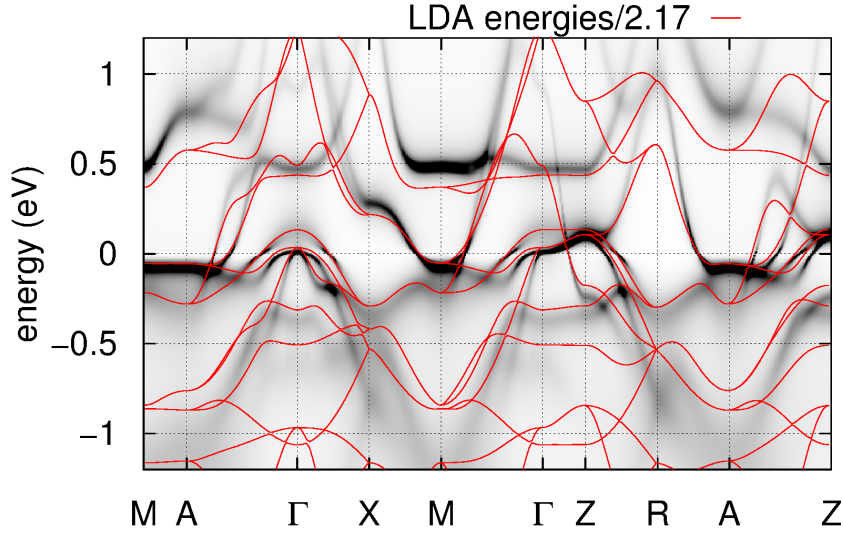


Figure 7.2: Momentum-resolved spectral function  $A(\mathbf{k}, \omega)$  together with LDA bands. For comparison, the LDA band energies are divided by the orbitally averaged value of the mass renormalization. The interaction parameters are the same as in Fig. 7.1.

For the previously specified interaction parameters, the self energy and spectral function thus show the characteristics of a Fermi liquid state in a metal with moderate correlations, a picture which also has been promoted for the 1111 and 122 family of iron pnictides in a number of previous publications [Anisimov09, Aichhorn09, Skornyakov09, Skornyakov10, Hansmann10]. Note that for multiorbital systems with sufficiently strong  $J$ , the absence of the rotationally invariant Hund's coupling in the calculation (*i.e.* the consideration of the density-density terms in  $J$  only) can lead to qualitatively wrong results by suppressing coherence and driving the system from a Fermi liquid into a non-Fermi liquid state [Haule09, Ishida10, Aichhorn10]. This is not observed here, indicating that the restriction to density-density terms in the Hund's coupling is not detrimental. However, coherence is quickly lost at temperatures  $\gtrsim 100$  K, see Sec. 7.3.2.

The mass enhancements as given in Tab. 7.1 exhibit pronounced orbital dependence, with stronger mass enhancement in the  $t_{2g}$  orbitals  $d_{xy}$  and  $d_{xz}/d_{yz}$ . As can be seen from Fig. 7.1, the band width  $W$  of the  $t_{2g}$  orbitals is smaller, leading to a larger ratio  $U/W$  and to increased correlations in these orbitals. Analysis of a low-energy Fe  $d$  tight-binding model, obtained by considering the localized Wannier orbitals, shows that the diagonal nearest neighbor hopping  $t_{\text{NN}}(xy, xy)$  for the  $d_{xy}$  orbital almost vanishes as the direct

hopping from the iron-iron overlap and the indirect hopping from the iron-pnictogen-iron overlap have opposite signs and almost cancel. Additionally, the diagonal hoppings to further iron neighbors for  $d_{xy}$  are small; this contributes to the localization of the  $d_{xy}$  quasiparticles and a stronger mass enhancement than in the other orbitals[Yin11]. The table lists the mass enhancements for both investigated structures, showing some quantitative but no qualitative differences. In particular, we checked that Fermi surfaces are practically not affected, though; we therefore continue to report results only for the structure from Ref. [Morozov10].

Table 7.1: Orbital-resolved quasiparticle weights  $Z$ , mass enhancements  $m^*/m_{\text{LDA}}$ , and scattering rates  $-\text{Im}\Sigma(i0^+)$  for interaction parameters  $U = 4$  eV,  $J = 0.8$  eV. The first (second) number in each cell refers to calculations performed on the structure from Ref. [Morozov10] (Ref. [Tapp08]).

Orbital	$d_{z^2}$	$d_{x^2-y^2}$	$d_{xy}$	$d_{xz/yz}$
$Z$	0.57 / 0.53	0.64 / 0.60	0.36 / 0.31	0.42 / 0.36
$m^*/m_{\text{LDA}}$	1.74 / 1.88	1.57 / 1.67	2.78 / 3.24	2.39 / 2.78
$-\text{Im}\Sigma(i0^+)$ (meV)	0.1 / 0.3	-1.0 / -0.7	2.4 / 5.2	1.7 / 3.8

For a comparison with ARPES measurements, Fig. 7.3 shows some cuts of the momentum-resolved spectral function  $A(\mathbf{k}, \omega)$  along the paths given in Fig. 2e in Ref. [Borisenko10]. Qualitatively, we find good agreement; quantitatively, the mass enhancement extracted from the cuts in Ref. [Borisenko10] is 3.1. This value should be compared to the mass enhancements of the orbitals that contribute most to the spectral weight at low energy. As can be seen in Fig. 7.1, these are the  $t_{2g}$  orbitals (the  $e_g$  orbitals show a dip around the Fermi level) with calculated mass enhancements of 2.4 – 2.8 (2.8 – 3.2, respectively). Thus, the mass enhancements are in good agreement, with ARPES pointing to moderately larger interactions. We will come back to this point further below.

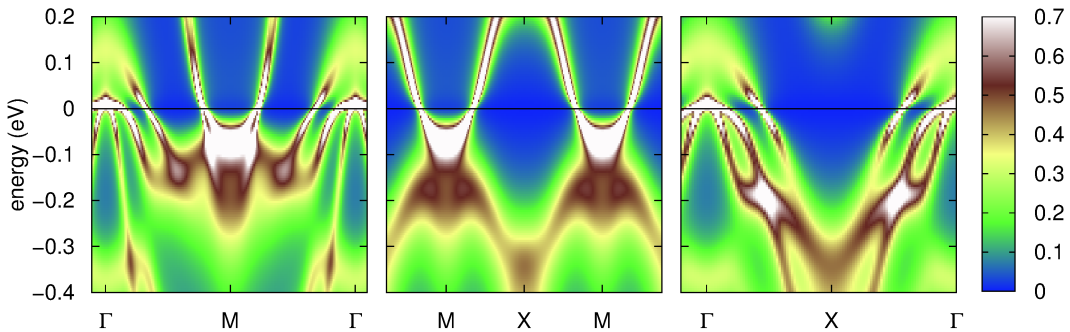


Figure 7.3: LDA+DMFT momentum-resolved spectral function  $A(\mathbf{k}, \omega)$  for LiFeAs along the paths in the Brillouin zone given in Ref. [Borisenko10], Fig. 2e. Interaction parameters as in Fig. 7.1.

In summary, we consider LiFeAs a metal in an intermediate range of interactions without significant spectral weight transfer; mass renormalizations are close to what has been calculated and measured in the 1111 and 122 systems.

We now turn our attention to the correlation effects on the Fermi surfaces of LiFeAs which have been experimentally accessed by ARPES[Borisenko10, Umezawa12] and dHvA [Putzke12] measurements. Figs. 7.4 and 7.5 show the Fermi surfaces in the  $k_z = 0$  and

$k_z = \pi$  plane obtained within LDA and LDA+DMFT. The pockets around  $(k_x, k_y) = (0, 0)$  are hole pockets, while the ones around  $(k_x, k_y) = (\pi, \pi)$  are electron pockets (compare Fig. 7.2). The most prominent effects of correlations are the shrinking of the middle  $d_{xz}/d_{yz}$  hole pocket which takes on a butterfly shape at  $k_z = 0$ , and the increase of the outer  $d_{xy}$  pocket, whereas the electron pockets almost do not change in size or form. This observation is in agreement with previous calculations[Yin11] and would support ARPES results. This analysis shows that correlations tend to weaken –if not suppress– nesting in this material.

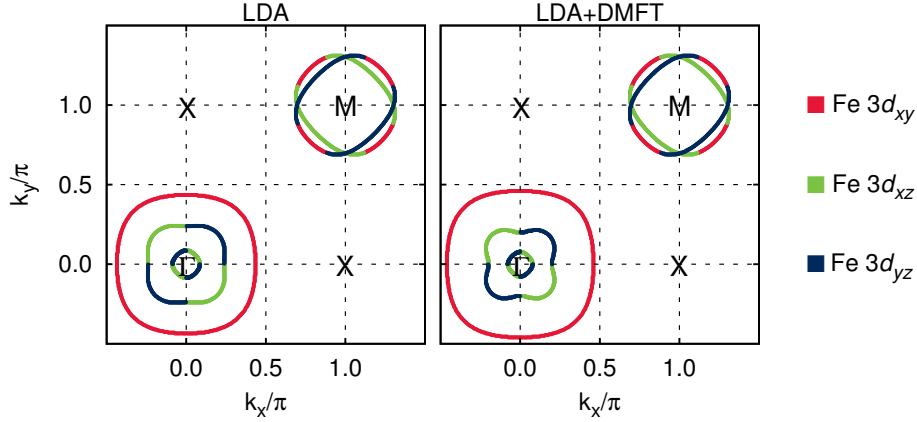


Figure 7.4: Fermi surface for  $k_z = 0$ . Interaction parameters as in Fig. 7.1.

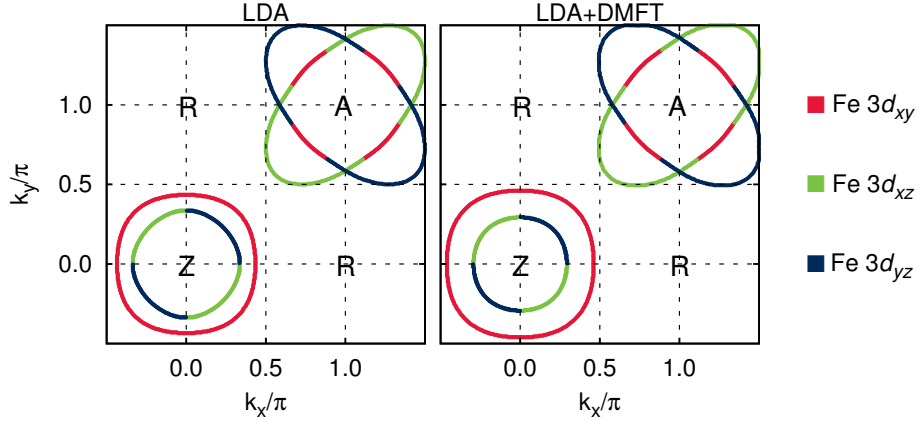


Figure 7.5: Fermi surface for  $k_z = \pi$ . Interaction parameters as in Fig. 7.1.

For the discussion of the electron pockets, we describe the Fermi surface in terms of an inner and outer pocket rather than by two crossed ellipsis-like pockets of equal size. This is motivated by the fact that spin-orbit (SO) coupling lifts the degeneracy between the ellipses and splits the electron pockets into an inner and outer sheet[Putzke12].<sup>1</sup> Note, however, that no SO coupling is taken into account in the present calculations. As can be seen from the comparison of Figs. 7.4 and 7.5, the thus defined outer pocket displays strong  $k_z$  dispersion, whereas the inner sheet depends only weakly on  $k_z$ .

In order to facilitate a quantitative comparison with experiment, we show in Fig. 7.6 dHvA frequencies calculated with respect to magnetic field angle as reported in Fig. 2c

<sup>1</sup>We performed fully relativistic calculations in FPLO[Koepernik99] of the Fermi surface of LiFeAs to confirm the avoided crossing of the electron sheets.

of Ref. [Putzke12], along with the data from the dHvA measurements and pocket sizes obtained from ARPES and quasiparticle scattering interference (QPI). The dHvA frequencies correspond to extremal pocket sizes (orbits) that are observed at a given angle  $\theta$  with respect to the  $k_z$  axis. The labeling of the orbits follows Ref. [Putzke12]: orbits 1, 2, and 3 refer to the inner, middle, and outer hole pocket, and orbits 4 and 5 to the outer and inner electron pocket (see Fig. 7.6 (a)), respectively. In order to define pocket sizes within LDA+DMFT (Fig. 7.6 (b)) in view of the finite broadening induced by the correlations, we track the maximum of  $A(\omega = 0)$  through the Brillouin zone.

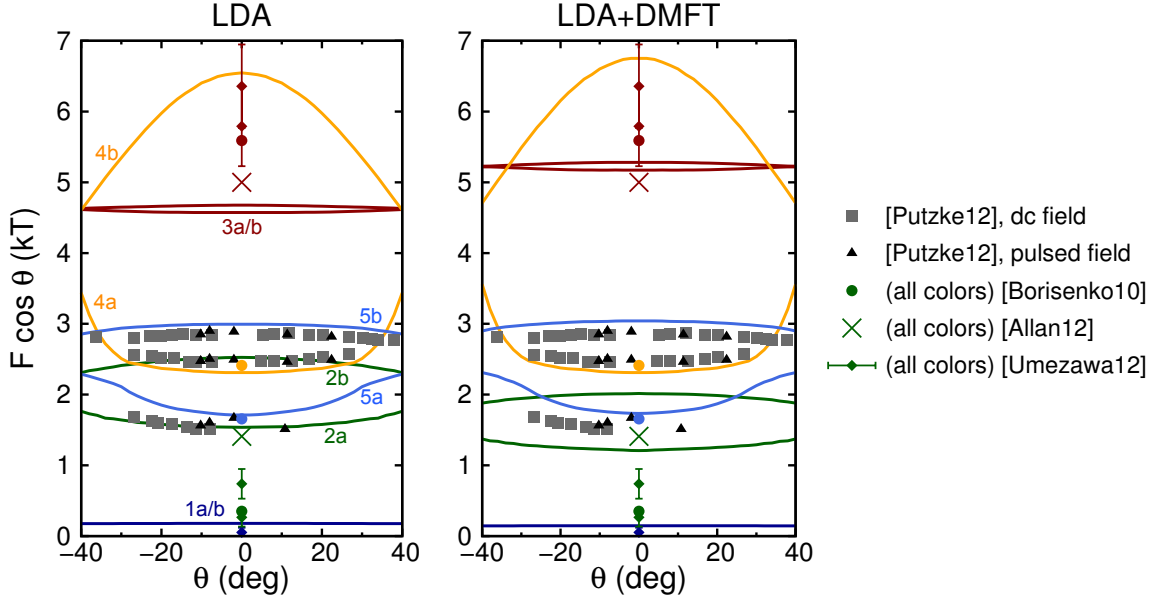


Figure 7.6: dHvA frequencies with respect to the magnetic field angle obtained within (a) LDA and (b) LDA+DMFT along with experimental data from the indicated references. The orbits refer to extremal pocket sizes (kT denotes kilotesla), where the pockets are identified as discussed in the text. We observe a shrinking of the middle hole pocket 2 and an increase of the outer hole pocket size 3 in agreement with ARPES[Borisenko10, Umezawa12] and QPI[Allan12]. This suggests an interpretation of the lowest dHvA frequency in terms of the electron pocket 5 rather than the hole pocket 2 (see text). Interaction parameters as in Fig. 7.1.

Compared to the calculated dHvA frequencies in Ref. [Putzke12] small differences are already visible on the LDA level (Fig. 7.6 (a)), *e.g.* the minima of orbit 2 and orbit 5 for small angles are not degenerate anymore. This is probably an effect of differences in the determination of the Fermi surface (*e.g.* due to effects of a finite  $\mathbf{k}$ -mesh) and illustrates the high sensitivity of the orbits to details of the calculation.

As already seen in Figs. 7.4 and 7.5, the effect of correlations on the Fermi surface manifests itself mainly in a shrinking of the middle hole pocket, and, preserving the electron count, an increase of the outer hole pocket size. This is reflected by a shift downwards of orbit 2 and a shift upwards of orbit 3 in Fig. 7.6 (b); orbits 4 and 5 remain essentially unchanged, in agreement with ARPES[Borisenko10, Umezawa12].

Analyzing the curvature and the size of the orbits, the authors of Ref. [Putzke12] attribute the experimentally measured frequencies to the electron Fermi surface sheets, where the

two higher frequencies are assigned to orbits 5b and 4a, and the lowest frequency is suspected to originate from orbit 5a. Our results support this interpretation: whereas the orbits 2a/5a and 2b/4a are of similar size in the LDA calculation, the correlations affect mainly the hole pockets and lift this (near-)degeneracy. As a result, the electron orbits 2a and 2b are unlikely to give rise to the measured frequencies as their sizes are rather different from the measured data. This offers a reconciliation of the dHvA and ARPES experiments: the shrunk middle hole pocket is only seen in ARPES which finds a correlated metal with poor nesting along with sizable mass renormalization. In contrast, the dHvA measurements resolve the (lighter) electron pocket sizes in LiFeAs that almost do not change under inclusion of correlation and therefore report good agreement with LDA. The large mass renormalizations (up to a factor  $\approx 5$ ) that are also measured in Ref. [Putzke12] suggest –even under consideration of a non-negligible electron-phonon contribution– a scenario of important electronic correlations which are accounted for correctly within LDA+DMFT.

### 7.3.1 Sensitivity Analysis

We analyze the sensitivity of our results to our choice of interaction parameters by applying some variation to  $U$  and  $J$  while keeping the respective other parameter fixed.

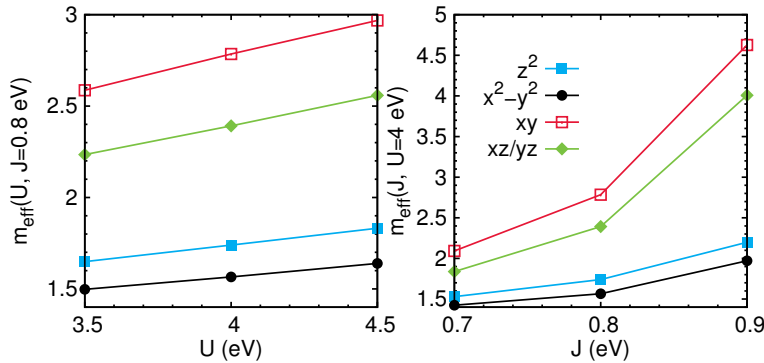


Figure 7.7: Sensitivity of effective masses  $m^*/m_{\text{LDA}}$  with respect to changes in the interaction parameters.

Fig. 7.7 shows the evolution of the mass enhancements  $m^*/m_{\text{LDA}}$  with the interaction parameters. A moderate dependence on  $U$  and a very strong dependence on  $J$  are observed (note that the applied variations of  $U$  and  $J$  are different in size). Whereas a change in  $U$  affects all orbitals roughly equally, a change in  $J$  leads to an immense mass enhancement particularly of the  $t_{2g}$  orbitals.

The decisive role of the Hund’s coupling for the physical properties of the iron pnictides has been discussed previously [Haule09]. For the different behavior of the  $e_g$  and  $t_{2g}$  orbitals it is important that the  $e_g$  states in LiFeAs lie energetically lower than the  $t_{2g}$  states. In the atomic limit, the energy gain from Hund’s rule exceeds the crystal field splitting already for rather small  $J$  and the ground state is a high spin state with the configuration  $e_g^3 t_{2g}^3$ , where the  $t_{2g}$  orbitals are occupied by three electrons of the same spin. In the atomic limit, this prevents mixing of the orbitals due to the Pauli principle; in the crystal, it still impedes inter-orbital fluctuations within the  $t_{2g}$  manifold [Medici11, Yin11]. This effect contributes to the high sensitivity of the  $t_{2g}$  effective masses with respect to  $J$ .

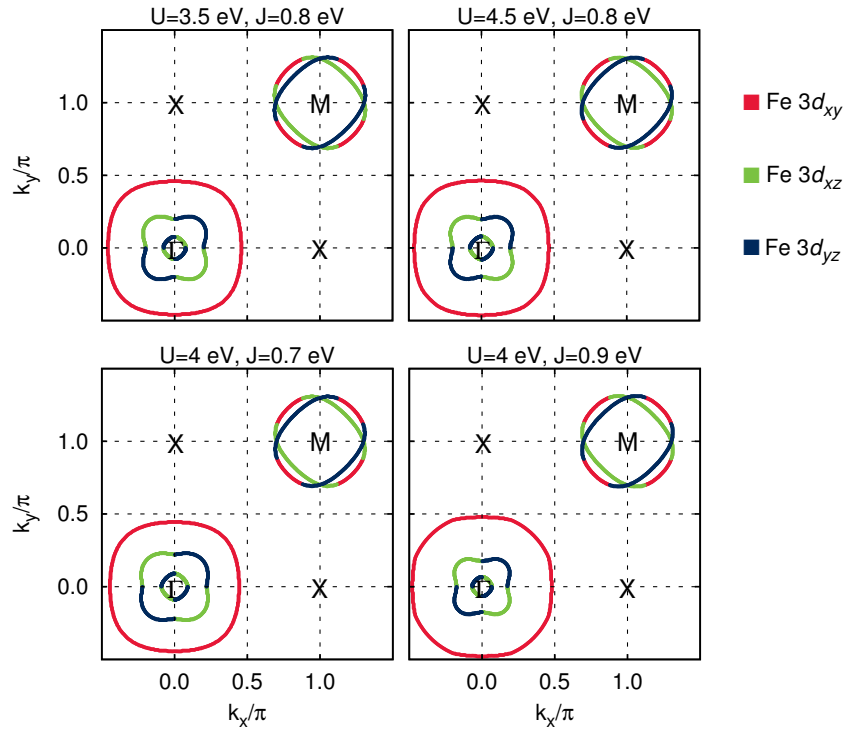


Figure 7.8: Sensitivity of the Fermi surface at  $k_z = 0$  with respect to changes in the interaction parameters.

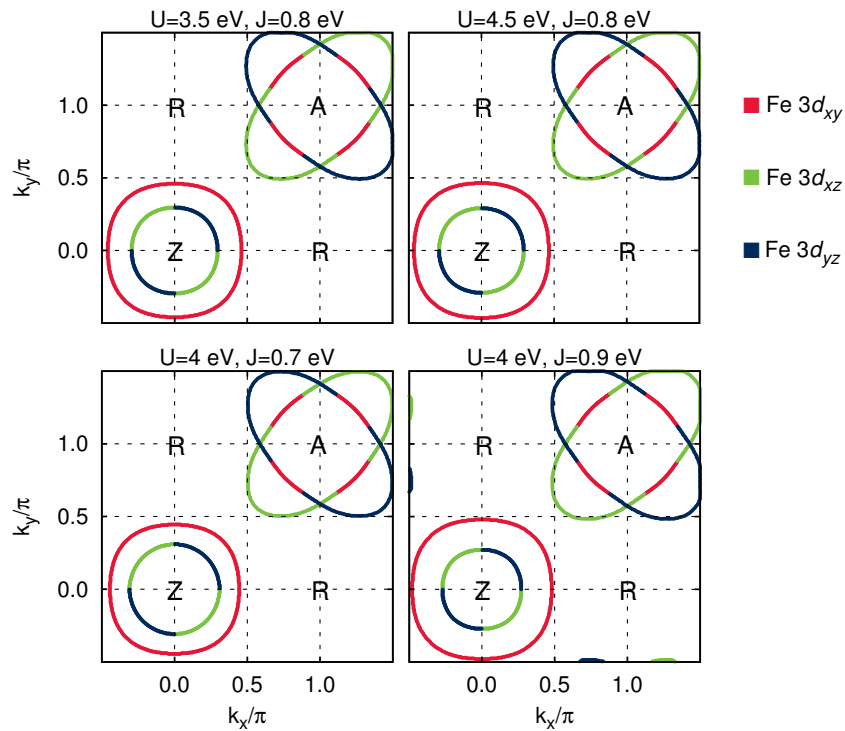


Figure 7.9: Sensitivity of the Fermi surface at  $k_z = \pi$  with respect to changes in the interaction parameters.

Accordingly, the Fermi surface is rather stable with respect to variation of  $U$ , but strongly depends on  $J$ , shown for  $k_z = 0$  in Fig. 7.8 and for  $k_z = \pi$  in Fig. 7.9. Following the trend discussed above, larger values of  $J$  promote a more pronounced shrinking (increase) of the middle (outer) hole pocket. Values as large as 0.9 eV for the Hund's coupling render the system rather incoherent, however, with significant scattering rates  $-\text{Im} \Sigma(i0^+)$  around 14 meV on the  $t_{2g}$  orbitals.

Regarding the robustness of our calculations we present in Fig. 7.10 the comparison to LDA+DMFT calculations with the full Hund's rule coupling from Ref. [Lee12a] that appeared after our publication. No substantial difference between the consideration of the rotationally invariant Hund's rule coupling and only density-density terms is visible: both predict a shrinking of the middle hole pocket and an extension of the outer hole pocket at  $\Gamma/Z$  of almost the same magnitude compared to LDA. Note, however, the different interaction parameters which suggest that neglecting spin-flip and pair-hopping terms in the density-density calculation has to be compensated via a slightly larger value of  $J$  compared to the consideration of the full Hund's rule terms.

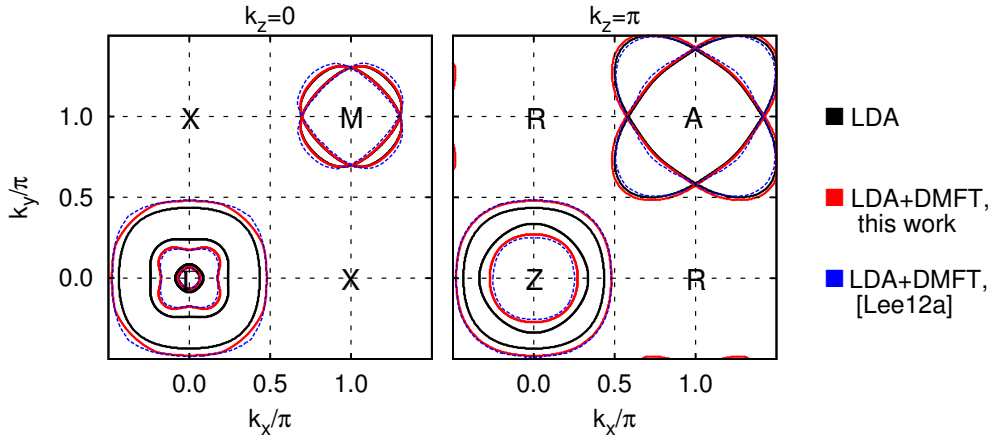


Figure 7.10: Effect of the consideration of the full (rotationally invariant) Hund's rule coupling on the Fermi surface of LiFeAs. Interaction parameters:  $U = 4$  eV,  $J = 0.9$  eV (density-density interactions only, this work);  $U = 5$  eV,  $J = 0.8$  eV (full  $J$  vertex, Ref. [Lee12a]).

### 7.3.2 Coherence-Incoherence Crossover

As mentioned above, the coherence of the quasiparticles in LiFeAs is quickly lost when going to higher temperatures or larger interaction values than considered here, in particular when increasing the value of  $J$ . Besides the inspection of scattering rates, an analysis of the coherence-incoherence crossover can be based on the temperature evolution of the (dynamical) local spin susceptibility,

$$\chi(\tau) = \langle S_z(\tau) S_z(0) \rangle = \frac{1}{N_{\text{orb}}^2} \sum_{mm'} \langle S_z^m(\tau) S_z^{m'}(0) \rangle, \quad (7.1)$$

with the spin density  $S_z^m(\tau) = \frac{1}{2}(d_{m,\uparrow}^\dagger(\tau)d_{m,\uparrow}(\tau) - d_{m,\downarrow}^\dagger(\tau)d_{m,\downarrow}(\tau))$ .<sup>2</sup> In Fig. 7.11,  $\chi(\tau)$  is plotted for different temperatures. In a Fermi liquid,  $\chi(\tau) \propto (T/\sin(\pi\tau T))^2$ , and thus

<sup>2</sup> $\sqrt{\chi(\tau=0)}$  (the instantaneous magnetic moment) and  $\chi(\omega=0) = \int_0^\beta d\tau \chi(\tau)$  are related to the formation of magnetic moments, see Ref. [Hansmann10].



$\chi(\beta/2) \propto T^2$ . The inset of Fig. 7.11 shows the temperature dependence of  $\beta^2\chi(\beta/2)$  taking on a constant value only below  $\approx 100$  K, the temperature below which coherent quasiparticles form in LiFeAs. This is different from *e.g.* LaFeAsO[Aichhorn11] and also LiFeP and LaFePO in the next chapter which are found to be coherent up to room temperature.

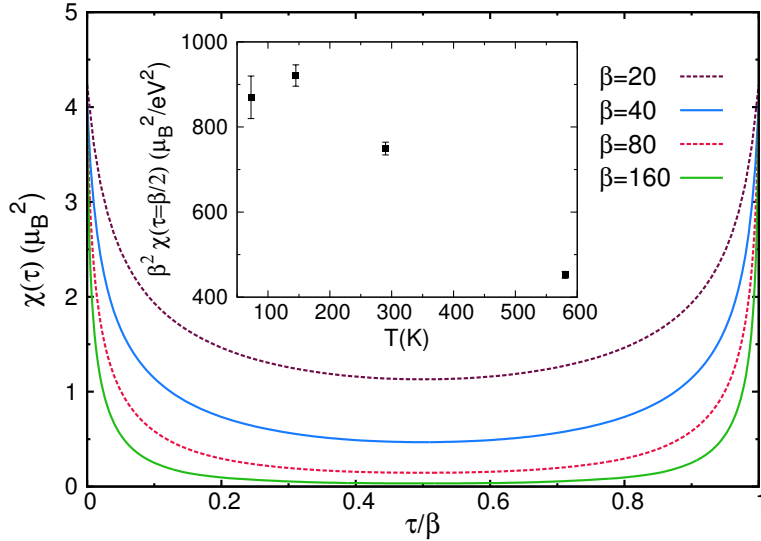


Figure 7.11: Paramagnetic local spin susceptibility for different temperatures. Inset:  $\beta^2\chi(\beta/2)$  as a function of temperature. Interaction parameters as in Fig. 7.1.

## 7.4 Conclusions

We demonstrated that within the considered range of interaction parameters LiFeAs behaves as a Fermi liquid and that correlation effects are very sensitive to the value of the Hund's rule coupling, in particular for the  $t_{2g}$  orbitals. The strong mass enhancements measured in both ARPES and dHvA experiments suggest sizable correlations of the size considered in this work. While electron-phonon effects have been reported[Kordyuk11] to be significant and contribute to the slightly higher mass enhancements measured experimentally, they alone cannot account for the large values observed. As for the Fermi surface, the correlations mainly affect the hole pockets that significantly change in size. We propose this as the source of the seeming discrepancy of the ARPES and dHvA experiments: whereas dHvA presumably observes only electron orbits with sizes close to their LDA values, ARPES finds the reduced size of the middle hole pocket as the most prominent feature. This way, the two experiments can be reconciled. The selective size reduction of the middle hole pocket also renders nesting less efficient.



# 8. Fermi Surface Topology of LaFePO and LiFeP

**J. Ferber**, H. O. Jeschke, and R. Valentí,  
Phys. Rev. Lett. **109**, 236403 (2012)

In this chapter, we study correlation effects on the Fermi surfaces of two more iron pnictides, LaFePO and LiFeP. We find a distinctive change in the topology of the Fermi surface in both compounds where a hole pocket with Fe  $d_{z^2}$  orbital character changes its geometry from a closed shape in LDA to an open shape upon inclusion of correlations. The opening of the pocket occurs in the vicinity of the  $\Gamma$  (Z) point in LaFePO (LiFeP). We discuss the relevance of these findings for the low superconducting transition temperature and the nodal gap observed in these materials.

## 8.1 Introduction

LaFePO is the iron pnictide in which superconductivity was reported for the first time at a critical temperature of about 6 K [Kamihara06]. In LaFePO superconductivity arises without doping or application of pressure, there is no long-range magnetic order [McQueen08], and the superconducting gap is nodal [Yamashita09, Fletcher09, Hicks09]. As a measure of electronic correlations, mass enhancement values have been reported by a number of different experiments including photoemission spectroscopy [Lu08], optical conductivity [Qazilbash09], dHvA [Coldea08], and specific heat measurements [Suzuki09]; all point to a range  $m^*/m_{\text{LDA}} \approx 1.7\text{-}2.2$ , consistent also with existing LDA+DMFT studies [Skornyakov10, Yin11].

Like LaFePO, LiFeAs exhibits superconductivity without doping or pressure at  $T_c = 18$  K and is nonmagnetic, see Sec. 7.1; furthermore, it cleaves between adjacent Li layers mitigating the issue of polar surfaces for surface-sensitive probes. LiFeP shares these properties, yet its lower superconducting transition temperature of 5 K [Deng09] did not trigger as much research. LiFeP shows contrasting behavior to LiFeAs in some respects, however. Most importantly, its superconducting order parameter is nodal [Hashimoto12] compared

to the nodeless gap in LiFeAs. This is unexpected as previous works suggested a relation between the lack of a third hole pocket at the  $\Gamma$  point and the formation of gap nodes [Kuroki09, Ikeda10, Thomale11, Hirschfeld11], but both LiFeAs and LiFeP show three hole sheets at  $\Gamma$ . Effective masses in LiFeP were extracted from resistivity and upper critical field measurements [Kasahara12], where the mass enhancements are estimated to be smaller by a factor of  $\sim 2$  compared to LiFeAs; this corresponds to a mass enhancement of 1.5-2 over the LDA value. De Haas-van Alphen experiments [Putzke12] report values 1.6-3.3 for the mass enhancements. So far no theoretical studies investigating the effects of correlations on LiFeP have been reported, though.

Thus, both compounds are considered rather weakly correlated. However, we argue in the following that the inclusion of correlations has a profound impact on the Fermi surface topology of both materials which in the case of LaFePO agrees with ARPES [Lu08] observations; for LiFeP, ARPES measurements are not yet reported and the available dHvA [Putzke12] data do not allow to decide unambiguously on the  $k_z$  extension of the Fermi surface sheets as will be discussed below. The features presented here have not been touched upon in the reported LDA+DMFT calculations on LaFePO [Skornyakov10, Yin11]; for LiFeP we present, to our knowledge, the first LDA+DMFT study in the literature.

## 8.2 Computational Details

As methodological improvement over the calculations presented in Ch. 7, we performed full charge self-consistent LDA+DMFT calculations as described in Sec. 5.2.4. We performed calculations on all available experimental structures as reported in Refs. [Kamihara06, McQueen08] (LaFePO) and Refs. [Deng09, Putzke12] (LiFeP) with space group  $P4/nmm$ . Results are shown for the structures from Ref. [Kamihara06] (LaFePO) and Ref. [Deng09] (LiFeP). The energy window for the construction of a localized Wannier basis was chosen to range from  $-5.4$  eV to  $2.7$  eV ( $-6$  eV to  $3.15$  eV) with respect to the Fermi energy for LaFePO (LiFeP). For an efficient and accurate determination of the impurity self energy we made use of recent improvements to the CT-HYB algorithm, namely the polynomial representation of the Green's functions [Boehnke11] and the improved estimators for the self energy [Hafermann12]. The Monte Carlo sampling was done at an inverse temperature  $\beta = 40$  eV $^{-1}$  with  $3 \times 10^6$  sweeps.

For the interaction parameters, we again use the definitions of  $U$  and  $J$  in terms of Slater integrals (B.13) with  $U = 4$  eV,  $J = 0.8$  eV, and the AMF double counting correction (2.38). Some low-energy features, in particular the size and shape of the Fermi hole pockets, which are of central interest here, turn out to be rather sensitive to details of the LDA+DMFT calculation like the choice of the double counting correction; however, we tested variations in these technical aspects and found the reported features –while being affected quantitatively– qualitatively consistent with calculations using the FLL double counting correction (2.37), as well as among different interaction parameters and reported crystal structures, see Sec. 8.3.1.

As in Chs. 4 and 7, orbital characters are labeled in a coordinate system which is  $45^\circ$  rotated with respect to the crystallographic axes.

## 8.3 Results

In Table 8.1 we list the orbital-resolved mass enhancements for both compounds. The mass enhancements for LaFePO are in line with the measured values  $\sim 1.7$ - $2.2$  from the various

experiments[Lu08, Qazilbash09, Coldea08, Suzuki09] as well as previous LDA+DMFT studies where mass enhancements  $\sim 1.6$ -2.2 were calculated[Skornyakov10, Yin11]. Note that for LaFePO the effective masses are higher for the  $e_g$  orbitals whereas in LiFeP, LiFeAs, and most other iron pnictides the  $t_{2g}$  orbitals show stronger renormalization. This is because of the crystal field splitting which in LaFePO puts the  $t_{2g}$  orbitals below the  $e_g$  orbitals, thereby promoting a ground state with configuration  $e_g^2 t_{2g}^4$  in the atomic limit. This suppresses inter-orbital fluctuations among the  $e_g$  states, rendering these orbitals more correlated in effect, cf. the discussion for LiFeAs in Sec. 7.3.1. As a consequence, the  $d_{z^2}$  orbital is the most strongly correlated one in LaFePO.

The values for LiFeP range between 1.4 and 1.7 which is roughly a factor of 2 smaller than in LiFeAs where ARPES[Borisenko10] and dHvA[Putzke12] experiments yield mass enhancements of 3-4. This is in agreement with resistivity and upper critical field measurements [Kasahara12] which also give a factor 2 reduction with respect to LiFeAs.

Table 8.1: Orbital-resolved mass enhancements  $m^*/m_{\text{LDA}}$ .

Orbital		$d_{z^2}$	$d_{x^2-y^2}$	$d_{xy}$	$d_{xz/yz}$
LaFePO:	$\frac{m^*}{m_{\text{LDA}}}$	1.85	1.70	1.54	1.69
LiFeP:	$\frac{m^*}{m_{\text{LDA}}}$	1.52	1.39	1.71	1.62

The momentum-resolved spectral function of the two materials is presented in Fig. 8.1 in comparison with the LDA band energies. The excitations around the Fermi energy are well-defined, revealing the Fermi liquid nature in accordance with resistivity measurements [Kasahara12]. Most importantly, both compounds feature a band placed just below the Fermi energy in LDA which gets shifted above  $E_F$  upon inclusion of correlations in the vicinity of the  $\Gamma$  ( $Z$ ) point in LaFePO (LiFeP). In both compounds this band has  $d_{z^2}$  orbital character around  $E_F$  for the path shown in Fig. 8.1 and originates from the hybridization with phosphorus  $p$  states.

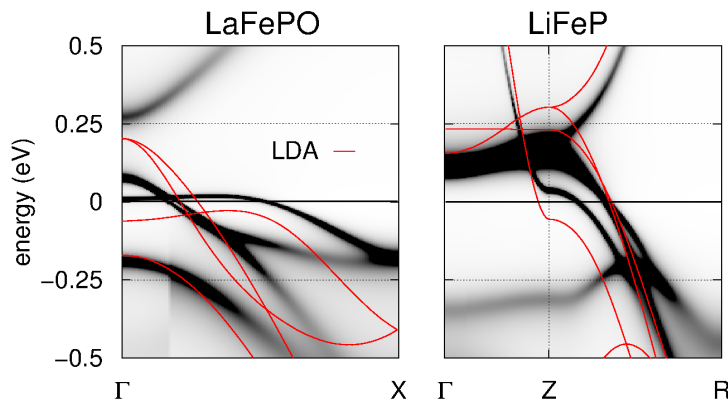


Figure 8.1: Momentum-resolved spectral function  $A(\mathbf{k}, \omega)$  together with LDA bands in the vicinity of the Fermi surface topology change.

As shown in Figs. 8.2 and 8.3, this crossing of the Fermi energy is naturally accompanied by the appearance of a hole pocket at the Fermi surface, an outer hole pocket centered at  $\Gamma$  in LaFePO (see Fig. 8.2(b)), and an inner hole pocket centered at  $Z$  in LiFeP (see Fig. 8.3(b)). As has been suggested[Kemper10] for the iron pnictides, the appearance of a pocket with  $d_{z^2}$  character may alter the superconducting pairing function to a nodal state

and reduce the strength of the pairing as it is observed in LaFePO and LiFeP in contrast to their arsenic counterparts LaFeAsO and LiFeAs.

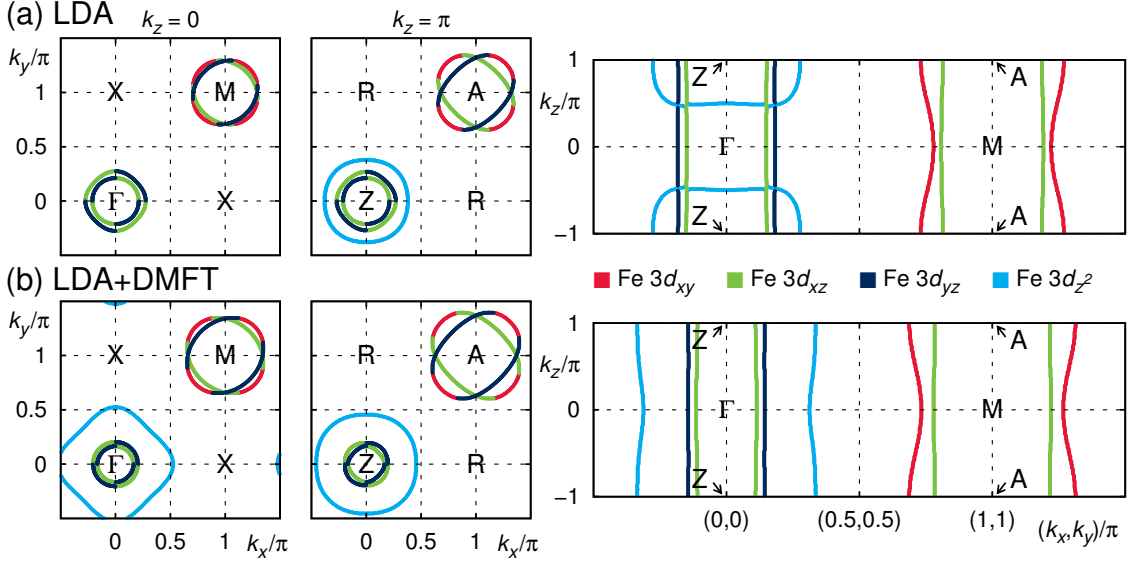


Figure 8.2: Fermi surfaces of LaFePO in the  $k_z = 0$  and  $k_z = \pi$  plane (left panels) and the  $k_x = k_y$  plane (right panels) for (a) LDA and (b) LDA+DMFT. The colors give the dominating orbital character.

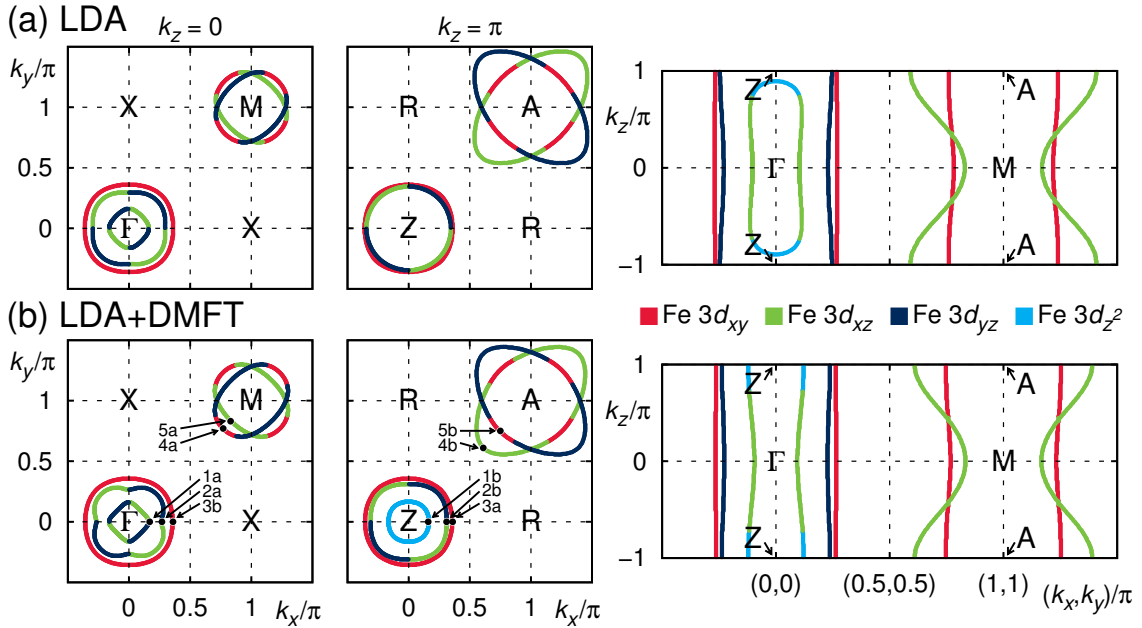


Figure 8.3: Fermi surfaces of LiFeP in the  $k_z = 0$  and  $k_z = \pi$  plane (left panels) and the  $k_x = k_y$  plane (right panels) for (a) LDA and (b) LDA+DMFT. The colors give the dominating orbital character. The arrows indicate the  $\mathbf{k}$ -points for the calculation of the effective masses in Tab. 8.2.

Due to the hybridization with the phosphorus states, the position of the crossing band in LDA is sensitive to the phosphorus  $z$  position and doping. Therefore, although the large outer hole pocket appearing in LaFePO has been observed in ARPES[Lu08], it has been suspected[Lu08, Coldea08] that the appearance of this pocket is caused by surface doping indicated by a too small electron count obtained in ARPES. In contrast, our calculations yield the change in the Fermi surface topology as a result of electronic correlations only. Note that the total charge in the crystal is conserved in our calculations and the opening of the pocket (*i.e.* increase of the Fermi surface volume) merely amounts to a charge transfer from the  $d_{z^2}$  orbital to the  $t_{2g}$  orbitals. Despite the sensitivity of the band position in LDA (for LaFePO the band energies differ by approx. 12 meV between the two published structures[Kamihara06, McQueen08]) we found the opening of the pocket in both structures and with very similar pocket sizes. As for the electron deficiency in ARPES, the huge size of the measured pocket ( $>12$  kT (kilotesla) as compared to  $<5$  kT in our calculations, cf. orbit 3a in Fig. 8.4(a)) probably still results from a charge effect.

As a result, the calculated dHvA frequencies for LaFePO experience significant shifts as shown in Fig. 8.4(a). The outer hole pocket experiences a large increase compared to LDA and the opening at  $Z$  adds a new frequency 3a for the minimal orbit. Because of charge conservation, the outer electron pocket 4a/b is also blown up. The enlargement of the electron pocket seen in our calculations is not observed in the dHvA experiment[Coldea08]. The hole pocket itself is not measured in dHvA (7 out of the 10 predicted frequencies are present in the measurements). In LDA, inclusion of spin-orbit (SO) coupling reduces the size of the inner hole pocket 1a/b but SO coupling is not included in our LDA+DMFT calculations. It is therefore likely that this pocket shrinks even more than predicted by us, thereby reducing the total Fermi surface volume enclosed by the hole pockets; this could approximately compensate for the added volume from the opened hole pocket without enlargement of the electron pocket.

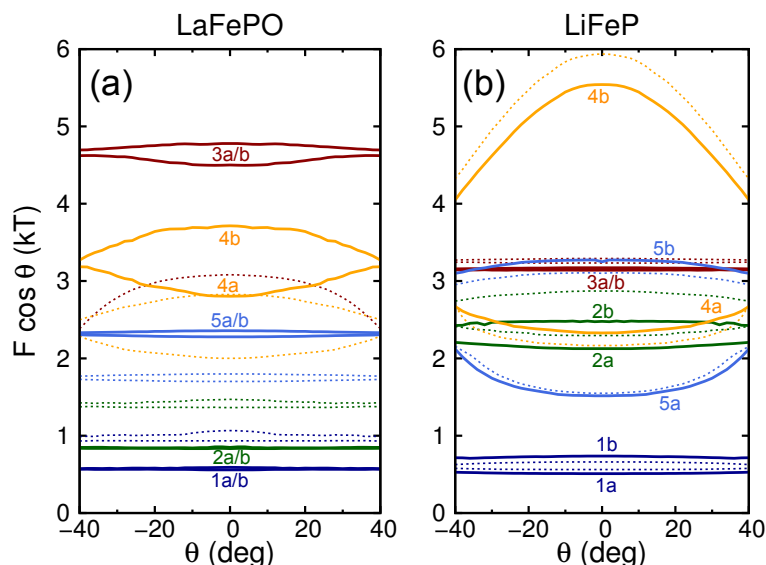


Figure 8.4: dHvA frequencies with respect to the magnetic field angle obtained within LDA (dashed thin lines) and LDA+DMFT (solid lines). Orbits 1, 2, and 3 refer to the inner, middle, and outer hole pocket, and orbits 4 and 5 to the outer and inner electron pocket, respectively.

For LiFeP, the inclusion of interactions induces only moderate changes in the sizes of the Fermi surface sheets, see Fig. 8.4(b). The frequency shifts with respect to LDA are in qualitative agreement with the experimental dHvA data from Ref. [Putzke12]: the middle hole pocket 2a/b shifts most and shrinks in size by approx. 0.39 kT (compared to approx. 0.95 kT in the experiment), and the other sheets are less affected (orbit 4b also shrinks substantially but it is not measured in dHvA). For comparison, in LiFeAs the inclusion of correlations leads to shifts up to 0.51 kT in LDA+DMFT (cf. orbit 2b in Fig. 7.6). This is another indication that LiFeP is less correlated than LiFeAs. However, due to the details of the band structure, the band generating the topology change in LiFeP stays below  $E_F$  in LiFeAs.

The opening of the inner hole pocket in LDA+DMFT has almost no effect on the dHvA frequencies: also in LDA, two frequencies for the inner hole pocket are expected due to a weak peanut-like distortion which gives a minimal orbit around  $\Gamma$  and a maximal orbit at  $k_z \approx \pi/2$ . In LDA+DMFT, the size of the pocket at  $Z$  (the new maximal orbit) essentially equals the maximal orbit size from LDA, thereby mimicking the LDA orbits. Since the position of the orbits in the BZ cannot be determined from dHvA, no clear distinction between the predictions from LDA and LDA+DMFT can be made from the published data. Measurements up to  $\theta = 90^\circ$  which, in principle, allow to differentiate between open and closed pockets ( $F \cos \theta$  drops to zero for a closed pocket) have been performed and indicate a tendency of  $F \cos \theta$  going towards small values but are not conclusive because of the very weak signal[C. Putzke, private communication].

While a good qualitative agreement is reached between our results and dHvA observations, our calculations do not lead to a sufficient shift to attain complete agreement with the experimental frequencies in LiFeP, in particular the calculated reduction of the middle hole pocket is not pronounced enough. Note that spin-orbit coupling helps with the size reduction of this pocket, but its effect is comparatively small here (about 0.2 kT). Limitations of our approach are also revealed by a comparison of the effective masses in LiFeP. The effective masses obtained from the dHvA measurements are rather uniform among all orbits except for the orbits 2a/b which show only half the mass enhancement of the other orbits. Since these mass enhancements refer to the Fermi surface orbits rather than the localized orbitals, we calculated the LDA+DMFT mass enhancements in the same basis by projecting the self energy in the localized Wannier basis  $|w_{\mathbf{k},m}\rangle$ ,  $\Sigma_{mm}$ , to the basis of Bloch states  $|\psi_{\mathbf{k},\nu}\rangle$ ,  $\Sigma_{\nu\nu'}(\mathbf{k})$ , according to Eq. (5.23),

$$\Sigma_{\nu\nu'}(\mathbf{k}, i\omega_n) = \sum_{mm'} P_{\nu m}^*(\mathbf{k}) \Sigma_{mm'}(i\omega_n) P_{\nu' m'}(\mathbf{k}), \quad (8.1)$$

where  $P_{\nu m}(\mathbf{k}) = \langle w_{\mathbf{k},m} | \psi_{\mathbf{k},\nu} \rangle$ . From the diagonal elements  $\Sigma_{\nu\nu}$  we obtain the mass enhancements of the respective Fermi surface pocket at the  $\mathbf{k}$ -points indicated in Fig. 8.3; the values are given in Table 8.2.

Table 8.2: Mass enhancements of the maximal/minimal Fermi surface orbits in LiFeP. The mass enhancements are measured at the  $\mathbf{k}$ -points indicated in Fig. 8.3.

orbit	1a/b	2a/b	3a/b	4a/b	5a/b
pocket	inner hole	middle hole	outer hole	outer electron	inner electron
$\frac{m^*}{m_{\text{LDA}}}$	1.47 / 1.34	1.48 / 1.47	1.69 / 1.70	1.49 / 1.46	1.52 / 1.37



The significantly smaller mass enhancements of the middle hole pocket (orbit 2) measured in the quantum oscillation experiments are not seen in LDA+DMFT. This suggests that this pocket is differently affected by the coupling to some scattering channel like spin fluctuations or nonlocal correlations which are not captured by our LDA+DMFT approach.

### 8.3.1 Sensitivity Analysis

In order to stress the robustness of our results with respect to variations in the computational details, we present in Fig. 8.5 results for different interaction parameters and different double counting corrections along the cuts where the predicted topological change occurs, *i.e.*  $k_z = 0$  ( $k_z = \pi$ ) for LaFePO (LiFeP). Smaller interactions as well as the change from AMF to FLL double counting both tend to reduce the opening of the respective pocket in both materials but only to a minor degree: the changes in the pocket sizes are small and the topology change is consistent among all calculations.

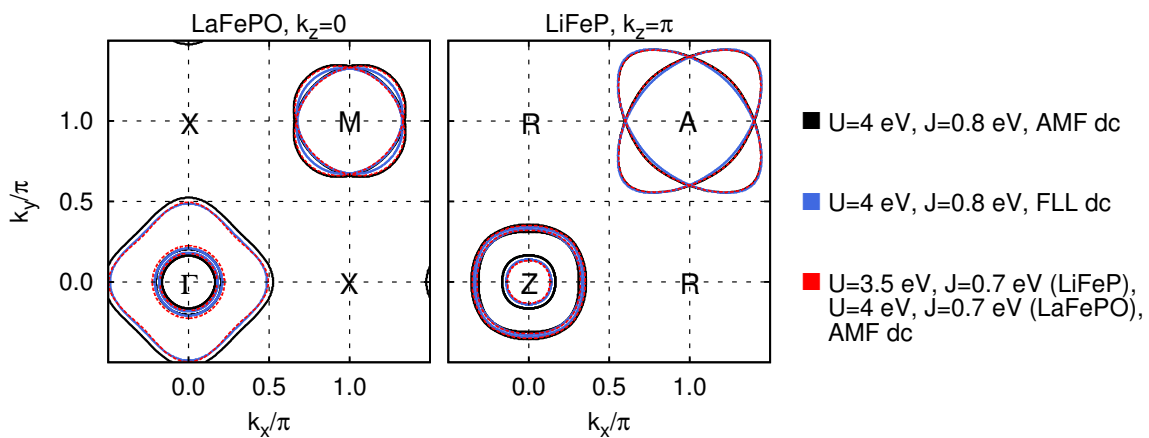


Figure 8.5: Effect of different values for the interaction parameters and different double counting corrections on the Fermi surfaces of LaFePO (LiFeP) at  $k_z = 0$  ( $k_z = \pi$ ).

## 8.4 Conclusions

In summary, we reported LDA+DMFT calculations on LaFePO and LiFeP and find a change of the Fermi surface topology upon inclusion of correlations in both compounds, namely the opening of an outer hole pocket at  $\Gamma$  in LaFePO and the opening of an inner hole pocket at  $Z$  in LiFeP, both with Fe  $d_{z^2}$  orbital character. As discussed by Kemper *et al.* [Kemper10], this might promote the nodal gap and weak pairing strength, *i.e.* low  $T_c$ , in these materials. Whereas this pocket has been observed in ARPES[Lu08] for LaFePO, the current experimental situation for LiFeP does not allow for a conclusive testing of our predictions and further experimental work is desired. Also we find that the peculiarities of the middle hole pocket in LiFeP observed in dHvA experiments but not reproduced in our LDA+DMFT approach reveal the importance of scattering channels beyond local correlations.



# 9. LDA+DMFT for molecular crystals: spectral and optical properties of $\kappa$ -(BEDT-TTF)<sub>2</sub>Cu[N(CN)<sub>2</sub>]Cl

J. Ferber, K. Foyevtsova, H. O. Jeschke, and R. Valentí,  
arXiv:1209.4466

In this chapter, we study correlation effects in an organic molecular crystal considering full molecular Wannier functions. For that purpose, we propose a scheme to construct molecular Wannier functions using atomic orbitals as a starting point. We compute spectral and optical properties of the layered charge-transfer (CT) salt  $\kappa$ -(BEDT-TTF)<sub>2</sub>Cu[N(CN)<sub>2</sub>]Cl and demonstrate from first principles that interdimer transitions are strongly affected by correlations –leading to a Hubbard peak in the optical conductivity– while intradimer transitions are uncorrelated, giving rise to a peak consistent with LDA predictions. We discuss our results in the context of reported infrared reflection measurements.

## 9.1 Introduction

An extensively studied class of CT salts (cf. Sec. 1.3) are based on the molecules bis-(ethylenedithio)tetrathiafulvalene (BEDT-TTF, or shorter ET) crystallized in the  $\kappa$  phase. In these  $\kappa$ -(ET)<sub>2</sub>X salts, electron donors (ET) and electron acceptors (X) form alternating layers, with two ET molecules facing each other in ET dimers; these dimers are arranged in a triangular lattice. For monovalent anions X one electron is transferred from each dimer (ET)<sub>2</sub> to each anion formula unit. In effect, the dimer layers possess one hole per dimer and their highest occupied molecular orbitals (HOMO) give rise to a half-filled conduction band. Hence, band structure calculations[Kandpal09, Nakamura09b] predict the dimer layers to be metallic. However, the experimentally observed ground state depends on the choice of the anion: even for the example of the isostructural compounds  $\kappa$ -(ET)<sub>2</sub>Cu[N(CN)<sub>2</sub>]Cl (in short  $\kappa$ -Cl) and  $\kappa$ -(ET)<sub>2</sub>Cu[N(CN)<sub>2</sub>]Br ( $\kappa$ -Br), the ground state

can be as different as a Mott insulator for  $\kappa$ -Cl and a Fermi liquid for  $\kappa$ -Br at low temperatures and ambient pressure.<sup>1</sup> In fact,  $\kappa$ -Cl can be driven through the insulator-to-metal transition (MIT) by the gradual substitution of Cl for isovalent Br, which changes the volume of the system and thereby decreases the ratio  $U/W$  of the Hubbard  $U$  to the band width  $W$ . Being close to the MIT,  $\kappa$ -Br is a ‘good’ (coherent) metal with a Drude peak only below a coherence temperature  $T^* \approx 50$  K. At higher temperatures  $\kappa$ -Cl is a semiconductor with a gap of  $E_g = 800$  K [Yasin11], while  $\kappa$ -Br shows ‘bad metal’ behavior with strong scattering preventing coherent transport and suppressing the Drude peak. Theoretically, this crossover from a Fermi liquid at low  $T$  to the ‘bad’ metal state at higher temperatures in  $\kappa$ -Br is obtained from DMFT calculations where gradual destruction of coherent quasiparticles occurs with increasing temperature [Merino00], albeit at higher  $T^*$  than observed experimentally.

The fact that small chemical modifications lead to qualitative changes in the behavior together with the importance of electronic correlations in these materials make it clear that a realistic description requires both (i) details of the band structure as well as (ii) a proper treatment of strong correlations. However, many body studies of the  $\kappa$ -(ET)<sub>2</sub> $X$  salts have so far been limited to minimal model calculations [Merino00, Parcollet04, Merino08] of the Hubbard or extended Hubbard Hamiltonian on an anisotropic triangular lattice [Powell06].

In this study, we go beyond model calculations, employing the LDA+DMFT framework introduced in Ch. 5 (in the ‘one-shot’ scheme). With this approach, the above requirements for a realistic description of these systems are fulfilled to a large extent. To our knowledge, this is the first LDA+DMFT calculation on an organic crystal considering full molecular HOMO Wannier functions. Specifically, we focus on the spectral and optical properties of  $\kappa$ -Cl at room temperature. While the kinetic part of the Hamiltonian is described with full DFT precision, we use a few values of the Hubbard interaction strength  $U$  in order to illuminate the effects of different  $U/W$  ratios. We will show that, whereas it is well known that the DMFT method does not yield a perfect description of the underlying Hubbard Hamiltonian on a triangular lattice in two dimensions, this approach provides insight into the contributions to the optical conductivity at an unprecedented level. Our calculations demonstrate that interdimer and intradimer transitions are responsible for two principal features observed in optical conductivity measurements at low temperatures and identify the interdimer feature to be related to correlations. These results corroborate previous conjectures based on phenomenological and minimal model assumptions [Faltermeier07, Dumm09].

## 9.2 Computational Details

While recent LDA+DMFT calculations on organic molecular crystals employed Wannier functions with a single atomic character [Weber12], the electronic structure of the CT salts requires the construction of localized Wannier functions from the full molecular HOMO orbital as presented in Sec. 5.2.2. The energy window  $\mathcal{W}$  for  $\kappa$ -Cl was chosen to range from  $-1.4$  eV to  $1.5$  eV with respect to the Fermi energy  $E_F$ , encompassing 44 bands in total. The real space representation of the resulting dimer HOMO Wannier function of  $\kappa$ -Cl (based on the crystal structure reported in Ref. [Williams90] with space group  $Pnma$ ) is shown in Fig. 9.1.

<sup>1</sup>Below 35 K,  $\kappa$ -(ET)<sub>2</sub>Cu[N(CN)<sub>2</sub>]Cl develops a weak magnetic order [Miyagawa95, Kanoda97] whereas  $\kappa$ -(ET)<sub>2</sub>Cu[N(CN)<sub>2</sub>]Br enters a superconducting state at  $T_c = 12$  K [Kini90]. We are not considering these very low temperature phases here.

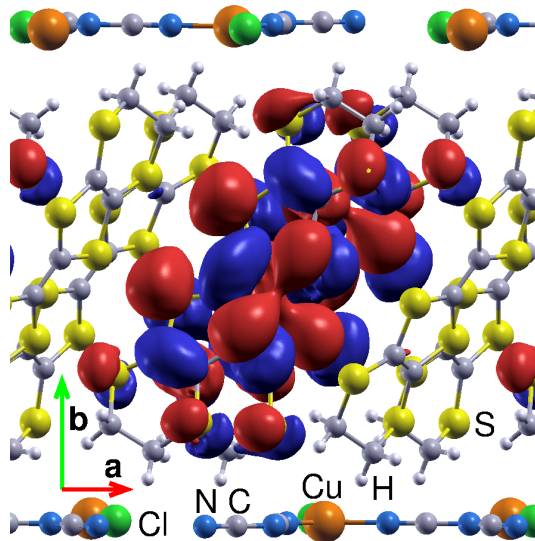


Figure 9.1: Structure of  $\kappa$ -(ET) $_2$ Cu[N(CN) $_2$ ]Cl seen along the  $c$  axis with a Wannier function corresponding to the bands crossing the Fermi level.

For solving the impurity problem we again employed the CT-HYB QMC solver described in Sec. 5.3, where we used  $2 \times 10^7$  Monte Carlo sweeps throughout our calculations at an inverse temperature  $\beta = 40 \text{ eV}^{-1}$ , corresponding to room temperature. Note that in the crystallographic unit cell, there is a manifold of four bands around  $E_F$  as the crystallographic unit cell contains two organic layers with a total of four dimers due to the presence of the anion. The dimers are equivalent, though, so that only one dimer HOMO has to be considered in our single-site DMFT; the other three orbitals are related by symmetry. Since the QMC algorithm operates on the imaginary frequency axis, the calculation of dynamical quantities like spectral functions and optical conductivity requires analytic continuation to the real axis. We performed stochastic analytic continuation on the self energy for obtaining the spectral functions and directly on the optical conductivity  $\sigma(i\Omega)$  for the calculation of optical properties.<sup>2</sup> Concerning appropriate interaction parameters for these systems, considerably distinct values for the Hubbard  $U$  have been reported. In this work we analyze the effect of the values  $U = 0.5/0.6/0.7/0.84 \text{ eV}$ . This range is guided by two estimates:  $U = 0.85 \text{ eV}$  obtained for a similar but arguably more strongly correlated compound  $\kappa$ -(ET) $_2$ Cu $_2$ (CN) $_3$  from constrained random phase approximation[Nakamura09b], and  $U \approx 0.27 \text{ eV}$  extracted from optical conductivity measurements[Faltermeier07] and model considerations[Merino08].

### 9.3 Results

In Fig. 9.2 we show the calculated band structure of  $\kappa$ -Cl in form of the momentum-resolved spectral function for  $U = 0.6 \text{ eV}$  along with the LDA band energies. The bands at the

<sup>2</sup>While we could have used the analytically continued self energy also for the calculation of  $\sigma(\omega)$  on the real axis, we chose to calculate  $\sigma(i\Omega)$  on the imaginary frequency axis and proceed with a subsequent analytic continuation for performance reasons: the summation over all elements of the four-index conductivity tensor along with the frequency convolution involved in the calculation of  $\sigma$  scales as  $N_b^4 \cdot N_f^2$  where  $N_b$  is the number of bands ( $N_b = 44$ ) and  $N_f$  the number of frequencies. While in imaginary frequencies  $N_f$  can be of the order of 100 at the temperature we considered, an accurate determination on the real frequency axis would require  $N_f \approx 1000$ . Due to the large number of bands involved in our calculations, this would make the direct real-frequency calculation of  $\sigma(\omega)$  rather expensive.

Fermi energy  $E_F = 0$  originate from the interdimer hopping, in particular hopping between dimers on the same layer; the interlayer hopping is very small, so that the four bands are composed of two almost degenerate pairs of bands. The correlation in band space acts almost exclusively on these bands, splitting them into renormalized excitations of (mass-enhanced) quasiparticles and a spectral weight transfer to an upper and lower Hubbard band which manifests itself as blurry background. On the other hand, the charge transfer between the ET molecules within a dimer (intradimer) induces the splitting between the bands right below the correlated manifold and the correlated bands. For the uncorrelated states, the excitations basically lie on top of the respective LDA energies which validates the accuracy of our analytic continuation.

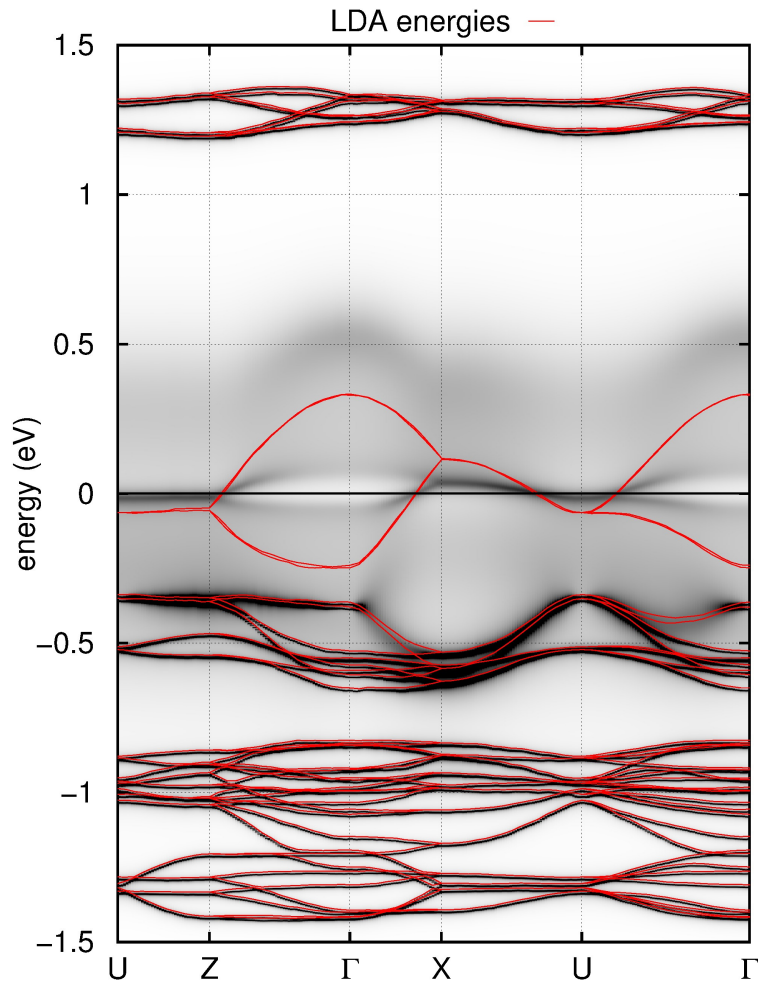


Figure 9.2: Momentum-resolved spectral function for  $U = 0.6$  eV.

The development of the Hubbard bands with  $U$  is visible from the momentum-integrated spectral functions in Fig. 9.3. At  $E_F$ , the spectral functions are suppressed compared to LDA, and Hubbard bands are formed for all values of  $U$ , getting more pronounced as  $U$  is increased; the maxima of the Hubbard peaks are located at  $\omega \approx \pm U/2$ , as expected. However, a quasiparticle peak at  $E_F$  remains present up to  $U = 0.7$  eV; the largest value of  $U$  shown,  $U = 0.84$  eV, is just on the verge of opening a gap at  $E_F$ . It is known, however, that the critical value of  $U$  for the MIT,  $U_c$ , is significantly overestimated by DMFT in low dimensions: for the triangular lattice in two dimensions as in our case, DMFT yields

$U_c \approx 15|t|$  [Merino08] whereas extrapolated cluster approximations [Sahebsara08] yield  $U_c \approx 7|t|$ .

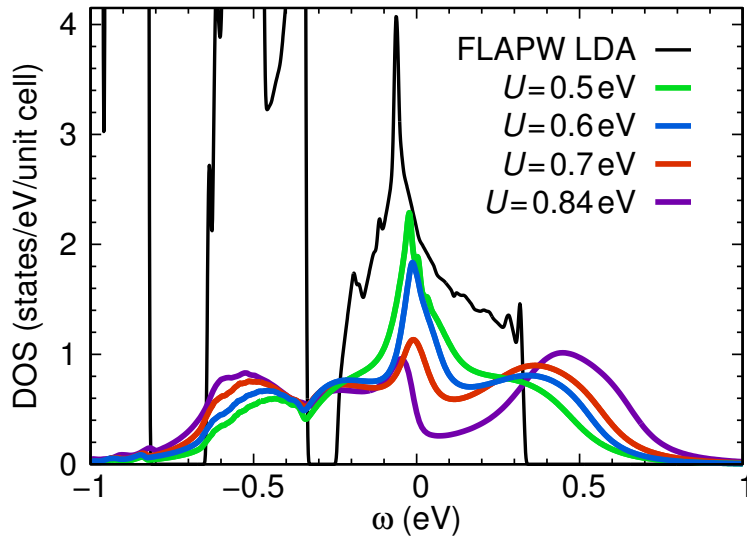


Figure 9.3: LDA density of states and the LDA+DMFT spectral functions for different values of  $U$ .

Next, we investigate the optical properties of  $\kappa$ -(ET) $_2$ Cu[N(CN) $_2$ ]Cl, where, like in previous works [Faltermeier07, Dumm09], we concentrate on the polarization  $E||c$ , *i.e.* along the linear chains in the triangular lattice. The authors of Ref. [Faltermeier07] performed a comprehensive study on the evolution of the optical conductivity spectra from infrared reflection measurements on  $\kappa$ -(ET) $_2$ Cu[N(CN) $_2$ ]Cl $_{1-x}$ Br $_x$  tuned through the MIT by increasing the Br concentration  $x$ . At room temperature, they observed a broad mid-infrared absorption peak between 1600  $\text{cm}^{-1}$  and 4200  $\text{cm}^{-1}$ , in agreement with previous optical studies on  $\kappa$ -Cl and  $\kappa$ -Br (see Ref. [Faltermeier07] and references therein). At low temperature, a Drude peak evolves for the compounds with high Br concentration which marks the onset of metallicity at  $x \approx 0.7$ , whereas no Drude peak is visible for lower Br content, indicating an insulating state without coherent quasiparticles.

Importantly, at low temperatures the broad mid-infrared peak splits into two peaks in the pure Cl and low Br concentration compounds, fitted by two Lorentzians at  $\approx 2200 \text{ cm}^{-1}$  and  $3200 \text{ cm}^{-1}$ ; for high Br content this splitting is very weak. From this doping dependence, it was concluded [Faltermeier07] that the first peak is a correlation-induced feature due to electron transitions between the lower and upper Hubbard bands, while the second ‘dimer peak’ was assigned to the intradimer charge transfer. For the metallic Br rich compounds, the spectral weight transfer from the Drude peak to the Hubbard peak is small and the Hubbard peak is suppressed or less pronounced. Since the Hubbard peak is expected to appear at  $\omega \approx U$ , this would determine the effective  $U$  as  $U \approx 2200 \text{ cm}^{-1} = 0.27 \text{ eV}$ .

Our method allows us to test this interpretation; as the energy window of our LDA+DMFT calculation contains both the correlated manifold at the Fermi energy as well as uncorrelated bands away from  $E_F$ , all transitions can be inspected on equal footing. As mentioned above, the symmetry of the organic layers is higher than the symmetry of the crystal; therefore the four bands around  $E_F$  can be considered to originate from one band which is folded due to the unit cell that is twice as large as required by the ET layer symmetry. These bands thus create the *intra*band contribution to the optical conductivity discussed in the

following; physically they correspond to the *interdimer* hopping. All other transitions are termed *interband* transitions; among others, these contain transitions related to the *intradimer* charge transfer.

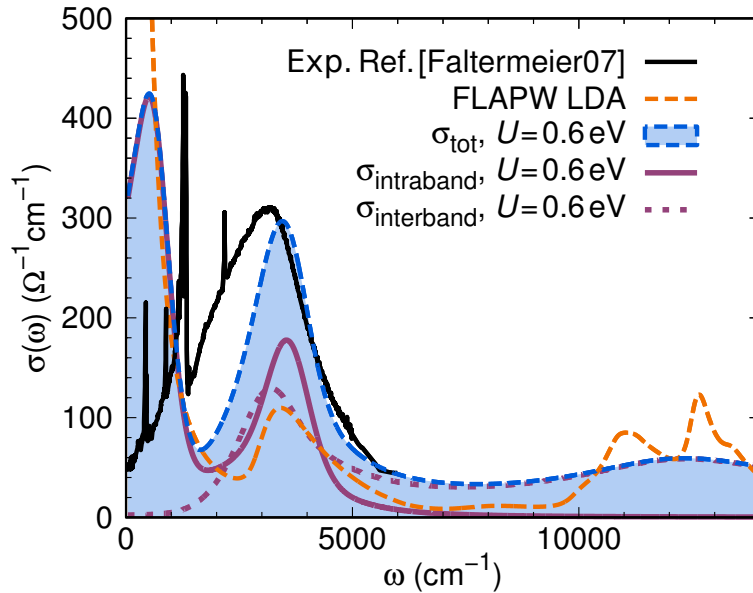


Figure 9.4: Calculated LDA+DMFT optical conductivity for  $U = 0.6$  eV together with the LDA result and the experimental curve at  $T = 300$  K.

The LDA+DMFT calculated optical conductivity for  $U = 0.6$  eV together with the experimentally measured spectrum of  $\kappa$ -Cl at  $T = 300$  K is shown in Fig. 9.4. Overall, the calculated total optical conductivity  $\sigma_{\text{tot}}$  features one dominant peak at approximately  $3450 \text{ cm}^{-1}$ , *i.e.* close to the experimental peak position (we do not consider vibronic modes)[Faltermeier07], and a second higher-frequency peak between  $8000 \text{ cm}^{-1}$  and  $17000 \text{ cm}^{-1}$ . The peak at higher frequencies originates from interband transitions between uncorrelated states and hence corresponds in frequency with LDA (also shown in the figure); the analytic continuation smears out the fine structure of this peak. The position of the low-frequency peak of  $\sigma_{\text{tot}}$  is roughly centered at the same position as the LDA results, but it is strongly enhanced in spectral weight, in accordance with experiment. While our calculations are at room temperature, they already capture the effects of correlation observed more pronounced in measurements at low  $T$ . Decomposed into intra- and interband contributions, we find that  $\sigma_{\text{interband}}$  roughly coincides with the LDA results in position and spectral weight. In addition, we find an intraband absorption at  $\omega \approx 3550 \text{ cm}^{-1} \approx 0.75U$  which we identify as intraband Hubbard transitions. While one expects a peak at  $\omega \approx U$  from transitions between the Hubbard bands, a  $U/2$  peak mixes in since a quasiparticle peak is still present in our calculations (for the chosen  $U = 0.6$  eV) and allows for transitions between the quasiparticle peak and the Hubbard bands. Accordingly, our data show a remnant of the Drude peak not observed experimentally for the pure Cl compound. The previously mentioned limitations of DMFT here force us in our choice of  $U$  values to make a compromise between the correct semiconducting phase (favored by a large  $U$ ) and the correct Hubbard peak position (favored by a moderate  $U$ ).



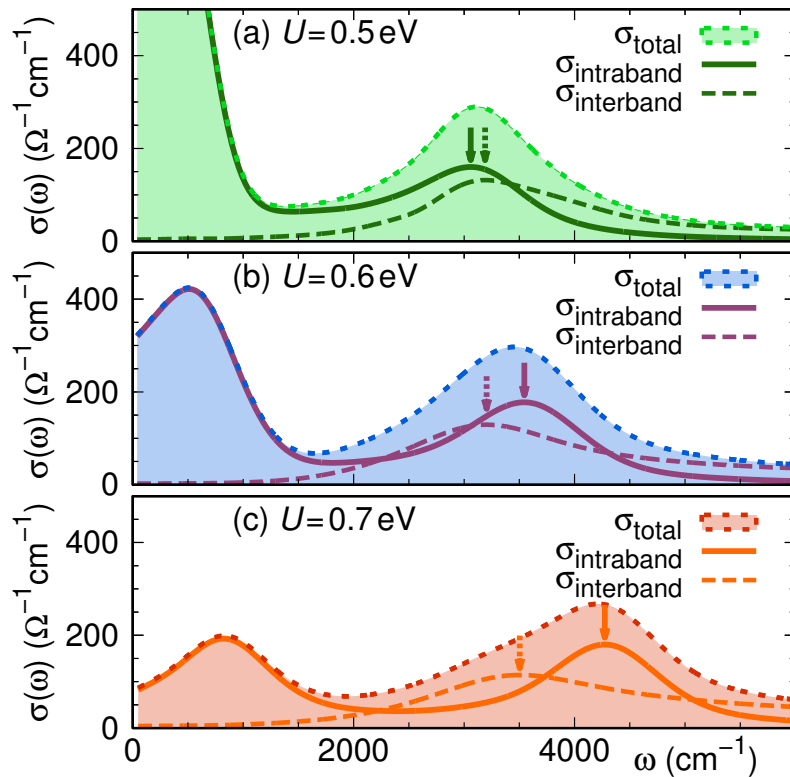


Figure 9.5: Optical conductivities for different values of  $U$ . The peak positions of the intraband (interband) contribution are:  $\omega \approx 3000$  ( $3200$ )  $\text{cm}^{-1}$  for  $U = 0.5$  eV,  $\omega \approx 3550$  ( $3200$ )  $\text{cm}^{-1}$  for  $U = 0.6$  eV, and  $\omega \approx 4250$  ( $3500$ )  $\text{cm}^{-1}$  for  $U = 0.7$  eV. The arrows show the respective peak positions.

As for the nature of the absorption peaks, Fig. 9.5 shows their evolution with  $U$ . The intraband contribution to the conductivity moves in frequency proportional to  $U$ , with the peak position consistently corresponding to  $\approx 0.75 U$  while the interband absorption is largely insensitive to  $U$ . This analysis demonstrates the correlated nature of  $\sigma_{\text{intraband}}$  and uncorrelated nature of  $\sigma_{\text{interband}}$ . In all cases, the two peaks are too close to each other to be individually resolved from the total optical conductivity alone. Furthermore, Fig. 9.5 shows how the Drude peak develops for decreasing  $U$  values; Fig. 9.5 (a) with  $U = 0.5$  eV is actually similar to the case of  $\kappa$ -Br as analyzed in Fig. 8 of Ref. [Faltermeier07].

Quantitatively, the suppression of the Drude peak as a function of  $U$  and the redistribution of the intraband spectral weight is presented in Fig. 9.6, where we follow Ref. [Merino08] and plot the integrated spectral weight  $\int_0^\omega \sigma_{\text{intraband}}(\omega') d\omega'$  representing the effective number of charge carriers  $N_{\text{eff}}$ . In this representation, the number of charge carriers in LDA by definition equals the number of conduction electrons, *i.e.* one, and all the weight is concentrated in the (infinitesimally narrow) coherent Drude peak which is only broadened by temperature. Upon inclusion of correlations, the kinetic energy of the electrons is diminished, which corresponds to mass enhancement (in Fermi liquid theory) or a reduction of the number of effective charge carriers.

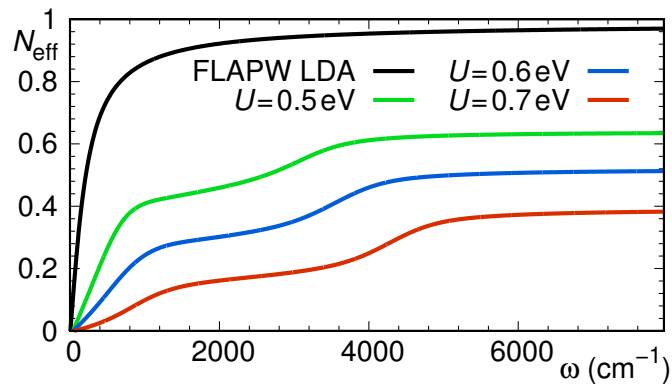


Figure 9.6: Distribution of the intraband spectral weight in terms of the effective number of charge carriers.

## 9.4 Conclusions

Summarizing the analysis of the optical conductivity calculations, we find agreement with the principal assessment of Ref. [Faltermeier07], namely that the two finite-frequency peaks in the experimental optical conductivity of  $\kappa$ -Cl at low temperatures originate, respectively, from correlation-induced intraband (interdimer) contributions (‘Hubbard peak’), scaling with  $U$ , and interband (intradimer) transitions which are unaffected by correlations (‘dimer peak’). The fact that DMFT overestimates the critical  $U$  of the triangular lattice in two dimensions forces us to describe  $\kappa$ -Cl with a somewhat high interaction strength of  $U = 0.6$  eV, suggesting that future studies combining LDA with many body techniques beyond DMFT like cluster extensions of DMFT [Lee12b] may further improve the quantitative agreement with experimental measurements. This is beyond the scope of the present work.

In conclusion, we presented the first LDA+DMFT study on the spectral and optical properties of the organic CT salt  $\kappa$ -(ET)<sub>2</sub>Cu[N(CN)<sub>2</sub>]Cl. Our results provide an *ab initio*-based theoretical evidence for the double-natured origin of the infrared peak in the optical conductivity of  $\kappa$ -(ET)<sub>2</sub>Cu[N(CN)<sub>2</sub>]Cl. We could identify intraband transitions within the correlated manifold and interband transitions due to charge-transfer within an ET dimer. The proposed projection method for constructing non-atom-centered Wannier functions in the LAPW framework is computationally efficient and can be applied to a great variety of correlated organic as well as inorganic systems with (quasi-)molecular orbitals.

## 10. Summary and Outlook

The effects of electronic correlations in real materials are multifaceted and often unanticipated. In this thesis, we have studied a range of correlated systems using different theoretical methods. While we found in Ch. 4 the optical and magnetic properties of different iron pnictides to be well reproduced within DFT –however at the cost of introducing a negative  $U$  parameter without intuitive physical meaning– the Fermi surfaces in the same family of materials can be subject to strong changes upon inclusion of correlations as discussed in Chs. 7 and 8. In fact, due to the interplay of different degrees of freedom in real materials, the details of the crystal structure and the numerical calculation matter, and even more so in the multiorbital systems investigated in this thesis. We therefore make the case for a transparent and careful analysis of the results and a routine test of their robustness with respect to computational details –like interaction parameters, the double counting correction, etc.–, as we have provided in Secs. 7.3.1 and 8.3.1. After all, while LDA+DMFT is a great conceptual leap forward from DFT, it misses some of the *ab-initio* character of DFT and thereby introduces some new potential pitfalls; this will likely become less of an issue as DMFT grows and matures.

For the iron pnictides, there exists moreover a great variability of the physical properties within the same family of materials. Sizable differences in the superconducting transition temperatures, nodal and nodeless superconductivity, presence and absence of magnetic ordering, and very different degrees of electronic correlation manifest this heterogeneity. In our studies, this is reflected *e.g.* by qualitative differences in the Fermi surface properties of LiFeAs and LiFeP: in both systems, the hole pockets of the Fermi surface are susceptible to correlations, but the topological change in the Fermi surface of LiFeP –as given by the opening of a hole pocket at the  $Z$  point in LDA+DMFT– is absent in LiFeAs.

We have also presented an LDA+DMFT calculation in the realm of molecular crystal systems, a field which has so far been accessible only by pure DFT or model calculations. This allowed us to perform a decomposition of the dominant mid-infrared peak in the optical spectrum into a correlation peak and a feature consistent with DFT predictions; the nature and assignment of this mid-infrared peak have been subject to discussion for many years.

For the future, we expect LDA+DMFT to be extended to even more classes of materials and to improve in terms of robustness, ease of use, and predictive power for the systems

to which it is already applied today. To that end, (i) controlled methods to account for screening effects in realistic settings have to be improved further to yield reliable estimates for the interaction parameters; (ii) DMFT extensions which (partially) reintroduce the  $\mathbf{k}$  dependence into the correlated problem have to make their way from the world of models to real materials; (iii) the form of the double counting correction, which is a source of ambiguity, may have to be reexamined; and (iv) other effects like spin-orbit coupling have to be incorporated consistently into the formalism. With these and other improvements, LDA+DMFT might one day take the role of the standard approach to electronic structure calculations that DFT constitutes today.

## A. Fourier Transforms and Expansion Coefficients

The representation of the impurity problem in the CT-HYB approach is formulated in imaginary time, *i.e.* the hybridization function  $F(\tau)$  is a function of  $\tau$ . The Dyson equation (5.19), however, is expressed (and is local) in the frequency domain. Therefore, a (discrete) Fourier transform is required,

$$G(\tau) = \frac{1}{\beta} \sum_{n=-\infty}^{\infty} e^{-i\omega_n \tau} G(i\omega_n), \quad (\text{A.1})$$

which we write here in the general form with an arbitrary Green's function  $G(\tau) = -\langle T_{\tau} c(\tau) c^{\dagger}(0) \rangle$ . This type of Fourier transform, which takes the form of a Matsubara sum, will be referred to as backward transform hereafter. From the fermionic commutation relations it follows that  $G(\tau)$  is antiperiodic,  $G(-\tau) = -G(\beta - \tau)$  (which is reflected by  $e^{-i\omega_n \beta} = -1$ ), and discontinuous at  $\tau = 0$ .

The opposite direction, *i.e.* the Fourier transform from imaginary time to Matsubara frequencies,

$$G(i\omega_n) = \int_0^{\beta} d\tau e^{i\omega_n \tau} G(\tau), \quad (\text{A.2})$$

can be avoided *e.g.* by the direct sampling of the Green's function [Haule07] or the self energy [Hafermann12] in frequency space or in another orthogonal basis which can be expanded into Matsubara frequencies [Boehnke11]. These recent techniques thereby avoid issues related to the discretization of the integral (A.2): although CTQMC is continuous in time conceptionally, in practice the sampled estimates for  $G(\tau)$  are binned into  $N$  bins on a discrete imaginary time grid (although the method allows for much larger  $N$  than *e.g.* Hirsch-Fye QMC due to different scaling with  $N$ ), which defines the Nyquist frequency  $\pi N/\beta$  as the maximal frequency that can be represented unambiguously by the binned samples. As  $\omega_n$  approaches (or exceeds) the Nyquist frequency, large aliasing errors in  $G(i\omega_n)$  arise which do not correspond to information contained in  $G(\tau)$ . In practice, this problem can be circumvented with good success by *e.g.* a spline interpolation of  $G(\tau)$ , exploiting the smoothness of  $G(\tau)$ . The integration is then done on the spline approximation, see Ref. [Blümer02] for details.

In contrast, an accurate evaluation of the backward transform (A.1) is essential not only for closing the selfconsistency equations but also for the calculation of occupations,  $\langle n \rangle = \langle T_\tau c^\dagger(0) c(0) \rangle = 1 + G(\tau = 0^+)$ , or convolutions of Green's functions as needed for the optical conductivity (3.37).

However, whereas the Matsubara sum, in principle, extends up to infinitely large frequencies, the numerical data is only given up to some finite frequency. In order to accurately reproduce *e.g.* the discrete jump of  $G(\tau)$  at  $\tau = 0$  (and thus the occupation), the inclusion of the high-frequency behavior is crucial.

The solution to this problem is to subtract the high-frequency tail—whose Fourier transform can be calculated exactly—from the Green's functions, and perform the numerical Fourier transform only on the remainder which falls off very quickly for large frequencies, so that the integration over the finite frequency range includes practically all the weight. After that, the analytically calculated Fourier transform of the tail and the result of the numerical Fourier transform of the remainder are combined again. To that end,  $G(i\omega_n)$  is expressed by a high-frequency expansion, starting from Eq. (A.2) and using integration by parts,

$$G(i\omega_n) = \int_0^\beta d\tau e^{i\omega_n\tau} G(\tau) = \sum_{k \geq 1} \frac{c_k}{(i\omega_n)^k}, \quad (\text{A.3})$$

with

$$c_k = (-1)^k \left( G^{(k-1)}(0) + G^{(k-1)}(\beta) \right), \quad (\text{A.4})$$

where  $G^{(k)}$  denotes the  $k$ -th derivative of  $G(\tau)$  with respect to  $\tau$ . In order to obtain expressions for the expansion coefficients  $c_k$ , one can employ the equations of motion technique to infer the derivatives in Eq. (A.4) from commutators and anticommutators of  $c$  and  $c^\dagger$  with the Hamiltonian governing the time evolution, in our case the Hubbard Hamiltonian; results are stated below.

Following the rules for the evaluation of fermionic Matsubara sums (see *e.g.* Ref. [Bruus04]), the Fourier transform of the basis functions  $\frac{1}{(i\omega_n)^k}$  of the high-frequency expansion can be evaluated analytically, with the first four orders being

$$\frac{1}{\beta} \sum_{n=-\infty}^{\infty} \frac{1}{i\omega_n} e^{-i\omega_n\tau} = -\frac{1}{2}, \quad (\text{A.5})$$

$$\frac{1}{\beta} \sum_{n=-\infty}^{\infty} \frac{1}{(i\omega_n)^2} e^{-i\omega_n\tau} = \frac{2\tau - \beta}{4}, \quad (\text{A.6})$$

$$\frac{1}{\beta} \sum_{n=-\infty}^{\infty} \frac{1}{(i\omega_n)^3} e^{-i\omega_n\tau} = \frac{\tau(\beta - \tau)}{4}, \quad (\text{A.7})$$

$$\frac{1}{\beta} \sum_{n=-\infty}^{\infty} \frac{1}{(i\omega_n)^4} e^{-i\omega_n\tau} = \frac{(\beta - 2\tau)(\beta^2 + 2\beta\tau - 2\tau^2)}{48}. \quad (\text{A.8})$$

In principle, higher orders can be calculated, but the corresponding expansion coefficients are typically not readily available, and the inclusion of higher order terms is quickly limited by machine precision; we will discuss these issues in the following.

Assuming known expansion coefficients  $c_k$ , the remainder which is to be Fourier transformed numerically is given by  $\tilde{G}(i\omega_n) = G(i\omega_n) - \sum_{k=1}^{k_{\max}} \frac{c_k}{(i\omega_n)^k}$ , and the total Fourier transform including the tails reads, *e.g.* for  $k_{\max} = 3$ ,

$$G(\tau) \approx -\frac{c_1}{2} + \frac{c_2(2\tau - \beta)}{4} + \frac{c_3\tau(\beta - \tau)}{4} + \frac{1}{\beta} \sum_{n=-N_{\max}}^{N_{\max}} \underbrace{\left( G(i\omega_n) - \frac{c_1}{i\omega_n} - \frac{c_2}{(i\omega_n)^2} - \frac{c_3}{(i\omega_n)^3} \right)}_{\tilde{G}(i\omega_n)} e^{-i\omega_n\tau}. \quad (\text{A.9})$$

By subtracting the first three terms of the high-frequency expansion, the remainder is guaranteed to fall off faster than  $\frac{1}{(i\omega_n)^3}$ , and a highly accurate Fourier transform can be computed even for moderate values of the cutoff  $N_{\max}$ . Note, however, that at low frequencies,  $\tilde{G}(i\omega_n)$  potentially takes on large absolute values with increasing tail expansion order: the  $k$ -th term in the high-frequency expansion at the lowest Matsubara frequency  $\omega_n = \frac{\pi}{\beta}$  reads  $\frac{c_k}{(i\pi)^k} \beta^k$  which for low temperatures (*e.g.*  $\beta = 100$ ) is large already for expansion order  $k \approx 6$  (in addition,  $c_k$  typically also gets bigger with increasing order). Hence, a new source for numerical errors is introduced when taking into account too many expansion orders; in our experience  $k_{\max} = 4$ -6 has proven to be a good compromise.

In practice, one only stores positive Matsubara frequencies of  $G(i\omega_n)$  and exploits its symmetry properties. For diagonal elements, *i.e.* if creation and annihilation operator act on the same flavor  $m$ , the real (imaginary) part of  $G_{mm}(i\omega_n)$  is symmetric (antisymmetric):  $\text{Re}[G_{mm}(i\omega_n)] = \text{Re}[G_{mm}(-i\omega_n)]$  and  $\text{Im}[G_{mm}(i\omega_n)] = -\text{Im}[G_{mm}(-i\omega_n)]$ . The backward transform (A.1) hence reads

$$G_{mm}(\tau) = \frac{1}{\beta} \sum_{n=-\infty}^{\infty} e^{-i\omega_n\tau} G_{mm}(i\omega_n) = \frac{2}{\beta} \sum_{n=0}^{\infty} \left( \text{Re}[G_{mm}(i\omega_n)] \cos \omega_n\tau + \text{Im}[G_{mm}(i\omega_n)] \sin \omega_n\tau \right), \quad (\text{A.10})$$

from which follows that  $G_{mm}(\tau)$  is purely real. This is a special case of the general relation  $G_{mm'}(-i\omega_n) = G_{m'm}^*(i\omega_n)$  which allows the contraction of the summation to positive frequencies also for offdiagonal elements  $m \neq m'$ ,

$$G_{mm'}(\tau) = \frac{1}{\beta} \sum_{n=0}^{\infty} \left( G_{mm'}(i\omega_n) e^{-i\omega_n\tau} + G_{m'm}^*(i\omega_n) e^{i\omega_n\tau} \right). \quad (\text{A.11})$$

For offdiagonal elements,  $G_{mm'}(\tau)$  is in general complex-valued.

In the following, we give results for the expansion coefficients of different objects on which Fourier transforms are performed in this work.

## A.1 Impurity Green's Function

For density-density interactions, the impurity Green's function  $G_{mm'}$  ( $m, m'$  being flavors, *i.e.* combined spin-orbital indices) is diagonal,  $G_{mm'} = G_m \delta_{mm'}$ , and the first three expansion coefficients for flavor  $m$  read

$$c_1^m = 1, \quad (\text{A.12})$$

$$c_2^m = \sum_{i \neq m} U_{mi} \langle n_i \rangle - \tilde{\mu}_m, \quad (\text{A.13})$$

$$c_3^m = \sum_{i, l \neq m} U_{mi} U_{ml} \left( \langle n_i n_l \rangle - \langle n_i \rangle \langle n_l \rangle \right) + (c_2^m)^2 + \langle \epsilon_m^2 \rangle - \langle \epsilon_m \rangle^2, \quad (\text{A.14})$$

with  $\tilde{\mu}_m$  according to Eq. (5.17),

$$\tilde{\mu}_m = \mu - \langle \epsilon_m \rangle, \quad (\text{A.15})$$

and

$$\langle \epsilon_m \rangle = \langle t_{mm} \rangle = \sum_{\mathbf{k}, \nu \nu'} P_{\nu m}(\mathbf{k}) H_{\nu \nu'}^0(\mathbf{k}) P_{\nu' m}^*(\mathbf{k}), \quad \langle \epsilon_m^2 \rangle = \sum_{\mathbf{k}, \nu \nu'} \left( P_{\nu m}(\mathbf{k}) H_{\nu \nu'}^0(\mathbf{k}) P_{\nu' m}^*(\mathbf{k}) \right)^2, \quad (\text{A.16})$$

being calculated from the LDA Hamiltonian  $H^0$ . These expansion coefficients are obtained using equations of motion with a Hubbard Hamiltonian including only density-density interactions[Comanac07]. The use of a Hubbard Hamiltonian is justified as in DMFT it can be identified with the corresponding (self-consistently determined) impurity Hamiltonian.

The occupations  $\langle n_i \rangle$  and occupation correlations  $\langle n_i n_l \rangle$  can be sampled directly in the QMC procedure. Higher order expansion coefficients require higher order correlations (starting with terms of the form  $\langle n_i n_l n_m \rangle$  for  $c_4$  *etc.*) which becomes exponentially expensive for multiorbital systems, however.

Note that for the special case of particle-hole symmetry, *e.g.* in the Bethe lattice, only the even moments of the energy are non-vanishing, and therefore  $\langle \epsilon \rangle = 0$ . In the Bethe lattice, the second moment is moreover related to the hopping,  $\langle \epsilon^2 \rangle = t^2$ .

## A.2 Impurity Self Energy

Upon selfconsistency, the impurity Green's function equals the local Green's function (5.20),

$$G_m(i\omega_n) = \sum_{\mathbf{k}, \nu \nu'} P_{\nu m}(\mathbf{k}) \left[ (i\omega_n + \mu) \delta_{\nu \nu'} - H_{\nu \nu'}^0(\mathbf{k}) - \sum_{m'} P_{\nu m'}^*(\mathbf{k}) \Sigma_{m'}(i\omega_n) P_{\nu' m'}(\mathbf{k}) \right]_{\nu \nu'}^{-1} P_{\nu' m}^*(\mathbf{k}), \quad (\text{A.17})$$

where we again only consider diagonal elements. This expression can be used to establish a relation between the expansion coefficients of the impurity self energy,

$$\Sigma_m(i\omega_n) = c_{0, \Sigma}^m + \frac{c_{1, \Sigma}^m}{i\omega_n} + \mathcal{O} \left( \frac{1}{(i\omega_n)^2} \right), \quad (\text{A.18})$$

and the expansion coefficients of  $G_m$  (A.12)-(A.14).



To that end we employ a recursion formula that relates the expansion coefficients of a function to the expansion coefficients of its inverse,

$$c_{\text{inv},k}^{\nu\nu'} = \begin{cases} (c_{k_{\text{min}}})_{\nu\nu'}^{-1} & \text{for } k = -k_{\text{min}} \\ -\sum_{ij} (c_{k_{\text{min}}})_{\nu i}^{-1} \sum_{p=-k_{\text{min}}}^{k-1} c_{\text{inv},p}^{ij} c_{k-p+k_{\text{min}}}^{j\nu'} & \text{for } k > -k_{\text{min}} \end{cases}, \quad (\text{A.19})$$

where we identify  $c_k$  with the expansion coefficients of the denominator [...] in Eq. (A.17) and  $c_{\text{inv},k}$  with the expansion coefficients of its inverse (the lattice Green's function), starting with  $k_{\text{min}} = -1$  (since the leading order of the denominator is  $i\omega_n$ ). The expansion of the local Green's function then reads

$$G_m(i\omega_n) = \frac{1}{i\omega_n} - \frac{\tilde{\mu}_m - \sum_{\mathbf{k},\nu\nu'} P_{\nu m}(\mathbf{k}) c_{0,\Sigma}^{\nu\nu'} P_{\nu' m}^*(\mathbf{k})}{(i\omega_n)^2} + \frac{\sum_{\mathbf{k},\nu\nu'} P_{\nu m}(\mathbf{k}) \left[ c_{1,\Sigma}^{\nu\nu'} + \left( \mu \delta_{\nu\nu'} - H_{\nu\nu'}^0(\mathbf{k}) - c_{0,\Sigma}^{\nu\nu'} \right)^2 \right] P_{\nu' m}^*(\mathbf{k})}{(i\omega_n)^3} + \mathcal{O}\left(\frac{1}{(i\omega_n)^4}\right), \quad (\text{A.20})$$

with the expansion coefficients of the lattice self energy

$$c_{k,\Sigma}^{\nu\nu'} = \sum_m P_{\nu m}^*(\mathbf{k}) c_{k,\Sigma}^m P_{\nu' m}(\mathbf{k}). \quad (\text{A.21})$$

Using the orthogonality of the projectors in orbital and band space,  $\sum_\nu P_{\nu m}(\mathbf{k}) P_{\nu' m}^*(\mathbf{k}) = \delta_{mm'}$  and  $\sum_m P_{\nu m}(\mathbf{k}) P_{\nu' m}^*(\mathbf{k}) = \delta_{\nu\nu'}$ , we obtain

$$\sum_{\nu\nu'} P_{\nu m}(\mathbf{k}) c_{k,\Sigma}^{\nu\nu'} P_{\nu' m}^*(\mathbf{k}) = c_{k,\Sigma}^m, \quad (\text{A.22})$$

therefore

$$G_m(i\omega_n) = \frac{1}{i\omega_n} - \frac{\tilde{\mu}_m - c_{0,\Sigma}^m}{(i\omega_n)^2} + \frac{c_{1,\Sigma}^m + \mu^2 - 2\mu\langle\epsilon_m\rangle + \langle\epsilon_m^2\rangle - 2\mu c_{0,\Sigma}^m + \sum_{\mathbf{k},\nu\nu'} P_{\nu m}(\mathbf{k}) \left( 2H_{\nu\nu'}^0(\mathbf{k}) c_{0,\Sigma}^{\nu\nu'} + (c_{0,\Sigma}^{\nu\nu'})^2 \right) P_{\nu' m}^*(\mathbf{k})}{(i\omega_n)^3} + \mathcal{O}\left(\frac{1}{(i\omega_n)^4}\right), \quad (\text{A.23})$$

which relates  $c_{0,\Sigma}^m$  to  $c_2^m$  as

$$c_{0,\Sigma}^m = c_2^m + \tilde{\mu}_m = \sum_{i \neq m} U_{mi} \langle n_i \rangle. \quad (\text{A.24})$$

Hence, the frequency-independent term of the self energy is simply the Hartree contribution. For equal orbitals, the relation for the next order is given by

$$c_{1,\Sigma}^m = c_3^m - (c_2^m)^2 - \langle\epsilon_m^2\rangle + \langle\epsilon_m\rangle^2 = \sum_{i,l \neq m} U_{mi} U_{ml} \left( \langle n_i n_l \rangle - \langle n_i \rangle \langle n_l \rangle \right). \quad (\text{A.25})$$

### A.3 Hybridization Function

For the hybridization function,

$$F_m(i\omega_n) = i\omega_n + \tilde{\mu}_m - [\mathcal{G}_0^{-1}(i\omega_n)]_m = i\omega_n + \tilde{\mu}_m - \Sigma_m(i\omega_n) - [G^{-1}(i\omega_n)]_m, \quad (\text{A.26})$$

the expansion coefficients are obtained using the recursion formula (A.19) on the coefficients of the local Green's function (A.23), starting with  $k_{\min} = 1$ ,

$$\begin{aligned} F_m(i\omega_n) &= i\omega_n + \tilde{\mu}_m - c_{0,\Sigma}^m - \frac{c_{1,\Sigma}^m}{i\omega_n} - \left\{ \frac{i\omega_n}{c_1^m} - \frac{c_2^m}{(c_1^m)^2} + \frac{(c_2^m)^2 - c_1^m c_3^m}{(c_1^m)^3 i\omega_n} \right\} + \mathcal{O}\left(\frac{1}{(i\omega_n)^2}\right) \\ &= \frac{-c_{1,\Sigma}^m - (c_2^m)^2 + c_3^m}{i\omega_n} + \mathcal{O}\left(\frac{1}{(i\omega_n)^2}\right) \\ &= \frac{\langle \epsilon_m^2 \rangle - \langle \epsilon_m \rangle^2 - (c_{0,\sigma}^m)^2 - 2\langle \epsilon_m \rangle c_{0,\sigma}^m + \sum_{\mathbf{k}, \nu\nu'} P_{\nu m}(\mathbf{k}) \left( 2H_{\nu\nu'}^0 c_{0,\Sigma}^{\nu\nu'} + (c_{0,\Sigma}^{\nu\nu'})^2 \right) P_{\nu'm}^*(\mathbf{k})}{i\omega_n} \\ &\quad + \mathcal{O}\left(\frac{1}{(i\omega_n)^2}\right), \end{aligned} \quad (\text{A.27})$$

which for equal orbitals simplifies to

$$F_m(i\omega_n) = \frac{\langle \epsilon_m^2 \rangle - \langle \epsilon_m \rangle^2}{i\omega_n} + \mathcal{O}\left(\frac{1}{(i\omega_n)^2}\right). \quad (\text{A.28})$$

### A.4 Lattice Green's Function

A backward Fourier transform of the lattice Green's function is required *e.g.* for the calculation of the charge density (5.44) to be fed back to the DFT code when performing full charge self-consistent calculations or for the determination of the total charge in the energy window  $\mathcal{W}$ , see Sec. 5.2.3.

The expansion coefficients for the lattice Green's function can be directly read off from Eq. (A.23) by upfolding to the band space, cf. Eq. (A.21), and are given in terms of the expansion coefficients of the impurity self energy (A.24)-(A.25) as

$$c_1^{\nu\nu'}(\mathbf{k}) = \delta_{\nu\nu'}, \quad (\text{A.29})$$

$$c_2^{\nu\nu'}(\mathbf{k}) = -\mu \delta_{\nu\nu'} + H_{\nu\nu'}^0(\mathbf{k}) + \sum_m P_{\nu m}^*(\mathbf{k}) c_{0,\Sigma}^m P_{\nu'm}(\mathbf{k}), \quad (\text{A.30})$$

$$c_3^{\nu\nu'}(\mathbf{k}) = \sum_m P_{\nu m}^*(\mathbf{k}) c_{1,\Sigma}^m P_{\nu'm}(\mathbf{k}) + (c_2^{\nu\nu'}(\mathbf{k}))^2. \quad (\text{A.31})$$

Note that in contrast to the diagonal cases above, the expansion coefficients (and Fourier transforms, *e.g.* charges) for offdiagonal elements  $\nu \neq \nu'$  are, in general, complex-valued.

### A.5 Convolution of Lattice Green's Functions

Eq. (3.42) can be cast into the form of a Fourier backward transform (A.1) with summation over a fermionic Matsubara frequency  $\omega_n$  and  $\tau \rightarrow 0$ ,

$$\tilde{\Pi}_{\nu''\nu'''}^{\nu\nu'}(\mathbf{k}, \Omega) = \frac{1}{\beta} \sum_{\omega_n} \tilde{\Pi}_{\nu''\nu'''}^{\nu\nu'}(\mathbf{k}, i\omega_n, \Omega), \quad (\text{A.32})$$

where

$$\begin{aligned}\tilde{\Pi}_{\nu''\nu'''}^{\nu\nu'}(\mathbf{k}, i\omega_n, \Omega) &= \lim_{\mathbf{q} \rightarrow 0} G_{\mathbf{k}+\mathbf{q}}^{\nu'\nu''}(i\omega_n + i\Omega) G_{\mathbf{k}}^{\nu'''\nu}(i\omega_n) \\ &= \left( \frac{c_1^{\nu'\nu''}(\mathbf{k})}{i\omega_n + i\Omega} + \frac{c_2^{\nu'\nu''}(\mathbf{k})}{(i\omega_n + i\Omega)^2} + \frac{c_3^{\nu'\nu''}(\mathbf{k})}{(i\omega_n + i\Omega)^3} + \dots \right) \left( \frac{c_1^{\nu'''\nu}(\mathbf{k})}{i\omega_n} + \frac{c_2^{\nu'''\nu}(\mathbf{k})}{(i\omega_n)^2} + \frac{c_3^{\nu'''\nu}(\mathbf{k})}{(i\omega_n)^3} + \dots \right).\end{aligned}\tag{A.33}$$

For the high-frequency expansion of  $\tilde{\Pi}(i\omega_n)$ , a Taylor expansion in  $x \equiv \frac{1}{i\omega_n}$  of the product of the two lattice Green's functions' expansions is performed and evaluated at  $x = 0$ ;  $\Omega$  is treated as a parameter.

As can be seen directly, the leading order in the expansion of  $\tilde{\Pi}(i\omega_n)$  is  $\frac{1}{(i\omega_n)^2}$ . The first four orders are given by

$$c_{1,\Pi}^{\nu'\nu''\nu'''\nu}(\mathbf{k}) = 0, \tag{A.34}$$

$$c_{2,\Pi}^{\nu'\nu''\nu'''\nu}(\mathbf{k}) = c_1^{\nu'\nu''}(\mathbf{k}) c_1^{\nu'''\nu}(\mathbf{k}), \tag{A.35}$$

$$c_{3,\Pi}^{\nu'\nu''\nu'''\nu}(\mathbf{k}, \nu_n) = c_1^{\nu'\nu''}(\mathbf{k}) c_2^{\nu'''\nu}(\mathbf{k}) + c_1^{\nu'''\nu}(\mathbf{k}) \left( c_2^{\nu'\nu''}(\mathbf{k}) - i\Omega c_1^{\nu'\nu''}(\mathbf{k}) \right), \tag{A.36}$$

$$\begin{aligned}c_{4,\Pi}^{\nu'\nu''\nu'''\nu}(\mathbf{k}, \nu_n) &= c_1^{\nu'''\nu}(\mathbf{k}) \left( -c_1^{\nu'\nu''}(\mathbf{k}) \Omega^2 - 2i\Omega c_2^{\nu'\nu''}(\mathbf{k}) + c_3^{\nu'\nu''}(\mathbf{k}) \right) \\ &\quad + c_2^{\nu'''\nu}(\mathbf{k}) \left( c_2^{\nu'\nu''}(\mathbf{k}) - i\Omega c_1^{\nu'\nu''}(\mathbf{k}) \right) + c_1^{\nu'\nu''}(\mathbf{k}) c_3^{\nu'''\nu}(\mathbf{k}).\end{aligned}\tag{A.37}$$

Note that when including *e.g.* the first three orders for the lattice Green's functions as in Eq. (A.33), the first four expansion orders of  $\tilde{\Pi}(i\omega_n)$  can be expressed exactly, whereas *e.g.* for the fifth order, terms like  $c_1^{\nu'\nu''} c_4^{\nu'''\nu}$  *etc.* enter.



## B. Interaction Matrix Elements for Multiorbital Systems

Both LDA+U and LDA+DMFT operate on a set of localized orbitals for which Coulomb interactions  $V^{ee}$  are to be taken into account beyond the local density approximation. Since  $V^{ee}$  is a symmetric and spin-independent two-particle operator, its matrix elements  $V_{mm''m'm'''}^{ee} = \langle m, m'' | V^{ee} | m', m''' \rangle$  in general depend on four (orbital) indices,

$$V^{ee} = \frac{1}{2} \sum_{mm''m'm'''}^{2\ell+1} \sum_{\sigma, \sigma'} \langle m, m'' | V^{ee} | m', m''' \rangle c_{m, \sigma}^\dagger c_{m', \sigma} c_{m'', \sigma'}^\dagger c_{m''', \sigma'} . \quad (\text{B.1})$$

For a one-orbital system like in Ch. 9, this contracts to

$$V^{ee} = \frac{U}{2} (n_\downarrow + n_\uparrow) + U n_\downarrow n_\uparrow , \quad (\text{B.2})$$

with  $U = V_{1111}^{ee}$ ; for multiorbital systems, one often distinguishes between terms with density-type interactions and the pair-hopping and spin-flip contributions. Density-type interactions occur between electrons on the same orbital,

$$H_{\text{intra}}^{\text{d-d}} = \frac{1}{2} \sum_{m, \sigma} V_{mmmm}^{ee} n_{m, \sigma} + \sum_m V_{mmmm}^{ee} n_{m, \downarrow} n_{m, \uparrow} , \quad (\text{B.3})$$

and between electrons on different orbitals with the same spin,

$$H_{\text{inter,ss}}^{\text{d-d}} = \sum_{m > m', \sigma} (V_{mm'mm'}^{ee} - V_{mm'm'm}^{ee}) n_{m, \sigma} n_{m', \sigma} + \sum_{m > m', \sigma} V_{mm'm'm}^{ee} n_{m, \sigma} , \quad (\text{B.4})$$

and different spin,

$$H_{\text{inter,ds}}^{\text{d-d}} = \sum_{m > m', \sigma} V_{mm'mm'}^{ee} n_{m, \sigma} n_{m', -\sigma} . \quad (\text{B.5})$$

The pair-hopping terms have the form

$$H_{\text{ph}} = - \sum_{m \neq m', \sigma} V_{mm'm'm'}^{ee} c_{m, \sigma}^\dagger c_{m', -\sigma}^\dagger c_{m', \sigma} c_{m, -\sigma} , \quad (\text{B.6})$$

and the spin-flip terms read

$$H_{\text{sf}} = - \sum_{m \neq m', \sigma} V_{mm'm'm}^{ee} c_{m,\sigma}^\dagger c_{m',-\sigma}^\dagger c_{m',\sigma} c_{m,-\sigma}. \quad (\text{B.7})$$

Note that the matrix element  $V_{mm'm'm}^{ee}$  appears both in Eqs. (B.4) and (B.7). Comparing Eqs. (B.4) and (B.5),  $V_{mm'm'm}^{ee}$  gives the energy difference between a configuration with parallel spins –which is favored for positive  $V_{mm'm'm}^{ee}$ – and a configuration with antiparallel spins. Similarly, the spin-flip term can be rewritten to

$$H_{\text{sf}} = -2 \sum_{m \neq m'} V_{mm'm'm}^{ee} \left( \hat{\mathbf{S}}_m \hat{\mathbf{S}}_{m'} + \frac{1}{4} \sum_{\sigma} n_{m,\sigma} \sum_{\sigma'} n_{m',\sigma'} \right), \quad (\text{B.8})$$

with spin operators  $\hat{\mathbf{S}} = (\hat{S}_x, \hat{S}_y, \hat{S}_z)^T$ . Also the spin-flip term thus induces a ferromagnetic coupling. The physical origin is the exchange coupling: with parallel alignment of the spins, the spin part of the two-electron state is symmetric. To enforce the antisymmetry of the state, the orbital wavefunctions are antisymmetric, minimizing the potential energy from the Coulomb interaction. In atomic physics, this manifests as Hund's rule, therefore  $V_{mm'm'm}^{ee}$  is called exchange or Hund's rule coupling and labeled with  $J$ ,  $J_{m,m'} \equiv V_{mm'm'm}^{ee}$ . Also, we set  $U_m \equiv V_{mmmm}^{ee}$ , in analogy to the one-orbital case. Typically, one imposes rotational invariance of the interaction Hamiltonian in orbital and spin space which eliminates the need for orbital-dependent double counting for which a reliable scheme has not been proposed yet. For degenerate orbitals, this fixes the parameters as  $U_m = U$ ,  $J_{m,m'} = J \forall m \neq m'$ , and  $V_{mm'mm'}^{ee} = U - 2J$ ,  $V_{mmmm'm'}^{ee} = J \forall m \neq m'$  [Kanamori63]; terms with three or four different orbital indices vanish. This so-called Kanamori scheme is often also used for non-degenerate orbitals.

In the Kanamori scheme, the interaction Hamiltonian has thus been parameterized by two numbers  $U$  and  $J$ . For our LDA+DMFT calculations, however, we choose a different parameterization in terms of Slater integrals  $F^k$  which reflects the symmetries of the orbitals, as outlined in the following where we follow Ref. [Liechtenstein95]. Eventually, we will again identify only two parameters  $U$  and  $J$ , albeit with a different definition. The two notations should not be confused.

To this end, we write the Coulomb interaction

$$\langle m, m'' | V^{ee} | m', m''' \rangle = \int d\mathbf{r}_1 \int d\mathbf{r}_2 \psi_m^*(\mathbf{r}_1) \psi_{m''}^*(\mathbf{r}_2) \frac{1}{|\mathbf{r}_1 - \mathbf{r}_2|} \psi_{m'''}(\mathbf{r}_2) \psi_{m'}(\mathbf{r}_1) \quad (\text{B.9})$$

as multipole expansion ( $\mathbf{r}_i = r_i(\sin \vartheta_i \cos \varphi_i, \sin \vartheta_i \sin \varphi_i, \cos \vartheta_i)$ ),

$$\frac{1}{|\mathbf{r}_1 - \mathbf{r}_2|} = \sum_{k=0}^{\infty} \frac{r_{<}^k}{r_{>}^{k+1}} \frac{4\pi}{2k+1} \sum_{q=-k}^k Y_{k,q}(\vartheta_2, \varphi_2) Y_{k,q}^*(\vartheta_1, \varphi_1), \quad (\text{B.10})$$

where  $r_{<} (r_{>})$  is the smaller (larger) of  $r_1$  and  $r_2$ .

Assuming a quasiatomic nature of the correlated orbitals,<sup>1</sup> the multipole functions (the complex spherical harmonics  $Y_{k,q}$  defined in Eq. (D.1)) are evaluated within an atomic

<sup>1</sup>Note that the definition of the correlated orbitals used in this work has pure angular momentum character (in the muffin tin sphere), cf. Eq. (5.33).

basis  $|n, \ell, m\rangle$  ( $n$  denoting the main quantum number,  $\ell$  the orbital quantum number, and  $m$  the magnetic quantum number), and one obtains

$$\langle m, m'' | V^{ee} | m', m''' \rangle = \sum_{k=0}^{2\ell} a_k(m, m', m'', m''') F^k, \quad (\text{B.11})$$

where

$$\begin{aligned} a_k(m, m', m'', m''') &= \frac{4\pi}{2k+1} \sum_{q=-k}^k \langle n, \ell, m | Y_{k,q} | n, \ell, m' \rangle \langle n, \ell, m'' | Y_{k,q}^* | n, \ell, m''' \rangle \\ &= \frac{4\pi}{2k+1} \sum_{q=-k}^k \langle n, \ell, m | Y_{k,q} | n, \ell, m' \rangle \langle n, \ell, m''' | Y_{k,q} | n, \ell, m'' \rangle, \end{aligned} \quad (\text{B.12})$$

with the Slater integrals

$$F^k = \int dr_1 r_1^2 \int dr_2 r_2^2 R_{n\ell}^2(r_1) \frac{r_1^k}{r_2^{k+1}} R_{n\ell}^2(r_2). \quad (\text{B.13})$$

The radial functions are

$$R_{n\ell}(r) = \sqrt{\left(\frac{2}{na_0}\right)^3 \frac{(n-\ell-1)!}{2n[(n+\ell)!]^3}} e^{-\rho/2} \rho^\ell L_{n-\ell-1}^{2\ell+1}(\rho), \quad (\text{B.14})$$

with the Bohr radius  $a_0$ , renormalized radial coordinate  $\rho = \frac{2r}{na_0}$ , and generalized Laguerre polynomial  $L$ .

The atomic orbitals read

$$\langle \mathbf{r} | n, \ell, m \rangle = R_{n\ell}(r) Y_{\ell,m}^{\text{real}}(\vartheta, \varphi). \quad (\text{B.15})$$

Here we use the real form of the spherical harmonics,  $Y_{\ell,m}^{\text{real}}$  in Eq. (D.4), which allows us to identify the  $m$  quantum number directly with the real (not complex) atomic orbitals. For the evaluation of the matrix elements in Eq. (B.12) only the angular part of the integrals needs to be calculated, since the radial part does not depend on  $m$  and is normalized,

$$\langle n, \ell, m | Y_{k,q} | n, \ell, m' \rangle = \int_{-\pi/2}^{\pi/2} d\vartheta \int_0^{2\pi} d\varphi \sin \vartheta Y_{\ell,m}^{\text{real}}(\vartheta, \varphi) Y_{k,q}(\vartheta, \varphi) Y_{\ell,m'}^{\text{real}}(\vartheta, \varphi). \quad (\text{B.16})$$

This can be separated into an integration over  $\varphi$ , which is a sum over integrals of the form

$$\int_0^{2\pi} d\varphi e^{-im\varphi} e^{iq\varphi} e^{im'\varphi} = 2\pi \delta_{q,m-m'}, \quad (\text{B.17})$$

and an integration over  $\vartheta$ ,

$$\begin{aligned} C(\ell, m) C(k, q) C(\ell, m') &\int_{-\pi/2}^{\pi/2} d\vartheta \sin \vartheta P_\ell^m(\cos \vartheta) P_k^q(\cos \vartheta) P_\ell^{m'}(\cos \vartheta) \\ &= C(\ell, m) C(k, q) C(\ell, m') \int_{-1}^1 dx P_\ell^m(x) P_k^q(x) P_\ell^{m'}(x), \end{aligned} \quad (\text{B.18})$$

which can be evaluated using the Gaunt formula.

That way, the interaction operator is parameterized in terms of the  $F^k$  and is by construction rotationally invariant. For  $d$  electrons,  $\ell = 2$ , and one needs  $F^0$  (monopole),  $F^2$  (quadrupole), and  $F^4$  (octupole). The definitions of  $U$  and  $J$  in terms of  $F^k$  vary; we adopt the most common definitions  $U = F^0$  and  $J = \frac{F^2+F^4}{14}$ , while the ratio  $\frac{F^4}{F^2} = 0.625$  is taken to be constant.

In our LDA+DMFT calculations, only the density-type terms are considered due to the design of the employed solver, cf. Sec. 5.3. The interaction Hamiltonian then takes the form

$$H^{d-d} = \sum_{m>m',\sigma} U_{mm'}^{\sigma,\sigma} n_{m,\sigma} n_{m',\sigma} + \frac{1}{2} \sum_{m,m',\sigma} U_{mm'}^{\sigma,-\sigma} n_{m,\sigma} n_{m',-\sigma}, \quad (\text{B.19})$$

where  $U_{mm'}^{\sigma,\sigma} = V_{mm'mm'}^{ee} - V_{mm'm'm}^{ee}$  and  $U_{mm'}^{\sigma,-\sigma} = V_{mm'mm'}$  from comparison with Eqs. (B.4) and (B.5). For the  $d$  shell,

$$V_{mm'mm'}^{ee} = b_0 F^0 + b_2 F^2 + b_4 F^4, \quad (\text{B.20})$$

$$V_{mm'm'm}^{ee} = c_0 F^0 + c_2 F^2 + c_4 F^4, \quad (\text{B.21})$$

where the coefficients are obtained from Eq. (B.18) using the Gaunt formula (order of orbitals  $d_{z^2}, d_{x^2-y^2}, d_{xy}, d_{xz}, d_{yz}$ ),

$$b_0 = \begin{pmatrix} 1 & 1 & 1 & 1 & 1 \\ 1 & 1 & 1 & 1 & 1 \\ 1 & 1 & 1 & 1 & 1 \\ 1 & 1 & 1 & 1 & 1 \\ 1 & 1 & 1 & 1 & 1 \end{pmatrix} b_2 = \frac{1}{49} \begin{pmatrix} 4 & -4 & -4 & 2 & 2 \\ -4 & 4 & 4 & -2 & -2 \\ -4 & 4 & 4 & -2 & -2 \\ 2 & -2 & -2 & 4 & -2 \\ 2 & -2 & -2 & -2 & 4 \end{pmatrix} b_4 = \frac{1}{49 \cdot 9} \begin{pmatrix} 36 & 6 & 6 & -24 & -24 \\ 6 & 36 & -34 & -4 & -4 \\ 6 & -34 & 36 & -4 & -4 \\ -24 & -4 & -4 & 36 & -4 \\ -24 & -4 & -4 & -4 & 36 \end{pmatrix} \quad (\text{B.22})$$

$$c_0 = \begin{pmatrix} 1 & 0 & 0 & 0 & 0 \\ 0 & 1 & 0 & 0 & 0 \\ 0 & 0 & 1 & 0 & 0 \\ 0 & 0 & 0 & 1 & 0 \\ 0 & 0 & 0 & 0 & 1 \end{pmatrix} c_2 = \frac{1}{49} \begin{pmatrix} 4 & 4 & 4 & 1 & 1 \\ 4 & 4 & 0 & 3 & 3 \\ 4 & 0 & 4 & 3 & 3 \\ 1 & 3 & 3 & 4 & 3 \\ 1 & 3 & 3 & 3 & 4 \end{pmatrix} c_4 = \frac{1}{49 \cdot 9} \begin{pmatrix} 36 & 15 & 15 & 30 & 30 \\ 15 & 36 & 35 & 20 & 20 \\ 15 & 35 & 36 & 20 & 20 \\ 30 & 20 & 20 & 36 & 20 \\ 30 & 20 & 20 & 20 & 36 \end{pmatrix}. \quad (\text{B.23})$$

The Slater  $U$  and  $J$  can be recovered from these reduced matrices  $U_{mm'}^{\sigma,\sigma}$  and  $U_{mm'}^{\sigma,-\sigma}$  via

$$U = \frac{1}{(2\ell+1)^2} \sum_{mm'} U_{mm'}^{\sigma,-\sigma}, \quad J = U - \frac{1}{2\ell(2\ell+1)} \sum_{m \neq m'} U_{mm'}^{\sigma,\sigma}, \quad (\text{B.24})$$

thus  $U$  ( $J$ ) is just the spherically averaged (*i.e.* averaged over all possible pairs  $m, m'$ ) matrix element  $V_{mm'mm'}^{ee}$  ( $V_{mm'm'm}^{ee}$ ). This allows to find a parameterization for interaction matrices reported *e.g.* from constrained RPA which are in general not spherically averaged. By following the procedure outlined above, the values for  $U$  and  $J$  obtained from Eq. (B.24) should be used to calculate the corresponding spherically averaged interactions, thereby avoiding orbital-dependent double counting.



## C. Calculation of Observables in LDA+DMFT

LDA+DMFT is a complex method which –besides its known assumptions and approximations– involves many little tweaks and modifications. As a consequence, the results of different LDA+DMFT calculations with the same setup, despite being intended to deliver identical results, typically show differences on a quantitative level. For the sake of transparency, we briefly summarize our method of calculating the observables discussed in this thesis. We expect convergence in the treatment of these technical details as LDA+DMFT matures and gets more established as the method of choice for many materials.

### C.1 Spectral Functions

For the spectral functions, we chose the analytic continuation of the self energy rather than the direct analytic continuation of the Green’s function, see Sec. 6.3 for details. Following the analytic continuation and the determination of the real part using Kramers-Kronig analysis, the self energy  $\Sigma_{mm'}(\omega)$  is projected onto the band (Bloch) basis to obtain the (retarded) lattice Green’s function in the real frequency domain,

$$[G^R(\mathbf{k}, \omega)^{-1}]_{\nu\nu'} = (\omega + i\eta + \mu)\delta_{\nu\nu'} - H_{\nu\nu'}^0(\mathbf{k}) - \sum_{mm'} P_{\nu m}^*(\mathbf{k}) \Sigma_{mm'}(\omega) P_{\nu' m'}(\mathbf{k}), \quad (\text{C.1})$$

where we used Wick rotation  $i\omega_n \rightarrow \omega + i\eta$  compared to Eq. (5.24). The spectral function as obtained from Eq. (C.1),  $A(\mathbf{k}, \omega) = -\frac{1}{\pi} \sum_{\nu} \text{Im} G_{\nu\nu}^R(\mathbf{k}, \omega)$ , is used directly for plots of the interacting band structure as *e.g.* in Fig. 9.2, or (after  $\mathbf{k}$  summation) as interacting equivalent to the total density of states, cf. Fig. 9.3.

For plots of (integrated) orbital-resolved quantities, *e.g.* Fig. 7.1, the spectral function of the respective local Green’s function is presented,

$$G_{mm}^R(\omega) = \sum_{\mathbf{k}, \nu\nu'} P_{\nu m}(\mathbf{k}) G_{\nu\nu'}^R(\mathbf{k}, \omega) P_{\nu' m}^*(\mathbf{k}). \quad (\text{C.2})$$

## C.2 Mass Enhancements

The mass enhancements are inferred from the self energy on the Matsubara axis,

$$m^*/m_{\text{LDA}} = 1 - \left. \frac{\partial \text{Im} \Sigma(i\omega)}{\partial \omega} \right|_{\omega \rightarrow 0^+}, \quad (\text{C.3})$$

where the derivative is extracted by fitting a fourth-order polynomial to the data for the lowest six Matsubara frequencies. This avoids uncertainties from the analytic continuation to the real frequency domain.

## C.3 Fermi Surfaces and de Haas-van Alphen Frequencies

The same polynomial as for the mass enhancements is used for the determination of the Fermi surfaces where we make use of the fact that the imaginary and real axes meet at zero,  $\Sigma(\omega = 0) \equiv \Sigma(i\omega = 0)$ . Inserting  $\Sigma(\omega = 0)$  into Eq. (C.1),  $A(\mathbf{k}, \omega = 0)$  is determined which –assuming  $\text{Im} \Sigma(\omega = 0) = 0$  for a Fermi liquid– diverges if  $\mathbf{k}$  lies on the Fermi surface and is zero otherwise. In practice, a finite imaginary part of the self energy, *i.e.* a finite broadening, is applied, reflecting the finite resolution of the  $\mathbf{k}$  mesh. The maximum of the resulting smooth spectral function is tracked through the Brillouin zone and defines the Fermi surface. The dominating orbital character at the respective  $\mathbf{k}$  points is taken from the comparison of the respective orbital-resolved spectral functions.

For the determination of the dHvA frequencies, the projections of the Fermi surface pockets along a given vector in the BZ are searched for the maximal cross-sectional area with a maximization algorithm based on the golden section search, where the area is approximated as the area of a polygon which has the  $\mathbf{k}$  points of the respective Fermi surface as corners.

A fine  $\mathbf{k}$  mesh is required for the accurate determination of Fermi surfaces and dHvA frequencies: we use a square lattice with 162,408 (20,301 in the irreducible wedge)  $\mathbf{k}$  points for plots in the  $k_x/k_y$  plane as *e.g.* in Fig. 7.4, and a cubic lattice with –depending on the actual crystal structure–  $\sim 1,000,000$  ( $\sim 100,000$  in the irreducible wedge)  $\mathbf{k}$  points for the determination of dHvA frequencies.

## C.4 Optical Conductivities

For the calculation of the optical conductivities presented in Ch. 9, we perform the convolution of the one-particle Green's functions in Matsubara frequencies as given in Eq. (3.42) where the optical matrix elements are taken from WIEN2K.

As Eqs. (3.37) and (3.42) take the canonical form of a Fourier backward transform (A.1) with summation over a fermionic Matsubara frequency  $\omega_n$  and  $\tau \rightarrow 0$ , the same techniques for the tail approximation can be applied, see Sec. A.5.

For the analytic continuation of the optical conductivity in imaginary (bosonic) frequencies, we used the stochastic maximum entropy method, see Secs. 6.2 and 6.4 for details.

In practice, the summation over momenta in Eq. (3.42) is performed in the irreducible Brillouin zone only and therefore needs to be supplemented by a symmetrization procedure

akin to Eq. (5.38). For the optical conductivity, the symmetrization acts on the product of the optical matrix elements  $v_\alpha^{\nu\nu'} v_\beta^{\nu''\nu'''}$  (for brevity, we drop the momentum and spin index in the following).

Let  $O_i$  ( $i = 1, \dots, N_s$ ) denote the real-space symmetry operation matrices (as opposed to symmetrization matrices  $\mathcal{O}$  in orbital space). Then, in terms of  $v_{\alpha,i}^{\nu\nu'}$ ,

$$\begin{pmatrix} v_{x,i}^{\nu\nu'} \\ v_{y,i}^{\nu\nu'} \\ v_{z,i}^{\nu\nu'} \end{pmatrix} = O_i \begin{pmatrix} v_x^{\nu\nu'} \\ v_y^{\nu\nu'} \\ v_z^{\nu\nu'} \end{pmatrix}, \quad (\text{C.4})$$

the symmetrized products are given as

$$\{v_\alpha^{\nu\nu'} v_\alpha^{\nu''\nu'''}\}^{\text{symm}} = \frac{1}{N_s} \sum_i v_{\alpha,i}^{\nu\nu'} v_{\alpha,i}^{\nu''\nu'''} , \quad (\text{C.5})$$

and

$$\{v_\alpha^{\nu\nu'} v_\beta^{\nu''\nu'''}\}^{\text{symm}} = \frac{1}{N_s} \sum_i \begin{cases} v_{\alpha,i}^{\nu\nu'} v_{\beta,i}^{\nu''\nu'''} & \text{if } \det(O_i) = 1 \\ (v_{\alpha,i}^{\nu\nu'} v_{\beta,i}^{\nu''\nu'''})^* & \text{if } \det(O_i) = -1 \end{cases} \quad (\text{C.6})$$

for different  $\alpha$  and  $\beta$ . Note that unlike in Eq. (5.38), the symmetrization cannot be performed after the  $\mathbf{k}$  summation because of the complex conjugation in Eq. (C.6).



## D. Spherical Harmonics

In this appendix, we collect some useful relations for the evaluation of expressions containing spherical harmonics.

The complex spherical harmonics are given by

$$Y_{\ell,m}(\vartheta, \varphi) = C(\ell, m) P_{\ell}^m(\cos \vartheta) e^{im\varphi}, \quad (\text{D.1})$$

with the associated Legendre polynomials  $P_{\ell}^m$  and a normalization constant

$$C(\ell, m) = \sqrt{\frac{2\ell+1}{4\pi} \frac{(\ell-m)!}{(\ell+m)!}}. \quad (\text{D.2})$$

The spherical harmonics are orthonormal,

$$\int_{\vartheta=0}^{\pi} \int_{\varphi=0}^{2\pi} Y_{\ell,m} Y_{\ell',m'}^* d\Omega = \delta_{\ell\ell'} \delta_{mm'}. \quad (\text{D.3})$$

A real form can be defined by

$$Y_{\ell,m}^{\text{real}} = \begin{cases} \frac{1}{\sqrt{2}} (Y_{\ell,m} + (-1)^m Y_{\ell,-m}) = \sqrt{2} C(\ell, m) P_{\ell}^m(\cos \vartheta) \cos(m\varphi) & \text{if } m > 0 \\ Y_{\ell,0} & \text{if } m = 0 \\ \frac{1}{i\sqrt{2}} (Y_{\ell,-m} - (-1)^m Y_{\ell,m}) = \sqrt{2} C(\ell, -m) P_{\ell}^{-m}(\cos \vartheta) \sin(m\varphi) & \text{if } m < 0 \end{cases}. \quad (\text{D.4})$$

For the evaluation of optical matrix elements in the LAPW basis, the following relations are useful:

$$e^{+i\varphi} \sin \vartheta Y_{\ell,m} = F_{\ell,m}^{(1)} Y_{\ell+1,m+1} + F_{\ell,m}^{(2)} Y_{\ell-1,m+1}, \quad (\text{D.5})$$

$$e^{-i\varphi} \sin \vartheta Y_{\ell,m} = F_{\ell,m}^{(3)} Y_{\ell+1,m-1} + F_{\ell,m}^{(4)} Y_{\ell-1,m-1}, \quad (\text{D.6})$$

$$\cos \vartheta Y_{\ell,m} = F_{\ell,m}^{(5)} Y_{\ell+1,m} + F_{\ell,m}^{(6)} Y_{\ell-1,m}, \quad (\text{D.7})$$

$$e^{+i\varphi} \left( \cos \vartheta \frac{\partial}{\partial \vartheta} + \frac{i}{\sin \vartheta} \frac{\partial}{\partial \varphi} \right) Y_{\ell,m} = -l F_{\ell,m}^{(1)} Y_{\ell+1,m+1} + (l+1) F_{\ell,m}^{(2)} Y_{\ell-1,m+1}, \quad (\text{D.8})$$

$$e^{-i\varphi} \left( \cos \vartheta \frac{\partial}{\partial \vartheta} - \frac{i}{\sin \vartheta} \frac{\partial}{\partial \varphi} \right) Y_{\ell,m} = -l F_{\ell,m}^{(3)} Y_{\ell+1,m-1} + (l+1) F_{\ell,m}^{(4)} Y_{\ell-1,m-1}, \quad (\text{D.9})$$

$$-\sin \vartheta \frac{\partial}{\partial \vartheta} Y_{\ell,m} = -l F_{\ell,m}^{(5)} Y_{\ell+1,m} + (l+1) F_{\ell,m}^{(6)} Y_{\ell-1,m}, \quad (\text{D.10})$$

where the  $F$ 's are given by:

$$F_{\ell,m}^{(1)} = -\sqrt{\frac{(\ell+m+1)(\ell+m+2)}{(2\ell+1)(2\ell+3)}}, \quad (\text{D.11})$$

$$F_{\ell,m}^{(2)} = \sqrt{\frac{(\ell-m)(\ell-m-1)}{(2\ell-1)(2\ell+1)}}, \quad (\text{D.12})$$

$$F_{\ell,m}^{(3)} = \sqrt{\frac{(\ell-m+1)(\ell-m+2)}{(2\ell+1)(2\ell+3)}}, \quad (\text{D.13})$$

$$F_{\ell,m}^{(4)} = -\sqrt{\frac{(\ell+m)(\ell+m-1)}{(2\ell-1)(2\ell+1)}}, \quad (\text{D.14})$$

$$F_{\ell,m}^{(5)} = \sqrt{\frac{(\ell-m+1)(\ell+m+1)}{(2\ell+1)(2\ell+3)}}, \quad (\text{D.15})$$

$$F_{\ell,m}^{(6)} = \sqrt{\frac{(\ell-m)(\ell+m)}{(2\ell-1)(2\ell+1)}}. \quad (\text{D.16})$$

# Bibliography

- [Aichhorn09] M. Aichhorn, L. Pourovskii, V. Vildosola, M. Ferrero, O. Parcollet, T. Miyake, A. Georges and S. Biermann. *Phys. Rev. B* **80**, 085101 (2009).
- [Aichhorn10] M. Aichhorn, S. Biermann, T. Miyake, A. Georges and M. Imada. *Phys. Rev. B* **82**, 064504 (2010).
- [Aichhorn11] M. Aichhorn, L. Pourovskii and A. Georges. *Phys. Rev. B* **84**, 054529 (2011).
- [Allan12] M. P. Allan, A. W. Rost, A. P. Mackenzie, Yang Xie, J. C. Davis, K. Kihou, C. H. Lee, A. Iyo, H. Eisaki and T.-M. Chuang. *Science* **336**, 563–567 (2012).
- [Ambrosch-Draxl06] C. Ambrosch-Draxl and J. O. Sofo. *Comp. Phys. Commun.* **175**, 1 – 14 (2006).
- [Andersen75] O. K. Andersen. *Phys. Rev. B* **12**, 3060–3083 (1975).
- [Andersen00] O. K. Andersen. Electronic Structure and Physical Properties of Solids. Lecture Notes in Physics Springer, New York (2000).
- [Anisimov91] V. I. Anisimov, J. Zaanen and O. K. Andersen. *Phys. Rev. B* **44**, 943–954 (1991).
- [Anisimov93] V. I. Anisimov, I. V. Solovyev, M. A. Korotin, M. T. Czyżyk and G. A. Sawatzky. *Phys. Rev. B* **48**, 16929–16934 (1993).
- [Anisimov97] V. I. Anisimov, F. Aryasetiawan and A. I. Lichtenstein. *J. Phys.: Condens. Matter* **9**, 767 (1997).
- [Anisimov05] V. I. Anisimov, D. E. Kondakov, A. V. Kozhevnikov, I. A. Nekrasov, Z. V. Pchelkina, J. W. Allen, S.-K. Mo, H.-D. Kim, P. Metcalf, S. Suga, A. Sekiyama, G. Keller, I. Leonov, X. Ren and D. Vollhardt. *Phys. Rev. B* **71**, 125119 (2005).
- [Anisimov09] V. I. Anisimov, Dm. M. Korotin, M. A. Korotin, A. V. Kozhevnikov, J. Kuneš, A. O. Shorikov, S. L. Skornyakov and S. V. Streltsov. *J. Phys.: Condens. Matter* **21**, 075602 (2009).
- [Arai01] T. Arai, K. Ichimura, K. Nomura, S. Takasaki, J. Yamada, S. Nakatsuji and H. Anzai. *Phys. Rev. B* **63**, 104518 (2001).
- [Beach04] K. S. D. Beach. arXiv:cond-mat/0403055 (2004).

- [Bethe31] H. Bethe. *Z. Phys.* **71**, 205–226 (1931).
- [Blaha01] P. Blaha, K. Schwarz, G. K. H. Madsen, D. Kvasnicka and J. Luitz. *WIEN2k, An Augmented Plane Wave + Local Orbitals Program for Calculating Crystal Properties*. Techn. Universität Wien, Austria (2001).
- [Blümer02] N. Blümer. Ph.D. thesis, Universität Augsburg (2002).
- [Boehnke11] L. Boehnke, H. Hafermann, M. Ferrero, F. Lechermann and O. Parcollet. *Phys. Rev. B* **84**, 075145 (2011).
- [Borisenko10] S. V. Borisenko, V. B. Zabolotnyy, D. V. Evtushinsky, T. K. Kim, I. V. Morozov, A. N. Yaresko, A. A. Kordyuk, G. Behr, A. Vasiliev, R. Follath and B. Büchner. *Phys. Rev. Lett.* **105**, 067002 (2010).
- [Bruus04] H. Bruus and K. Flensberg. *Many-body quantum theory in condensed matter physics: an introduction*. Oxford University Press (2004).
- [Bryan90] R. Bryan. *Eur. Biophys. J.* **18**, 165–174 (1990).
- [Brydon11] P. M. R. Brydon, M. Daghofer, C. Timm and J. van den Brink. *Phys. Rev. B* **83**, 060501(R) (2011).
- [Bulla98] R. Bulla, A. C. Hewson and Th. Pruschke. *J. Phys.: Condens. Matter* **10**, 8365 (1998).
- [Caffarel94] M. Caffarel and W. Krauth. *Phys. Rev. Lett.* **72**, 1545–1548 (1994).
- [Capelle06] K. Capelle. *Brazilian Journal of Physics* **36**, 1318 – 1343 (2006).
- [Ceperley80] D. M. Ceperley and B. J. Alder. *Phys. Rev. Lett.* **45**, 566–569 (1980).
- [Chao77] K. A. Chao, J. Spalek and A. M. Oles. *Journal of Physics C: Solid State Physics* **10**, L271 (1977).
- [Chen10] Z. G. Chen, R. H. Yuan, T. Dong and N. L. Wang. *Phys. Rev. B* **81**, 100502(R) (2010).
- [Chu10] J.-H. Chu, J. G. Analytis, D. Press, K. De Greve, T. D. Ladd, Y. Yamamoto and I. R. Fisher. *Phys. Rev. B* **81**, 214502 (2010).
- [Coldea08] A. I. Coldea, J. D. Fletcher, A. Carrington, J. G. Analytis, A. F. Bangura, J.-H. Chu, A. S. Erickson, I. R. Fisher, N. E. Hussey and R. D. McDonald. *Phys. Rev. Lett.* **101**, 216402 (2008).
- [Comanac07] A. Comanac. Ph.D. thesis, Columbia University (2007).
- [Cricchio10] F. Cricchio, O. Grånäs and L. Nordström. *Phys. Rev. B* **81**, 140403(R) (2010).
- [Cruz08] C. de la Cruz, Q. Huang, J. W. Lynn, J. Li, W. Ratcliff, J. L. Zarestky, H. A. Mook, G. F. Chen, J. L. Luo, N. L. Wang and P. Dai. *Nature* **453**, 899–902 (2008).



- [Czyżyk94] M. T. Czyżyk and G. A. Sawatzky. Phys. Rev. B **49**, 14211–14228 (1994).
- [Deng09] Z. Deng, X. C. Wang, Q. Q. Liu, S. J. Zhang, Y. X. Lv, J. L. Zhu, R. C. Yu and C. Q. Jin. Europhys. Lett. **87**, 37004 (2009).
- [Dongen94a] P. G. J. van Dongen. Phys. Rev. B **50**, 14016–14031 (1994).
- [Dongen94b] P. G. J. van Dongen. Phys. Rev. B **49**, 7904–7915 (1994).
- [Drechsler08] S.-L. Drechsler, M. Grobosch, K. Koepernik, G. Behr, A. Köhler, J. Werner, A. Kondrat, N. Leps, C. Hess, R. Klingeler, R. Schuster, B. Büchner and M. Knupfer. Phys. Rev. Lett. **101**, 257004 (2008).
- [Dumm09] M. Dumm, D. Faltermeier, N. Drichko, M. Dressel, C. Mézière and P. Batail. Phys. Rev. B **79**, 195106 (2009).
- [Dusza11] A. Dusza, A. Lucarelli, F. Pfuner, J.-H. Chu, I. R. Fisher and L. Degiorgi. Europhys. Lett. **93**, 37002 (2011).
- [Faltermeier07] D. Faltermeier, J. Barz, M. Dumm, M. Dressel, N. Drichko, B. Petrov, V. Semkin, R. Vlasova, C. Mézière and P. Batail. Phys. Rev. B **76**, 165113 (2007).
- [Fletcher09] J. D. Fletcher, A. Serafin, L. Malone, J. G. Analytis, J.-H. Chu, A. S. Erickson, I. R. Fisher and A. Carrington. Phys. Rev. Lett. **102**, 147001 (2009).
- [Fuchs10] S. Fuchs, Th. Pruschke and M. Jarrell. Phys. Rev. E **81**, 056701 (2010).
- [Georges92a] A. Georges and G. Kotliar. Phys. Rev. B **45**, 6479–6483 (1992).
- [Georges92b] A. Georges and W. Krauth. Phys. Rev. Lett. **69**, 1240–1243 (1992).
- [Georges96] A. Georges, G. Kotliar, W. Krauth and M. J. Rozenberg. Rev. Mod. Phys. **68**, 13 (1996).
- [Gorshunov10] B. Gorshunov, D. Wu, A. A. Voronkov, P. Kallina, K. Iida, S. Haindl, F. Kurth, L. Schultz, B. Holzapfel and M. Dressel. Phys. Rev. B **81**, 060509(R) (2010).
- [Gull08a] E. Gull. Ph.D. thesis, ETH Zürich (2008).
- [Gull08b] E. Gull, P. Werner, O. Parcollet and M. Troyer. Europhys. Lett. **82**, 57003 (2008).
- [Gull11] E. Gull, A. J. Millis, A. I. Lichtenstein, A. N. Rubtsov, M. Troyer and P. Werner. Rev. Mod. Phys. **83**, 349–404 (2011).
- [Gunnarsson10] O. Gunnarsson, M. W. Haverkort and G. Sangiovanni. Phys. Rev. B **82**, 165125 (2010).
- [Hafermann12] H. Hafermann, K. R. Patton and P. Werner. Phys. Rev. B **85**, 205106 (2012).

- [Han09] M. J. Han, Q. Yin, W. E. Pickett and S. Y. Savrasov. *Phys. Rev. Lett.* **102**, 107003 (2009).
- [Hansmann10] P. Hansmann, R. Arita, A. Toschi, S. Sakai, G. Sangiovanni and K. Held. *Phys. Rev. Lett.* **104**, 197002 (2010).
- [Harris67] A. Brooks Harris and Robert V. Lange. *Phys. Rev.* **157**, 295–314 (1967).
- [Hashimoto12] K. Hashimoto, S. Kasahara, R. Katsumata, Y. Mizukami, M. Yamashita, H. Ikeda, T. Terashima, A. Carrington, Y. Matsuda and T. Shibauchi. *Phys. Rev. Lett.* **108**, 047003 (2012).
- [Haule07] K. Haule. *Phys. Rev. B* **75**, 155113 (2007).
- [Haule08] K. Haule, J. H. Shim and G. Kotliar. *Phys. Rev. Lett.* **100**, 226402 (2008).
- [Haule09] K. Haule and G. Kotliar. *New J. Phys.* **11**, 025021 (2009).
- [Haule10] K. Haule, C.-H. Yee and K. Kim. *Phys. Rev. B* **81**, 195107 (2010).
- [Held01] K. Held, A. K. McMahan and R. T. Scalettar. *Phys. Rev. Lett.* **87**, 276404 (2001).
- [Held07] K. Held. *Adv. Phys.* **56**, 829 (2007).
- [Hettler98] M. H. Hettler, A. N. Tahvildar-Zadeh, M. Jarrell, T. Pruschke and H. R. Krishnamurthy. *Phys. Rev. B* **58**, 7475(R) (1998).
- [Hicks09] C. W. Hicks, Th. M. Lippman, M. E. Huber, J. G. Analytis, J.-H. Chu, A. S. Erickson, I. R. Fisher and K. A. Moler. *Phys. Rev. Lett.* **103**, 127003 (2009).
- [Hirsch86] J. E. Hirsch and R. M. Fye. *Phys. Rev. Lett.* **56**, 2521–2524 (1986).
- [Hirschfeld11] P. J. Hirschfeld, M. M. Korshunov and I. I. Mazin. *Rep. Prog. Phys.* **74**, 124508 (2011).
- [Hohenberg64] P. Hohenberg and W. Kohn. *Phys. Rev.* **136**, B864–B871 (1964).
- [Hu08] W. Z. Hu, J. Dong, G. Li, Z. Li, P. Zheng, G. F. Chen, J. L. Luo and N. L. Wang. *Phys. Rev. Lett.* **101**, 257005 (2008).
- [Huang08] Q. Huang, Y. Qiu, Wei Bao, M. A. Green, J. W. Lynn, Y. C. Gasparovic, T. Wu, G. Wu and X. H. Chen. *Phys. Rev. Lett.* **101**, 257003 (2008).
- [Ikeda10] H. Ikeda, R. Arita and J. Kuneš. *Phys. Rev. B* **81**, 054502 (2010).
- [Ishida09] K. Ishida, Y. Nakai and H. Hosono. *J. Phys. Soc. Jpn.* **78**, 062001 (2009).
- [Ishida10] H. Ishida and A. Liebsch. *Phys. Rev. B* **81**, 054513 (2010).
- [Jarrell92] M. Jarrell. *Phys. Rev. Lett.* **69**, 168–171 (1992).

- [Jarrell96] M. Jarrell and J. E. Gubernatis. *Physics Reports* **269**, 133 – 195 (1996).
- [Jesche08] A. Jesche, N. Caroca-Canales, H. Rosner, H. Borrmann, A. Ormezi, D. Kasinathan, H. H. Klauss, H. Luetkens, R. Khasanov, A. Amato, A. Hoser, K. Kaneko, C. Krellner and C. Geibel. *Phys. Rev. B* **78**, 180504(R) (2008).
- [Johnston10] D. C. Johnston. *Adv. Phys.* **59**, 803–1061 (2010).
- [Kajueter96] H. Kajueter and G. Kotliar. *Phys. Rev. Lett.* **77**, 131–134 (1996).
- [Kamihara06] Y. Kamihara, H. Hiramatsu, M. Hirano, R. Kawamura, H. Yanagi, T. Kamiya and H. Hosono. *J. Am. Chem. Soc.* **128**, 10012–10013 (2006).
- [Kamihara08] Y. Kamihara, T. Watanabe, M. Hirano and H. Hosono. *J. Am. Chem. Soc.* **130**, 3296–3297 (2008).
- [Kanamori63] J. Kanamori. *Prog. Theor. Phys.* **30**, 275–289 (1963).
- [Kandpal09] H. C. Kandpal, I. Opahle, Y.-Z. Zhang, H. O. Jeschke and R. Valentí. *Phys. Rev. Lett.* **103**, 067004 (2009).
- [Kaneko08] K. Kaneko, A. Hoser, N. Caroca-Canales, A. Jesche, C. Krellner, O. Stockert and C. Geibel. *Phys. Rev. B* **78**, 212502 (2008).
- [Kanoda97] K. Kanoda. *Physica C* **282-287**, 299 – 302 (1997).
- [Kanoda11] K. Kanoda and R. Kato. *Annu. Rev. Condens. Matter Phys.* **2**, 167–188 (2011).
- [Kasahara12] S. Kasahara, K. Hashimoto, H. Ikeda, T. Terashima, Y. Matsuda and T. Shibauchi. *Phys. Rev. B* **85**, 060503 (2012).
- [Kemper10] A. F. Kemper, T. A. Maier, S. Graser, H.-P. Cheng, P. J. Hirschfeld and D. J. Scalapino. *New J. Phys.* **12**, 073030 (2010).
- [Kini90] A. M. Kini, U. Geiser, H. H. Wang, K. D. Carlson, J. M. Williams, W. K. Kwok, K. G. Vandervoort, J. E. Thompson and D. L. Stupka. *Inorg. Chem.* **29**, 2555–2557 (1990).
- [Koepernik99] K. Koepernik and H. Eschrig. *Phys. Rev. B* **59**, 1743–1757 (1999).
- [Kohn65] W. Kohn and L. J. Sham. *Phys. Rev.* **140**, A1133–A1138 (1965).
- [Kordyuk11] A. A. Kordyuk, V. B. Zabolotnyy, D. V. Evtushinsky, T. K. Kim, I. V. Morozov, M. L. Kulić, R. Follath, G. Behr, B. Büchner and S. V. Borisenko. *Phys. Rev. B* **83**, 134513 (2011).
- [Kotliar01] G. Kotliar, S. Y. Savrasov, G. Pálsson and G. Biroli. *Phys. Rev. Lett.* **87**, 186401 (2001).
- [Kotliar06] G. Kotliar, S. Y. Savrasov, K. Haule, V. S. Oudovenko, O. Parcollet and C. A. Marianetti. *Rev. Mod. Phys.* **78**, 865–951 (2006).

- [Ku02] W. Ku, H. Rosner, W. E. Pickett and R. T. Scalettar. Phys. Rev. Lett. **89**, 167204 (2002).
- [Kuroki09] K. Kuroki, H. Usui, S. Onari, R. Arita and H. Aoki. Phys. Rev. B **79**, 224511 (2009).
- [Kutepov10] A. Kutepov, K. Haule, S. Y. Savrasov and G. Kotliar. Phys. Rev. B **82**, 045105 (2010).
- [Laad09] M. S. Laad, L. Craco, S. Leoni and H. Rosner. Phys. Rev. B **79**, 024515 (2009).
- [Lee12a] G. Lee, H. S. Ji, Y. Kim, C. Kim, K. Haule, G. Kotliar, B. Lee, S. Khim, K. H. Kim, K. S. Kim, K.-S. Kim and J. H. Shim. arXiv:1205.6526 (2012).
- [Lee12b] H. Lee, K. Foyevtsova, J. Ferber, M. Aichhorn, H. O. Jeschke and R. Valentí. Phys. Rev. B **85**, 165103 (2012).
- [Lichtenstein98] A. I. Lichtenstein and M. I. Katsnelson. Phys. Rev. B **57**, 6884–6895 (1998).
- [Lichtenstein01] A. I. Lichtenstein, M. I. Katsnelson and G. Kotliar. Phys. Rev. Lett. **87**, 067205 (2001).
- [Lieb68] Elliott H. Lieb and F. Y. Wu. Phys. Rev. Lett. **20**, 1445–1448 (1968).
- [Lichtenstein95] A. I. Lichtenstein, V. I. Anisimov and J. Zaanen. Phys. Rev. B **52**, R5467–R5470 (1995).
- [Lu08] D. H. Lu, M. Yi, S.-K. Mo, A. S. Erickson, J. Analytis, J.-H. Chu, D. J. Singh, Z. Hussain, T. H. Geballe, I. R. Fisher and Z.-X. Shen. Nature **455**, 81–84 (2008).
- [Lucarelli10] A. Lucarelli, A. Dusza, F. Pfuner, P. Lerch, J. G. Analytis, J.-H. Chu, I. R. Fisher and L. Degiorgi. New J. Phys. **12**, 073036 (2010).
- [Lumsden10] M. D. Lumsden and A. D. Christianson. J. Phys.: Condens. Matter **22**, 203203 (2010).
- [Ma09] F. Ma, W. Ji, J. Hu, Z.-Y. Lu and T. Xiang. Phys. Rev. Lett. **102**, 177003 (2009).
- [McQueen08] T. M. McQueen, M. Regalacio, A. J. Williams, Q. Huang, J. W. Lynn, Y. S. Hor, D. V. West, M. A. Green and R. J. Cava. Phys. Rev. B **78**, 024521 (2008).
- [Medici11] L. de’ Medici. Phys. Rev. B **83**, 205112 (2011).
- [Merino00] J. Merino and R. H. McKenzie. Phys. Rev. B **61**, 7996–8008 (2000).
- [Merino08] J. Merino, M. Dumm, N. Drichko, M. Dressel and R. H. McKenzie. Phys. Rev. Lett. **100**, 086404 (2008).

- [Metropolis53] N. Metropolis, A. W. Rosenbluth, M. N. Rosenbluth, A. H. Teller and E. Teller. *J. Chem. Phys.* **21**, 1087–1092 (1953).
- [Metzner89] W. Metzner and D. Vollhardt. *Phys. Rev. Lett.* **62**, 324–327 (1989).
- [Miyagawa95] K. Miyagawa, A. Kawamoto, Y. Nakazawa and K. Kanoda. *Phys. Rev. Lett.* **75**, 1174–1177 (1995).
- [Miyake08] T. Miyake, L. Pourovskii, V. Vildosola, S. Biermann and A. Georges. *J. Phys. Soc. Jpn.* **77**, 99–102 (2008).
- [Miyake10] T. Miyake, K. Nakamura, R. Arita and M. Imada. *J. Phys. Soc. Jpn.* **79**, 044705 (2010).
- [Morozov10] I. Morozov, A. Boltalin, O. Volkova, A. Vasiliev, O. Kataeva, U. Stockert, M. Abdel-Hafiez, D. Bombor, A. Bachmann, L. Harnagea, M. Fuchs, H.-J. Grafe, G. Behr, R. Klingeler, S. Borisenko, C. Hess, S. Wurmehl and B. Büchner. *Cryst. Growth Design* **10**, 4428–4432 (2010).
- [Müller-Hartmann89] E. Müller-Hartmann. *Z. Phys. B* **74**, 507–512 (1989).
- [Nakajima10] M. Nakajima, S. Ishida, K. Kihou, Y. Tomioka, T. Ito, Y. Yoshida, C. H. Lee, H. Kito, A. Iyo, H. Eisaki, K. M. Kojima and S. Uchida. *Phys. Rev. B* **81**, 104528 (2010).
- [Nakamura09a] H. Nakamura, N. Hayashi, N. Nakai, M. Okumura and M. Machida. *Physica C* **469**, 908 – 911 (2009).
- [Nakamura09b] K. Nakamura, Y. Yoshimoto, T. Kosugi, R. Arita and M. Imada. *J. Phys. Soc. Jpn.* **78**, 083710 (2009).
- [Negele78] W. Negele and H. Orland. *Quantum Many-Particle Systems*. Addison-Wesley (1978).
- [Paglione10] J. Paglione and R. L. Greene. *Nat Phys* **6**, 645–658 (2010).
- [Parcollet04] O. Parcollet, G. Biroli and G. Kotliar. *Phys. Rev. Lett.* **92**, 226402 (2004).
- [Pavarini04] E. Pavarini, S. Biermann, A. Poteryaev, A. I. Lichtenstein, A. Georges and O. K. Andersen. *Phys. Rev. Lett.* **92**, 176403 (2004).
- [Penn66] D. R. Penn. *Phys. Rev.* **142**, 350–365 (1966).
- [Perdew92] J. P. Perdew and Y. Wang. *Phys. Rev. B* **45**, 13244–13249 (1992).
- [Perdew96] J. P. Perdew, K. Burke and M. Ernzerhof. *Phys. Rev. Lett.* **77**, 3865–3868 (1996).
- [Pitcher08] M. J. Pitcher, D. R. Parker, P. Adamson, S. J. C. Herkelrath, A. T. Boothroyd, R. M. Ibberson, M. Brunelli and S. J. Clarke. *Chem. Commun.* pages 5918–5920 (2008).
- [Platt11] C. Platt, R. Thomale and W. Hanke. *Phys. Rev. B* **84**, 235121 (2011).

- [Potthoff03] M. Potthoff, M. Aichhorn and C. Dahnken. *Phys. Rev. Lett.* **91**, 206402 (2003).
- [Powell06] B. J. Powell and R. H. McKenzie. *J. Phys.: Condens. Matter* **18**, R827 (2006).
- [Powell11] B. J. Powell and R. H. McKenzie. *Rep. Prog. Phys.* **74**, 056501 (2011).
- [Prokof'ev96] N. Prokof'ev, B. Svistunov and I. Tupitsyn. *JETP Lett.* **64**, 911–916 (1996).
- [Pruschke89] Th. Pruschke and N. Grewe. *Z. Phys. B* **74**, 439–449 (1989).
- [Putzke12] C. Putzke, A. I. Coldea, I. Guillaumón, D. Vignolles, A. McCollam, D. LeBoeuf, M. D. Watson, I. I. Mazin, S. Kasahara, T. Terashima, T. Shibauchi, Y. Matsuda and A. Carrington. *Phys. Rev. Lett.* **108**, 047002 (2012).
- [Qazilbash09] M. M. Qazilbash, J. J. Hamlin, R. E. Baumbach, Lijun Zhang, D. J. Singh, M. B. Maple and D. N. Basov. *Nat. Phys.* **5**, 647–650 (2009).
- [Qureshi10] N. Qureshi, Y. Drees, J. Werner, S. Wurmehl, C. Hess, R. Klingeler, B. Büchner, M. T. Fernández-Díaz and M. Braden. *Phys. Rev. B* **82**, 184521 (2010).
- [Qureshi12] N. Qureshi, P. Steffens, Y. Drees, A. C. Komarek, D. Lamago, Y. Sidis, L. Harnagea, H.-J. Grafe, S. Wurmehl, B. Büchner and M. Braden. *Phys. Rev. Lett.* **108**, 117001 (2012).
- [Rohringer11] G. Rohringer, A. Toschi, A. Katanin and K. Held. *Phys. Rev. Lett.* **107**, 256402 (2011).
- [Rozenberg92] M. J. Rozenberg, X. Y. Zhang and G. Kotliar. *Phys. Rev. Lett.* **69**, 1236–1239 (1992).
- [Rubtsov05] A. N. Rubtsov, V. V. Savkin and A. I. Lichtenstein. *Phys. Rev. B* **72**, 035122 (2005).
- [Rubtsov08] A. N. Rubtsov, M. I. Katsnelson and A. I. Lichtenstein. *Phys. Rev. B* **77**, 033101 (2008).
- [Sahebsara08] P. Sahebsara and D. Sénéchal. *Phys. Rev. Lett.* **100**, 136402 (2008).
- [Sakai94] O. Sakai and Y. Kuramoto. *Solid State Commun.* **89**, 307 – 311 (1994).
- [Sandvik91] A. W. Sandvik and J. Kurkijärvi. *Phys. Rev. B* **43**, 5950–5961 (1991).
- [Sandvik98] A. W. Sandvik. *Phys. Rev. B* **57**, 10287–10290 (1998).
- [Sanna11] A. Sanna, F. Bernardini, G. Profeta, S. Sharma, J. K. Dewhurst, A. Lucarelli, L. Degiorgi, E. K. U. Gross and S. Massidda. *Phys. Rev. B* **83**, 054502 (2011).

- [Savrasov01] S. Y. Savrasov, G. Kotliar and E. Abrahams. *Nature* **410**, 793–795 (2001).
- [Sekiyama04] A. Sekiyama, H. Fujiwara, S. Imada, S. Suga, H. Eisaki, S. I. Uchida, K. Takegahara, H. Harima, Y. Saitoh, I. A. Nekrasov, G. Keller, D. E. Kondakov, A. V. Kozhevnikov, Th. Pruschke, K. Held, D. Vollhardt and V. I. Anisimov. *Phys. Rev. Lett.* **93**, 156402 (2004).
- [Shimizu10] Y. Shimizu, H. Kasahara, T. Furuta, K. Miyagawa, K. Kanoda, M. Maesato and G. Saito. *Phys. Rev. B* **81**, 224508 (2010).
- [Si94] Q. Si, M. J. Rozenberg, G. Kotliar and A. E. Ruckenstein. *Phys. Rev. Lett.* **72**, 2761–2764 (1994).
- [Si08] Q. Si and E. Abrahams. *Phys. Rev. Lett.* **101**, 076401 (2008).
- [Singh08] D. J. Singh. *Phys. Rev. B* **78**, 094511 (2008).
- [Singh09] D. J. Singh. *Physica C* **469**, 418 – 424 (2009).
- [Skornyakov09] S. L. Skornyakov, A. V. Efremov, N. A. Skorikov, M. A. Korotin, Yu. A. Izyumov, V. I. Anisimov, A. V. Kozhevnikov and D. Vollhardt. *Phys. Rev. B* **80**, 092501 (2009).
- [Skornyakov10] S. L. Skornyakov, N. A. Skorikov, A. V. Lukoyanov, A. O. Shorikov and V. I. Anisimov. *Phys. Rev. B* **81**, 174522 (2010).
- [Stauber10] T. Stauber and G. Gómez-Santos. *Phys. Rev. B* **82**, 155412 (2010).
- [Stewart11] G. R. Stewart. *Rev. Mod. Phys.* **83**, 1589–1652 (2011).
- [Su09] Y. Su, P. Link, A. Schneidewind, Th. Wolf, P. Adelman, Y. Xiao, M. Meven, R. Mittal, M. Rotter, D. Johrendt, Th. Brueckel and M. Loewenhaupt. *Phys. Rev. B* **79**, 064504 (2009).
- [Suzuki09] S. Suzuki, S. Miyasaka, S. Tajima, T. Kida and M. Hagiwara. *J. Phys. Soc. Jpn.* **78**, 114712 (2009).
- [Tapp08] J. H. Tapp, Z. Tang, B. Lv, K. Sasmal, B. Lorenz, P. C. W. Chu and A. M. Guloy. *Phys. Rev. B* **78**, 060505 (2008).
- [Taylor11] A. E. Taylor, M. J. Pitcher, R. A. Ewings, T. G. Perring, S. J. Clarke and A. T. Boothroyd. *Phys. Rev. B* **83**, 220514(R) (2011).
- [Tegel08] M. Tegel, M. Rotter, V. Weiß, F. M. Schappacher, R. Pöttgen and D. Johrendt. *J. Phys.: Condens. Matter* **20**, 452201 (2008).
- [Thomale11] R. Thomale, C. Platt, W. Hanke and B. A. Bernevig. *Phys. Rev. Lett.* **106**, 187003 (2011).
- [Thomas25] W. Thomas. *Naturwissenschaften* **13**, 627 (1925).
- [Torikachvili08] M. S. Torikachvili, S. L. Bud'ko, N. Ni and P. C. Canfield. *Phys. Rev. Lett.* **101**, 057006 (2008).

- [Toschi07] A. Toschi, A. A. Katanin and K. Held. *Phys. Rev. B* **75**, 045118 (2007).
- [Umezawa12] K. Umezawa, Y. Li, H. Miao, K. Nakayama, Z.-H. Liu, P. Richard, T. Sato, J. B. He, D.-M. Wang, G. F. Chen, H. Ding, T. Takahashi and S.-C. Wang. *Phys. Rev. Lett.* **108**, 037002 (2012).
- [Vollhardt11] D. Vollhardt, P. Blöchl, F. Lechermann, J. Kuneš, M. Kollar, E. Pavarini, F. Aryasetiawan, E. Koch, N. Blümer, P. Werner, A. I. Lichtenstein, H. Ebert, K. Held and H. Tjeng. The LDA+DMFT approach to strongly correlated systems. Forschungszentrum Jülich (2011).
- [Wang09] X. Wang, E. Gull, L. de' Medici, M. Capone and A. J. Millis. *Phys. Rev. B* **80**, 045101 (2009).
- [Weber12] C. Weber, D. D. O'Regan, N. D. M. Hine, P. B. Littlewood, G. Kotliar and M. C. Payne. arXiv:1206.0412 (2012).
- [Werner06a] P. Werner, A. Comanac, L. de' Medici, M. Troyer and A. J. Millis. *Phys. Rev. Lett.* **97**, 076405 (2006).
- [Werner06b] P. Werner and A. J. Millis. *Phys. Rev. B* **74**, 155107 (2006).
- [Williams90] J. M. Williams, A. M. Kini, H. H. Wang, K. D. Carlson, U. Geiser, L. K. Montgomery, G. J. Pyrka, D. M. Watkins and J. M. Kommers. *Inorg. Chem.* **29**, 3272–3274 (1990).
- [Wimmer81] E. Wimmer, H. Krakauer, M. Weinert and A. J. Freeman. *Phys. Rev. B* **24**, 864–875 (1981).
- [Wu09a] D. Wu, N. Barišić, N. Drichko, S. Kaiser, A. Faridian, M. Dressel, S. Jiang, Z. Ren, L. J. Li, G. H. Cao, Z. A. Xu, H. S. Jeevan and P. Gegenwart. *Phys. Rev. B* **79**, 155103 (2009).
- [Wu09b] G. Wu, Y. L. Xie, H. Chen, M. Zhong, R. H. Liu, B. C. Shi, Q. J. Li, X. F. Wang, T. Wu, Y. J. Yan, J. J. Ying and X. H. Chen. *J. Phys.: Condens. Matter* **21**, 142203 (2009).
- [Wu10] D. Wu, N. Barišić, P. Kallina, A. Faridian, B. Gorshunov, N. Drichko, L. J. Li, X. Lin, G. H. Cao, Z. A. Xu, N. L. Wang and M. Dressel. *Phys. Rev. B* **81**, 100512(R) (2010).
- [Yamashita09] M. Yamashita, N. Nakata, Y. Senshu, S. Tonegawa, K. Ikada, K. Hashimoto, H. Sugawara, T. Shibauchi and Y. Matsuda. *Phys. Rev. B* **80**, 220509 (2009).
- [Yang09] L. X. Yang, Y. Zhang, H. W. Ou, J. F. Zhao, D. W. Shen, B. Zhou, J. Wei, F. Chen, M. Xu, C. He, Y. Chen, Z. D. Wang, X. F. Wang, T. Wu, G. Wu, X. H. Chen, M. Arita, K. Shimada, M. Taniguchi, Z. Y. Lu, T. Xiang and D. L. Feng. *Phys. Rev. Lett.* **102**, 107002 (2009).
- [Yasin11] S. Yasin, M. Dumm, B. Salameh, P. Batail, C. Me'zière and M. Dressel. *Eur. Phys. J. B* **79**, 383–390 (2011).



- [Yi09] M. Yi, D. H. Lu, J. G. Analytis, J.-H. Chu, S.-K. Mo, R.-H. He, M. Hashimoto, R. G. Moore, I. I. Mazin, D. J. Singh, Z. Hussain, I. R. Fisher and Z.-X. Shen. *Phys. Rev. B* **80**, 174510 (2009).
- [Yildirim08] T. Yildirim. *Phys. Rev. Lett.* **101**, 057010 (2008).
- [Yin11] Z. P. Yin, K. Haule and G. Kotliar. *Nature Mater.* **10**, 932–935 (2011).
- [Ylvisaker09] E. R. Ylvisaker, W. E. Pickett and K. Koepernik. *Phys. Rev. B* **79**, 035103 (2009).
- [Zhang93] X. Y. Zhang, M. J. Rozenberg and G. Kotliar. *Phys. Rev. Lett.* **70**, 1666–1669 (1993).
- [Zhang10] Y.-Z. Zhang, I. Opahle, H. O. Jeschke and R. Valentí. *Phys. Rev. B* **81**, 094505 (2010).



# *Acknowledgments*

The completion of this thesis marks the end of a three year period at the University of Frankfurt which has shaped my way of thinking and acting to a substantial degree.

First and foremost, I thank my supervisor Roser Valentí who gave me the opportunity to write this thesis in her group. Back then, my application was on a very short notice and very informal, yet I was granted to start my work just a few days after. I'm still very grateful for this leap of faith. In all this time, I enjoyed most that our collaboration was based on trust and goodwill rather than control, giving me the chance to grow on my own successes and failures.

I also would like to thank Harald Jeschke for his constant support and guidance over these years. His attention to detail is unmatched and many of our discussions were valuable learnings for me.

Kateryna Foyevtsova has been my office mate during all this time and while I never managed executing my evil plan of getting her office corner by the window, I greatly benefited from countless discussions on density functional theory and many other topics, and her great work on the LAPW projectors.

I would like to thank Lorenz Bartosch for taking over the role of the second referee of my thesis, and Karsten Held and Markus Aichhorn for their consent to be potential co-referees. I'm also grateful to Markus for his very valuable help and advice with LDA+DMFT which helped me out more than once when I was stuck.

Thanks goes to Moritz Püschel and Kateryna for the careful and tedious proofreading of this thesis.

Finally, I deeply thank my wife Blanca for her patience and support during this time. I'm very sorry for the many night shifts that I invested in this work; this is over now.

I acknowledge financial support from the Deutsche Forschungsgemeinschaft through SPP 1458, TR49, and FOR1346, and from the Helmholtz Association through HA216/EMMI.



## RESUME

### PERSONAL DETAILS

---

Full Name	Johannes Friedrich Constantin Ferber
Date and Place of Birth	5 September 1979 in Munich
Citizenship	German
Marital Status	Married, one daughter

### EDUCATION

---

since 10/2009	PhD in Theoretical Solid State Physics, University of Frankfurt: <i>Density Functional Theory and Dynamical Mean Field Theory: Applications to Correlated Electron Materials</i> , supervised by Prof. Dr. Roser Valentí
01/2007–07/2009	M.Sc. in Mathematical Finance at University of Oxford, UK
08/2005–09/2005	Research visit at University of California, Berkeley, USA
10/2000–08/2005	Diploma in Physics at Ludwig-Maximilians-Universität Munich: <i>3-Qubit Interactions for Superconducting Quantum Computers</i> , supervised by Prof. Dr. Frank Wilhelm
07/2003–09/2003	Summer Student at CERN, Geneva, Switzerland

### EMPLOYMENT

---

01/2006–12/2008	Consultant, d-fine GmbH, Frankfurt
07/2002–12/2005	Freelance software developer, Inst. Prof. Neuburger & Partner, Munich

## PUBLICATIONS

---

- 2012 *LDA+DMFT for organic molecular crystals: spectral and optical properties of  $\kappa$ -(BEDT-TTF)<sub>2</sub>Cu[N(CN)<sub>2</sub>]Cl*,  
**J. Ferber**, K. Foyevtsova, H. O. Jeschke, R. Valentí, arXiv:1209.4466
- 2012 *Fermi surface topology of LaFePO and LiFeP*,  
**J. Ferber**, H. O. Jeschke, R. Valentí,  
Phys. Rev. Lett. **109**, 236403 (2012)
- 2012 *LDA+DMFT study of the effects of correlation in LiFeAs*,  
**J. Ferber**, K. Foyevtsova, R. Valentí, H. O. Jeschke,  
Phys. Rev. B **85**, 094505 (2012)
- 2012 *Dynamical cluster approximation within an augmented plane wave framework: Spectral properties of SrVO<sub>3</sub>*,  
H. Lee, K. Foyevtsova, **J. Ferber**, M. Aichhorn, H. O. Jeschke, R. Valentí,  
Phys. Rev. B. **85**, 165103 (2012)
- 2010 *Analysis of spin-density wave conductivity spectra of iron pnictides in the framework of density functional theory*,  
**J. Ferber**, Y.-Z. Zhang, H. O. Jeschke, R. Valentí,  
Phys. Rev. B. **82**, 165102 (2010)
- 2010 *Efficient creation of multipartite entanglement in flux qubits*,  
**J. Ferber**, F. K. Wilhelm, Nanotechnology **21**, 274015 (2010)
- 2007 *Optimal control of coupled Josephson qubits*,  
A. Spörl, T. Schulte-Herbrüggen, S. J. Glaser, V. Bergholm, M. J. Storcz,  
**J. Ferber**, F. K. Wilhelm, Phys. Rev. A. **75**, 012302 (2007)
- 2003 *Physik für die Westentasche*,  
Harald Lesch und das QUOT-Team. Piper Verlag, 2003
-

